Design and Characterization of Novel Protein Kinase Inhibitors Involved in Neuronal Complications of Diabetes

THESIS

Submitted in partial fulfilment of the

requirements for the degree of

DOCTOR OF PHILOSOPHY

by

RAM KUMAR MISHRA

2006PH08441H

Under the supervision of

Prof. P. Yogeeswari

BIRLA INSTITUTE OF TECHNOLOGY & SCIENCE, PILANI

2015

BIRLA INSTITUTE OF TECHNOLOGY & SCIENCE, PILANI

CERTIFICATE

This is to certify that the thesis entitled *"**Design and Characterization of Novel Protein Kinase Inhibitors Involved in Neuronal Complications of Diabetes**"* and submitted by RAM KUMAR MISHRA, ID NO. 2006PH08441H for award of Ph.D. degree of the Institute embodies original work done by him under my supervision.

Signature in of the Supervisor:

Name in capital letters: **P. Yogeeswari**

Designation: Professor

Date:

ACKNOWLEDGEMENTS

It is a great pleasure and privilege in expressing my deep gratitude towards my research supervisor, **Prof. P. Yogeeswari**, Professor and Associate Dean (Sponsored Research and Consultancy Division), Department of Pharmacy, BITS-Pilani, Hyderabad Campus for her continuous guidance, suggestions and support. She was always an inspiration to me for my work.

I deeply acknowledge and heartfelt thanks to my DAC members, **Prof. D. Sriram**, (B. K. Birla & Sarala Birla Chair Professor) and **Dr. Onkar P. Kulkarni**, (Assistant Professor), Department of Pharmacy, BITS-Pilani, Hyderabad Campus for their valuable suggestions and encouragements during this period.

I am grateful to **Prof. Bijendra N. Jain**, Vice-Chancellor, BITS-Pilani and **Prof. V. S. Rao**, Director, BITS-Pilani, Hyderabad Campus for allowing me to carry out my doctoral research work in the institute.

I am thankful to **Prof. M. M. S. Anand**, Registrar and **Prof. S. K. Verma**, Dean, Academic Research (Ph.D. Programme), BITS Pilani for their support to do my research work.

I would like to express my sincere thanks to **Prof. M. B. Srinivas**, Dean, Administration and **Dr. Vidya Rajesh**, Associate Dean, Academic Research (Ph.D. Programme), BITS-Pilani, Hyderabad campus for their continuous support and encouragement during my research work.

I would like to express my gratitude to **Dr. Srikant Charde**, Assistant Professor and Head, Department of Pharmacy, BITS-Pilani, Hyderabad campus for providing me necessary laboratory facilities and for having helped me at various stages of my research work.

I sincerely acknowledge the help rendered by **Dr. Punna Rao** and other faculty members, Department of Pharmacy, BITS-Pilani, Hyderabad campus.

I am grateful to express my sincere thanks and acknowledgement to my supervisor's collaborator **Dr. Neerja Kaushik Basu**, Rutgers Cancer Institute of New Jersy, USA for contributing to suggestions and support in biological assays.

I am very much grateful to all my colleagues including **Dr. Pritesh Bhat**, **Dr. Arvind Semwal**, **Dr. Monika Semwal**, **Dr. Jean Kumar**, **Dr. Mallika Alwala**, **Ms. Reshma Alokam**, **Mr. Gangadhar Matharsala**, **Mr. Ganesh Pedgaonkar**, **Mr. Madu Babu Battu**,

Ms. Rukaiyya, **Ms. Shalini**, **Mr. Srikant**, **Mr. Saketh Sriram**, **Ms. Brindha**, **Mr. Koushik**, **Mrs. Renuka**, **Ms. Priyanka Suryadevara**, **Ms. Priyanka Purkayastha**, **Mr. Praveen**, **Mr. Mahibalan S.**, **Mr. Brahmam**, **Mr. Ganesh S**., **Mr. Manoj**, **Mr. Bobesh**, **Ms. Sreedevi**, **Mrs. Hasitha Shilpa**, **Mr. Shailender Joseph**, **Mr. Suman Labala**, **Mr. Guilherme Peterson**, **Mr. Bomba Tatsinku Francis Desire**, **Mr. Abhik Seal**, **Mr. Poornesh M**., **Mr. Anup Jose**, **Mr. Omkar**, **Ms. Preethi**, **Mrs. Radhika N.**, **late Thimmappa** and **late Srividya** for the time they had spent for me and helped me to complete my work.

I also would like to thank my students **Mr. Aquib Gaus**, **Mr. Deepak Sharma**, **Mr. Prabhu**, **Mr. Ranga Charyulu**, **Mr. Sarthak Singhal**, **Mr. Geetasai Srivatsav**, **Mr. Saketh M.**, **Ms. Khushbu Gupta** and **Ms. Sanjana** for their help and assistance.

I express my thanks to laboratory attendants **Mr. Rajesh**, **Mrs. Rekha**, **Mr. Srinivas**, **Mr. Ram** and **Mrs. Sarita** for all their support.

Many friends have helped me stay sane through these difficult years. Their support and joyous nature helped me overcome setbacks and stay focused on my studies-**Mr. Ujjwal Prasad**, **Mr. Prakash N Singhdeo**, **Mr. Diwakar Jha**, **Mr. Amit Kumar**, **Mr. Shantam Majumdar**, **Mr. Tapesh Rathod** and **Mr. Santosh Mishra**. I greatly value their friendship and I deeply appreciate their belief in me.

I would like to thank my loving parents **Mr. Ashok Kumar Mishra** and **Mrs. Jyoti Mishra**, my siblings: **Major Shyam Kumar Mishra**, **Mrs. Shweta Tripathi** for all their financial and moral support.

Last but most important I would like to thank and deeply appreciate my beloved wife **Mrs. Rashmi Mishra** for her invaluable patience and support, and the youngest member of my family, **Master Rishit Mishra** for showering me with the joys of fatherhood.

Lastly, I would like to thank **Goddess Saraswati** who has given me this opportunity.

Date: **Ram Kumar Mishra**

DEDICATION

This thesis is dedicated to my beloved son, Rishit Mishra.

(Born: October 9, 2014)

ABSTRACT

Diabetes mellitus is recognized as a group of heterogeneous disorder with the common elements of hyperglycemia and glucose intolerance due to insulin deficiency, impaired effectiveness of insulin action, or both. More than 20 disorders, including neuropathy have been identified as long term diabetic complications. With the intention of developing novel protein kinase inhibitors effective against painful diabetic neuropathy and neurodegeneration, in this study we explored two different protein kinases, which were reported to be overexpressed: Rho kinase (ROCK) and protein kinase C β-II (PKCβ-II). To identify new lead molecules for ROCK and PKCβ-II inhibition, we employed a series of computer-aided drug design approaches, utilizing the knowledge of previously known active inhibitors and successfully derived novel diverse scaffolds. In addition, we also identified inhibitors from *in house* dataset, which were found to be active against PKCβ-II.

Inhibitor bound crystal structures were used to generate e-pharmacophore and shape based queries, and were validated against different sets of databases containing known actives and drug-like molecules. The validated e-pharmacophore model and shape-based queries for ROCK inhibitors were used as templates for virtual database screening of publicly available Asinex database which contained 525,807 molecules. The output of database screening process was refined and was subjected to docking. Finally 8 molecules were selected considering their docking score, pharmacophoric overlap (fitness score), visual inspection and their calculated pharmacokinetic properties. The most potent molecule, compound **R8** exhibited an IC_{50} value of 1.5 µM against ROCK activity and in cell-based assays inhibited methylmercury (MeHg) induced neurotoxicity of IMR-32 cells with GI_{50} value of 0.27 µM. Notably, differential scanning fluorimetric analysis revealed that ROCK protein complexed with compound **R8** was found to have enhanced stability relative to fasudil, a validated nanomolar range ROCK inhibitor. The identified lead thus constituted a prototypical molecule for further optimization and development as anti-ROCK inhibitor.

In another approach, we carried out the design, synthesis and characterization of novel 2,6-diaminopyrimidine derivatives as potential ROCK inhibitors. We selected this previously reported 7-azaindole hinge-binding scaffold, which was tethered to aminopyrimidine core. We retained the aminopyrimidine core and applied various substitutions in the head region of the molecule. These compounds were docked to the ROCK active site and finally we selected 8 compounds based on docking score, visual inspection and pharmacokinetic parameters.

These compounds were synthesized and subjected to *in vitro* as well as extensive pre-clinical studies in a single dose using neuropathic pain models in rodents to assess their potential to alleviate neuropathic pain including diabetic neuropathy. Compounds were also evaluated at 10 mg/kg dose for their behavioural effect on MeHg induced neurotoxic model to study their effects against memory, cognition, gait impairment and depression which were indicated in diabetic patients. Since diabetes-induced neurodegeneration is a long term complications, and is tedious to replicate in animals, we employed MeHg induced model as it was specific for ROCK activation. Compound N^4-(4-(naphthalene-2-yloxy)phenyl)pyrimidine-2,4,6-triamine (**RK7**) emerged as the most potent ROCK inhibitor (IC_{50}=2.37 nM) with encouraging *in vitro* and *in vivo* profiles indicating its usefulness in the treatment of various neurological disorders including diabetic neuropathy.

We also undertook the design and characterization of novel PKCβ-II inhibitors by utilizing energy based pharmacophore model derived from the ligand-bound crystal structure of PKCβ-II. A systematic structure-based design protocol was employed to identify diverse compounds. First, a number of e-pharmacophores were generated from available crystal structure, and validated to be used as template for database screening. The publicly available Asinex database was used for virtual screening processes and docking studies. In addition, we also utilized to test the likelihood of finding suitable molecules from our *in house* BITS-database (BITS-DB); we docked the molecules to PKCβ-II active site. The output from Asinex and BITS-DB docking runs were further refined considering their docking score, visual inspection and their calculated pharmacokinetic properties. Finally, we shortlisted 13 molecules from Asinex and 15 from BITS-DB for biological screening. Overall, **PB9** was identified as the most promising molecule with PKCβ-II inhibition with IC_{50}=12.72 μM, and exhibited no cytotoxicity at 100 μM. Compound **PB9** exhibited better potency in diabetic neuropathy as well as MeHg-induced neurodegeneration in animal models, and emerged as promising lead for further optimization.

TABLE OF CONTENTS

LIST OF TABLES

LIST OF ILLUSTRATIONS

LIST OF ACRONYMS

A	Acceptor atom
ACC	Anterior cingulate cortex
AGC	Protein kinase A, G, and C families (PKA, PKC, PKG)
AGE	Advanced glycation end products
AD	Alzheimer disease
ADME	Absorption, distribution, metabolism, elimination
ADP-Glo	A luminescent kinase detection assay
ANOVA	Analysis of variance
AUC	Area under curve
ATP	Adenosine tri phosphate
BEDROC	Boltzmann-enhanced discrimination of receiver operating characteristic
BITS-DB	BITS-Pilani, Hyderabad Campus *in house* database
CC_{50}	Concentration that kills 50% of cultured cells
CCI	Chronic constriction injury
cGMP	Cyclic guanosine monophosphate
CMC	Carboxymethyl cellulose
CNS	Central nervous system
CPI	C-kinase potentiated protein phosphatase-1 inhibitor, 17 kDa
D	Donor atom
DAG	Diacyl glycerol
DCFH-DA	Dichloro-dihydro-fluorescein diacetate assay
DME	Diabetic macular edema
DMF	Dimethyl formamide
DMSO	Dimethyl sulfoxide

DR	Diabetic retinopathy
DRG	Dorsal root ganglion
DRS	Diabetic retinopathy study
DSF	Differential scanning fluorimetry
DTT	Dithiothreitol
DUD	Directory of useful decoys
E-pharmacophore	Energetically optimized structure-based pharmacophores
ED	Erectile dysfunction
EF	Enrichment factor
EON	Electrostatics comparison program by OpenEye scientific software
ERM	Ezrin/radixin/moesin proteins
ETDRS	Early treatment diabetic retinopathy study
FBS	Fetal bovine serum
GAP	GTPase activating proteins
GDI	Guanine dissociation inhibitors
GDM	Gestational diabetes mellitus
GDP	Guanosine diphosphate
GEF	Guanine exchange factors
GGTase-1	Geranylgeranyltransferase-1
GH	Goodness of hit
GI_{50}	Concentration of the drug which inhibits the growth of cells by 50%
Glide HTVS	High throughput virtual screening mode of Glide docking
Glide SP	Standard precision mode of Glide docking
Glide XP	Xtra precision mode of Glide docking
GTP	Guanosine tri phosphate
H	Hydrophobic moiety

HEK	Human embryonic kidney cells
HEPES	(4-(2-hydroxyethyl)-1-piperazineethanesulfonic acid), buffering agent
HTVS	High throughput virtual screening mode of docking
IC_{50}	Concentration of the drug exhibiting 50% response
IMR	A human neuroblastoma cell line
IOP	Intraocular pressure
IPTG	Isopropyl β-D-1-thiogalactopyranoside
IRS-1	Insulin receptor substrate-1
LDH	Lactate dehydrogenase
LIM	LIM domain kinase
MBP	Myelin basic protein
MDCK	Madin-darby canine kidney epithelial cell line
MeHg	Methylmercury (II) chloride
MEM	Minimum essential medium, a cell culture media
MLC	Myosin light-chain kinase
MTT	((3-(4,5-Dimethylthiazol-2-yl)-2,5-diphenyltetrazolium bromide)
MW	Molecular weight (D)
MYPT-1	Myosin phosphatase target subunit 1
NAD	Nicotinamide adenine dinucleotide
NADH	Reduced form of NAD
NCV	Nerve conduction velocity
NOR	Novel object recognition test
NPDR	Non-proliferative diabetic retinopathy
OPLS	The optimized potentials for liquid simulations force field
PBSG	Phosphate-buffered saline supplemented with glucose
PDB	Protein data bank repository (http://www.rcsb.org/pdb)

PE	Plating efficiency
PEP	Phosphoenolpyruvate
pH	Measure of acidity or basicity
PH	Pleckstrin homology domain
PHASE	Package of pharmacophore modeling tools
PK	Pyruvate kinase
pK_a	Negative base-10 logarithm of the acid dissociation constant
p-PKC	Polyclonal IgG, corresponding to phosphorylated protein kinase C
PKCβ-II	β-II subtype of protein kinase C
PROPKA	Package to predict the pKa value of a residue
PTEN	Phosphatase and tensin homolog protein
PTSA	p-toluene-sulfonic acid
PWT	50% Paw withdrawal threshold
QPlogBB	Predicted brain/blood partition coefficient
QPlogHERG	Predicted IC_{50} value for blockage of HERG k^+ channels
QPlogkP	Predicted skin permeability
QPlogPo/w	Predicted octanol and water coefficient
QPlogS	Predicted aqueous solubility
QPPCaco	Predicted caco cell-2 permeability
QPPMDCK	Predicted apparent MDCK cell permeability
R	Aromatic ring
RACK	Receptors for activated C kinases
RHEL	Red hat enterprise linux operating system
ROCK	Rho Kinase enzyme
ROCs	Receiver operating characteristics
ROCS	Shape-based virtual screening tool

ROS	Reactive oxygen species
SA	Swiss albino mice
SDS-PAGE	Sodium dodecyl sulfate polyacrylamide gel electrophoresis
SEM	Standard error of mean
SF	Survival fraction
STZ	Streptozotocin
TBG	Thyroxine binding globulin
VEGF	Vascular endothelial growth factor
VSMC	Vascular smooth muscle cells

"A man is but the product of his beliefs.
What he believes, he becomes."
-Mahatma Gandhi

Chapter 1. Introduction

1.1 History and worldwide prevalence of diabetes

The first documented case of diabetes was recognized back in 1500 B.C. by the ancient Egyptians [1]. They considered it as a rare condition, in which a person lost weight, urinated excessively and the urine tasted sweet. Indian physicians around the same time identified the disease as madhumeha (madhu=honey, meha=urine) by observing that the urine would attract ants. The term diabetes mellitus was first used by the Greek physician Aretaeus during 80 to 138 C.E. For the first time in 1776, Matthew Dobson, an English physician and experimental physiologist measured the concentration of glucose and found it to be elevated [2]. Diabetes was recognized clinically in around 1812 [1].

Diabetes is also considered as a lifestyle disease. A lifestyle disease (also referred as diseases of longevity or diseases of civilization) is a disease occurring frequently in industrialized countries. In recent years, the total number of people getting diagnosed with diabetes are rising rapidly worldwide. According to a recent report published by International Diabetes Association, about 8.3% of adults or 382 million people worldwide are reported to have diabetes. Among these, almost 80% live in under-developed or developing countries. If the data is extrapolated assuming the same trend to be continued, by 2035,592 million people or $1/10^{th}$ of the adult population worldwide would have diabetes. In other terms, this means approximately three new cases per sec, or almost 10 million people per year (Figures 1-1, 1-2) [3].

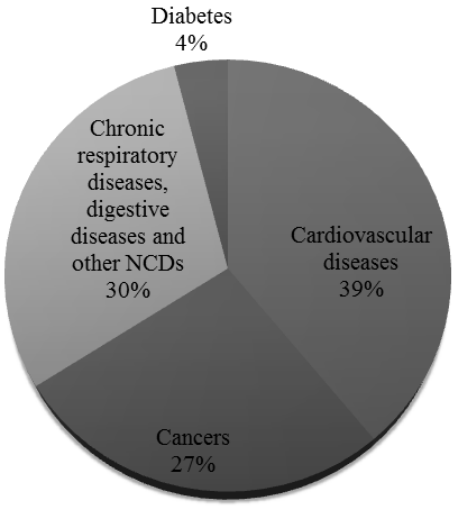

Figure 1-2. Proportion of non-communicable disease deaths by cause [3].

The main reason behind the prevalence of diabetes could be attributed to changes in patterns like reduced physical activity and dietary changes. Multiple theories have been proposed to explain the pathogenesis of various complications involving retina, glomeruli, peripheral nerves, cardiovascular tissues, wound healing, and pregnancy. Although a single theory has not been demonstrated to explain all these changes, a few have emerged that encompasses most of the data that have accumulated in this area.

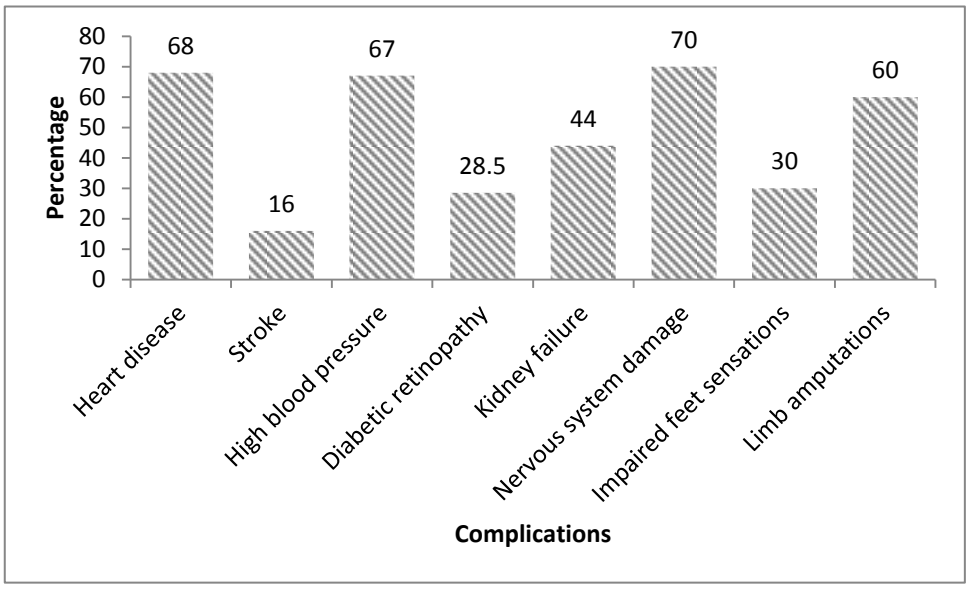

Figure 1-1. Statistics on diabetes complications [3].

1.2 Classification of diabetes mellitus

Normally diabetes can be divided into three types:

1.2.1 Type 1 diabetes

This form of diabetes accounts for 5-10% of diabetes cases. It has also been previously known as insulin-dependent or juvenile-onset diabetes. It results from a cell-mediated autoimmune destruction of the β-cells of the pancreas.

1.2.2 Type 2 diabetes

This form of diabetes accounts for almost 90-95% of diabetes cases. It was also previously referred to as non-insulin dependent diabetes or adult onset diabetes. It is also often thought that these individuals do not need insulin treatment to survive. Obesity is the most common symptom of type 2 diabetes, which itself causes some degree of insulin resistance.

1.2.3 Gestational diabetes mellitus

For many years, gestational diabetes mellitus (GDM) has been recognized during pregnancy and has been indicated as a degree of glucose intolerance. In most of the cases, it gets cured with delivery, but there are cases where the glucose intolerance stays for a longer period which would lead to type 2 diabetes in adult women.

1.2.4 Other types of diabetes

Diabetes could be a consequence of (a) pancreatic tissue removal or pancreatic disease, (b) endocrine diseases like acromegaly, cushing's syndrome, pheochromocytoma, somatostatinoma and primary aldosteronism, or (c) administration of drugs or chemicals causing hyperglycaemia. Diabetes could also be associated with genetic syndromes leading to defects in insulin receptors or antibodies to receptors with or without associated immune disorders [4].

1.3 Diabetes complications

Diabetes can cause many serious complications like hypertension, heart failure, angina, myocardial infarction, atherosclerosis, coronary and cerebral vasospasm, alzheimer's disease (AD), multiple sclerosis, spinal cord injury, neuropathic pain, osteoporosis, cancer, bronchial asthma, glaucoma, fungal cystitis and mucomycosis. These complications can be briefly classified into four major categories: (a) cardiovascular, (b) nephropathy, (c) neuropathy and (d) infections (Figure 1-3). If these complications are not diagnosed in the early stages, over the years, these might emerge as long-term diabetic complications resulting in reduced quality of life and increased mortality. Symptomatic treatments seem to be the only way for

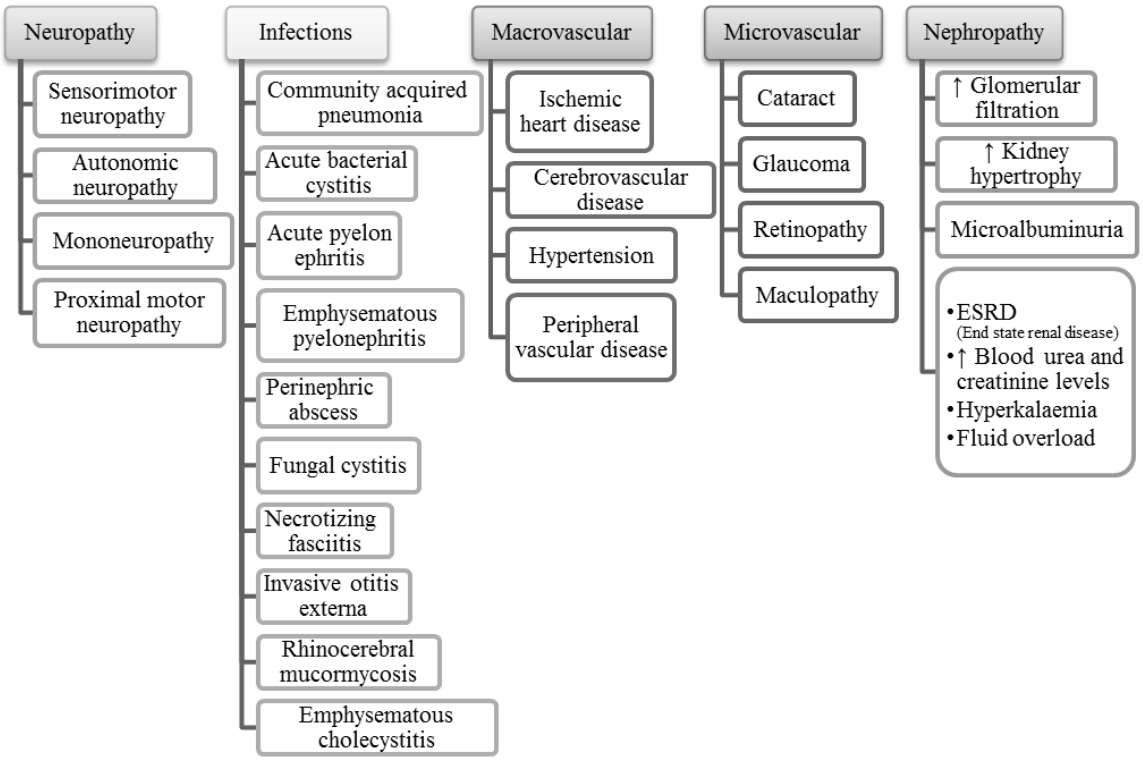

Figure 1-3. Major diabetic complications.

these complications if detected at the early stage. But since these long-term complications go undetected for years, when the symptoms start to appear due to damage, and there are limited options for the treatment of long term complications.

1.4 Neuronal complications of diabetes

1.4.1 Diabetic neuropathy

Diabetic peripheral neuropathy is the most common complication of long term diabetes [5]. The pathophysiology includes demyelination and axonal degeneration of myelinated fibres, along with, degeneration with regeneration of unmyelinated fibres [6]. Loss of sensation, foot ulcers, pain and gangrene are major indications of diabetic neuropathy. If not taken care of, it could result in limb amputation. Sensory neuropathy is characterized by lancinating pain and burning sensation in distal regions of lower limbs. It was also reported that diabetes seem to be a common cause of chronic kidney disease and could result in kidney failure even when diabetes was under control [7]. Though there were few evidences to link diabetes with increased susceptibility to infection, but it had been observed that diabetic patients were especially prone to foot infections, yeast infections, urinary tract infections and surgical site infections. It was believed that changes in various aspects of immunity played key roles in

diabetic infections [8]. It was also believed that immune function could be improved by glycemic control.

1.4.2 Nociceptive pathway in diabetes

Diabetic painful neuropathy results from peripheral nervous system damage. Hyperglycaemia disrupts the normal function of micro-vessels which supply blood to nerves causing hypoxia, which eventually results in neuronal dysfunction. The neural ischemia is believed to be involved in both structural and functional changes of the nervous system. Sensory nerve fibres like C- and Aδ-fibres have relatively high surface area than their volume and are possibly prone to damage due to hyperglycaemia. C-fibres are sensitive to metabolic changes as they don't have myelin sheath. The damage to these fibres can be linked with origin of hyperalgesia (increased sensitivity to pain) and allodynia (a pain due to a stimulus which does not normally provoke pain) in the early stage of diabetic neuropathy. A wide range of sensory fibres are influenced by diabetic neuropathy and that a prolonged effect leads to axonal degeneration and functional changes within the central nervous system [9]. The death of C-fibres causes effective de-afferentiation of these neurons. Within weeks of death of C-fibres, the branches of Aβ-fibres project to deeper lamina of the spinal cord, and develop new pathological connections with differentiating C-fibre interneurons by making new connections. This remodelling is associated with central sensitization which is common in allodynia and hyperalgesia. Hence, the central sensitization by small sensory fibre differentiation might be involved in diabetic painful neuropathy.

Chronic hyperglycaemia represents the main causative factor involved in the pathogenesis of diabetic micro-vascular complications. Nerve damage may be directly induced by the accumulation of intracellular glucose and its increased flux through the polyol, leading to generation of glycating sugars and advanced glycation end products (AGE), enhanced oxidative damage and activation of protein kinases [10]. Also, ischemia caused by decreased neurovascular flow also could be one of the reasons [11]. The impairment of essential fatty acid synthesis and compromised vasoactive prostanoid production in diabetes could also be a contributing factor [12]. Early changes in vascular function evolve into progressive chronic endoneurial vascular damage [13]. Deficiencies of neurotrophic factors and their receptors are also involved in the development of diabetic neuropathy. Insulin and C-peptide deficiencies have been implicated as potential contributors to the generally more severe neuropathy of type 1 rather than that of type 2 diabetes. There is also some evidence that autoimmune mechanisms may contribute to the development of symptomatic autonomic neuropathy in

diabetic patients. Increased levels of glucose cause an increase in intracellular diacylglycerol (DAG), which activates various protein kinases which play important role in the formation of long-term potentiation in hippocampus and anterior cingulate cortex (ACC). Thus, the activation of kinases is involved in the disruption of synaptic plasticity in the central nervous system.

1.4.3 Neurodegeneration

Diabetes and AD have many similarities- both primarily being age-related diseases, and both are increasing in prevalence. Also, recent studies have suggested that patients with diabetes have an increased risk of developing AD compared with healthy individuals. Ongoing research, focuses on confirming the link between diabetes and AD. The link between type 2 diabetes and Alzheimer's may occur as a result of the complex ways that type 2 diabetes affects the ability of the brain and other body tissues to use sugar (glucose) and respond to insulin. The underlying pathways linking diabetes development with AD have not been fully understood. Some of the possible mechanisms include abnormal protein processing, abnormalities in insulin signalling, dysregulated glucose metabolism, oxidative stress, AGE, and the activation of inflammatory pathways [14].

Diabetes also may increase the risk of developing mild cognitive impairment, a condition in which people experience more thinking (cognitive) and memory problems than are usually present in normal aging. Mild cognitive impairment may lead to AD and other types of dementia. In addition to the above factors, oxidative stress, which is common in diabetes as well as AD and other related neurological diseases, have been related to cause neurodegeneration. Studies had also confirmed that diabetes accelerated the memory dysfunction *via* cerebrovascular inflammation and Aβ deposition in an AD mouse model with diabetes [15]. Thus, any research involving neuronal complications of diabetes might also help in understanding of subsequent behavioural as well as cognitive changes (memory loss and learning impairment).

"If you know the enemy and know yourself,
you need not fear the result of a hundred battles."
— Sun Tzu, The Art of War

Chapter 2.
Literature Review

2.1 Background

A systematic survey of literature was carried out to define the objectives and to have a logical summary of the current knowledge already available in public domain (research articles, review articles, patents, newsletters) on Rho Kinase enzyme (ROCK) and protein kinase C β-II (PKCβ-II). A PubMed search (www.ncbi.nlm.nih.gov/pubmed) and Google scholar search (www.scholar.google.co.in/) of the literature published between 1995 and 2014 was conducted using the following search terms individually or combined: 'Rho kinase inhibitor', 'PKCβ-II inhibitor', 'novel rho kinase inhibitor', 'design', 'synthesis', 'diabetic neuropathy', 'methylmercury' and 'neurodegeneration'. The bibliographies of the included studies were searched for additional references.

2.2 Role of protein kinases in diabetic neuropathy

2.2.1 Rho kinase (ROCK)

Rho proteins comprise a subfamily of highly conserved small molecular G proteins that belong to the Ras superfamily. In neuronal cells, RhoA is involved in the guidance and extension of axons and the development and structural plasticity of dendrites and dendritic spines [16,17]. Several studies have suggested that RhoA regulates the stability of dendritic branches and spines in neurons [18]. RhoA has been shown to play an important role in the formation of long-term potentiation in hippocampal neurons [19]. Thus, the activation of RhoA signalling is involved in the formation of synaptic plasticity in the CNS.

Rho-associated protein kinase (ROCK) belongs to the AGC family of serine-threonine kinases. There are 22 mammalian genes encoding Rho-guanosine tri phosphatases (GTP)-ases have been described. Two types of ROCK isoforms were identified: ROCK1 (ROKβ, p160ROCK) and ROCK2 (ROKβ). Both isoforms have 65% overall structural identity, and have highest similarity that is 92% identity in their kinase domains. While both isoforms are abundantly expressed, ROCK1 expression is more in lung, liver, spleen, kidney, and testis, whereas ROCK2 is more prominent in the brain and heart [20]. In *Drosophila melanogaster* seven, in *Caenorhabditis elegans* five, and in *Dictyostelium discoideum*, fifteen of Rho family members are present respectively and most of them participate in key mechanism in cell migration and/or other morphogenesis.

Human ROCK1 has a molecular mass of 158 kDa and is a major downstream effector of the small GTPase RhoA. It has an amino terminal kinase domain, followed by a coiled-coil region and a Pleckstrin homology (PH) domain at carboxyl terminal which has an internal cysteine-rich domain. These carboxy terminal domains constitute an auto inhibitory region that reduces the kinase activity of ROCKs. The coiled-coil region is estimated to interact with other alpha helical proteins, and PH domain in the carboxyl terminal may participate in protein localization (see Figures 2-1, 2-2). An inactive GDP-bound form and an active GTP-bound forms are involved in Rho GTPases cycle. The cycle is governed chiefly by guanine exchange factors (GEFs), GTPase activating proteins (GAPs) and guanine dissociation inhibitors (GDIs). The active forms of Rho GTPases perform their regulatory function through a conformation-specific interaction with target (effector) proteins *per se* kinases and scaffold proteins [21]. GEFs accelerate to generate the activated form by the exchange of GDP to GTP, which is then capable of recognizing downstream targets, or effector proteins.

Figure 2-1. ROCK functional domains.

ROCK sequences comprise a kinase domain located at the amino terminus of the protein, followed by a coiled-coil region containing the RBD and PH domain with a cysteine-rich domain. ROCK-1 and ROCK-2 are highly homologous with an overall amino acid sequence identity of 65%.

GTPase activating proteins (GAPs) accelerate the intrinsic GTPase activity of Rho family members to inactivate the switch. Eventually, GDIs interact with the prenylated GDP-bound form to control cycling between membranes and cytosol [22].

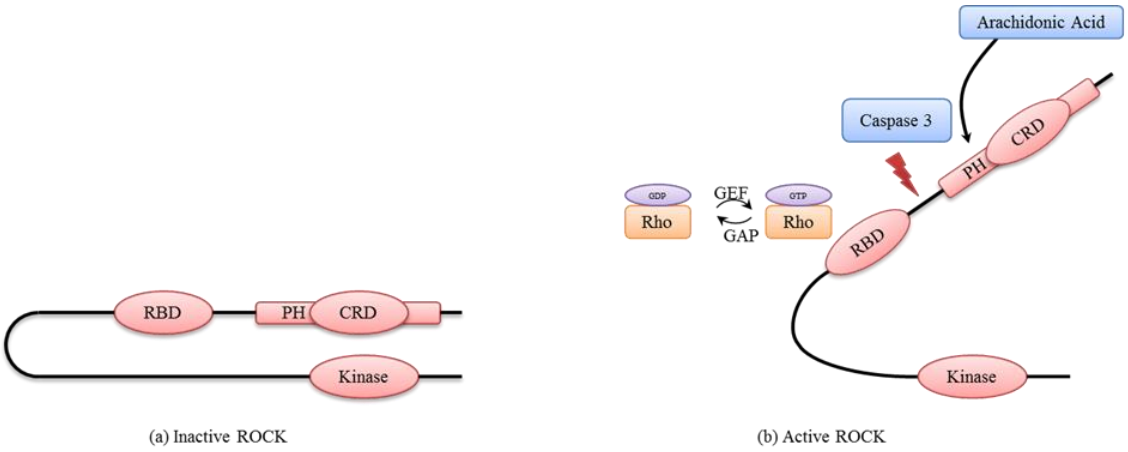

Figure 2-2. Regulation of ROCK function.

Panel (a) In the inactive form, the pleckstrin homology (PH) domain and the Rho-binding domain (RBD) of ROCK bind to the amino-terminal region of the protein, which forms an autoinhibitory loop. Panel (b) Activated, GTP-bound Rho binds to the RBD of ROCk, which results in an open conformation of the kinase and frees the catalytic activity. In addition, ROCK can be activated by caspase-3-mediated cleavage near the carboxyl terminus. CRD, cysteine rich domain; GAP, GTPase activating protein; GEF, guanine nucleotide exchange factor.

Most of ROCK substrates were identified from *in vitro* experiments performed either after activation of endogenous ROCK or by transfection of one of the two ROCK isoforms. Because the kinase domains of both isoforms were nearly identical, it was thought that ROCK-1 and ROCK-2 shared the same substrates. However ROCK-1, but not ROCK-2 bind to and phosphorylated RhoE, providing evidence that ROCK-1 and ROCK-2 had different targets. The N-terminal regions, upstream of the kinase domains of ROCKs, were involved in the interaction with the substrates and could play a role in determining substrate specificity of the ROCK isoforms [23]. Till now, more than 15 ROCK substrates have been identified. For many ROCK substrates, the functional consequence of ROCK-mediated phosphorylation was related to actin filament formation, organization and cytoskeleton rearrangements.

A major group of ROCK targets included the myosin phosphatase target subunit (MYPT-1), CPI-17 [24], the 20-kDa MLC (Myosin light chain) [25], LIM kinase (LIM Domain kinase) [26], ERM (ezrin-radixin-moesin) and calponin [27], which were known to modulate smooth muscle cell contraction. The proteins involved in regulating actin-filament assembly and contractibility could be phosphorylated by ROCKs. Cardiac troponin was another ROCK

substrate. Phosphorylation of troponin by ROCK caused reduction in tension generation in cardiac myocytes [28]. The phosphorylation of motor protein myosin II which was present in non-muscle cells had a role in regulating actomyosin contractility.

Phosphatase and tensin homologue (PTEN) was a newly identified ROCK substrate. Phosphorylation of PTEN by ROCK stimulated its phosphatase activity, and ROCK inhibitors could reduce ROCK- mediated PTEN phosphorylation and thereby enhancd Akt signaling in endothelial cells. Active ROCK also interacted and phosphorylated the insulin receptor substrate-1 (IRS-1) in VSMCs (Vascular smooth muscle cells), leading to inhibition of both insulin-induced IRS-1 tyrosine phosphorylation and PI3-kinase activation. VSMCs from hypertensive rats showed increased ROCK/IRS-1 association, and markedly reduced insulin signaling [29].

ROCK has multi-faceted functions which could be either biochemical or biological and included maintenance of cell structure, cell movement or migration, cell polarity, phagocytosis, proliferation and directional sensing. ROCKs induce neurite retraction by increasing actomyosin contractility. ROCK inhibition triggers outgrowth of axonal processes in cerebellar granule neurons and LPA (Lysophosphatidic acid) induced growth collapses. Inhibition of ROCKs also stimulates axon regeneration and recovery after spinal cord injury [30].

A growing body of evidence indicated that the synaptic plasticity of dorsal horn neurons contributed to pain hypersensitivity after strong noxious stimulation [31]. Several intracellular protein kinase cascades mediated the formation of synaptic plasticity of dorsal horn neurons [32]. Rho/ROCK pathway has been shown to play important roles in the development and/or maintenance of chronic pain [33,34]. There have been reports that intrathecal treatment with ROCK inhibitor Y27632 attenuated cold hyperalgesia [35]. Recently it was also reported that intrathecal administration of mevalonate produced thermal hyperalgesia through the activation of spinal RhoA/ROCK signalling [36]. In an acute pain model, systemic treatment with ROCK inhibitor Y27632 produced anti-nociceptive effect in the hot-plate and acetic acid writhing tests [37]. Therefore, spinal activation of the RhoA/ROCK pathway sensitized nociceptive transmission and is involved in the development and maintenance of hyperalgesia. Y27632 was the oldest synthesized and reported specific inhibitor of Rho-kinase family enzymes. Y27632 inhibited ROCK activity by competitive binding with ATP at the catalytic domain. Another novel ROCK inhibitor was H1152, which was a more

specific, stronger and membrane permeable inhibitor of ROCK with a Ki value of 1.6 nM. Both inhibitors have greater specificity for ROCK, than for PKA and PKC.

2.2.2 ROCK and diabetic complications

Extracellular, glucose has been demonstrated to react nonenzymatically with primary amines of proteins forming glycated compounds or oxidants. These products can secondarily act on inflammatory cells or vascular cells directly *via* receptor or non-receptor-mediated processes to cause vascular dysfunctions [38].

The cytosolic GDP bound inactive form of RhoA translocates to the cell membrane and becomes GTP-bound active form upon stimulation by agonists. The translocation of inactive RhoA to the membrane fraction is required for its activation. Hence, presence of RhoA in the membrane fraction indicates RhoA activation. Phosphorylation by cAMP-dependent protein kinase (PKA) and by cyclic guanosine monophosphate (cGMP)-dependent protein kinase (PKG) inhibited RhoA signalling; hence they interfered with the translocation of RhoA to the membrane (Figure 2-3) [39].

It appears that activation of the RhoA/ROCK pathway is a common component of the pathogenesis of diabetic complications. RhoA activation was first observed in the mesenteric

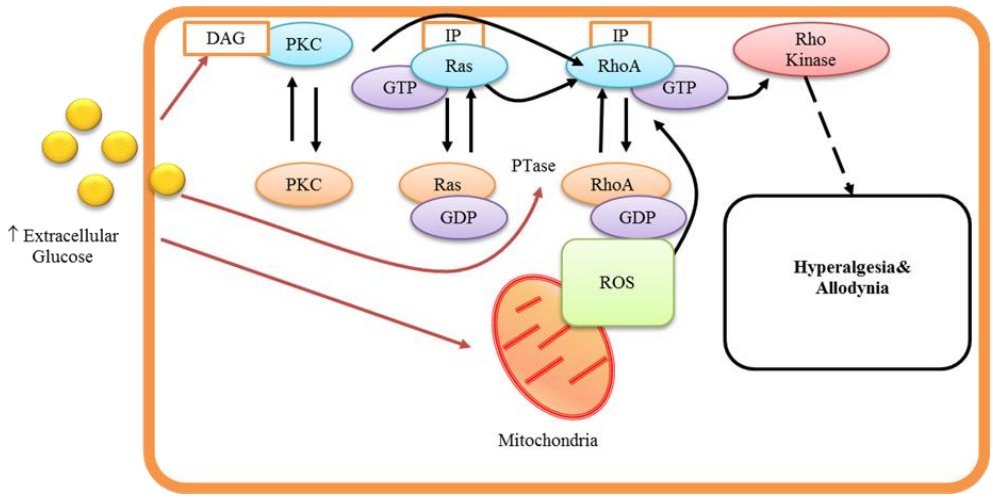

Figure 2-3. Rho activation in diabetic condition.

Representation of the RhoA/ROCK pathway in the spinal cord in diabetes mellitus. high glucose levels can induce the activation of RhoA through multiple mechanisms mediated by PKC, PKG and reactive oxygen species. Elevated extracellular glucose levels increase the intracellular DAG and reactive oxygen species (ROS). Glucose also stimulates prenyltransferase. The increase in DAG causes activation of PKC. This activation of PKC, the increase in intracellular ROS and the activation of prenyltransferase induce the activation of RhoA and Ras proteins. This activation of small molecular G proteins could sensitize nociceptive transmission in the spinal cord dorsal horn followed by ROCK activation DAG: DAG; diacylglycerol, IP; isoprenoid, PKC; protein kinase C, PTase; prenyltransferase, ROS; reactive oxygen species [39].

arteries and aorta from diabetic mice [40]. Later, activated RhoA/ROCK was reported in skeletal muscles and aortic tissues of Zucker obese rats and was found to cause insulin resistance and vascular dysfunctions [41]. RhoA was highly expressed in the renal cortex of streptozotocin (STZ)-induced diabetic rats [42]. RhoA/ROCK inhibition alleviated insulin resistance [43] and diabetic nephropathy [44]. Several mechanisms have been hypothesized for the hyperglycaemia-induced RhoA activation. As discussed earlier, elevated blood glucose levels induced the membrane translocation of RhoA and Ras in mesangial cells and involvement of protein isoprenylation in the activation of RhoA and Ras proteins in hyperglycaemic state supported the fact that translocation was suppressed by the inhibition of mevalonate pathway. The fact that RhoA is a downstream effector of activated Ras [45] further supports the above statement. Moreover, glucose activates prenyltransferase, such as geranylgeranyltransferase-1 (GGTase-1) and FTase in pancreatic islet β-cells, leading to the activation of small molecular G proteins [46]. All the above facts indicate towards activation of RhoA and Ras proteins by glucose through an increase in protein isoprenylation. Altered regulation of isoprenoids synthesis for protein prenylation might also activate RhoA and Ras proteins in diabetes mellitus. Elevated glucose levels lead to increased intracellular DAG levels, which activates PKC [47] which, in turn phosphorylates and activates RhoA, eventually inactivating the Rho-guanine nucleotide dissociation inhibitor (GDI) [48]. The Rho-GDI phosphorylation translocate RhoA to the membrane and activates the same. It has been also found that in addition to PKC, reactive oxygen species (ROS) are responsible for RhoA activation. Elevated glucose levels increase the mitochondrial production of ROS, hence it activates RhoA [49]. PKG inactivation by Glucose also leads to the activation of RhoA [50] therefore; PKC, PKG and ROS can induce the activation of RhoA through multiple mechanisms, under the influence of high glucose levels. The increased expression of cleaved product of ROCK in rats fed a high-fructose diet [51] suggested that ROCK is constitutively active and thus can also be directly activated in diabetes mellitus [52].

The pathogenesis of diabetic neuropathy includes elevated activity of polyol pathway resulting in accumulation of sorbitol and fructose and imbalances in NAD, formation of ROS due to auto-oxidation of glucose [53], generation of AGE by non-enzymatic glycation of proteins [54], activation of PKC [55] and a deficiency of neurotrophic supports (see Figure 2-4).

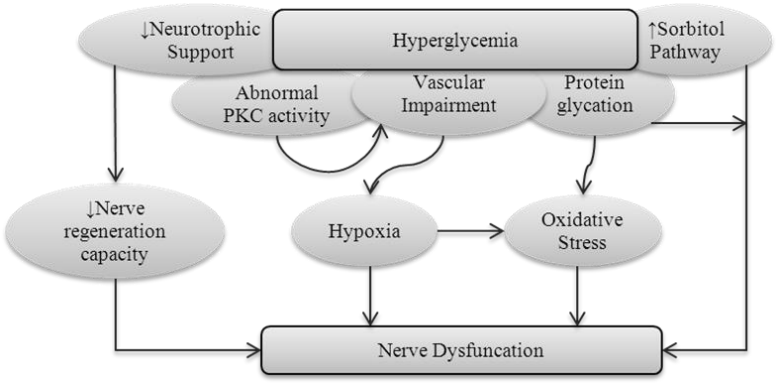

Figure 2-4. Possible causative factors of diabetic neuropathy.

The pathology of diabetic neuropathy involves (a) axonal atrophy, (b) demyelination, (c) loss of nerve fibers and (d) the blunted regeneration of nerve fibers [56]. Hence any therapy for diabetic neuropathy must include prevention of nerve degenerative process and augmentation of nerve fiber regenerative capacity. It has been found that RhoA is involved in the guidance, extension and stability of axons [57]. Rho A is also involved in the development and structural plasticity of dendrites and dendritic spines. RhoA has also been found to play an important role in the formation of long-term potentiation in hippocampal neurons [19], which indicated the involvement of RhoA in formation of the synaptic plasticity in the central nervous system. Recently Inoue *et al.* [58] and Tatsumi *et al.* [59] reported participation of RhoA/ROCK pathway in the development and/or maintenance of chronic pain. Simultaneously, it was also found that intrathecal delivery of ROCK inhibitor Y-27632 attenuated cold hyperalgesia in C7/8 rhizotomy [60]. Similarly, Ohsawa *et al.* [61] indicated that spinal RhoA/ROCK signalling was involved in mevalonate that produced thermal hyperalgesia. Also, Y-27632 produced an anti-nociceptive effect in the hot-plate and acetic acid writhing tests [62]. All the above facts supported that activation of the RhoA/ROCK pathway sensitized nociceptive transmission and was somehow involved in the development and maintenance of hyperalgesia.

2.3 ROCK inhibition to treat diabetic complications

2.3.1 ROCK inhibitors for treatment of diabetic neuropathy

Recently James *et al.* [63] reported that Rho-inhibition and nerve regeneration were somehow linked events. They showed that ROCK inhibitor Y-27632 could initiate regeneration of damaged nerves following cisplatin treatment. In their experiment, post-treatment with Y-27632 improved both the sural nerve distal latency and sensory threshold whereas sural nerve

histology deteriorated in the absence of Y-27632 during recovery. Similarly Yoshimi *et al.* [64] evaluated the effects of repeated dosing with a novel and selective ROCK inhibitor AS1892802 (see Figure 2-5, structure 7) on rat models of monoiodoacetate-induced arthritis and STZ-induced diabetic neuropathy. AS1892802 exhibited a long-lasting and more potent analgesic effect in both models. Furthermore, the analgesic effect was sustained for seven days after the last administration. These results suggested that peripheral ROCK pathway

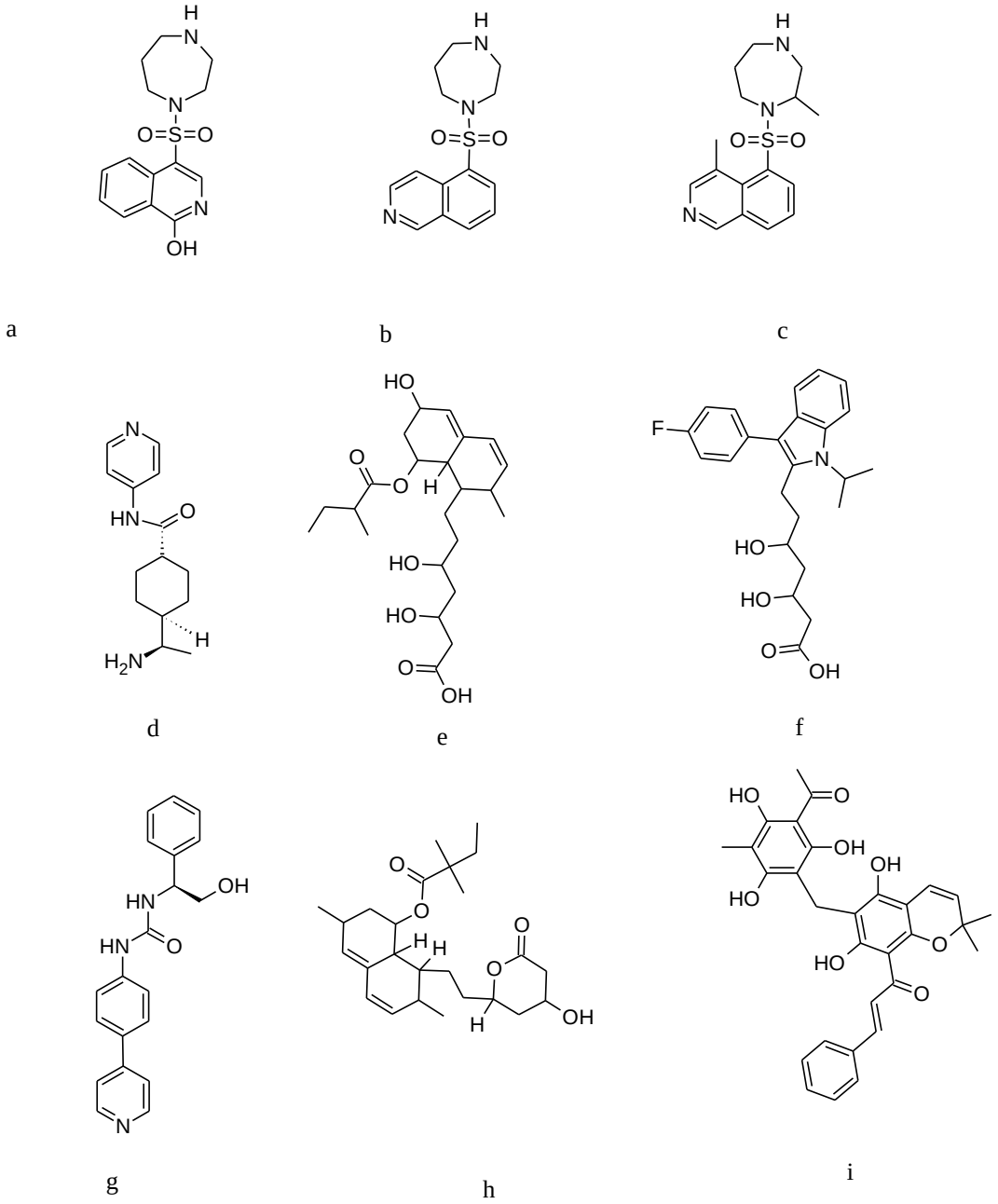

Figure 2-5. Some important ROCK pathway modulators.

a, Hydroxyfasudil ; b, Fasudil; c, H1152; d, Y-27632; e: Pravastatin; f, Fluvastatin; g, AS1892802; h, Simvastatin and i, Rottlerin.

participated in chronic pain maintenance. Also, AS1892802 or its derivatives might be useful in treating chronic pain in diabetic neuropathy. Some important ROCK modulators are shown in Figure 2-5.

Ohsawa *et al.*[61] investigated the role of RhoA/ ROCK pathway in thermal hyperalgesia in diabetic mice. They showed that increased membrane-bound RhoA in the spinal cord of STZ -treated diabetic mice was found when compared to non-diabetic control. Treatment with the RhoA inhibitor exoenzyme C3, from *Clostridium botulinum*, and the ROCK inhibitor Y-27632 attenuated thermal hyperalgesia and mechanical allodynia in diabetic mice. Likewise, they also proposed that HMG-CoA reductase inhibitors showed an inhibitory effect on thermal hyperalgesia in diabetic mice, due to increased production of NO through the inhibition of RhoA/ROCK pathways. These results indicated that ROCK inhibitors combined with HMG-CoA inhibitors might be useful for the treatment of painful diabetic neuropathy [65].

2.3.2 ROCK inhibitors for treatment of erectile dysfunction (ED)

Popular therapies increase corporal smooth muscle relaxation to improve erectile function. A potential new approach for the treatment of ED may be based on directly inhibiting biochemical pathways that control smooth muscle contraction. The RhoA/ROCK-mediated Ca^{+2} sensitization pathway was relevant to the pathogenesis of ED. It had been reported that intra-cavernosal injection or topical application of Y-27632 to the penis resulted in increased blood flow into erectile tissue causing erection. Rho-kinase inhibitors usually showed systemic effects like lowering mean arterial blood pressure. Keeping this side effect in mind, only local administration of ROCK inhibitors was possible. Identifying tissue specific isoforms of RhoA regulatory proteins might be an alternative. Another way for treating ED would be to increase genital-tissue-specific RhoGDI and RhoGAP activity or suppressing specific RhoGEF activity. Other possible treatment might include targeting RhoA or ROCK by gene transfer. Since targeting the RhoA/ROCK pathway in the penis remain to be investigated, studies on animal models might also help to clarify the beneficial effects and side effects of long-term inhibition of RhoA/ROCK in the penis [66].

2.3.3 ROCK inhibitors for treatment of diabetic nephropathy

Peng *et al.* [67] demonstrated the importance of RhoA/ ROCK pathway in diabetic nephropathy by using STZ treated rats which showed hyperglycaemia and low circulating insulin levels. Treatment of these rats with fasudil (30 mg/kg/day for about 6.5 months) and ACE inhibitors like enalapril were investigated. Control, STZ, fasudil and enalapril rats

showed no difference in blood pressure, no difference in serum creatinine and developed renal hypertrophy as evidenced by higher kidney to body ratio. The increase in glomerular sclerosis was prevented in both the treatment groups. The thickness of glomerular basement membrane measured by electron microscopy revealed that there was an increase in thickness in diabetic animals whereas decrease in fasudil treated rats. Focal areas of podocyte foot process effacement were seen in diabetic group. Two rats in each group were assessed for immunoblotting by phospho MYPT-Thr696 which resulted in significant increase in ROCK activation. However the other factors like hyperglycaemia and fibronectin upregulation (ROS) independently induced the activation of ROCK signaling pathway [44].

ROCK inhibitors exhibited renoprotective effects in a number of models of kidney damage. Fasudil was a specific inhibitor for ROCK which also inhibited other kinases like PKC and mitogen and stress activated protein kinase1 with less effectiveness. Kikuchi *et al.* [68] analyzed the effects of fasudil in insulin resistant diabetic rats. Insulin resistant diabetic rats when administered with high dose of fasudil (100 mg/kg) showed improved metabolic parameters with decreased diabetes induced proteinuria, glomerulosis, interstitial fibrosis, and macrophage infiltration. Despite lower dose (30 mg/kg) which had no effect on glycemic control, but was found to have significantly reduce interstitial fibrosis and macrophage infiltration and not glomerulosclerosis or proteinuria. Statins (HMG CoA inhibitors) were used as lipid lowering agents but also had beneficial effects in kidney disease. These drugs suppressed the prenylation of small GTPases proteins *viz* RhoA. The prenylation of RhoA was essential for localization in membranes. Statins prevented diabetes induced increase in RhoA activity and had renal functional effects similar to fasudil. The study by Gojo *et al.* [69] clearly demonstrated the effect of RhoA/ROCK inhibition is independent of glycemic control when treated with fasudil. Catherine *et al.* [70] demonstrated that LPS (Lipopolysaccharide) induced nephritis could be prevented and treated by ROCK inhibition. The two inhibitors of ROCK, fasudil (also known as HA-1077) and Y-27632 were used for this study. Fasudil was a potent inhibitor which underwent clinical trials in human. Rat models when given low dosage of HA-1077 daily, showed decreased inflammation. Lohn *et al.* [71] identified a novel inhibitor of ROCK (SAR407899, structure not shown) which was an ATP competitive inhibitor equally potent against ROCK2 with inhibition constants of 36 nM and 41 nM respectively. It was 8 fold more active than fasudil. Also, *in vivo* studies showed decrease in blood pressure when administered in the dose range of 3 to 30 mg/kg. Hence SAR407899 could be a novel potent inhibitor of ROCK with antihypertensive activity.

2.3.4 ROCK inhibitors for treatment of diabetic retinopathy

Y-27632 when administered topically and intracamerally, intravitreally showed decrease in IOP in rabbit eyes. It had shown a two fold increase in total arterial blood flow measured by two-level constant pressure perfusion system. ROCK inhibition reduced IOP and elevated out flow facility [72].

Simvastatin in varied doses (1 nm to 10 µm), administered to STZ induced diabetic rats dilated retinal arterioles and also IOP. Simvastatin could have inhibited calcium release from cells and decreased calcium entry into aortic rings. The immediate action of simvastatin on endothelial cells released prostacyclin. The release of increased NO and prostacyclin caused acute dilation in microvessels, this protected vascular wall from anti-thrombogenic attacks. The statins are potent inhibitors of HMG-CoA reductase in mevalonate synthesis leading to several post translational modifications of cell signaling molecules like Rho GTPase [73]. Some more statins which showed inhibitory effects in proliferative retinal diseases like pravastatin, fluvastatin (Figure 2-5) were found more effective in reducing MLC phosphorylation and the collagen contraction [74].

Fasudil is a potent and selective inhibitor of ROCK effective in the treatment of cardiovascular diseases like cerebral and coronary vasospasm, angina, hypertension and heart failure. It could inhibit VEGF-induced retinal capillary endothelial cell migration, hence possessed anti-angiogenic property.

2.3.5 Other ROCK inhibitors

As discussed in earlier sections, ROCK inhibitors were being targeted as suitable candidates for the treatment of diabetes related complications like diabetic neuropathy, diabetic cardiac complications, diabetic retinopathy and diabetic nephropathy. Considering the importance of the role of ROCK in multiple disease mechanisms, the chemical space seem to be attractive for further exploration of novel and effective ROCK inhibitors. In the following sections we attempted to search some of the recent approaches of novel ROCK inhibitor design. Until recently, mainly x-ray crystallography studies have helped to explore the interactions between ROCK and their inhibitors [75-77]. Wang *et al.* [78] docked a series of inhibitors into the binding pocket of intracellular kinase domain of ROCK. The predicted binding affinities were consistent with the activities of these inhibitors. They also proposed a ligand based pharmacophore using HipHop [79] comprising of one hydrogen bond acceptor (HBA) feature and two hydrophobic features (H). Recently, Gong *et al.* [80] developed a common pharmacophore and screened their *in house* database. Hits were further docked to ROCK-1

crystal structure and were scored using ligand fit module and dock score module [81] of Discovery Studio 2.0 [79]. Ten hits had shown greater than 70% inhibition at 10 µmol/L with IC_{50} values greater than 10 µmol l^{-1}. Qin *et al.* [82] conducted molecular docking and 3D-QSAR studies on ROCK inhibitors. The 3D contour maps obtained from CoMFA and CoMSIA studies along with the docking results suggested that 1H-indazole derivatives were superior than the isoquinoline derivatives.

Researchers are continuously trying to explore the chemical space to get better and efficacious ROCK inhibitors. Takami *et al.* [83] reported some moderately binding ROCK inhibitors. They performed an immobilized ELISA using hit compounds followed by another enzyme kinetic assay employing [γ-^{32}P]-ATP and a synthetic peptide. Totally 417 hits were identified in the above high throughput screening method. But none of them showed better activity than standard inhibitor fasudil. Further, they performed homology modeling and designed a virtual library based on a docking model of scoring hits using FlexiDock module of Sybyl suite of softwares (Ver 6.5) [84]. The designed compounds were then synthesized that belonged to pyridine, 1H-indazole, isoquinoline, and phthalimide derivatives. The activities of the synthesized compounds were found to be consistent with the docking results. Some of the inhibitors were then tested for their selectivity for other kinases like MAP kinase, PKC and cAMP dependent protein kinases and the result showed that the compounds were specific towards ROCK.

Same research group in 2007 optimized the 1H-indazole derivatives based on the inhibition of chemotaxis of CCR2 over-expressing cells [85]. They found that inhibitors with piperidine and pyrrolidine linkers, but not with urea linkers, showed inhibitory activity on the MCP-1/CCR2 chemotaxis and in the cell-free ROCK enzyme assay. They further optimized the substitution group on the 1H-indazole ring and the substructures for the surface bound C region of the ligand-binding pocket of the ROCK. The 3,4-difluoro analogue was found to exhibit better inhibition of chemotaxis than HA-1077, which indicated that ROCK inhibitors could suppress a wide range of leucocyte migration. They also optimized ROCK inhibitors bearing isoquinoline analogues. Inhibition of ROCK expression in rat serum was assessed by administering isoquinoline analogues [86]. Nearly at the same time, another group reported some dihydropyridone and indazole derivatives as ROCK inhibitors (see Figure 2-6) [87].

The same group reported variation of 3-acetamide in the 6-position of the azabenzimidazole core which showed >10 fold increase in ROCK I potency with >1000 fold selectivity over rCDK2 and GSK3β, whereas morpholino-ethoxy substitution resulted in compound which showed the overall best kinase selectivity, half-life, bioavailability and potency in the rat aortic contraction assay (see Figure 2-7) [88]. Properties like effective reduction in intraocular pressure, high aqueous solubility, better corneal penetration and good systemic clearance were desired characteristics for drugs for glaucoma and these compounds fulfilled all the above criteria, and found to be useful in the treatment of diabetes-related eye problems.

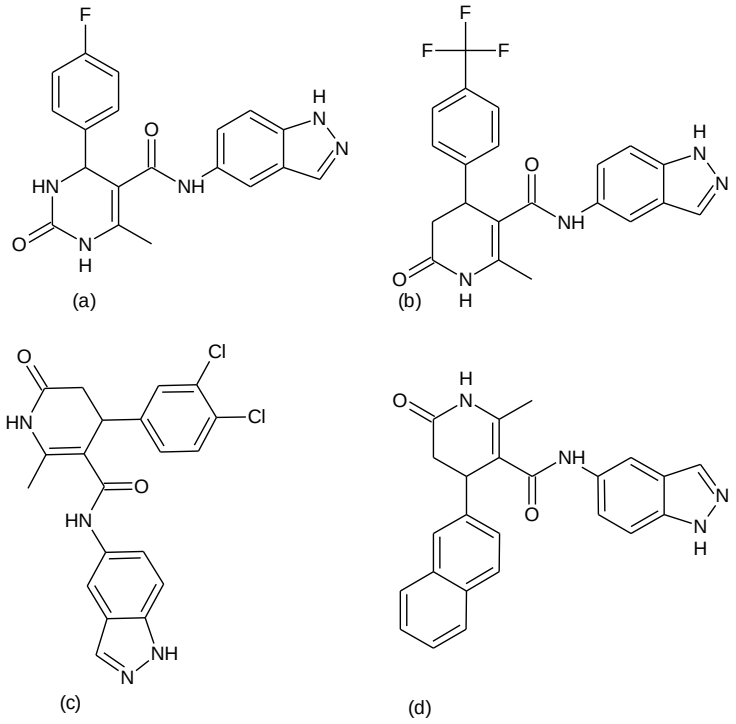

Figure 2-6. Dihydropyridone indazole amide based ROCK inhibitors.

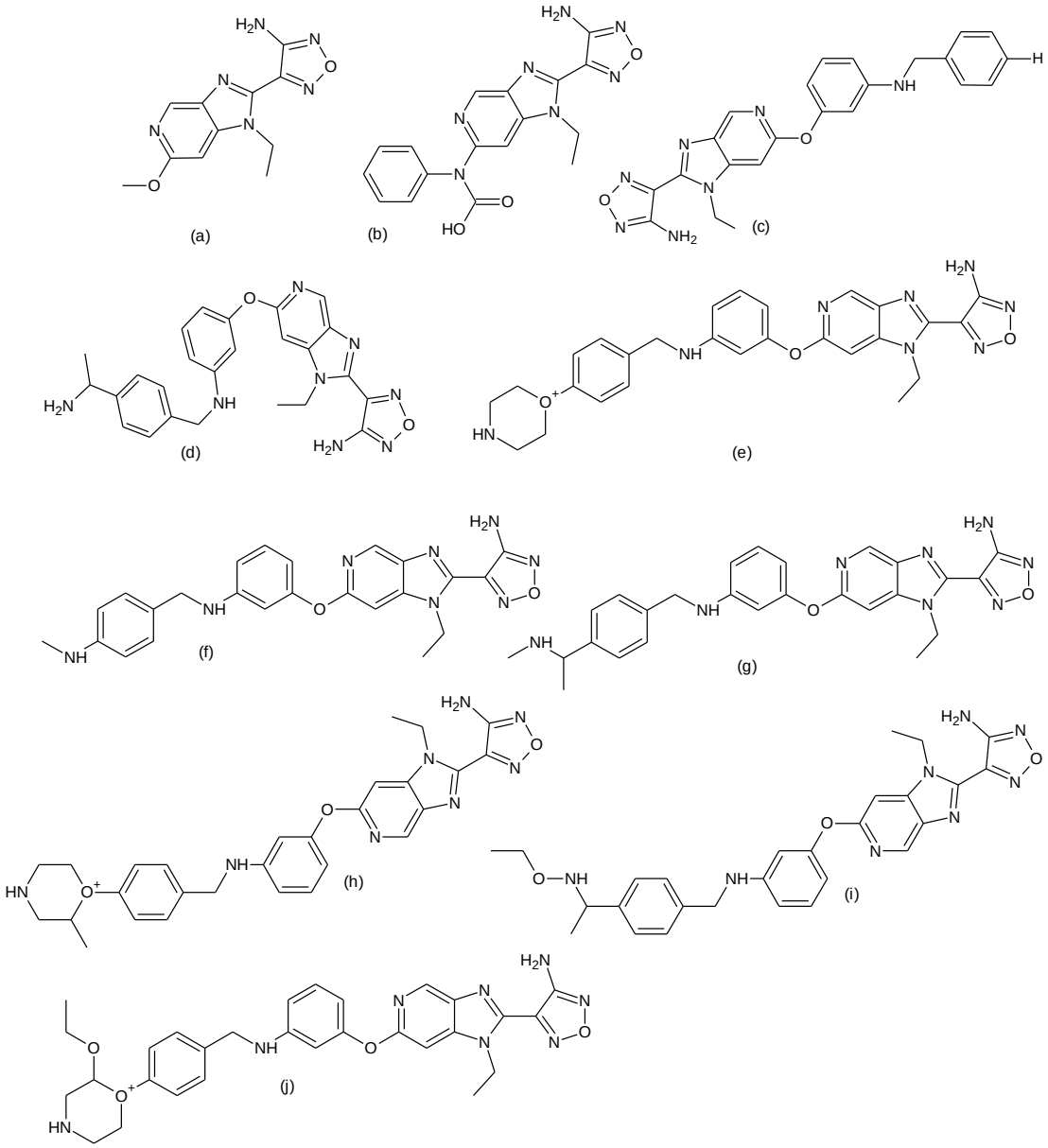

Figure 2-7. Aminofurazan-azabenzimidazoles based novel ROCK inhibitors.

Recently it was reported that some α–amino-anilide-based ROCK inhibitors showed potent ROCK II inhibition (IC_{50}< 1 nM) with potent cell-based activity (IC_{50} ranging from 10-50 nM), low oral bioavailability to prevent systemic exposure after topical application, and IOP-lowering ability with long duration of action (see Figure 2-8) [89].

In addition, another research group recently published bisbenzamide and ureidobenzamide series of ROCK inhibitors through HTS discovery approach in which they screened corporate compound collection in a homogeneous luciferase assay using ROCK-II.

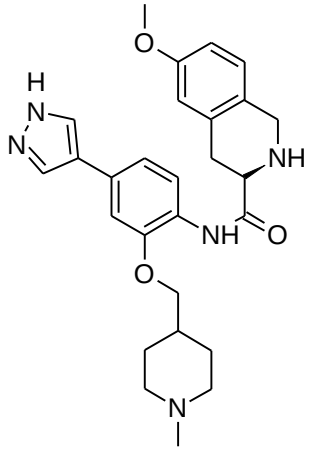

Figure 2-8. Tetrahydroisoquinoline derivative as ROCK inhibitor.

The identified hits were then further enriched using docking studies on a homologous protein of AGC subfamily. They concluded that presence of dimethoxyphenyl moiety was important for potency. They also conducted SAR (structure-activity relationship) studies, a selectivity assessment, target-independent profiling (TIP) and analysis of functional activity using a rat aortic ring. The potent compound identified in this study is given in Figure 2-9.

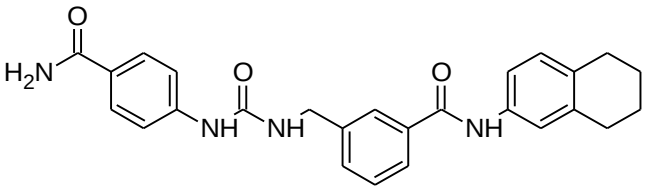

Figure 2-9. Bisbenzamide as ROCK inhibitor.

2.4 Protein Kinase C-β

Another important kinase involved in RhoA/ROCK pathway are PKCs. Calcium and phospholipid-dependent protein kinases (PKCs) represent a family of second messenger-dependent protein kinases that are stimulated by Ca^{2+} and/or phospholipid [90]. PKC plays a pivotal role in mediating cellular responses to extracellular stimuli involved in proliferation, differentiation, apoptosis, and exocytotic release in a number of non-neuronal systems such as islet cells, chromaffin cells and paramecium. PKC has also been implicated in phosphorylation of several neuronal proteins, which were thought to regulate neurotransmitter release and establish long-term potentiation in memory formation [91,92]. PKC is not a single enzyme but a family of serine/threonine kinases. At least 10 isoforms of PKC are known and were classified by their activation requirements (Table 2-1) [93].

Table 2-1. Mammalian PKC isoenzymes.

Type	Activators	Isoenzyme	Distribution
Conventional	Ca, PS, DAG	α	Widespread
		βI	Widespread (low levels)
		βII	Widespread
		γ	Brain, Spinal cord
Novel	PS, DAG	δ	Widespread
		ε	Brain, Hematopoietic tissues
		η	Heart, Lung, Skin
		θ	Hematopoietic tissues, Brain, Skeletal muscle
Atypical	PS, PI-3,4,5-P3	ζ	Widespread
		ι/λ	Brain, Kidney, Lung
Recently identified	DAG, PI-4,5-P2	μ/PKD	Lung, Epithelial cells
		ν	Widespread

Ca=Calcium; PS=Phosphatidylserine; DAG=Diacylglycerol; PI-3,4,5-P3=phosphatidylinositol-3,4,5-triphosphate, PI-4,5-P2=phosphatidylinositol 4,5 diphosphate [102].

PKC activation occurs when plasma membrane receptors coupled to phospholipase C are activated, releasing DAG. The conventional isoforms, α, βI, βII, and γ, are activated by phosphatidylserine, DAG and Ca^{2+}. The unconventional isoforms δ, ε, η, and θ require phosphatidylserine and DAG but do not require Ca^{2+}. The ζ and λ isoforms are called atypical and require only phosphatidylserine for activation (Figure 2-10).

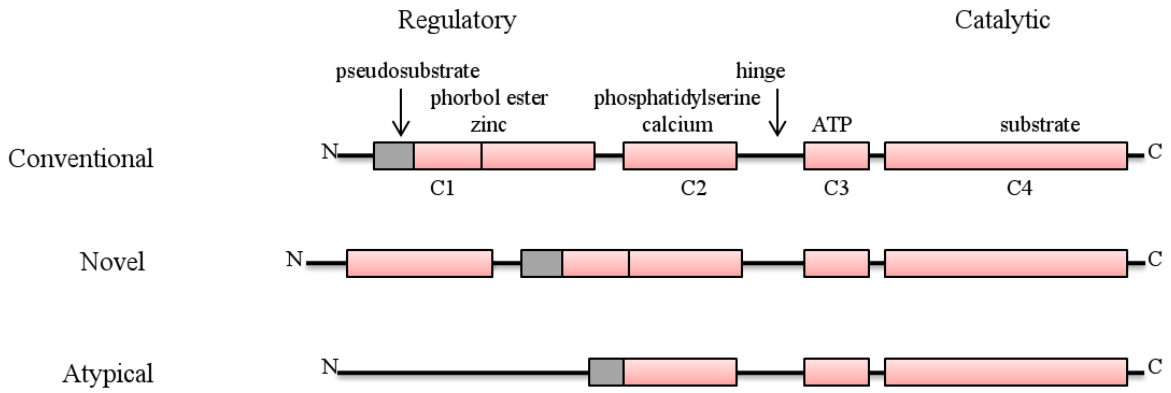

Figure 2-10. Schematic representation of the primary structure of PKCs.

Indicated are the pseudosubstrate domain, C1 domain comprising one or two Cys-rich motifs, C2 domain in the regulatory half, and the ATP-binding lobe (C3) and substrate-binding lobe (C4) of the catalytic region. The C2 domain of novel protein kinase Cs lacks amino acids involved in binding calcium but has key conserved residues involved in maintaining the C2 fold (hence its description as "C2-like"). Atypical protein kinase Cs have only one Cys-rich motif, and phorbol ester binding has not been detected.

PKCs playan essential partt in facilitating cellular responses to extracellular stimuli involved in proliferation, differentiation, apoptosis, and exocytotic release in a number of non-neuronal systems like islet cells, chromaffin cells and paramecium [94]. The prevalence of this enzyme family in signaling was exemplified by the diverse transduction mechanisms that resulted in the generation of protein kinase C activator, DAG. Interestingly, signals stimulating large families of G protein-coupled receptors, tyrosine kinase receptors, or non-receptor tyrosine kinases could evoke DAG production, either; rapidly by activation of specific phospholipase Cs or slowly by activation of phospholipase D to yield phosphatidic acid and then DAG [95, 96].

PKC has also been implicated in phosphorylation of several neuronal proteins, which were thought to regulate neurotransmitter release and establish long-term potentiation in memory formation [92]. In addition, fatty acid generation by phospholipase A2 activation modulated protein kinase C activity [97]. Hence, multiple receptor pathways feeding into multiple lipid pathways have common end results of activating protein kinase C by production of its second messenger.

Phorbol esters, potent tumor promoters, could substitute for DAG in activating protein kinase C [67]. Phorbol esters, unlike DAG were not readily metabolized, and treatment of cells with these molecules resulted in prolonged activation of protein kinase C. Thus, phorbol esters have proved invaluable in dissecting out protein kinase C-catalyzed phosphorylations *in vivo*.

In addition to regulation by DAG or phorbol esters, all protein kinase C isozymes require an acidic lipid, phosphatidylserine which is located exclusively on the cytoplasmic face of membranes, and some isozymes require Ca^{2+} for optimal activity [98,99].

The PKC family of enzymes has been shown to control signals for essential processes, such as cell growth, differentiation, transformation and signal transduction of extracellular receptors, including those for neurotransmitters, hormones, antigens, and growth factors. It is thus not surprising that PKC has been implicated in a wide range of physiological functions, such as oncology, immunology, cardiovascular functions and neurobiology, including pain transmission.

In the absence of activators, PKC is found primarily in the cytosol (Figure 2-11). Activation is accompanied by dissociation of the pseudosubstrate region from the catalytic domain and involves association with specific membrane proteins. These proteins, termed receptors for activated C kinases (RACK), function as selective scaffolds for activated PKC at discrete subcellular compartments [100]. PKC activation terminates with decay of the second-messenger signal followed by re-localization of PKC to the cytosol.

2.4.1 PKC activation and nociception

For the past two decades, scientists were trying to study and design novel PKC inhibitors. Studies using non-subtype selective PKC inhibitors have been suggested to be critically

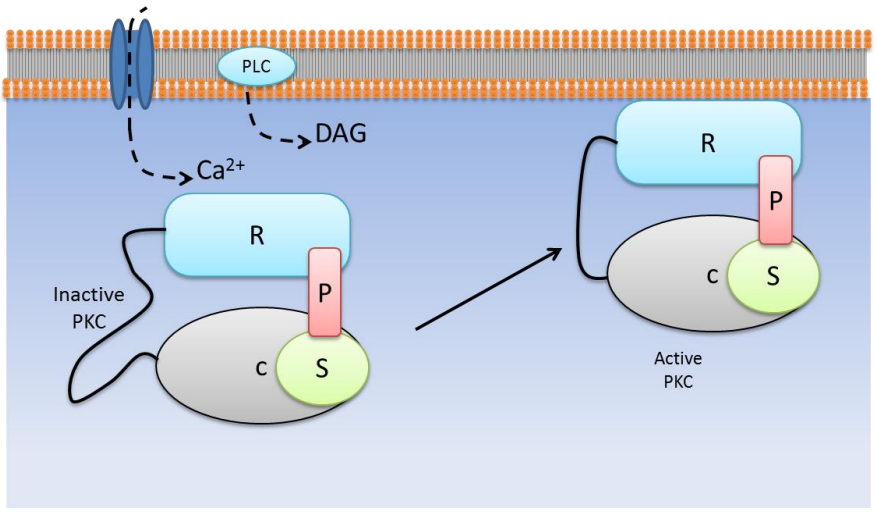

Figure 2-11. PKC activation.

PKC consists of a regulatory domain (R) attached by a hinge region to a catalytic domain (C). The regulatory domain contains the auto inhibitory pseudosubstrate (P) sequence. The catalytic domain includes the substrate binding site (S). In the absence of activators, PKC is found primarily in the cytosol. Activation is accompanied by dissociation of the pseudosubstrate region from the catalytic domain and involves association with specific membrane proteins.

involved in persistent pain states, including pain behaviours following tissue or nerve injury [101-103]. These studies proposed that PKC was involved in NMDA-receptor mediated hyper-excitability of dorsal horn neurons in the spinal cord. However, PKC isozymes were highly expressed in neuronal tissues of peripheral nervous system (PNS) and central nervous system (CNS) and might interfere with nociception at the both levels. For a better understanding of the involvement of PKC in nociception, focus has to be on specific isozymes and the expression pattern of the isozymes. An excellent review by Battaini, F. [104], highlighted that at the time of discovery; PKC was the receptor for tumour promoting phorbol esters, thus connecting a signal transduction process to tumour promotion/carcinogenesis [105]. Since then PKC has been demonstrated to be involved in a variety of other pathologies, such as cardiovascular [106], pulmonary [107], immune and infectious diseases [108]. PKC got more attention in the scientific community in 1996 after the identification of LY333531 that antagonized retinal, cardiac and renal vascular dysfunctions (associated with tissue specific increases in PKC β II levels) in diabetic rats and also was found to be a specific PKC β inhibitor [109]. LY333531 was found active after oral administration as it had shown positive results on retinal blood flow and circulation in types I and II diabetes mellitus patients [110,111]. In another report, Kim *et al*. [112] tried to find out whether PKC inhibition ameliorated diabetic hyperalgesia and, if so, whether the effect was obtained through action on neurons by testing nociceptive threshold in normal and STZ-induced diabetic rats treated with or without PKC-selective inhibitor LY333531. They found that a single intradermal injection of LY333531 into the footpads for 4 weeks significantly increased the nociceptive threshold which got decreased after diabetes induction. Also, after 6 weeks of treatment, LY333531 significantly decreased p-PKC and ameliorated a decrease in cGMP content in DRG of diabetic rats.

2.4.2 PKC in diabetic condition

As seen with ROCK, the underlying mechanisms of painful symptoms may be closely associated with hyperglycaemia and/or the pathogenic mechanism of diabetic neuropathy itself. Various hypotheses have been proposed to explain the pathogenesis of diabetic neuropathy [113,114]: polyol pathway hyperactivity, decreased nerve blood flow followed by endoneurial hypoxia, increased glycation of proteins, abnormal activity of PKC, decreased neurotrophism, and the associated exaggeration of oxidative stress. Among these hypotheses, the involvement of PKC may be one of the most relevant. Hyperglycaemia activates PKC, especially its isoform II, through increased de novo synthesis of DAG in retina [115],

glomeruli [116], aorta and heart [117]. This increased activity of PKCβ-II may impair retinal and endoneurial blood flow [118], causing renal hyperfiltration [119] and in the development of diabetic retinopathy, nephropathy, and neuropathy. In addition, selective PKCβ-II inhibitors ameliorated these abnormalities [110,120].

The role of PKCβ-II hyperactivity has also been well investigated with reference to pain generation, using not only phorbol esters and PKC activators [121], but also various members of the PKC superfamily. Chronic inflammation-evoked thermal hyperalgesia may involve several protein kinases, including PKCγ and PKA [122]. PKCε has also been shown to regulate nociceptive function in the experiments using either PKCε mutant mice or a PKCε-selective inhibitor peptide in DRG neurons [123]. Increase in PKCβ-II activity has been reported to participate in hyperalgesia caused by adjuvant-induced inflammation in the rat hind paw [124].

2.5 PKCβ-II inhibitors for treatment of diabetic indications

Protein kinase inhibitors represent an important and still emerging class of targeted therapeutic agents. Drug discovery and development strategies have explored numerous approaches to target the inhibition of protein kinase signalling. The following section highlights some of the strategies that have led to successful clinical development of therapeutic protein kinase inhibitors, based on a thorough literature search.

Human protein kinases are important therapeutic targets because they regulate a wide variety of signalling pathways. And include a great deal of distinct protein molecules. But since PKC family is too large, thus widely distributed across the body, a generalized inhibitor of PKCβ-II is likely to have serious or fatal systemic consequences [125]. However, the effects of inhibitors specific for one or a very few PKC subclasses might be limited to specific organs or biochemical pathways, and if such effects were therapeutic, such inhibitors could then be highly beneficial [126]. There is evidence that this is likely to be the case for PKCβ-II with regard to the prevention and treatment of diabetic retinopathy.

Several compounds have been developed that were specific inhibitors of PKCβ-II isoforms [126]. Synthetic inhibitors of protein kinases include small molecules that may be easily administered as oral therapeutic compounds. These inhibitors can rapidly and often specifically alter the activation state of a target kinase [127]. Several PKC inhibitors have gone under clinical investigations claiming to reduce microvascular complications in diabetic patients. The most important inhibitors are PKC 412 and ruboxistaurin (RBX).

PKC412 (Midostaurin, see Figure 2-12) is an N-benzoyl derivative of the naturally occurring alkaloid staurosporine (Figure 2-12) [128]. It is an inhibitor of several kinases but predominantly the PKC enzyme family. PKC412 inhibited the α, β, and γ isoform with similar half-maximal inhibition concentration (IC_{50}) values ranging from 22 to 31 nM/L and might be useful for treatment of diabetic retinopathy and other disorders [129]. The kinase domain of the human VEGF receptor-2 (KDR) and the platelet-derived growth factor receptor 2 were also inhibited by PKC 412 at IC_{50} values ranging from 20 to 100 nM/L.

In an animal model of neovascularization, PKC412 inhibited ischemia-induced angiogenesis as well as retinal vessel formation during development [110]. However, early pharmacodynamic studies of PKC412 have resulted in some adverse outcomes, which may reflect PKC412's relative lack of specificity. The principle toxicities of PKC412 are nausea/vomiting and fatigue. Additional significant side effects such as diarrhoea, anorexia, and headache could appear. Adverse effects were dose related but clinical relevant myelo-

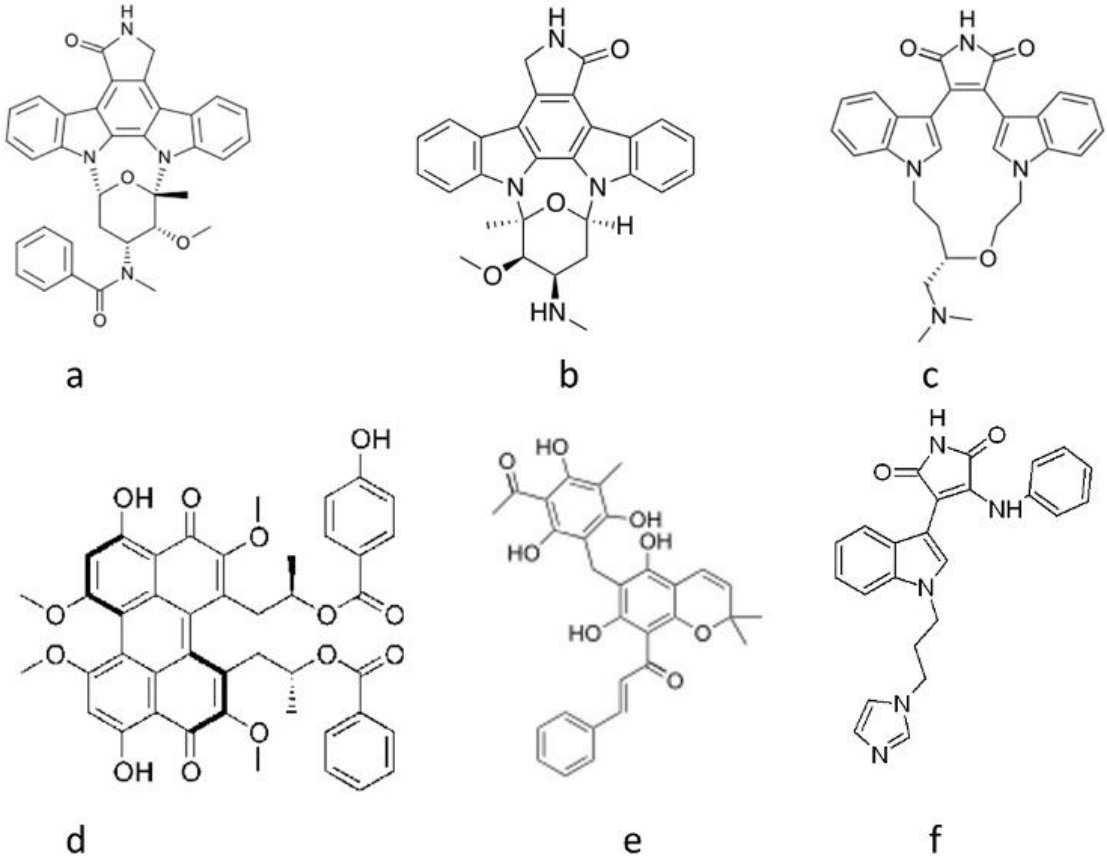

Figure 2-12. PKCβ-II inhibitors.

The figure shows some important PKCβ-II inhibitors a, PKC 412; b, Staurosporin; c, Ruboxistaurin; d, calphostin; e, Rottlerin and f, 539654.

suppression was not described. The best tolerated dose was 150 mg/d for chronic administration [130].

The important contribution of PKCβ-II to hyperalgesia has also been reported in diabetic animals. Phorbol esters enhanced thermal hyperalgesia in diabetic mice. Hyperalgesia and C-fibre hyperexcitability to mechanical stimuli observed in diabetic rats were reduced by intradermal injection of agents that inhibited PKCβ-II [131]. In an *in vitro* study using rat sensory neurons, PKCβ-II was shown to mediate release of substance P and calcitonin gene-related peptide (CGRP) from sensory neurons. This PKC-induced enhancement of peptide release might be a mechanism underlying the neuronal sensitization that produced hyperalgesia [132,133]. Thus, although the hyperactivity of PKCβ-II was thought to contribute to hyperalgesia in diabetes, the responsible mechanism has not yet been identified.

It had been known that diabetes and hyperglycaemia triggered the de novo synthesis of DAG, leading to the activation of PKC in the retina, kidney, heart, and blood vessels [11]. This increased PKC activity resulted in impaired retinal blood flow and renal hyperfiltration, thus contributing and accelerating the development of diabetic retinopathy and nephropathy. Among the many isoforms of PKC, the PKCβ-II isoform has been reported to be predominantly activated by hyperglycaemia in the retina, kidney, aorta, and heart of diabetic rats and in cultured rat mesangial cells [134,135]. These observations have been confirmed by the fact that the PKCβ-II selective inhibitor LY333531 (LY), a macrocyclic bisindolylmalemide compound, prevented these deficits in the retina and kidney [136]. Ruboxistaurin (RBX) is an orally active PKCβ-II inhibitor. It binds to the active site of PKCβ-II, thus interfering with ATP binding and inhibiting phosphorylation of substrates. RBX gets metabolized by CYP3A4 to its main equipotent metabolite, N-desmethyl RBX [137]. It could also be used for other diabetic complications like retinopathy, nephropathy, and heart failure. Treatments that could prevent, improve or even slow the progression of DPN would result in decreased morbidity and would improve the quality of life of diabetic mellitus.

Campochiaro and the C99PKC412003 Study Group published in 2004 [138] the results of the treatment with this drug in patients with diabetic macular edema. It was a randomized (1:1:1:1), multi centre, double masked, parallel group study in which subjects (n=141) received placebo or PKC 412 (50, 100, or 150 mg/d) for up to 3 months. Visual acuity and retinal thickening were evaluated. The results were strongly dose dependent, with no treatment effect in the placebo or 50 mg/d groups and a significant effect at the two higher

doses. The results were time dependent. The two high dose groups showed a trend toward decreased thickening at 1 month and definite decreases in 3 months. Signs of liver toxicity, primarily manifested as elevations in serum transaminases, were observed in some patients during treatment with higher doses of PKC412, especially the 150 mg/d dose. The concern regarding liver toxicity with systemic therapy made local delivery an appealing approach.

In 1996, the chemical characterisation and *in vivo* pharmacological profile of a highly selective and orally active PKCβ inhibitor, LY333531 (RBX mesylate, Eli Lilly, Figure 2-12), was reported in Science [110], and it was found to block vascular complications of diabetes, including abnormalities in retinal blood flow, neovascularization, and VEGF mediated effects on permeability in animal models. RBX had considerable selectivity and reversibility for inhibiting PKCβ-I and PKCβ–II with IC_{50} values around 5 nM which was 0.100 times lower than the IC_{50} values for other PKC isoforms and other kinases. The experimental profile of RBX and related analogues with PKCβ-II inhibitory activity have been evaluated in a range of experimental models related to diabetic retinopathy and other microvascular complications [140,141].

Early clinical studies in patients with minimal DR, RBX reversed retinal blood flow abnormalities and was well tolerated. This molecule has also an important effect on VEGF expression in ocular tissues. It has been demonstrated in animals models that RBX reduced VEGF induced retinal permeability and attenuated new vessel formation on the retina and optic nerve [142,143]. The clinical development of RBX began with phase I tolerability and pharmacokinetic studies in healthy volunteers, followed by phase II efficacy studies in patients with diabetes [111, 144].

Having confirmed the basic safety and tolerability of RBX, and demonstrated that it had pharmacodynamic activity on retinal blood flow, large international RCTs were initiated to evaluate the safety and efficacy of the treatment in larger patient groups during longer term administration (2–4 years). The PKC Diabetic Retinopathy Study (DRS) and the PKC Diabetic Macular Edema (DME) Study were internationally randomised, placebo controlled trials designed to evaluate whether oral treatment with RBX will delay progression in patients with moderate to severe non-proliferative diabetic retinopathy at baseline, including progression from non-clinically significant to clinically significant macular edema [140,145].

The PKC study group published in 2005 the effects of RBX in diabetic retinopathy progression. It was a randomized, placebo controlled, multicenter clinical trial designing to

test the primary hypothesis that RBX, a β-isoform–selective PKC inhibitor, would delay either the progression of DR on the ETDRS retinopathy severity scale or the application of laser photocoagulation in patients with moderately severe to very severe NPDR, 20/125 or better visual acuity, and no prior scatter (panretinal) photocoagulation for DR. Three different doses of RBX (8, 16, or 32 mg/day) were administered to 256 patients during 36 to 46 months. RBX was well tolerated without significant adverse effects but had no significant effect on the progression of DR. The authors justified the lack of effect to several reasons. Study patients had moderately severe to very severe NPDR at baseline. It has been well established that PKC was activated very early in diabetes, well before clinically apparent retinopathy. So significant biochemical and pathologic retinal changes that were no longer amenable to PKCβ inhibition might have already occurred before enrolment of the participants Alternatively, RBX might not be potent enough to overcome these effects. It was also known that the majority of the neovascular response in the retina was mediated by VEGF [140].

However, in this study there did appear to be a beneficial effect of RBX on the secondary study outcomes of preventing visual loss. Treatment with RBX for 36 to 46 months reduced the relative risk of moderate visual loss by 63% (P=0.012) even accounting for potential confounding variables and despite having no effect on progression of DR. This effect was primarily evident in eyes with definite diabetic macular edema at baseline, reducing the risk of moderate visual loss sustained over 6 moderate visual loss sustained over 6 months from 25% in placebo to 10% in the 32 mg/d RBX treated group (P=0.017).

In 2006 the PKC group reported the effects of the PKCβ inhibitor RBX on visual loss in patients with diabetic retinopathy. A 3 year multicenter randomized trial at 70 sites across the United States tested the effects of 32 mg RBX *versus* a placebo. The major findings were (1) the risk of sustained moderate visual loss was reduced by nearly half, from 9% in the placebo group to 5.5% in the RBX treated patients; (2) RBX treated patients were twice as likely to gain >15 letters in acuity from baseline to the end of the study compared with the placebo treated patients; (3) RBX reduced the risk of progression and worsening of a specific measure of diabetic macular edema; and (4) RBX reduced the use of focal/grid photocoagulation by 26% [142,145].

To evaluate the safety and efficacy of orally administered RBX in patients with diabetic macular edema (DME), the PKC DMES Group was stablished and a phase III clinical trial was designed. It was a multicenter, double masked, randomized, placebo controlled study of

686 patients receiving placebo or RBX orally (4, 16, or 32 mg/d) for 30 months. At baseline, patients had DME farther than 300 μm from the centre of the macula, an ETDRS revealed increased severity level without prior photocoagulation, and an ETDRS visual acuity of 75 or more letters in the study eye. The primary study outcome was progression to sight threatening DME or application of focal/grid photocoagulation for DME. The thirty month results of this study were published in 2007 [146]. No serious adverse events were reported more frequently in RBX treatment groups. Although the non-serious adverse event occurrence frequency of diarrhoea, flatulence, nephropathy, proteinuria, and coronary artery disease was highest among patients in the 16 mg/day RBX treatment group, there did not appear to be RBX dose response effects.

RBX appeared as a new alternative in the control of ocular complications of diabetes and it was necessary to define if it was good enough to be used alone or if it had to be used in combination with other treatments to prevent visual loss in patients with diabetes. According to Gardner [144] RBX represent the beginning of a new era in diabetes complications treatments, with increased emphasis on pharmacologic and medical therapy and less emphasis on destructive surgical procedures.

In addition to these molecules, there were some more recently reported PKCβ-II inhibitors: Go 6976, Go6983, Ro-31-8220, Ro-31-8425, Ro-32-0432 and CGP41251 (Figure 2-13).

In addition to affecting DAG levels, diabetic conditions also brought alterations in AGEs which had been recognized as a pivotal inducer in diabetes and kinds of aging-related vasculopathy. Endothelial dysfunction and inflammatory cells adhesion to endothelium have been regarded as important and early factors in the pathogenesis of vascular complications in diabetic patients [147]. Also, a recent research using mesangial cell model of diabetes indicated towards possible oxidative stress mediated cross-activation between PKC and AGE in and high protein diet. The study used calphostin C and PLY379196 as PKC inhibitors. They also proposed that PKC might amplify cellular injury by promoting AGE accumulation [147].

Current research is exploring the variation in ROCK and PKCβ-II levels in diabetic condition. The increased activation might produce instability of axonal cells leading to nerve degeneration. Since the complexity of these two kinases have been acknowledged widely, therefore future success in combating diabetic neuropathy depends on the definitive mechanisms of ROCK and PKCβ-II in diabetic neuropathy. Studies presented in this chapter

suggested that activation and overexpression of these two proteins might be involved in the resultant diabetic neuropathy, and their inhibition is a promising target for intervention. Also, since the inhibitors will be useful candidates for a wide range of clinical indications including diabetes-related long term complications and AD. Thus these two kinases pose as attractive target for inhibitor design and were considered important for our study.

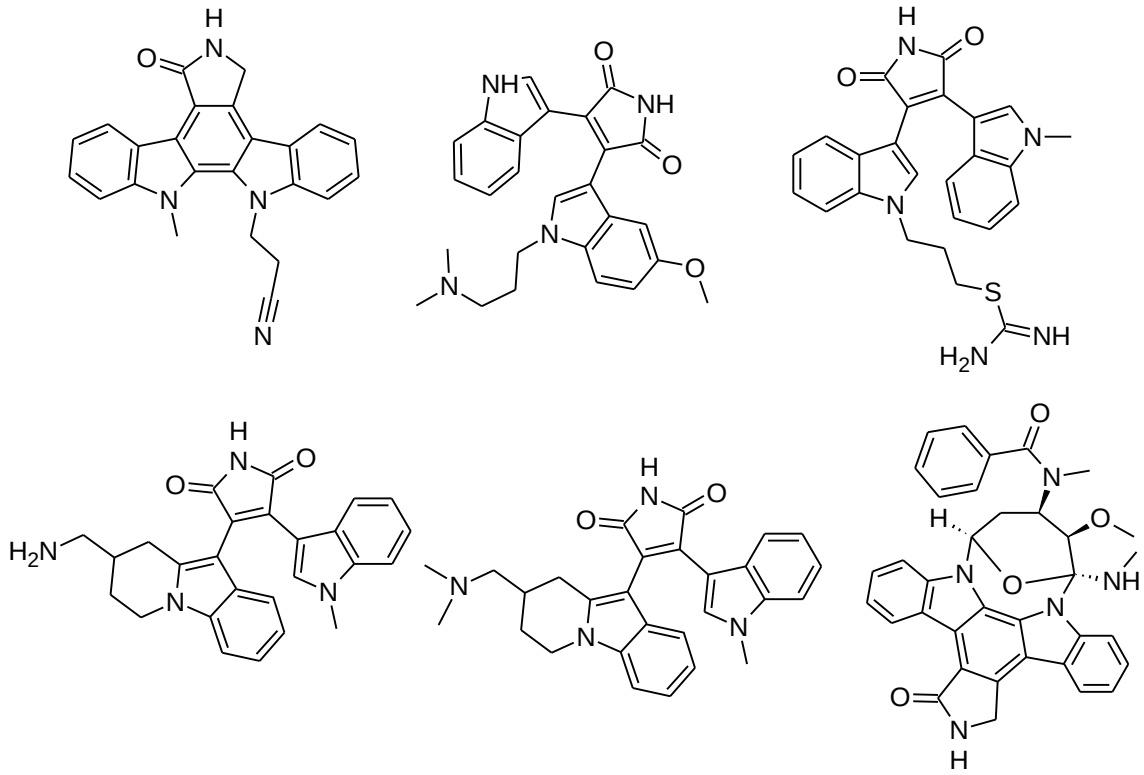

Figure 2-13. Newly identified PKCβ-II inhibitors.

Figure shows recently discovered PKCβ-II inhibitors (Clockwise from top left) Gö 6976, Gö 6983, Ro-31-8220, Ro-31-8425, Ro-32-0432 and CGP41251

“Begin at the beginning," the King said, very gravely, "and go on till you come to the end: then stop.”

— Lewis Carroll, Alice in Wonderland

Chapter 3.
Objectives and Plan of Work

Neuropathy is one of the long-term complications of diabetes which affects the nerves. Nerves carry messages between brain and every parts of body, thus making it possible to see, hear, feel and move. Nerves also carry signals that we are not aware of such as beating of heart and pain sensation. Thus, any damage to the nerves could cause problems in various parts of the body. Diabetes causes neuropathy as a result of high blood glucose levels damaging small blood vessels which supply the nerves. There are other mechanisms also involved. Increased levels of extracellular glucose activates enzymes like ROCK and PKCβ-II, which further causes hyperalgesia. Thus, these enzymes play a critical role in pathophysiology of diabetic neuropathty.

Based on the literature review, it was clear that protein kinase inhibitors could be used for treatment of various neurological disorders including painful diabetic neuropathy. Recent studies have reported abnormal activation of the protein kinase pathway in various disorders of central nervous system. Injury to the brain and spinal cord activates these protein kinases, thereby inhibiting neurite growth and sprouting. Inhibition of these protein kinases results in accelerated regeneration, thus leading to advanced functional recovery [148,149]. Thus protein kinase inhibitors have potential of preventing neurodegeneration and initiating neuro-regeneration in various neurological disorders [150]. Such findings implicated protein kinase inhibitors as potential targets for drug discovery against neurological disorders. Thus, design of potent protein kinase inhibitors against multiple disease conditions has received widespread attention in the scientific community. This can be further supported by recent

reports on crystal structures which provided an extensive sampling of the active site of these proteins. These newer developments are of immense importance in the development of newer drugs through rational studies to introduce a whole new class of drugs in the market which could combat the problem of neuropathy with better efficacy. Thus, to identify novel inhibitors, we have utilized energy-based-pharmacophore as design approach followed by virtual screening to identify potential hits. Hence the present objectives were devised to include the following.

3.1 Objectives

The objective of the proposed work was to design novel potential protein kinase inhibitors for the treatment of diabetic complications including neuropathy by utilizing the knowledge from the fields of computational chemistry and drug design, bioinformatics, medicinal chemistry, biotechnology and pharmacology. We utilized ROCK and PKCβ-II as primary targets. Lead molecules were identified using *in silico* methods. Identified compounds were further characterized using enzyme inhibition, cell-based and extensive pre-clinical studies using animal models.

3.2 Plan of work

The compounds were identified *in silico* using Schrödinger suite of softwares. Biophysical characterization, neuroprotective and anti-neuralgic profile of identified compounds were established using various *in vitro* and *in vivo* models assays as outlined below:

1. Protein kinase inhibitors
    a. Identification and validation of suitable feature template (pharmacophore) from crystal structures
    b. Virtual screening of commercially available and *in house* database to identify potential hits
    c. Biological evaluation of identified hits
        i. Enzyme inhibition studies
        ii. Thermal stability studies using differential scanning fluorimetry
        iii. Cell based assays and cytotoxicity studies
    d. Pharmacological assays
        i. Determination of neurotoxicity
        ii. Efficacy in neuropathic pain models
            a. Streptozotocin induced diabetic neuropathy model
            b. Chronic constriction injury model

iii. Efficacy in MeHg-induced model of neurodegeneration

"Always aim at complete harmony of thought and word and deed.
Always aim at purifying your thoughts and everything will be well."
-Mahatma Gandhi

Chapter 4.
Materials and Methods

4.1 Computational details

All computations were carried out on an Intel Core 2 Duo E7400 2.80 GHz capacity processor with a memory of 2 GB RAM running with the RHEL 5.2 operating system. Glide 5.8 module of Schrödinger suite was used to screen the public database like Asinex. Phase 3.4 implemented in Maestro 9.3 software package (Schrödinger, LLC) was used to generate pharmacophore.

4.2 Protein structure preparation

We selected eight crystal structures of ROCK I bound with inhibitors from protein data bank (PDB) that included 2ESM, 3D9V 2ETK, 3NCZ, 3NDM, 3TV7, 3TWJ and 3V8S. Similarly, 2I0E was selected for PKCβ-II. Protein preparation wizard in Maestro software was used to prepare the proteins (Maestro, v9.2, Schrödinger, LLC, New York, NY). Co-crystallized water molecules beyond 5 Å of bound inhibitor were removed. Proteins were minimized using OPLS_2005 [151] force field. Bond orders and formal charges were added for hetero groups and missing hydrogen atoms were added to correct the ionization and tautomeric states of amino acid residues using Epik module.

The method of protein preparation had significant effect on the study [152]. The protein preparation wizard of Schrödinger could predict the protonation states using the PROPKA program [152-154]. A recent update enabled Maestro to employ PROPKA for its pK_a prediction instead of Epik, which was used to assign the protonation states of ligands. PROPKA used an empirical approach to predict pK_a values by perturbating the standard pK_a

values for each amino acid residues with terms (whose coefficients have been fit to experimental data) that reflected local hydrogen bonding, desolvation effects, and charge-charge interactions. PROPKA had proven its capability of reliably predicting pK_a values (<1 log unit from experiment) for an entire protein in a matter of sec [153].

The pK_a values of the protein were predicted by selecting "Use PROPKA" option in protein preparation wizard interface. A target pH of 7 was specified to simulate biological condition. Based on the PROPKA output, hydrogen bonds were automatically assigned. Resulting crystal structure was used further for e-pharmacophore hypotheses generation.

4.3 E-pharmacophore generation

Energetic descriptions of the ligand-receptor complexes were retrieved using G scoring function which was a part of docking program Glide 5.7. The procedure followed was as reported earlier by our group [155]. Briefly, based on the XP descriptor information, pharmacophore features were generated using Phase 3.4 using the default set of six chemical features: hydrogen bond acceptor (A), hydrogen bond donor (D), hydrophobe (H), negative ionizable (N), positive ionizable (P), and aromatic ring (R). Hydrogen bond acceptor sites were represented as vectors along the hydrogen bond axis in accordance with the hybridization of the acceptor atom. Hydrogen bond donors were represented as projected points, located at the corresponding hydrogen bond acceptor positions in the binding site. Each pharmacophore feature was first assigned an energetic value equal to the sum of the Glide XP contributions of the atoms comprising the site, allowing sites to be quantified and ranked on the basis of the energetic terms. ChemScore, hydrogen bonding and lipophilic atom pair interaction terms were included when the Glide XP terms for hydrogen binding and hydrophobic enclosure were zero.

4.4 E-pharmacophore validation

For e-pharmacophore validation, we needed a set of already known actives and another set of drug-like inactive molecules (decoys). E-pharmacophores were validated using receiver operating characteristic (ROC) calculations. In a ROC curve the true positive rate (sensitivity) is plotted in function of the false positive rate (100-specificity) for different cut-off points of a parameter. Each point on the ROC curve represents a sensitivity/specificity pair corresponding to a particular decision threshold [156]. ROC represented a plot of true positive rate as a function of the false positive rate. AUC, the area under the ROC curve represented quantification of the curve, as a measure of how well a parameter can distinguish

between two diagnostic groups (diseased/normal). Thus AUC facilitated an easier comparison of results. AUC was calculated as follows:

$$AUC = 1 - \frac{1}{N_{actives}} \sum_{i}^{N_{actives}} \frac{N^{i}_{decoys\ seen}}{N_{decoys}}$$

Where $N_{actives}$ depicted the number of actives, N_{decoys} represented the number of decoys and $N^{i}_{decoys\ seen}$ described number of decoys ranked higher than *i-th* active structure. AUC ranged between 0 and 1 and a value of 0.5 indicated a random performance. AUC metrics could be considered as a measure to evaluate the performance on the complete data. However, additional matrices were also needed to retrieve actives form a small fraction of database. To solve this problem, enrichment factor (EF) [156] at a predefined fraction of the data set (x%) was calculated as follows:

$$EF_{x\%} = \frac{\frac{N_{actives\ seen}}{N_{x\%}}}{\frac{N_{actives}}{N_{actives} + N_{decoys}}}$$

Where $N_{actives\ seen}$ was the number of actives identified out of $N_{actives}$ molecules. $N_{x\%}$ was predefined fraction containing x% of database molecules. The enrichment factor depended on the number of actives, and therefore it was not a robust metric. Other popular metrics for the early enrichment evaluation were the Boltzmann-enhanced discrimination of receiver operating characteristic (BEDROC) score [156]. All e-pharmacophores were checked for the enrichment factor (EF), BEDROC (α=160.9, 20 and 8), based on recovery rate of actives against the ranked decoy database. ROC was calculated by screening a database consisting of some known inhibitors and 1000 drug-like ligand decoys set available at Schrödinger (http://www.schrodinger.com/Glide/Ligand-Decoys-Set). Manual EF (EF_{manual}) and goodness of hit (GH) values were calculated using following formulae:

$$\mathrm{EF}_{\mathrm{manual}} = \frac{H_a \times D}{H_t \times A}$$

$$GH = \left(\left(\frac{H_a}{4H_tA}\right) \times (3A + H_t)\right) \times \left(1 - \left(\frac{H_t - H_a}{D - A}\right)\right)$$

Where H_t represented number of hit molecules from the database, H_a was the number of active molecules in hit list, D was the number of decoys and A the number of actives.

Despite the early recognition problem the EF has some problems ignoring complete ranking of the whole dataset molecules [156]. To address the problem, Sheridan et al. developed an

exponential weighted scoring scheme RIE (robust initial enhancement) which gives heavier weight in early recognized hits [157].

$$RIE = \frac{\frac{1}{n}\sum_{i=1}^{n} e^{-\propto x_i}}{\frac{1}{n}\left(\frac{1-e^{\alpha}}{e^{\frac{\alpha}{n}}-1}\right)}$$

Where *x*i=ri/N is the relative rank of the *i*-th active compound and α is the tunning parameter. Changing the parameter α, one can control the early ranking of hits. BEDROC values ranges in between 0,1 and can be defined as the probability that an active is ranked before a randomly selected compound was exponentially distributed with parameter α. BEDROC and RIE have a linear relationship [158].

4.5 Molecular shape generation

All the PDBs of ROCK utilized for e-pharmacophore generation were also employed for molecular shape analysis after preparing the protein. The query was prepared using default Omega parameters and ImplicitMillsDean force field. Molecular shape and colour atoms were automatically assigned to the query. One query was generated from each prepared PDB structure. The software employed was from OpenEye systems [156].

4.6 Shape validation

Each shape based query was validated using directory of useful decoys (DUD) dataset (http://dud.docking.org). Actives used in e-pharmacophore validation were also used for shape validation. "Perform ROCS validation" script available in ROCS module of OpenEye suite was used for shape validation. Decoys and active databases were prepared using Omega with default settings. AUC for the ROC curve and enrichment at 0.5%, 1% and 2% were calculated. Based on AUC and enrichment factors, final shapes were selected for further studies.

4.7 Ligand preparation

Commercially available Asinex database (http://www.asinex.com) containing 525,807 molecules was processed through redundancy checking and Lipinski filters. Structures were prepared using LigPrep 2.5 module to expand protonation and tautomeric states at 7.0±2.0 pH. Conformational sampling was also performed for all database molecules using the ConfGen search algorithm with OPLS_2005 force field. Duplicate poses were eliminated if the RMSD was less than 2.0 Å. A distance-dependent dielectric constant of 4 and maximum relative energy difference of 10 kcal mol^{-1} were applied. The database was indexed using

Phase which also automatically created pharmacophoric sites for each conformer, thus allowing rapid database alignments and screening.

4.8 E-pharmacophore and shape-based virtual screening

Commercially available Asinex database containing 525,807 molecules was used for virtual screening. The database was prepared using LigPrep 2.5 module of Schrödinger suite. Phase 3.4 module of Schrödinger suite was employed for database screening. Each e-pharmacophores were individually subjected to database search using "Find matches" option. Database was screened with the following conditions (a) conformation of the database molecules was generated on the fly by implementing flexible search, (b) at least three of the total sites of the quantitative common pharmacophore were matched and (c) it should not consider partial matches involving more sites. Outputs from all database screening runs were merged and duplicates were identified. Among duplicates, only the molecules with highest fitness score were retained. Finally, molecules with fitness ≥2 were selected for docking.

For the shape based filtering, the Asinex database was prepared using Omega 2.3.2 module in OpenEye systemic software. The final selected shapes were subjected to database screening. Hits were pooled and sorted by tanimoto combo rankings. Duplicates were identified and only those with highest tanimoto scores were retained. Top molecules with high tanimoto scores were selected as hits for further studies.

4.9 Molecular docking

Filtered hits from e-pharmacophore and shape-based queries were subjected to docking studies into the respective crystal structure active sites. Three modules of Glide were used for docking: high throughput virtual screening (HTVS), followed by standard precision mode (SP) and extra precision mode (XP). Glide HTVS was faster and more tolerant to suboptimal fits than Glide XP, making it better for comparison in this work. The centre of the Glide grid was defined by the position of the co-crystallized ligand. Default settings were used for both the grid generation and docking. Post docking minimization was implemented to optimize the ligand geometries. Compounds with best docking and Glide scores were then subjected to Glide SP and XP screening. Finally we identified top ranked molecules based on docking score and visual inspection. ADME properties of the top ranked molecules were calculated using QikProp module [160] of Schrödinger suite.

4.10 *In house* database screening

In addition to the commercially available Asinex database, we also employed screening of our *in house* database (BITS-DB) for PKCβ-II design. The *in house* database was a central

repository of structurally diverse (3000) compounds earlier synthesized in the Drug Discovery Research Laboratory (DDRL) – BITS Pilani, Hyderabad Campus. The molecules were stored in Maestro's native ".maegz" file format. The molecules were first drawn in 2D format using ACD/Chemsketch software, where 3D structures were generated and ionization states were optimized for pH 7 using LigPrep module of Schrödinger suite.

The BITS-DB molecules were directly subjected to molecular docking. Docking process was the same like previously described in section 4.9. After XP docking, the molecules were sorted according to their docking score and were visually inspected. The molecules were selected considering their docking score and availability. ADME properties were calculated using QikProp module [160].

4.11 Biological characterization of ROCK inhibitors

Top hits were procured from Asinex. The cloned ROCK construct *pET-21(+)* ROCK was obtained from our collaborator at National Institute of Immunology, New Delhi, India.

4.11.1 ROCK expression and purification

Plasmid *pET-21(+)*ROCK was transformed in *E. coli* BL21(DE3) and was used for purification of ROCK-I. This plasmid carried a hexahistidine tag (His-Tag) at its N-terminus which facilitated purification by Ni-NTA affinity chromatography. The protein was induced at 18 ^{o}C for 16 h by addition of 0.1 mM isopropylthio-β-galactoside (IPTG). Cell pellet was homogenized in lysis buffer containing 10 mM Na_2HPO_4, 1.8 mM KH_2PO_4, pH 7.4, 137 mM NaCl, 2.7 mM KCl, 1 mM DTT, protease inhibitors cocktail (Sigma Cat. NO P8465) and 5% phosphate-buffered saline supplemented with glucose (PBSG), sonicated and centrifuged at 10,000 rpm for 35 min. The clarified lysate was mixed with pre-equilibrated Ni-NTA resin, and gently twirled at 4 ^{o}C for 3½ h for facilitating binding of the His-Tag protein. The resin bound protein was centrifuged at 500 rpm for 5 min, packed on a Bio-Rad column in PBSG, and bound protein eluted step wise with TBG (thyroxine binding globulin) elution buffer (50 mM Tris-HCl pH 7.4, 137 mM NaCl, 2.7 mM KCl and 5% glycerol) containing 0, 10, 25, 50, 100 or 200 mM imidazole, and monitored by the Bradford colorimetric assay. The purity of ROCK-I was determined by Coomassie-blue stained SDS-PAGE analysis. Fractions enriched with ROCK-I (>95% purity) were pooled and dialysed against TBG containing 50% glycerol, divided into aliquots and stored at -80 ^{o}C till further use.

4.11.2 ROCK enzyme inhibition assay

Inhibition of ROCK activity was evaluated spectrophotometrically in a coupled assay format, wherein a molecule of NADH was oxidized to NAD^+ each time a phosphate was transferred

by ROCK [161]. The assay was conducted in a 96-well plate format in a reaction mix (90 µL) containing 0.1 M HEPES (pH 7.6), 10 mM $MgCl_2$, 2.5 mM PEP, 0.2 mM NADH, 0.01 mg/ml LDH, 2 mM DTT, 100 nM of ROCK protein and myelin basic protein (MBP) as the universal kinase substrate. Reaction was initiated by the addition of 10 µl ATP and absorbance measured at 340 nm in a multi-plate reader (PerkinElmer Victor V3 spectrophotometer). Preliminary screening was conducted at 40 µM concentration and active compounds were further investigated in a dose-response assay and IC_{50} values were computed using GraphPad prism 5.03 software (La Jolla, CA, USA).

4.12 Biological characterization of PKCβ-II inhibitors

Top hits obtained from Asinex database search were procured from Asinex. The ADP-Glo kit was procured from Promega India. All supplies were procured from Sigma-Aldrich or Himedia.

4.12.1 Inhibition of PKCβ-II activity

PKCβ-II inhibition assay was performed using ADP-Glo reagent. The assay was performed in two steps. First, the kinase acted on the substrate and after the ATPase reaction was completed, ADP-Glo reagent was added to terminate the kinase reaction to deplete the remaining ATP. In the next step, the kinase detection reagent was added to convert ADP to ATP thus allowing the newly synthesized ATP to be measured using a luciferase/luciferin reaction [160]. The light generated was correlated to the amount of ADP generated in the kinase or ATPase assay, which was indicative of kinase or ATPase activity.

4.13 Cell based assays

HEK-293 and IMR-32 cells were utilized for the cell based assays and were procured from NCCS Pune. MeHg was obtained from Sigma-Aldrich, India. Other supplies were procured from Sigma-Aldrich or Himedia. The cells were cultured in MEM medium supplemented with FBS (10%), L-glutamine (1%), penicillin (10,000 units) and streptomycin (10 mg/ml) at 37 ºC in 5% CO_2 atmosphere. For all assays, cells were maintained at 90% confluence and was used as required. MeHg (10 mM) was prepared in double distilled water and further diluted as per requirement. All test compounds were dissolved in DMSO (10%).

4.14 Cytotoxicity studies

MTT ((3-(4,5-dimethylthiazol-2-yl)-2,5-diphenyltetrazolium bromide) reduction assay was used to measure cytotoxicity [163]. Briefly, exponentially growing HEK-293 cells (10,000 cells/ well) seeded in 96-well plate in MEM medium containing 1% FBS were treated with 100 µM of test compounds for 48 h. For cell viability evaluations, 10 mg/ml of MTT solution

in 1X PBS was added to the wells and incubated for 3 h. The violet crystals formed were dissolved in 100% DMSO and absorbance was measured at 595 nm in spectrophotometer (Perkin Elmer victor X3). The experiment was done in triplicates and percent cytotoxicity was reported.

4.15 Growth inhibition assay

Inhibition of growth of IMR-32 cells induced with MeHg by the test compounds was measured in a dose-response curve in triplicates. Approximately 5000 cells per well were utilized for this study [164]. Cell cultures were first treated with MeHg (10 µM) for 2 h. After MeHg exposure, the cells were treated with test compounds (0.01-100 µM). Growth inhibition was measured by MTT addition, similar to the cell cytotoxicity studies. GI_{50} values were calculated using GraphPad prism 5.03.

4.16 Measurement of ROS production

Intracellular ROS estimation was measured using DCFH-DA [164]. Approximately 5000 IMR-32 cells per well were plated in 96 well plate, treated with 5 µM DCFH-DA for 1 h followed by 20 µM MeHg for 2 h. Compounds were added at varying concentrations for 3 h, fresh medium replenished and cells cultured further for 24 h. Oxidized DCFH excitation and emission were measured at 485 and 525 nm respectively in a spectrophotometer (SpectraMax M4, Molecular Devices, Sunnyvale, USA). Fasudil was employed as a positive control. Percent ROS inhibition was calculated using GraphPad prism 5.03.

4.17 Synthesis of lead compounds

Synthesis of 2,6-diaminopyrimidine derivatives (**RK1-8**) was achieved as presented in Figure 4-1. Synthesis started with 1-iodo-4-nitrobenzene which was subjected to etherification with different substituted phenols in the presence of K_2CO_3 and DMF to yield corresponding ethers (**1a-1h**). Further nitro function was reduced to corresponding amines in presence of Zn and ammonium formate to yield corresponding amines (**2a-2h)**. These amines were further subjected to microwave assisted N-alkylation with 2,6-diamino-4-chloropyrimidine in the presence of PTSA as catalyst to afford the final compounds (**RK1-8**) in yields ranging between 56-75%. All commercially available chemicals and solvents were used without further purification. TLC experiments were performed on alumina-backed silica gel 40 F254 plates (Merck, Darmstadt, Germany). The homogeneity of the compounds was monitored by thin layer chromatography (TLC) on silica gel 40 F254 coated on aluminium plates, visualized by UV light and Iodine (I_2) treatment. Flash chromatography was performed on a Biotage Isolera with prepackaged disposable normal phase silica columns. All ^{1}H and ^{13}C

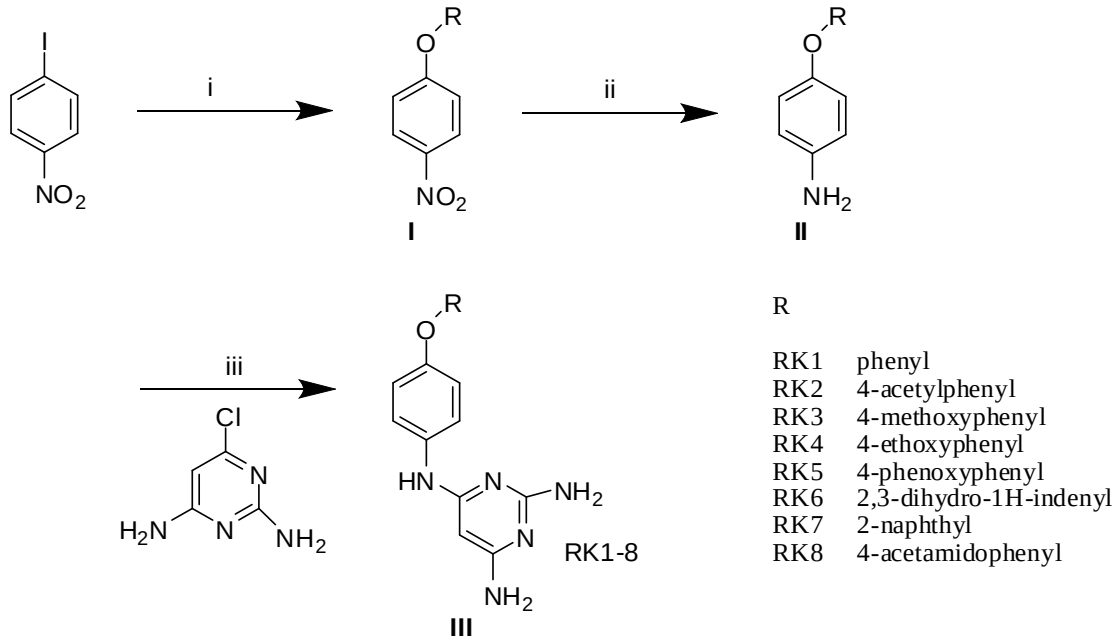

Figure 4-1. Synthetic protocol of substituted 2,6-diaminopyrimidine derivatives.

Reagents and conditions: i. K_2CO_3, R-OH (substituted phenols), DMF, SiO_2, 110 ºC, 3-4 h reflux; ii. Zn, $HCOONH_4$, CH_3OH, 0 ºC; iii. MeOH, PTSA, 90 ºC, Microwave (90 W), 20 min.

NMR spectra were recorded on a Bruker AM-300 (300.12 MHz, 75.12 MHz) NMR spectrometer, Bruker BioSpin Corp, Germany. Chemical shifts are reported in ppm (δ) with reference to the internal standard TMS. Coupling constants are referred to as J values in Hz. Molecular weights of the synthesized compounds were checked by LCMS 6100B series Agilent Technology. Elemental analyses were carried out on an automatic Flash EA 1112 Series, CHN Analyzer (Thermo). Melting points were determined using a VMP-CM digital melting point apparatus and were uncorrected.

4.17.1 General procedure for the synthesis of substituted ethers (1a-1h)

To a stirred solution of substituted phenols (1.2 equiv), in dimethyl formamide at 110 ºC, was added K_2CO_3 (2.5 equiv) stirred for few minutes and then added 1-iodo-4-nitrobenzene (1 equiv) and 20 mol% SiO_2 (60-120 mesh) at same temperature, and allowed to reflux at 110 ˚C for 3 h. Then the reaction mixture was quenched with ice cold water and partitioned between EtOAc and water. The organic phase was extracted with brine for 3-4 times. The organic layer was dried over anhydrous $MgSO_4$, filtered, evaporated to dryness and was purified by flash chromatography using EtOAc/Hexane (1:9) as eluent to afford compounds **1a-1h** (55-70%) [165].

4.17.2 General procedure for the synthesis of substituted amines (2a-2h)

To the stirred solution of **1a-1h** in methanol at 0 ºC under N_2 atmosphere, was added Zn (5 equiv) followed by ammonium formate (5 equiv) and allowed to stir at room temperature for 1 h. Then the reaction mixture was quenched with ice cold water and diluted with EtOAc and washed with brine solution. The separated organic layer was dried over anhydrous Na_2SO_4 and evaporated under *vacuo*. The obtained product was purified by column chromatography using EtOAc/Hexane (0.5:9.5) as eluent to afford compounds **2a-2h** (75-80%) [166].

4.17.3 General procedure for the synthesis of RK1-8

To the stirred solution of compounds 2,6-diamino-4-chloropyrimidine (1.2 equiv) in MeOH, was added the compounds **2a-2h** (1 equiv) followed by addition of catalytic amount of *p*-toluene sulfonic acid (PTSA, 10 mol %) and allowed to stir under microwave activation for 20 min at 90 ºC (90 Watt closed system). The crude reaction mixture was poured into water and extracted with EtOAc. The aqueous layer was extracted with EtOAc and the combined organic layer was dried over anhydrous $MgSO_4$, filtered, evaporated to dryness and purified by flash chromatography (DCM/MeOH 9.5:0.5) to afford compounds **RK1-8** (56-75%) [167].

4.18 Differential scanning fluorimetry (DSF) experiments

The ability of compounds to bind and stabilize the target protein ROCK was further investigated using DSF technique [168]. The target enzymes were step-wise heated alone, and with test compounds from 20-100 ºC in presence of fluorescence dye (SYPRO orange). During heat-denaturation process, the fluorescence of sypro orange increased after interacting with hydrophobic residues. Fluorescence was measured three times per minute using a LED/photodiode set matched to the excitation and emission wavelengths of sypro orange. The recorded fluorescence reads were fitted to the Boltzmann sigmoid function using CFX Manager software 3.0. Melting temperature of the protein was obtained as the lowest point of the first derivative plot. Melting temperature (T_m) was defined as the inflection point of each fitted curve. The observed temperature shift, ΔT_m, was recorded as the difference between T_m of a naïve protein and in complex with the ligand in the same plate.

4.19 Pharmacological methods

4.19.1 Materials

Wistar rats (male, 4 weeks, 250-350 g) and Swiss albino (SA) mice (male, 4 weeks, 25-30 g) were used for the experiments. Animals were maintained in a temperature-controlled room (22±2 ºC) with a 12 h light/dark cycle. All behavioural experiments were conducted in a quiet

room between 9 am to 1 pm to avoid diurnal variation. Before each experiment, the animal was acclimatized for 10 min. The investigator was blinded to the treatment groups. The procedure was adhered to the guidelines from the Institutional Animal Ethical Committee of the host institute. MeHg was obtained from Sigma Chemical Co. (St. Louis, MO, USA). Animals (n=6) were randomly assigned into groups.

4.19.2 *In vivo* neurotoxicity determination using rotarod

The minimal motor impairment was measured in mice by the rotarod test [169]. Before drug administration, mice were trained to stay on rotating rod (diameter 3 cm), rotating at 30 revolutions per minute. Neurotoxicity was indicated by the inability of the animal to maintain balance on the rotating rod for at least 1 min. All the animals received dose of the test compounds in the order of 300, 100 and 30 mg/kg respectively independently. The animals were subjected to rotating rod before dosing and 1 and 2 h after dosing respectively.

4.19.3 *In vivo* neurotoxicity determination using actophotometer

Similarly, the effect of the test compounds on spontaneous motor activity was measured using actophotometer [170]. The animal was kept in a digital actophotometer (Dolphin, India), which consisted of a dark rectangular chamber (30 x 30 cm), and was lined with six photoelectric cells. The instrument recorded a count when the rays of lights were blocked (cut-off) by the animal. Hence the counts represented the measure of locomotor activity of animals. These cut-offs were counted for a period of 5 min and the wire-mesh bottom of the actophotometer was cleaned before the next reading.

4.19.4 Painful diabetic neuropathy model

4.19.4.1 Diabetes induction

STZ (Sigma-Aldrich, India) was dissolved in citrate buffer (0.1 M citric acid monohydrate, 0.1 M tri-sodium citrate, pH 4.5). Each rat received a single 30 mg/kg intraperitonial (*i.p.*) injections of STZ after 18 h of fasting. Animals in the control group received the same buffer solution without STZ. Animals had free access to food and water after post injection. Blood glucose was measured from the 2^{nd} day after induction with blood samples collected from the tip of the tail. Only animals with blood glucose levels >200 mg/dL (Accu-Chek, Performa, Roche) were included in diabetic group [171]. All animals received weekly blood glucose check-up. The standard drugs used in *in vivo* studies were fasudil (Tocris Bioscience, India) and gabapentin (Sigma-Aldrich, India). Drugs were dissolved in 30% CMC solution.

4.19.4.2 Assessment of neuropathic pain in diabetic animals

Animals were tested on 21st day post diabetes induction as reported earlier [171]. After recording the baseline values, animals were dosed using a single *i.p.* injection (30 mg/kg) of compounds and tested 1 h post drug and was compared with baseline values. Fasudil was used as standard drug for comparison.

4.19.4.3 Mechanical allodynia using von-Frey filaments

The 50% paw withdrawal threshold (PWT) to mechanical stimuli was measured using von-Frey filaments and the up-and-down method of sensitivity testing as described by Chaplan *et al.*[172]. Briefly, rats were placed in a plexiglass chamber with a metal wire mesh floor. The animals were then allowed to acclimatize for 10 min. A series of eight calibrated von-Frey filaments (0.4-15.0 g) were applied. Paw withdrawal or flinching was considered as positive response. Threshold was defined as the lowest force causing three withdrawals out of five stimuli at a gap of 30 sec.

4.19.4.4 Hot plate test

This test measured the latency of the rat to demonstrate hind paw licking/shaking and jumping when kept on a hot plate [173]. The hot plate (Eddy's hot plate, Techno Electronics, Lucknow) was maintained at 50±2 ºC, and the animals were placed in plexiglass chamber on the hot plate. Response latency was measured by recording the time delay between placing in the chamber and shaking/licking of the paw. To prevent possible burn injury, a cut-off time was set at 15 sec.

4.19.4.5 Cold water tail immersion test

Similar to hot plate test, cold water immersion test measured the latency of the rat to demonstrate tail withdrawal latency when dipped in ice-cold water [174]. Ice-cold water was taken in a 500 ml beaker and the temperature was maintained below 7±2 ºC. The animal was restrained and lower 3/4th of the tail was immersed in a beaker of ice-cold water. Response latency was measured by recording the time delay between placing the tail in the cylinder and tail withdrawal. A 15 sec cut-off time was set for each animal.

4.19.4.6 Measurement of nerve conduction velocity

Caudal nerve conduction velocity studies were conducted in all the animal groups [175]. The animals were anaesthetized by giving a single *i.p.* injection of mixture of xylazine chlorohydrate (10 mg/kg) and ketamine (80 mg/kg) at 0.1 ml/100 g. The animal was then

positioned ventrally for their tail to be completely loose and the tail was cleaned with 70% alcohol to remove fat and other debris. Animal's body temperature was measured using a rectal probe and was maintained using hot plate at 37±2 ºC. Stimulating electrode was placed proximally and recording electrodes were placed distally at a distance of 10 cm. The electrophysiological parameter studied was onset of latency in nerve conduction velocity (m/s). Measurement was repeated 3 times and averaged.

4.19.5 Surgically induced pain: Chronic constriction injury

Unilateral mononeuropathy was surgically induced in rats using chronic constriction injury (CCI) model [176]. Surgery was performed under the influence of anaesthetics (xylazine chlorohydrate, 10 mg/kg; and ketamine, 80 mg/kg; at 0.1 ml/100 g), with additional doses of the anaesthetics administered if needed. Briefly, the lateral side of the left hind limb was shaved and a small incision (2-3 cm) was made at mid-thigh level. The left femoris muscle was then separated and common left sciatic nerve was exposed. Four loose ligatures were tied around sciatic nerve using 4-0 braided silk suture, with a spacing of about 1 mm. The wound was closed using absorbable chromic catgut using a continuous suture pattern. The skin was closed using silk thread using horizontal mattress suturing pattern. Povidone-iodine solution was topically applied to the wound for 5 days to prevent infection. Animals were then transferred to their home cages for recovery. The animals were screened 9^{th} day post-surgery. Contralateral paw served as control for comparison and Gabapentin was used as standard drug.

4.19.5.1 Mechanical allodynia using von-Frey filaments

Threshold responses to mechanical (tactile) stimulus were determined by placing each animal in an elevated observation chamber having a wire mesh floor whereupon the planter surface of the ipsilateral hind paw could be stimulated with a graduated series of eight von-Frey filaments [172].

4.19.5.2 Acetone induced cold allodynia

Purpose of this test was to screen the animals for the development of cold sensitivity. Acetone (100 µL) was lightly sprayed through the mesh flooring on the planter surface of the left hind paw to produce evaporative cooling [177]. Cumulative paw-licking duration was recorded over 1 min. A compound was considered effective only when it demonstrated >50% reversal. The %reversal was calculated using the following formula:

$$\% \text{ Reversal} = \frac{(\text{post dose value} - \text{pre dose value}) \times 100}{(\text{contralateral paw value} - \text{pre dose value})}$$

4.19.5.3 Mechanical hyperalgesia

The nociceptive flexion reflex was quantified by an Ugo Basile analgesiometer (Stoelting, Chicago, IL), which applied an incremental mechanical force *via* an automatic gauge to the dorsal surface of the rat's hind paw. Pressure was noted when the animal showed the first withdrawal reflex in terms of squeak/withdrawal movement [178]. A cut-off pressure of 250 g was considered to avoid damage to the paw. Three consecutive trials separated by 10 sec intervals were taken and the responses were averaged. A compound was considered effective only when it demonstrated >50% reversal. The %reversal was calculated using the formula as described above.

4.19.6 MeHg induced memory and cognition evaluation

4.19.6.1 MeHg induction

Mice were divided in three groups; naïve, control and treatment and each group contained six animals (n=6). The naive group received drinking water *ad libitum*, while the MeHg group received 20 mg/L MeHg dissolved in drinking water *ad libitum*. Test compound group received MeHg mixed with water for first seven days, followed by a mixture of test compound and MeHg for three weeks. Daily water consumption was monitored. Detailed descriptions for each test are provided in following sections. The MeHg group mice received MeHg dissolved in regular drinking water for the entire duration of experiment, whereas test compound group mice received similar treatment for 1-2 weeks and the drug dissolved in drinking water for the next 3-4 weeks.

4.19.6.2 Behavioural assessments

Animals from all groups were used for behavioural testing. Determination of dyskinetic posture and gait analysis using footprint analysis, spontaneous locomotion, motor coordination on rotating rod, spatial learning in morris water maze, depression like behaviour in tail suspension test, novel object recognition test for memory testing and determination of mechanical allodynia were studied according to standard protocols. Detailed descriptions for each test are provided in following sections.

4.19.6.2.1 Hind limb clasping observation

After three weeks, mice were tested for the manifestation of hind limb clasping phenomenon. Hind limb clasping was characterized as a dyskinetic posture whereby mice clasped their hind limbs tightly into their abdomen when suspended by their tail [179].

4.19.6.2.2 Locomotor test

The tests were performed by placing individual animals in digital actophotometer (Dolphin CAT No- 1126) with a square enclosed chamber (dimensions 30 x 30 x 10 cm) [169], and locomotor behaviour was recorded as a digital score for a period of 5 min.

4.19.6.2.3 Motor co-ordination test

One animal at a time was placed on a rotating rod (Dolphin, diameter-3 cm, 20 rpm) [170]. The latency to fall down was recorded with 5 min cut-off time. Mice were given three consecutive trials with a maximum trial time of 5 min and 15 min rest interval.

4.19.6.2.4 Gait analysis

The footprint test was used to compare the gait of the three groups. This test was performed immediately before exposure and at 1, 2 and 3 weeks after MeHg exposure [180]. To obtain footprint, hind feet of the mice were coated with blue nontoxic ink. The animal was then allowed to walk along a 30 cm long, 2 cm wide runway, coated with white paper. Each mouse had maximum of three trials per day till clear footprints were obtained.

4.19.6.2.5 Tail suspension test

Mice were individually suspended by their tail with firm horizontal rod using an adhesive tape placed at 2 cm from tip of the tail. The mice were suspended at 60 cm above the ground for 5 min. The mice were at least 15 cm away from the nearest object and were visually isolated. The test comprised of periods of agitation (active) and immobility (depressed), where the total time of immobility was noted. This immobility time was interpreted as a measure of depressive behaviour [181].

4.19.6.2.6 Novel object recognition test

This test was carried out according to the procedure of Ennaceur and Delacour [182] with minor modifications. Briefly, individual mice were placed in plexiglass cage (20 x 26 x 14 cm) illuminated by a 60-W lamp suspended 50 cm above the cage. The objects to be discriminated were glass beakers (100 ml), painted with grey color from inside. On the day of test, a session of two trials separated by intertribal time of 60 min was carried out (see Figure

4-2). In the first trial which lasted for 5 min, two identical objects were introduced in the cage. Exploration was defined as directing nose at a distance of <2 cm from the object and/or touching it with the nose. During the second trial, a novel object replaced one of the objects present in the first test and the mice were left in the box for 5 min.

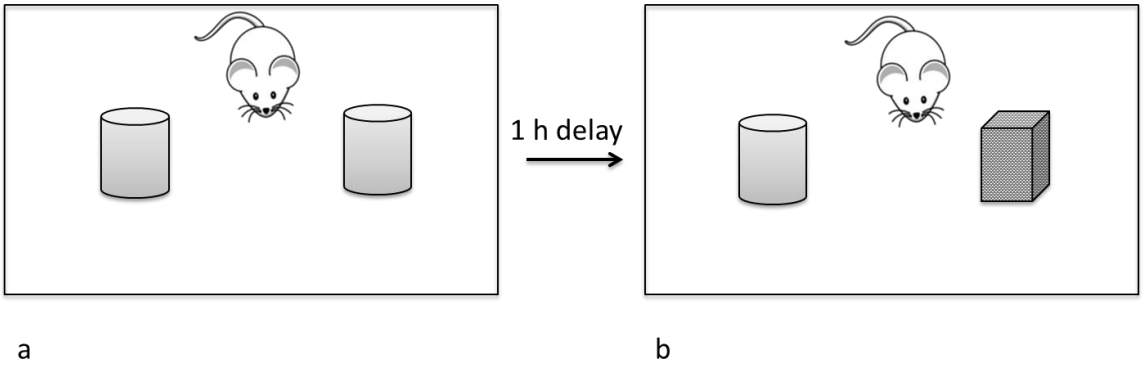

Figure 4-2. Novel object recognition test.

Training phase is illustrated in panel a in which the animal was allowed to explore two identical (similar) objects. After 1 hr, one of the object was replaced with another object having different shape (novel object, panel b). The time spent in exploration of familiar and novel objects was observed and differentiation score was calculated. A positive differentiation score indicated memory retention as the animal recognized the familiar object by memory and thus, explored the novel object for longer duration.

The time spent in the exploration of familiar and the novel object was recorded separately and differentiation score was calculated for each test as follows:

$$\text{Differentiation score} = T_n - T_f$$

Where T_n was time spent in exploring the novel object and T_f was time spent in exploring the familiar object. The objects were cleaned before each test to avoid olfactory stimulation.

4.19.6.2.7 Morris water maze test for spatial reference memory

The water maze test was conducted as described by Morris, R. [183]. The Morris water maze task was conducted in a circular stainless steel pool (180 cm diameter, 50 cm high) filled with room temperature (20-26 ºC) water (see Figure 4-3). The maze was illuminated with 60-W lamp, located at 50 cm above the water surface. A yellow coloured paper was adhered to the north east quadrant 5 cm above water surface and a transparent, hidden platform was submerged 1 cm below the surface. The platform was constantly located near visual clue at predefined position. Each mouse was subjected to test phase only when it could spot the hidden platform in three consecutive trials, each starting from different random points, with the help of visual clue. After 15 sec on the platform, the mouse was removed from the maze

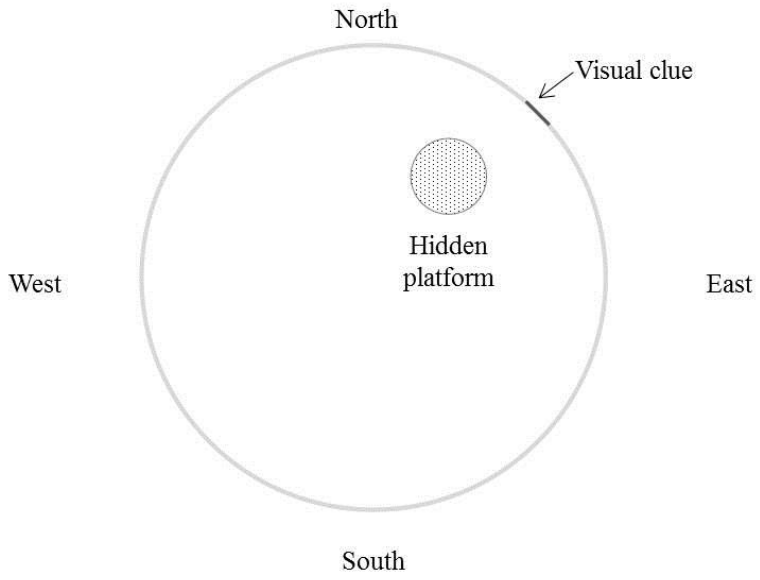

Figure 4-3. Morris water maze test.

Morris water maze is a spatial reference memory task. During training phase, mice must locate a submerged, hidden platform which remained in a constant location near the visual clue. During test phase, the hidden platform was removed and the latency of the mice to directly reach the location where the hidden platform was kept, was noted.

and dried with cotton cloth. The maximum swimming time for every trial was 5 min, followed by 1 min interval. Retention test was performed after a gap of 5 min after the last training session, without the hidden platform. Latency of the animal to reach and/or stay within <5 cm of the visual clue was recorded.

4.19.6.2.8 Mechanical allodynia (von-Frey filament test)

This test was carried out in all the groups of mice after 3 weeks. A series of von-Frey filaments (Ugo Basile, Italy) calibrated in terms of different bending forces (0.4-15 g) were applied to mid plantar surface of the paw. The filaments were applied 5 times in the same region starting with mid-range filament (4 g). A brisk withdrawal of the paw was considered as a positive response. If the animal did not respond, another fibre with increased stiffness was selected and vice versa [172].

4.20 Statistical analysis

Data were analysed as mean±SEM. Statistical significance of the test compounds was determined either by unpaired Student's t test or one way analysis of variance (ANOVA) followed by Dunnett's post-hoc test for individual comparisons with control values. Results with p<0.5 were considered statistically significant. The statistical software package GraphPad Prism-5 was used for the analyses.

You have the right to work only but never to its fruits.
Let not the fruits of action be your motive,
nor let your attachment be to inaction.

-Bhagavat Gita.

Chapter 5.
Results and Discussion:
Design of novel ROCK inhibitors

5.1 Lead identification

In this chapter, we introduce the key concepts, illustrate strategies and applied techniques and explain their results. In a nutshell, the entire process of novel ROCK inhibitor design could be divided into two major phases:

(a) **Design I**: It involved multiple crystal structures for the design and validation of pharmacophore hypotheses utilizing *in silico* techniques, followed by biophysical and *in vitro* biological characterization of lead molecules.

(b) **Design II**: It involved lead optimization of a reported scaffold, *in silico* modelling followed by biophysical, *in vitro* biological and *in vivo* pharmacological characterization of lead molecules.

5.2 Design I: Multiple crystal structure-based e-pharmacophore modelling

Since our drug design strategy was based on structure-based approach, it was important to employ the crystal structure of ROCK bound to a reported inhibitor. In this work we selected eight co-crystallized structures from the PDB repository (http://www.rcsb.org/pdb) of ROCK-bound with ligands and having resolutions from 2.29 to 3.30 Å (see Figure 5-1 and Figure 5-2). The bottom of ROCK active site pocket was flat in shape and was lined by hydrophobic residues. The hydrophobic cavity featured Met156, which was utilized for ligand-receptor interaction in all crystal structures. On the other hand, the distal region contained polar residues and was exposed to the solvent. Out of eight crystal structures, five

(2ETK, 2ESM, 3D9V, 3NCZ and 3NDM) contained isoquinoline based ligands including fasudil, H1152 and hydroxyfasudil, whereas three crystal structures (3TV7, 3V8S and 3TWJ) contained thiazole-based urea derivatives. Protein preparation was performed on the

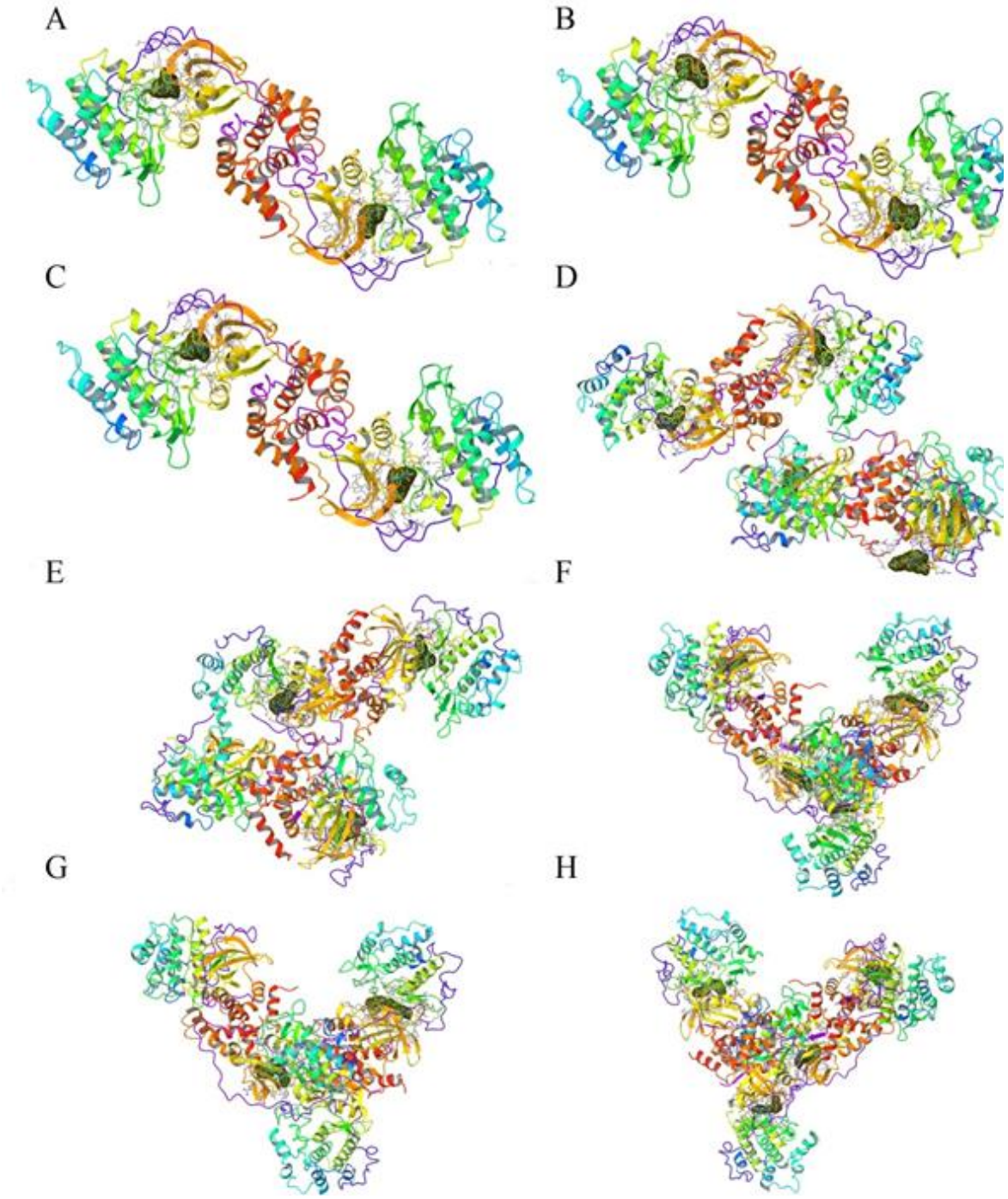

Figure 5-1. Eight ROCK pdb structures selected for the study.

A: 2ETK; B, 2ESM; C, 3D9V; 4, 3NCZ; 5, 3NDM; 6, 3TV7; 7, 3TWJ AND 8, 3V8S. The protein is shown in rainbow colour ribbons and the bound inhibitor is shown as green sticks with van-Der-wall radii as yellow surface. Residues closer than 6 Å to the bound inhibitor are shown as sticks.

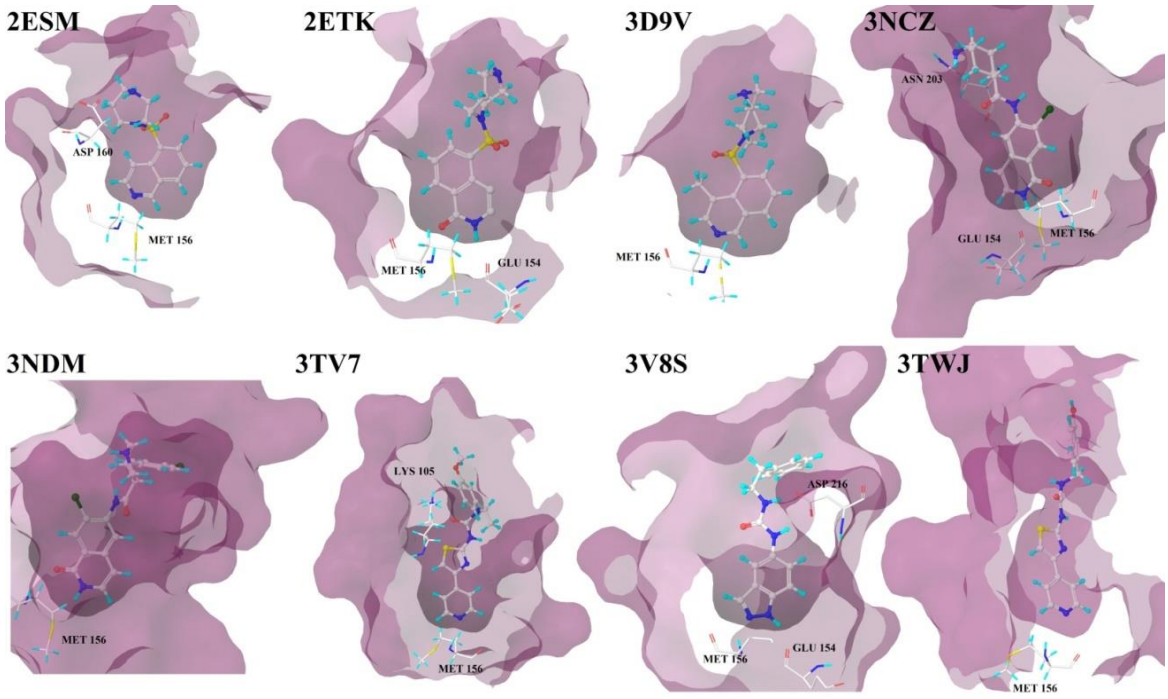

Figure 5-2. Binding site pocket of the selected crystal structures.

The binding site is shown in purple surface. The bound ROCK inhibitor is shown in its binding conformation as ball-and-stick model. Interacting residues are shown as pipes. Crystal structures contained these bound ligands; 2ESM: fasudil, 2ETK: Hydroxyfasudil, 3D9V: H1152, 3NCZ and 3NDM: substituted 2H-isoquinolin-1-one derivatives, 3TV7,3V8S and 3TWJ contained urea derivatives.

downloaded PDB structures essentially to correct missing hydrogen atoms, ambiguous protonation states and flapped residues. The ligands were subjected to energy minimization by converging the heavy atoms until the root mean square deviation (RMSD) became equal to 0.30 Å using OPLS_2005 as force field, after removal of water molecules and subsequently the protein structures were refined. The drug design strategies employed in this study were energy-based pharmacophore and shape-based modelling using crystal structures of protein bound with ligands. These methods were considered favourable as they incorporated both the ligand information as well as the protein information along with favourable contacts with energetic information between the protein and the ligand into the pharmacophore model.

5.2.1 E-pharmacophore identification and validation

The energy-optimized structure based pharmacophore approach was based on mapping of the energetic terms from the Glide XP score function onto the atom centres. The known inhibitors obtained from PDB were re-docked using Glide XP and the pose was refined. E-pharmacophores were obtained by mapping the energetic terms from Glide XP scores for all eight inhibitors. Pharmacophore sites were predicted by providing the results from Glide XP

as input for e-pharmacophore script. Based on the energies, the sites were ranked. The most favourable sites which showed good site scores were selected for generation of pharmacophore hypotheses. Pharmacophore sites were automatically generated from the protein-ligand complex with Phase. Phase provided a standard set of six pharmacophore features, hydrogen bond acceptor (A), hydrogen bond donor (D), hydrophobic (H), negative ionizable (N), positive ionizable (P), and aromatic ring (R). The grids utilized for this purpose for each crystal structure are presented in Table 5-1. The RMSD for all the eight docked ligands was < 2 Å, when compared to their crystal bound conformations. This was performed to validate the active site grid and also the reproduction of binding pose of the ligands. The RMSDs for all the 8 protein structures were within 2 Å which ascertained the validation of the docking process.

Table 5-1. Glide grid coordinates used for various e-pharmacophore generation.

S. No.	PDB	X-Centre	Y-Centre	Z-Centre
1	2ESM	41.11	88.38	17.31
2	2ETK	40.08	90.29	18.06
3	3D9V	40.69	91.10	18.34
4	3NCZ	-27.20	-14.59	28.63
5	3NDM	-25.14	11.94	74.59
6	3TV7	-54.60	-31.20	51.13
7	3TWJ	16.22	40.24	52.67
8	3V8S	-58.03	-9.80	19.17

The table shows X, Y and Z coordinates of grid used for e-pharmacophore generation.

Initial number of pharmacophore sites were set up to ten for all the crystal structures. Pharmacophore sites for each ligand prior to energy–based site selection and the optimized sites for hypothesis generation for the 8 crystal structures of ROCK are presented in Figure 5-3.

The crystal ligand from 3V8S gave the maximum pharmacophoric feature of 7 (RRRDDDA) while 3NCZ revealed 6 point feature as RRAADH. Two of the crystal ligands (3NDM and 3TV7) yielded 5-point pharmacophore features and 3 crystal ligands (2ETK, 3D9V,and 3TWJ) yielded 4 point pharmacophore, among which the features from 2ETK and 3NDM were similar (RRAD). One aromatic (R) and acceptor (A) features were common in all the eight crystal ligands and except 3TWJ all other crystal ligands had an extra aromatic feature. The distance mapping among the features is presented in Table 5-2. The distance between the two aromatic features in the afore-mentioned 8 crystal ligands were equal (2.45-2.47 Å) except in 3TV7 which was found to be 4.18 Å due to the fact that the R groups were way

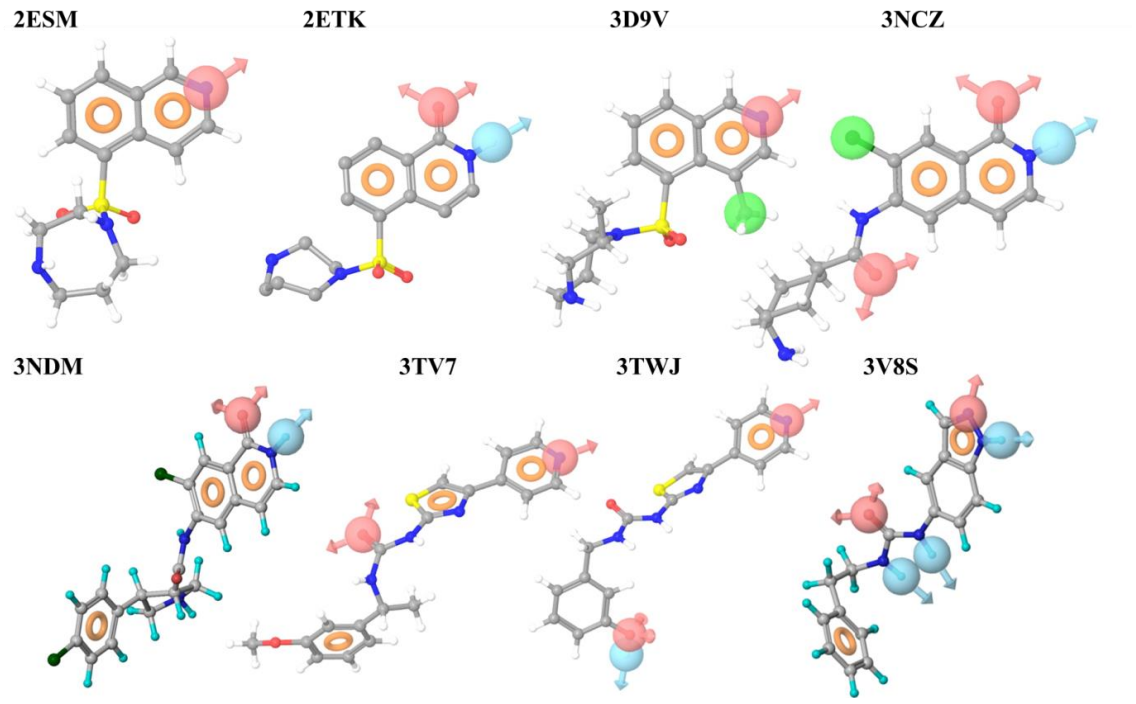

Figure 5-3. E-Pharmacophore based hypothesis.

E-pharmacophores derived from the crystal structures. (left to right, top row: 2ESM, 2ETK, 3D9V, 3NCZ; bottom row: 3NDM, 3TV7, 3TWJ and 3V8S). Pharmacophoric features have been depicted in different shapes and colors; pink sphere denote acceptor atom feature; cyan sphere, donor atom feature; green sphere, hydrophobic feature whereas orange donuts represent aromatic feature. Ligand atoms have been shown as ball and stick model. The figures were generated in Maestro.

apart unlike fused system in most of the ligands. Furthermore, most of the common features among the e-pharmacophores showed similar distances except in 3TV7, where R1-R2 and R1-A1 distances were greater.

To test the efficiency of the pharmacophore hypothesis to be utilized for HTVS, (ability to quickly identify active molecules), parameters like $EF_{1\%}$, BEDROC, ROC, AUC and EF_{manual} were then applied as validation steps on the e-pharmacophores (Table 5-3). The enrichment

Table 5-2. Distance between e-pharmacophore features.

S. No.	PDB	Distance Between Features (Å)								
		R1-R2	R1-A1	R2-A1	R1-H1	R2-H1	A1-H1	R1-D1	R2-D1	A1-D1
1	2ESM	2.45	3.73	1.41	-	-	-	-	-	-
2	2ETK	2.47	3.72	2.67	-	-	-	4.70	2.38	2.49
3	3D9V	2.45	3.73	1.41	4.02	2.91	3.75	-	-	-
4	3NCZ	2.46	3.73	2.67	5.40	3.13	5.41	4.69	2.37	2.50
5	3NDM	2.46	3.71	2.68	-	-	-	4.69	2.38	2.51
6	3TV7	4.18	5.54	1.36	-	-	-	-	-	-
7	3TWJ	-	1.42	1.42	-	-	-	11.92	-	13.21
8	3V8S	2.12	3.33	1.15	-	-	-	3.45	2.14	2.11

Various e-pharmacophore features have been depicted as R, aromatic ring; A, acceptor atom; H, hydrophobic; D, donor atom.

results for all 8 crystal ligands using the e–pharmacophore method were compared for the enrichment factor ($EF_{1\%}$), BEDROC, based on recovery rate of actives against the ranked decoy database that consisted of 1035 compounds in which 35 were known inhibitors obtained from literature [62,64,72,80,81,83,85-89], and were drawn manually. As can be seen in Table 5-3, e-pharmacophores 3TV7 and 3TWJ exhibited no yield at 1% of the decoy dataset ($EF_{1\%}$=0). In addition, these two e-pharmacophore models showed poor manual enrichment factor (EF_{manual} < 2.1) and low GH (GH < 0.1). One possible explanation for low $EF_{1\%}$ and EF_{manual} parameters could be given in terms of distance geometry among the pharmacophore feature sets (Table 5-2). It was evident that 3TV7 pharmacophore (RRRAA) exhibited greater distance between R1-R2 and R1-A1 features, as compared to other e-pharmacophores. In addition, 3TWJ exhibited only one such feature set (R2-A1) due to presence of only one energetically favoured aromatic ring system (R2).

A low enrichment indicated poor efficacy of the pharmacophore models towards virtual screening runs. Thus, based on their rankings in enrichment calculations values ($EF_{1\%}$, EF_{manual} and GH scores), we selected six out of eight e-pharmacophores with high enrichment

Table 5-3. E-pharmacophore validation.

PDB	e-Pharmcophore	EF (1%)	BEDROC (α=160.9)	BEDROC (α=20.0)	BEDROC (α=8.0)
2ESM	ARR	21	0.64	0.77	0.79
2ETK	ADRR	29	0.07	0.60	0.72
3D9V	AHRR	15	0.53	0.69	0.83
3NCZ	AADHRR	3	0.11	0.04	0.03
3NDM	ADRRR	15	0.48	0.76	0.79
3TV7	AARRR	0	0.00	0.06	0.13
3TWJ	AADR	0	0.01	0.08	0.10
3V8S	ADDDRRR	8.9	0.37	0.12	0.10

PDB	ROC	RIE	AUC	EF (Manual)	GH
2ESM	1.00	11.30	0.99	10.25	0.44
2ETK	0.99	8.74	0.87	10.90	0.46
3D9V	0.98	9.97	0.96	4.32	0.28
3NCZ	1.02	0.54	1	5.71	0.15
3NDM	1.00	11.10	0.98	14.28	0.55
3TV7	0.98	0.88	0.96	0.82	0.06
3TWJ	1.01	1.21	1.00	2.07	0.07
3V8S	1.02	1.67	1.00	14.28	0.39

$EF_{1\%}$, enrichment factor at 1% of the decoy dataset; BEDROC, Boltzmann-enhanced discrimination of receiver operating characteristics; EF, overall enrichment factor; GH, Goodness of hit, ROC, receiver operating characteristic curve; RIE, robust initial enhancement.

values for virtual screening. Among these one was a seven-point e-pharmacophore model (3V8S), one from 6-point (3NCZ), 5-point (3NDM) and 3-point (2ESM) models, and two 4-point pharmacophore hypotheses (3ETK and 3D9V).

5.2.2 Shape-based modelling and validation

As a second strategy, all the eight crystal ligands bound in the active site pocket were subjected to molecular shape analysis using Omega parameters of the OpenEye software and shapes were created as presented in Figure 5-4. This method was based on the electrostatic and shape matching protocol for the ligand within the active site pocket of the protein. In this study we used the programs ROCs and EON (OpenEye Scientific Software, Inc.). The idea behind shape-based screening was that the molecules had similar shape if their volumes overlapped well and any volume mismatch was a measure of non-compatibility. ROCs module of OpenEye employed smooth Gaussian function to represent the molecular volume [184], thus minimizing to the best global match. This method also considered overlap of different functional groups using force-fields, thus incorporating a sense of pharmacophoric feature in the resulting shape-based queries. All the eight shapes were validated using enrichment calculations in which the decoy set consisted of 6319 compounds. Of these 6284 compounds were drug-like inactive molecules (decoys) and were downloaded from

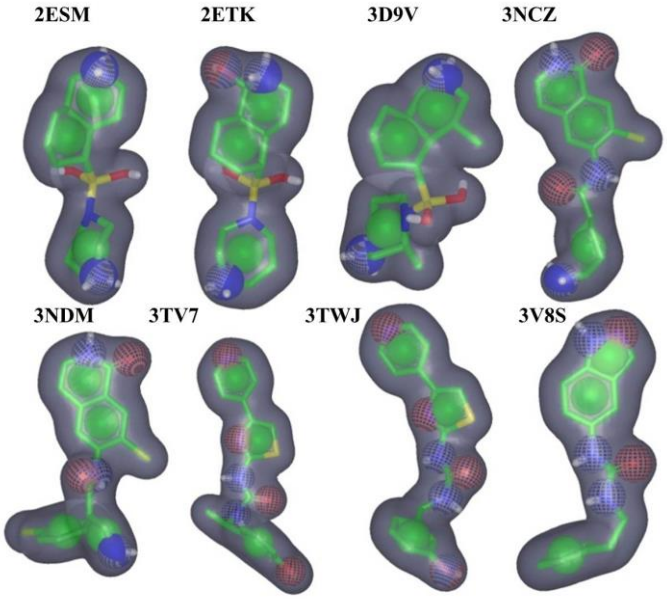

Figure 5-4. Shape based queries.

Shape based queries generated from the eight crystal structures (left to right, top row: 2ESM, 2ETK, 3D9V, 3NCZ; bottom row: 3NDM, 3TV7, 3TWJ and 3V8S). The molecular shapes are shown as shaded greyed region and the molecule is shown as stick model.

Table 5-4. Validation of shape based queries.

PDB	AUC	EF		
		(0.50%)	(1%)	(2%)
2ESM	0.95	108.40	56.61	31.16
2ETK	0.90	53.65	29.34	16.84
3D9V	0.98	134.85	80.70	43.98
3NCZ	0.86	35.54	27.85	22.93
3NDM	0.94	71.30	51.90	32.30
3TV7	0.74	68.08	36.72	22.10
3TWJ	0.81	39.87	21.75	11.97
3V8S	0.94	104.61	55.98	31.94

AUC, area under the curve; $EF_{(n\%)}$, enrichment factor at n% of the decoy dataset.

http://dud.docking.org. We utilized the same 35 known ROCK inhibitors, which were already used for validation of e-pharmacophores. As indicated in Table 5-4, all 8 shape-based queries showed good enrichment (>10) and exhibited high AUC (<0.70) and hence were utilized for virtual screening process.

The difference between the two enrichment calculations of e-pharmacophores and shape-based queries could be attributed to the way they were generated. E-pharmacophore considered only bound pose of the inhibitor, whereas shape-based query was based on one of the feasible low energy conformation of the bound ligand.

5.2.3 HTVS and molecular docking

In the present study, virtual screening involved two stages: a preliminary shape matching phase which utilized the validated molecular shape queries based on each of the eight active scaffolds and in the second strategy, selected e-pharmacophores were utilized as initial filters in the virtual screening protocol. The combination of shape matching and e-pharmacophore comparison step for refinement was a relatively novel approach and was successfully applied against this target. The output of shape-based and e-pharmacophore filters were then combined and the top ligands based on a cut-off value (fitness score >1.5; Tanimoto combo >0.4) were subjected to docking procedures using various Glide modules (HTVS, SP and XP docking) as depicted in Figure 5-5. A key advantage to the use of shape-matching and e-pharmacophore filtering as virtual screening strategy was that the actual structure of the crystal ligand may not strongly influence the final hit selection and the use of multiple crystal structures could yield diversity in the lead structures.

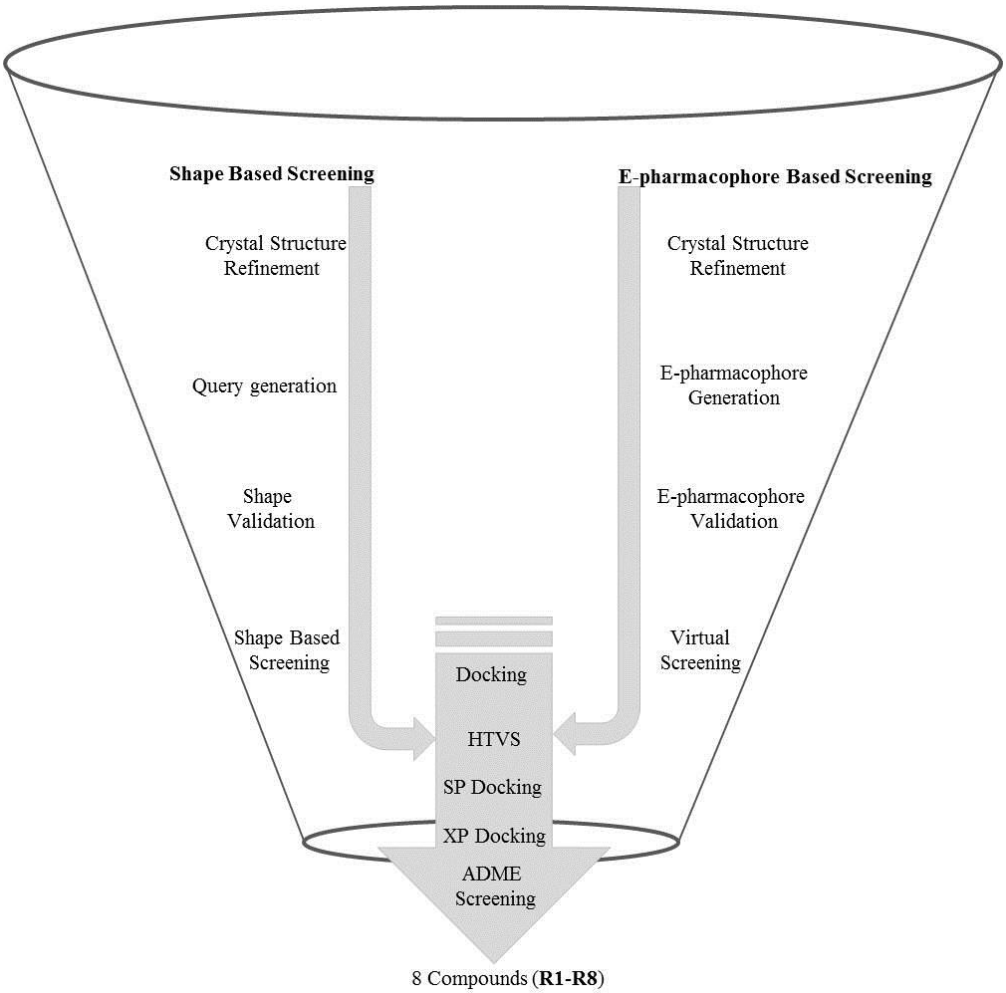

Figure 5-5. Flowchart of *in silico* screening process for ROCK inhibitor design.

We employed two different approaches to screen commercially available Asinex database. The eight crystal structures were refined and e-pharmacophores and shape-based queries were generated. These e-pharmacophores and shape-based queries were validated and only selected ones were used for database screening. Output of the virtual screening process was subjected to docking studies. Hits identified from docking process were further evaluated based on their docking score, pharmacokinetic properties and visual inspection.

High-throughput virtual screening was performed with the commercial database (Asinex, www.asinex.com). The library consisted of 525,807 compounds that were then prepared in 3D format and charges assigned using the LigPrep program of Schrödinger, LLC as described in the methods section 4.7. Based on docking score (docking score < -4) and number of hydrogen bonds (>2), 25,890 compounds from HTVS output were subjected to Glide-SP docking. The output of SP was further refined and 2,035 molecules were selected for XP docking based on docking score (docking score < -5). After XP run, top 50 molecules with best docking score were selected for visual inspection, where molecules were checked for any clash with cavity surface. Also, the molecules were checked to make sure that they interacted

with key amino acid residues like Met156. We finally shortlisted 8 compounds based on these criteria, availability and were procured from Asinex for biological evaluation. The *in silico* parameters of the compounds are listed in Table 5-5.

The structures of identified molecules are shown in Figure 5-6. It could be observed that most of the identified lead molecules were either pyrazolopyrimidine analogues or thiazolopyrimidine derivatives. These heterocyclic leads maintained a rich structural diversity amongst them as indicated by the presence of bicyclic and tricyclic ring systems. The tricyclic rings, thus presented as planar, rigid molecules, whereas compounds with bicyclic rings consisted of another ring connected by a small linker chain, thus providing flexibility to the structure.

Table 5-5. *In silico* parameters of selected compounds.

Compound No.	Fitness	Tanimoto Combo	Glide G Score	Docking Score
R1	2.45	0.58	-7.62	-6.21
R2	2.58	0.48	-8.36	-8.33
R3	2.57	0.54	-8.10	-8.04
R4	2.65	0.48	-7.63	-7.41
R5	2.63	0.57	-6.93	-6.93
R6	2.54	0.48	-7.02	-7.14
R7	2.50	0.79	-7.02	-7.02
R8	2.54	0.48	-6.93	-6.94
Fasudil	2.90	0.87	-8.51	-8.62

Table depicts important *in silico* parameters of the identified hits. Fitness score depicts pharmacophore fit and ranges between 0 to 3, 0 being no match between ligand and pharmacophore whereas 3 means 100% match. Tanimoto combo ranking indicates shape-based similarity search ranking. Higher ranking corresponds to better shape similarity. The standard compound fasudil was subjected to docking during e-pharmacophore generation, and was not used for database screening.

As described in earlier literature reports, interaction with Met156 was crucial for ROCK inhibition. Interestingly, all 8 molecules exhibited at least two interactions and one of them was Met156. Also, the hydrophobic ring systems of all 8 compounds occupied the hydrophobic cavity lined by Ala103, Val137, Met153 and Tyr155, thus, favouring hydrophobic interactions. Interestingly, standard inhibitors fasudil, H1152 and hydroxyfasudil also showed interactions with Met156 and their ring systems occupied the bottom of the cavity as depicted in Figures 5-2 and 5-7.

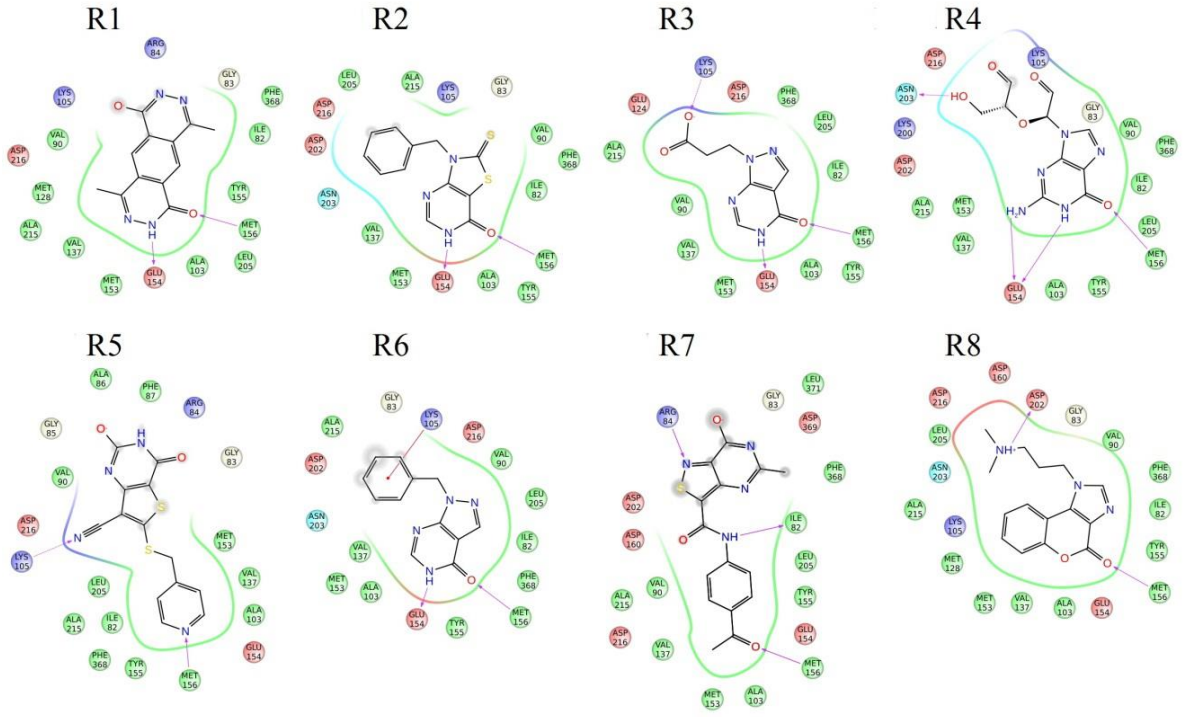

Figure 5-6. Newly identified leads as ROCK inhibitors and their interactions.

Schematic representation of ligand-receptor interactions of the identified molecules. Binding pocket characteristics are displayed using color-coded spheres indicating surrounding amino acids, whereas protein-ligand interactions are represented as lines: hydrogen bonds as purple arrows, and π-π stacking interactions as green lines. Colour coding of amino acids spheres: light-orange, negatively charhed; purple, positively charged; cyan, polar; green, hydrophobic; yellow, glycine. Grayed out areas represent solvent exposure. These images were generated using Ligand interaction diagram module of Schrodinger.

5.2.4 ROCK enzyme inhibition studies

Interestingly, most of the compounds were either pyrazolopyrimidine analogues or thiazolopyrimidine derivatives as seen in Figure 5-6. The ROCK-I inhibition assay was performed in a NADH oxidation-phosphate transfer coupled format, as described in methods section 4.11.2. Preliminary screening was conducted for all test compounds at 40 µM concentration. All the eight compounds showed significant ROCK inhibitory activity at 40 µM (data not shown) and thus, were further evaluated at serial dilutions to estimate their IC_{50} values. The activity data of eight compounds is presented in Table 5-6, wherein the IC_{50} ranged from 1.50 to 17.73 µM.

To compare the inhibitory activity, the ligand interaction diagrams of all the leads along with crystal ligands were compared. Fasudil, a known ROCK inhibitor, employed as standard showed hydrogen bonds with Met156 and Asp202, whereas the other known inhibitors like H1152 and hydroxyfasudil showed interactions only with Met156 (Figure 5-7). The structures and the binding mode of all 8 compounds could be seen in Figure 5-6. Among these, compound **R8** (1-[3-(dimethylamino)propyl]chromeno[3,4-*d*]imidazol-4(*1H*)-one) was the most active with IC_{50} of 1.5 µM and its structure could be divided into rigid and flexible regions. Rigid region was planar and madeup of three rings of chromeno[3,4-*d*]imidazol-4(*1H*)-one moiety and the flexible dimethylaminopropyl group in tail region was found oriented towards hydration site of active site pocket. **R8** was found to form two hydrogen bonds with the protein. Carbonyl oxygen atom present in rigid portion acted as hydrogen bond acceptor and formed hydrogen bond with NH of Met156, which acted as hydrogen bond donor. Another hydrogen bond was formed between the lone pair of the N atom of dimethylamino group of the flexible region which acted as hydrogen bond donor and formed hydrogen bond with O atom of Asp202. All other compounds showed IC_{50} less than 10 µM except **R1**, which displayed an IC_{50} of 17.73 µM. All the compounds showed important interaction with Met156. Another residue Glu154 located at the base of the active site exhibited interactions with compounds **R1**-**R4**. On the other hand, **R3**, **R5** and **R6** formed interactions with Lys105, due to the presence of electron-rich functional groups located at the solvent-exposed tail region of the ligands.

Table 5-6. IC_{50} of designed compounds for ROCK as target.

Compound No.	IC_{50} (µM)
R1	17.73±0.34
R2	4.62±0.80
R3	5.50±0.23
R4	3.60±0.50
R5	6.41±0.21
R6	2.37±0.34
R7	2.23±0.40
R8	1.50±0.04
Fasudil	10.7±0.05

Each value represented mean±SEM of three observations.

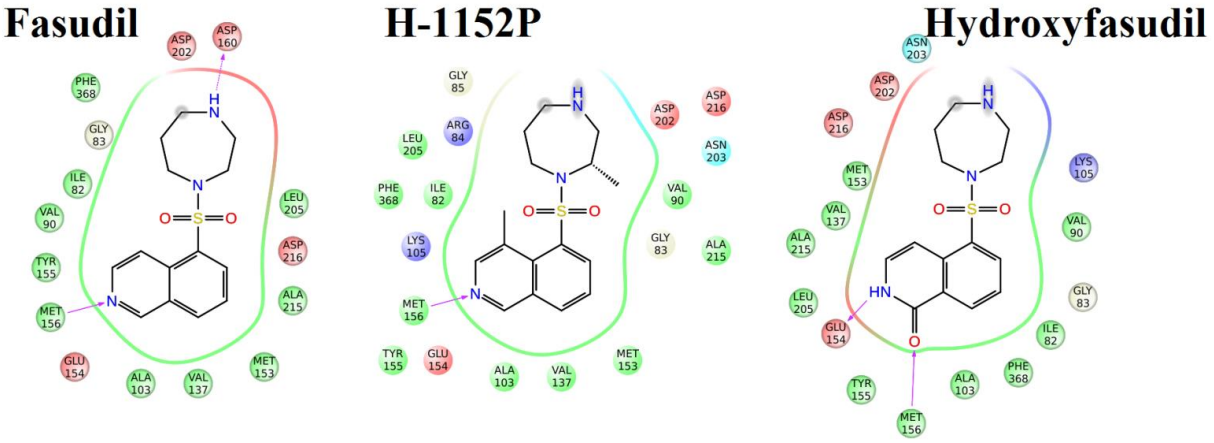

Figure 5-7. 2D ligand interaction diagrams of fasudil, H1152 and hydroxyfasudil with active site residues.

Binding pocket characteristics are displayed using color-coded spheres indicating surrounding amino acids, whereas protein-ligand interactions are represented as lines: hydrogen bonds as purple arrows, and π-π stacking interactions as green lines. Colour coding of amino acids spheres: light-orange, negatively charhed; purple, positively charged; cyan, polar; green, hydrophobic; yellow, glycine. Grayed out areas represent solvent exposure. These images were generated using Ligand interaction diagram module of Schrodinger.

Comparison of the docked poses of the eight inhibitors revealed that **R8** occupied the maximum pocket volume among the eight compounds (Figure 5-6). The rings of **R1**-**7** occupied the hydrophobic pocket with near vertical orientation, whereas the rings of **R8** was aligned in horizontal direction. Due to this unusual conformation, the hydrophobic rings of **R8** were well oriented in the hydrophobic cavity of the active site pocket, leading to enhanced hydrophobic interactions. In addition, the docked pose of **R8** was quite similar to that of fasudil as is evident from Figure 5-8. Hence, the orientation of the hydrophobic rings towards the hydrophobic region with good occupancy and orientation of polar tail towards the hydrophilic site justified the bioactivity of **R8** compared to the other leads **R1**-**7**.

Of the eight inhibitors, **R8** was of special interest, not only because of its highest ROCK inhibitory activity in this study, but also for its interesting conformation. Alignment of **R8** with fasudil not only showed perfect overlap of the rigid rings, but also the tail region containing dimethylamine group was aligned to the homo-piperazine ring of fasudil (Figure 5-8).

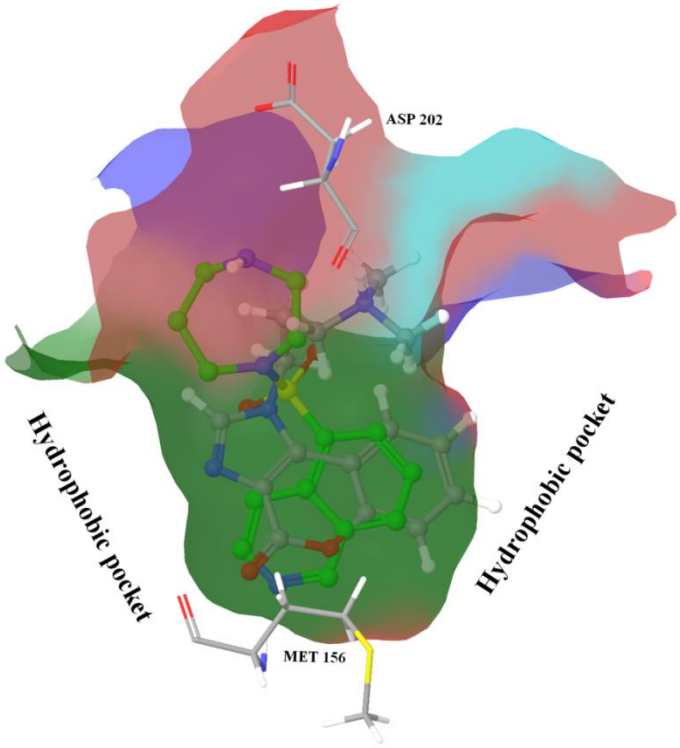

Figure 5-8. ROCK active site showing docked pose of **R8** and binding pose of fasudil.

Fasudil binding pose is shown in green. Molecular surface of 2ESM active site is shown and is colored according to amino acid properties. Green portion of pocket is lined by hydrophobic residues, Red is lined by residues bearing negative charge and, Blue indicates molecular surface belonging to positively charged residues.

5.2.5 ADME prediction

The ADME properties were calculated using QikProp module of Schrodinger (Table 5-7). For each successfully processed molecule, QikProp produced a set of descriptors and properties as follows, MW denoted molecular weight of the molecule; QPlogPo/w was the predicted partition coefficient between octanol and water (recommended range: –2.0 – 6.5); QPlogS represented predicted aqueous solubility, where S (mol dm^{-3}) was the concentration of the solute in a saturated solution in equilibrium with the crystalline solid. Recommended range should lie between –6.5 and – 0.5. QPlogHERG denoted predicted IC_{50} value for blockade of HERG K^+ channels (acceptable range <-5) which was an indicator of cardiotoxicity, QPPCaco indicated predicted apparent Caco-2 cell (human colon cell line) permeability in nm/sec. Caco-2 cell was a model for the gut-blood barrier (recommended range: <25, poor permeability; >500, good permeability), and QPlogBB represented predicted brain/blood partition coefficient for orally delivered drugs (recommended range: -3.0 to -1.2).

QPPMDCK was predicted apparent Madin-darby canine kidney (MDCK) epithelial cell permeability in nm/sec. MDCK cells were considered to be a good mimic for the blood-brain barrier (recommended range: <25, poor permeability; >500, good permeability). QPlogKp meant predicted skin permeability with log K_p in the recommended range of -8.0 to -1.0. The assessments used knowledge-based set of rules, including checking for suitable values of % human oral absorption, number of rotatable bonds, logP, solubility and cell permeability. Another QikProp prediction was the percent human oral absorption which was predicted on 0 to 100% scale. The prediction was based on a quantitative multiple linear regression model. Last but not the least properties which QikProp predicted was Lipinski's rule of five. The rules were: MW < 500, octanol/water partition coefficient <5, number of hydrogen bond donors ≤ 5, number of hydrogen bond acceptors ≤ 10. Compounds satisfying these rules were considered drug-like. Maximum limit of allowed violations was 2.

Interestingly, **R8** shared more similarities with fasudil as it also showed similar calculated ADME properties. Almost all compounds exhibited acceptable oral absorption and there were no violations of Lipinski's rule of five [185]. These results suggested that these compounds might be suitable for oral dosing and topical application. In addition, they might serve as template for further lead modification and optimization. With regards to LogP predictions, all compounds except **R1** and **R4** were better than the standard ROCK inhibitor fasudil. All compounds except **R1**, **R3** and **R4** exhibited better QPlogHERG values whereas standard drug fasudil showed acceptable value. On the other hand, all compounds except **R1**, **R3** and **R4** exhibited good QPPCaco values. It could be noted that **R8** showed QPPCaco value similar to standard drug fasudil. All compounds except **R2**, **R6**, **R8** and fasudil exhibited acceptable QPlogBB values. Compounds **R1**, **R3** and **R4** exhibited poor QPPMDCK values indicating poor MDCK cell permeability. Interestingly, compounds **R2**, **R7** and **R8** showed equivalent or better %human oral absorption than standard drug fasudil.

Table 5-7. ADME properties of hits in comparison with fasudil.

Compound	MW	Qplog Po/w	QPlogS	Qplog HERG	QPP Caco	QPlog BB	QPP MDCK	QPlog Kp	% Human Oral Absorption	Rule of Five Violations
R1	241.2	-1.92	-1.32	-3.81	5.84	-2.87	1.90	-6.82	29.39	0
R2	275.3	2.01	-3.26	-4.67	990.1	-0.23	1688	-2.42	92.33	0
R3	208.2	-0.08	-1.41	-1.83	23.74	-1.37	11.04	-4.79	51.09	0
R4	281.2	-2.51	-0.89	-3.97	6.23	-2.90	2.04	-6.74	26.46	0
R5	316.4	0.99	-4.22	-4.79	50.21	-1.76	47.15	-4.81	63.21	0
R6	272.3	0.59	-0.62	-4.97	119.4	-0.48	55.03	-5.25	67.60	0
R7	328.3	1.76	-4.08	-5.37	115.6	-1.61	90.28	-4.29	74.17	0
R8	271.3	0.99	-0.30	-4.41	234.3	-0.13	114	-4.56	75.16	0
Fasudil	291.3	0.76	-1.31	-5.01	249.5	-0.03	122.1	-4.58	74.34	0

MW: molecular weight, QPlogPo/w: Predicted octanol and water coefficient (acceptable range -2.0 - 6.0); Qplogs: Predicted aqueous solubility (acceptable range -6.5 - 0.5); QplogHERG: Predicted IC_{50} value for blockage of HERG k+ channels (acceptable range: below -5); QPPcaco: Predicted caco cell-2 permeability (<25 is poor and >500 high); QPlogBB: Predicted brain/blood partition coefficient (acceptable range -3.0 - 1.2); QPPMDCK: Predicted apparent MDCK cell permeability (<25 is poor and >500 is high); QPlogKp: Predicted skin permeability (acceptable range -8.0 to -1.0); % Human oral absorption (<25% is poor and >80% is high); Rule of 5: Number of violations of Lipinski's rule of 5 (mol_MW < 500, QPlogPo/w < 5, donorHB≤5, accptHB≤10) acceptable maximum 1.

5.2.6 Biophysical characterization

The interaction of the most potent compound **R8** with ROCK was further evaluated by measuring the thermal stability of the protein–ligand complex employing DSF biophysical experiments. Experiments with ROCK-I in complex with fasudil was also performed for comparison. The DSF approach measured the melting temperature (T_m) of a protein as an indicator of its thermal stability and an increase in T_m indicated higher stability. Fuigure 5-9 shows the melting curves of ROCK-I alone and in complex with compound **R8** or fasudil. Native ROCK exhibited a T_m of 35.3 °C, which increased to 49.4 °C (ΔT_m=+14.1 °C) upon compound **R8** (100 µM) binding, in contrast to that observed upon fasudil (75 µM) binding (T_m=35.8 ^{o}C). Thus, the higher T_m of ROCK-**R8** protein-ligand complex relative to ROCK alone signified a stabilization of ROCK upon **R8** binding, thus accounting for its more potent inhibition, better than fasudil.

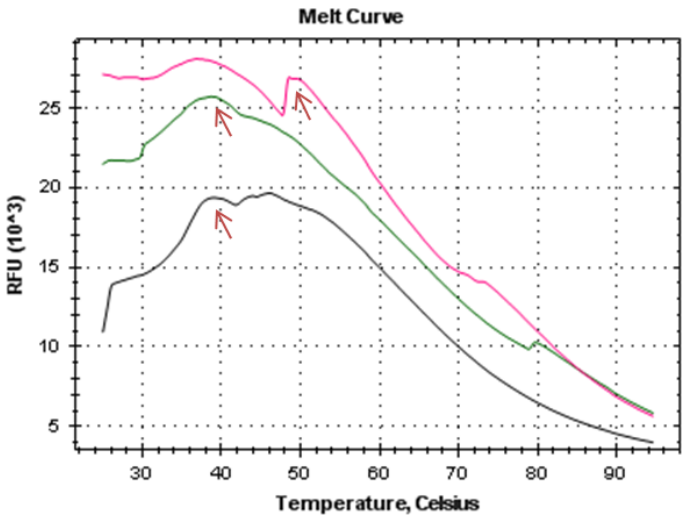

Figure 5-9. DSF analysis of **R8** and fasudil.

Stabilization of ROCK-inhibitor complexes as measured by DSF technique. Native ROCK (green), and ROCK in presence of fasudil (black); **R8** (pink). Arrows indicate the infliction temperatures.

5.2.7 Cell based assays

It has been already reported that MeHg, an environmental pollutant induce serious degenerative effect on neuronal system by inducing neuropharmacological changes in both central nervous and peripheral sensory nervous systems. MeHg has been also reported to overexpress ROCK [186]. Also, inhibition of ROCK pathway prevented MeHg-intoxication using IMR-32 cell lines. The results suggested that Rho/ROCK pathway inhibition prevented MeHg-induced axonal degeneration and apoptotic neuronal cell death [187]. This assay was considered important to understand the neuroprotective effects of ROCK inhibitors after

MeHg exposure to IMR-32 cell lines. Thus, in order to find the effectiveness of these molecules against MeHg induced assault to the neuronal cells, we conducted cell based assays.

5.2.7.1 Cell cytotoxicity studies

The effect of the designed inhibitors on normal cell toxicity was tested. MTT assay measured cell proliferation rate and could be applied to determine apoptosis or necrosis. The reduction of yellow tetrazolium MTT by metabolically active cells was indicated by the formation of intracellular purple formazan which could be solubilized and quantified by spectrophotometric methods. After subjecting HEK 293 cells to MTT assay, lead compounds **R1**, **R2**, **R4**, **R6** and **R8** showed less toxicity (≤50%) at 100 µM, which was considerably a higher concentration (Table 5-8). Interestingly, **R8** showed lower percent cytotoxicity than standard drug fasudil. Thus, MTT assay clearly indicated that these compounds showed low level of cytotoxicity, while leads **R3**, **R5** and **R7** were found to be cytotoxic at 100 µM.

5.2.7.2 Growth inhibition assay

Since MTT reduction was a marker of viable cell metabolism [187], we performed growth inhibition assay using neuroblastoma cell line (IMR-32). We decided to use IMR-32, which was a human neuroblastoma cell line, which when differentiated, mimicked large projections of the human cerebral cortex and under certain tissue culture conditions, formed intracellular fibrillary material, commonly observed in brains of patients affected with AD and other neurological disorders. Also, MeHg exposure caused ROCK overexpression [186], thus we decided to investigate the protective effects of ROCK inhibitors after MeHg exposure. Briefly, cells were subjected to different inhibitor concentrations (0.01-100 µM) and cell viability was measured in terms of GI_{50} values. GI_{50} was the concentration of the test drug which inhibited the growth of cells by 50%. Thus, GI_{50} value indicated growth inhibitory power of a compound. GI_{50} results indicated that all compounds except **R4** were able to inhibit growth of IMR-32 cells with $GI_{50} < 1$ µM. Involvement of ROCK in neuronal growth and guidance was already known [188]. This was further supplemented by the fact that ROCK was involved in differentiation of neuroblastoma cells [189]. Hence it could be postulated that lower GI_{50} values for neuroblastoma cells in presence of the test compounds could be due to ROCK inhibition (Table 5-8). **R1** was found to be equipotent to fasudil. Lead compound **R8** which was promising as the most effective ROCK inhibitor exhibited GI_{50} of 0.27 µM.

Table 5-8. Cell based studies on ROCK inhibitors.

Compound Code	%Cytotoxicity (100 µM)	GI_{50} (µM)	ROS IC_{50} (µM)
R1	34.00±1.73	0.02±0.0	6.24±0.79
R2	44.83±0.91	0.05±0.0	4.13±0.97
R3	52.30±0.39	0.33±0.0	4.55±0.67
R4	31.88±1.78	34.03±0.0	5.49±0.45
R5	50.57±0.76	0.89±0.7	4.89±0.98
R6	47.21±09	0.70±0.51	4.40±0.59
R7	73.70±1.73	0.20±0.03	5.25±0.11
R8	14.23±0.07	0.27±0.22	5.80±1.1
Fasudil	30.00±0.34	0.02±0.1	4.96±0.56

% Cytotoxicity was studied using HEK-293 cell lines whereas GI_{50}, IC_{50} for ROS inhibition were studied in IMR-32 cell lines.

5.2.7.3 Measurement of ROS production

ROCK signaling and ROS production were two simultaneous events [190]. Fasudil played a role in the production of vascular endothelium through ROCK inhibition and reduction of ROS generation [191]. We decided to study the effect of leads **R1**-**8** on intracellular ROS production. Intracellular ROS production was estimated using DCFH-DA. Cells were treated with 20 µM MeHg followed by **R1**-**8** (0.01-100 µM) treatment. All compounds showed significant ROS inhibition as described in Table 5-8. Thus, reduction in ROS production by inhibitors indicated that the lead compounds **R1**-**8** down-regulated ROS production, through ROCK pathway. Compounds **R2**, **R3, R5** and **R6** were potent than fasudil.

To conclude, in the present study structure-based e-pharmacophore and shape-based matching were employed to identify structurally diverse, small molecule inhibitors of ROCK useful in the treatment of neuronal disorders. Eight promising compounds were identified as prototypical leads with compound **R8** emerging as the most active ROCK inhibitor (Figure 5-10). In cell based assays, several of these compounds were found to be effective in growth

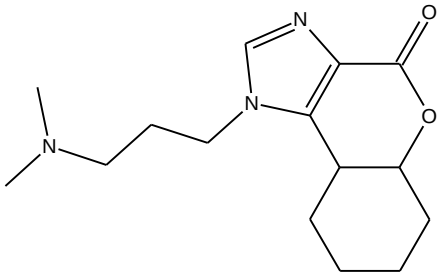

IC_{50}: 1.5±0.04 µM

GI_{50}: 0.27±0.22 µM

ROS IC_{50}: 5.80±1.1 µM

Figure 5-10. Structure of **R8**

and ROS inhibition and compound **R1**was the most effective in the cell based studies. Thus, these eight scaffolds could be utilized as promising leads for further optimization and development as ROCK inhibitors.

5.3 Design-II: Lead optimization of reported scaffold

5.3.1 Design and synthesis of lead compounds

As reported earlier by Takami *et al.* [83], we analysed the ligand binding pocket of ROCK protein that could be divided into three regions (Figure 5-11). The bottom of the pocket was flat and hydrophobic, and also hosted an important bond with Met156. The second region of the pocket consisted of hydrophobic residues. The third region was distal. A cleft-like shape was found to accommodate a wide range of chemical fragments.

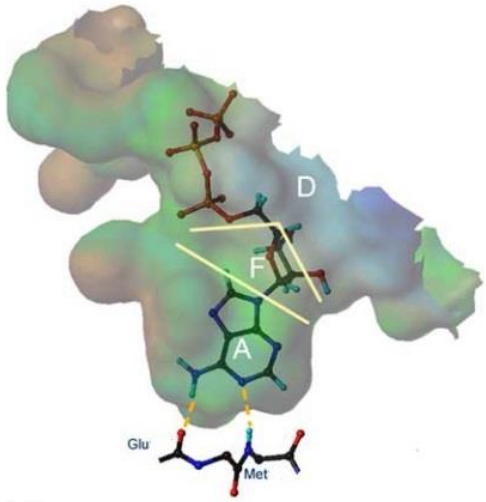

Figure 5-11. Ligand-binding pocket of ROCK protein.

The pocket was partitioned into three parts; adenine region: A, franose region: F, and distal region: D. The pocket was visualized by the channel surface representation [83]. The Connolly module available in the SYBYL software package. The surface was colored by lipophilicity; brown > green > blue. A docking model of ATP was shown. Hydrogen bonds between N1of ATP and HN of Met, and the amino group at the 6-position and C=O of Glu165 are indicated as dashed lines.

In 2008, Schirok *et al.* [192] reported a newer class of ROCK inhibitor with aminopyrimidine core. Most of the compounds were found to be highly selective ROCK inhibitors and exhibited good oral bioavailability. The most active compound of the series exhibited significant ROCK inhibition (IC_{50}= 3 nM), and featured 7-azaindol moiety linked to aminopyrimidine derivative. Docking studies of these aminopyrimidine derivatives with crystal structure of ROCK (PDB ID: 2ESM, Figure 5-12) suggested that the 7-aza-indole head group served as both H-bond donor and acceptor, making two key hydrogen bonds with the hinge region (Glu154 and Met156) of the ATP-binding site. Thus, considering promising ROCK inhibitory profile, and acceptable oral bioavailability, we decided to conduct a thorough literature search. Though aminopyrimidine derivatives were a lucrative ROCK

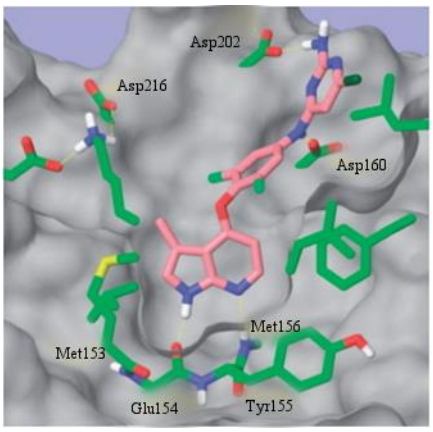

Figure 5-12. ROCK active site with aminopyrimidine derivative.

Docked pose of inhibitor into ROCK-1. The inhibitor is shown in pink, while the protein surface is given in grey with key amino acids labelled and highlighted in green. Heteroatoms and polar hydrogens are color coded (N, blue; O, red; S, yellow; F, light green; Cl, dark green; polar H, white) and hydrogen bonds are shown as yellow dotted lines.

inhibitor, it was found that these aminopyrimidine analogues were not subjected to *in vivo* characterization using diabetes-based disease models.

In order to explore the chemical space around aminopyrimidine based ROCK inhibitors, we initiated the design of novel ROCK inhibitors keeping the aminopyrimidine core in focus. The core was retained and various substitutions were applied to the corresponding head region of the molecule (Figure 5-13). The structures were drawn in 2D format using ACD/ChemSketch freeware (version 12.01) [193] and saved structures were converted to energy-minimized 3D structures using LigPrep 2.5 module [194] of Schrödinger suite [195]. The prepared molecules were docked to ROCK active site crystal structure (PDB ID: 2ESM) [196] using XP mode of Glide. Briefly, the downloaded crystal structure was refined using protein preparation wizard [197]. The pK_a values of the protein were predicted by selecting

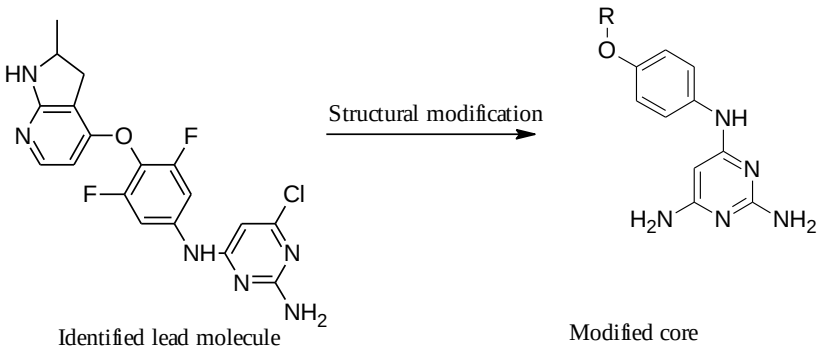

Figure 5-13. Schematic representation of lead optimization.

"Use PROPKA" option in protein preparation wizard interface. A target pH of 7 was specified to simulate biological condition. Based on the PROPKA output, hydrogen bonds were automatically assigned.

Newly generated 3D structures were then docked to the receptor using XP mode of Glide 5.7 module [198]. Top 10 molecules were shortlisted based on their docking score. After visual inspection, we finalized a total of eight molecules for synthesis. The ADME properties of these 8 molecules were also calculated using QikProp module (Table 5-9).

All the molecules showed good predicted octanol/water partition coefficient, and molecules except **RK6** and **RK7** were found to be predicted with good %oral absorption. None of the compounds were found to be cardiotoxic as predicted by QPlogHERG values which were <-5. All the molecules showed good skin permeability indicating their suitability as topical medication. Similarly, all molecules showed good predicted aqueous solubility and no Lipinski's rule of five were violated by all except **RK8** which showed one violation which could be acceptable. Overall, all molecules showed good predicted ADME properties.

Ullmann type intermolecular coupling of aryl halides with different substituted phenols was a key reaction in the formation of carbon-oxygen bond in the present scheme. We did an efficient and economic route for the synthesis of O-arylation *via* Ullmann coupling by using SiO_2 (60-120 mesh) as a catalyst. Second step involved the reduction of NO_2 group of O-arylated product by using Zn and ammonium formate. Final step involved microwave irradiated N-alkylation of amine with 2,6-diamino-4-chloropyrimidine in the presence of PTSA as a catalyst. The scheme has been depicted in materials and methods section (Figure 4-1).

Table 5-9. ADME properties of synthesized ROCK inhibitors.

Compound	QPlogPo/w	QPlogS	QPlogHERG	QPPCaco	QPlogBB	QPPMDCK	QPlogKp	% Human Oral Absorption	Rule of Five Violations
RK1	2.05	-3.37	-6.15	269.45	-1.39	119.88	-2.58	82.49	0
RK2	1.67	-3.92	-6.17	85.77	-2.07	34.78	-3.70	71.38	0
RK3	2.19	-3.69	-6.06	269.47	-1.49	119.89	-2.69	83.30	0
RK4	2.61	-4.29	-6.44	269.46	-1.65	119.89	-2.59	85.76	0
RK5	3.59	-5.10	-7.38	269.54	-1.66	119.93	-1.94	91.49	0
RK6	4.28	-6.24	-7.25	269.46	-1.75	119.89	-2.26	95.53	0
RK7	4.51	-6.28	-8.01	269.45	-1.75	119.88	-1.69	96.89	0
RK8	1.52	-4.12	-6.50	74.26	-2.23	29.77	-3.78	56.42	1

MW: molecular weight, QPlogPo/w: Predicted octanol and water coefficient (acceptable range -2.0 - 6.0); Qplogs: Predicted aqueous solubility (acceptable range -6.5 - 0.5); QplogHERG: Predicted IC_{50} value for blockage of HERG k+ channels (acceptable range: below -5); QPPcaco: Predicted caco cell-2 permeability (<25 is poor and >500 high); QPlogBB: Predicted brain/blood partition coefficient (acceptable range -3.0 - 1.2); QPPMDCK: Predicted apparent MDCK cell permeability (<25 is poor and >500 is high); QPlogkP: Predicted skin permeability (acceptable range -8.0 to -1.0); % Human oral absorption (<25% is poor and >80% is high); Rule of 5: Number of violations of Lipinski's rule of 5 (mol_MW < 500, QPlogPo/w < 5, donorHB≤5, accptHB≤10) acceptable maximum 1.

Table 5-10. Physicochemical properties of synthesized compounds (**RK1-8**).

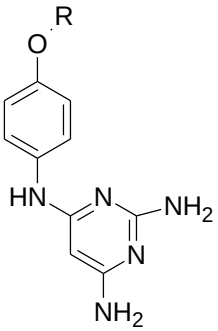

Compound	Docking Score	R	%Yield	MP (ºC)
RK1	-4.11	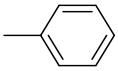	66	111-114
RK2	-3.16	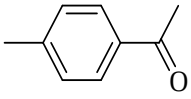	58	121-123
RK3	-3.13	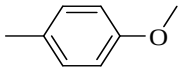	72	130-132
RK4	-2.61	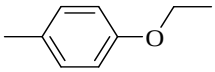	62	122-124
RK5	-3.95	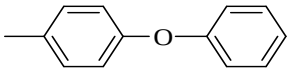	56	147-149
RK6	-3.16	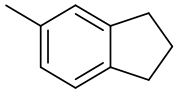	64	151-153
RK7	-3.42	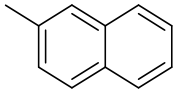	75	153-155
RK8	-3.07	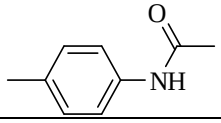	69	188-190

The compounds were purified by flash chromatography and characterized by ^{1}H NMR, ^{13}C NMR, electrospray ionization (ESI) and elemental analyses techniques. Table 5-10 presents the *in silico* and physical properties. The structures of the synthesized compounds are shown in Figure 5-14.

Analytical and spectral characterization data (^{1}H NMR, ^{13}C NMR mass spectra and elemental analysis) of the synthesized compounds are presented as follows:

N^4-(4-Phenoxyphenyl)pyrimidine-2,4,6-triamine (**RK1**): Reddish brown solid; ^{1}H NMR (300 MHz, DMSO-d_6): δ_H.8.48 (s, 2H), 8.29 (s, 2H), 7.72 (s, 1H), 7.54 (d, J=8.1 Hz, 2H), 7.39-7.11 (m, 5H), 7.02 (d, J=7.8 Hz, 2H), 4.91 (s, 1H). ^{13}C NMR (DMSO-d_6): δ_C. 169.9, 161.3, 160.1, 158.2, 146.2, 133.3, 129.4 (2C), 120.4, 120.0 (2C), 119.2 (2C), 118.2 (2C), 72.2.

MS(ESI) *m/z* 294.3 $[M+H]^+$, Anal. Calcd for $C_{16}H_{15}N_5O$: C, 65.52; H, 5.15; N, 23.88; Found: C, 65.50; H, 5.18; N, 23.92.

1-(4-(4-((2,6-Diaminopyrimidine-4-yl)amino)phenoxy)phenyl)ethanone (**RK2**): Dark brown solid; ^{1}H NMR (300 MHz, DMSO-d_6): δ_H. 9.12 (s, 2H), 7.69 (s, 1H), 7.63 (s, 2H), 7.56 (d, *J*=8.1 Hz, 2H), 7.49 (d, *J*=8.7 Hz, 2H), 7.24-7.02 (m, 4H), 4.88 (s, 1H), 2.34 (s, 3H). ^{13}C NMR (DMSO-d_6): δ_C. 192.2, 172.9, 163.5, 160.2 (2C), 145.8, 133.6, 130.4, 124.2 (2C), 120.8 (2C), 118.1 (2C), 117.2 (2C), 72.9, 27.6. MS(ESI) *m/z* 336.2 $[M+H]^+$, Anal. Calcd for $C_{18}H_{17}N_5O_2$: C, 64.47; H, 5.11; N, 20.88; Found: C, 64.43; H, 5.18; N, 20.92.

N^4-(4-(4-Methoxyphenoxy)phenyl)pyrimidine-2,4,6-triamine (**RK3**): White solid; ^{1}H NMR (300 MHz,DMSO-d_6): δ_H. 7.72 (s, 1H), 7.54 (d, *J*=8.1 Hz, 2H), 7.27 (d, *J*=8.4 Hz, 2H), 7.11-6.91 (m, 4H), 6.74 (d, *J*=7.8 Hz, 2H), 6.03 (s, 2H), 5.01 (s, 1H), 3.94 (s, 3H). ^{13}C NMR (DMSO-d_6): δ_C. 169.8, 160.4, 159.8, 154.2, 150.2, 142.1, 134.2, 121.8 (2C), 120.2 (2C), 117.9 (2C), 116.2 (2C), 73.6, 57.4. MS(ESI) *m/z* 324.2 $[M+H]^+$, Anal. Calcd for $C_{17}H_{17}N_5O_2$: C, 63.15; H, 5.30; N, 21.66; Found: C, 63.18; H, 5.26; N, 21.69.

N^4-(4-(4-Ethoxyphenoxy)phenyl)pyrimidine-2,4,6-triamine (**RK4**): Dark yellow solid; ^{1}H NMR (300 MHz,DMSO-d_6): δ_H. 7.69 (s, 1H), 7.48 (d, *J*=8.1 Hz, 2H), 7.39 (s, 2H), 7.29 (d, *J*=8.4 Hz, 2H), 7.09-6.88 (m, 4H), 6.69 (d, *J*=8.1 Hz, 2H), 4.94 (s, 1H), 3.89 (q, *J*=6.9 Hz, 2H), 1.29 (t, *J*=6.6 Hz, 3H), ^{13}C NMR (DMSO-d_6): δ_C. 169.2, 161.3, 160.2, 154.2, 149.8, 143.2, 135.0, 120.6 (2C), 119.2 (2C), 118.8 (2C), 117.4 (2C), 72.9, 68.4, 16.2. MS(ESI) *m/z* 338.2 $[M+H]^+$, Anal. Calcd for $C_{18}H_{19}N_5O_2$: C, 64.08; H, 5.68; N, 20.76; Found: C, 64.12; H, 5.63; N, 20.81.

N^4-(4-(4-Phenoxyphenoxy)phenyl)pyrimidine-2,4,6-triamine (**RK5**): White solid; ^{1}H NMR (300 MHz,DMSO-d_6): δ_H. 8.47 (s, 1H), 7.57 (d, *J*=9.0 Hz, 2H), 7.37 (t, *J*=8.1 Hz, 2H), 7.02-6.90 (m, 9H), 5.78 (s, 2H), 5.59 (s, 2H), 5.16 (s, 1H). ^{13}C NMR (DMSO-d_6): δ_C. 169.6, 161.8, 160.4, 157.9, 151.8 (2C), 143.2, 136.0, 127.3 (2C), 122.6, 120.9 (2C), 119.3 (2C), 118.4 (4C), 117.8 (2C), 74. MS(ESI) *m/z* 386.2 $[M+H]^+$, Anal. Calcd for $C_{22}H_{19}N_5O_2$: C, 68.56; H, 4.97; N, 18.17; Found: C, 68.59; H, 5.03; N, 18.14.

N^4-(4-((2,3-Dihydro-1H-inden-5-yl)oxy)phenyl)pyrimidine-2,4,6-triamine (**RK6**): Crystalline orange solid; ^{1}H NMR (300 MHz,DMSO-d_6): δ_H. 7.82 (s, 1H), 7.60 (d, *J*=8.4 Hz, 2H), 6.99 (d, *J*=7.8 Hz, 1H), 6.92 (d, *J*=7.8 Hz, 1H), 6.84 (s, 1H), 6.70 (d, *J*=9.0 Hz, 2H), 6.03 (s, 2H), 5.22 (s, 2H), 4.94 (s, 1H), 2.72 (t, *J*=7.2 Hz, 4H), 1.81-1.78 (m, 2H). ^{13}C NMR (DMSO-d_6): δ_C. 169.4, 161.2, 160.6, 153.1, 142.2, 141.9, 137.5, 133.2, 129.8, 122.2 (2C), 119.3 (2C),

117.9, 117.1, 76.2, 38.4, 36.2, 26.4. MS(ESI) *m/z* 334.2 $[M+H]^+$, Anal. Calcd for $C_{19}H_{19}N_5O$: C, 68.45; H, 5.74; N, 21.01; Found: C, 68.43; H, 5.76; N, 21.04.

N^4-(4-(Naphthalene-2-yloxy)phenyl)pyrimidine-2,4,6-triamine (**RK7**): Dark brown solid; ^{1}H NMR (300 MHz, DMSO-d_6): δ_H. 8.88 (s, 2H), 7.90 (s, 1H), 7.71 (d, *J*=7.2 Hz, 2H), 7.27-6.99 (m, 5H), 6.92-6.78 (m, 4H), 5.78 (s, 2H), 4.97 (s, 1H). ^{13}C NMR (DMSO-d_6): δ_C. 169.3, 161.5, 159.8, 155.8, 142.1, 136.2, 134.3, 130.6, 129.2, 128.4, 127.8, 125.4, 124.1, 120.9 (2C), 118.8, 117.9 (2C), 116.8, 78. MS(ESI) *m/z* 344.1 $[M+H]^+$, Anal. Calcd for $C_{20}H_{17}N_5O$: C, 69.96; H, 4.99; N, 20.40; Found: C, 69.92; H, 5.03; N, 20.42.

N-(4-(4-((2,6-Diaminopyrimidin-4-yl)amino)phenoxy)phenyl)acetamide (**RK8**): Light brown solid; ^{1}H NMR (300 MHz,DMSO-d_6): δ_H. 8.89 (s, 2H), 8.01 (s, 2H), 7.83 (s, 1H), 7.56 (d, *J*=7.8 Hz, 2H), 7.48 (s, 1H), 7.24 (d, *J*=8.1 Hz, 2H), 7.18-6.97 (m, 4H), 4.93 (s, 1H), 2.14 (s, 3H). ^{13}C NMR (DMSO-d_6): δ_C. 168.1, 167.8, 163.8, 160.4, 152.3, 141.0, 133.8, 130.1, 122.1 (2C), 120.8 (2C), 118.1 (2C), 117.4 (2C), 81.1, 25.4. MS(ESI) *m/z* 351.2 $[M+H]^+$, Anal. Calcd for $C_{18}H_{18}N_6O_2$: C, 61.70; H, 5.18; N, 23.99; Found: C, 61.72; H, 5.14; N, 23.98.

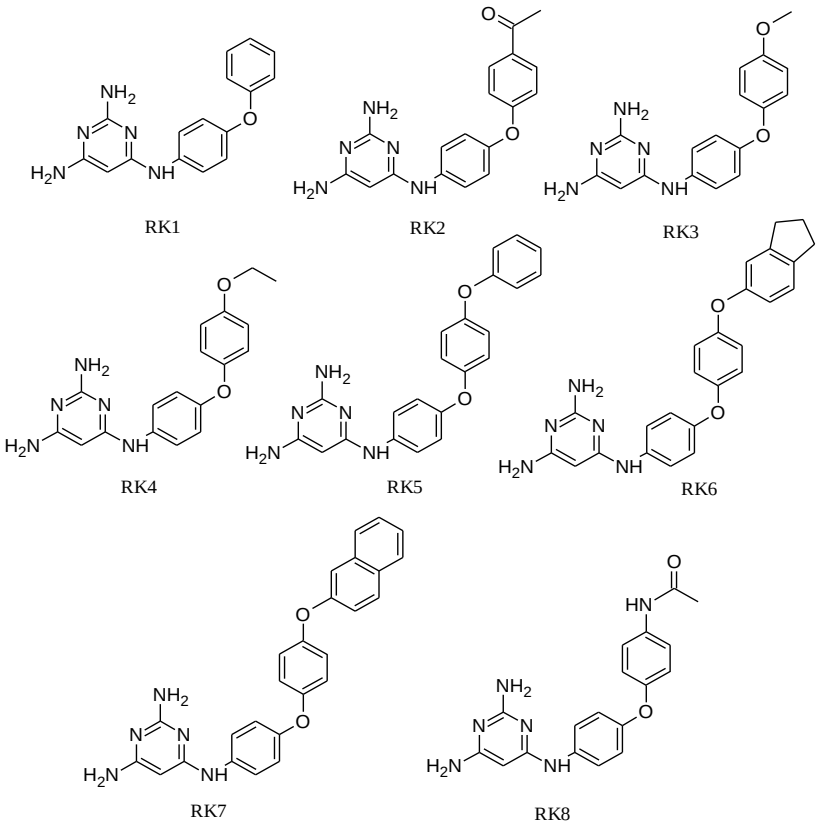

Figure 5-14. Structures of synthesized compounds.

5.3.2 ROCK enzyme inhibition studies

ROCK inhibitory activity was measured spectrophotometrically in a coupled assay format where NADH was oxidized to NAD^+ whenever a phosphate was transferred by ROCK and the optical density was checked. NADH showed high optical absorbance at 340 nm, whereas NAD^+ did not, thus providing a convenient and sensitive spectrophotometric estimation. ROCK inhibition by a compound resulted in increased optical density due to excess NADH. MBP was used as ROCK substrate with HEPES (4-(2-hydroxyethyl)-1-piperazine-1-ethanesulphonic acid) buffer. IC_{50}s were determined using a range of serial inhibitor dilutions (0.001-1000 µM). The reaction mixture consisted of MBP, PEP, NADH, $MgCl_2$, DTT, PK (pyruvate kinase) and LDH (lactose dehydrogenase). The reaction was initiated by the addition of 10 µL ATP. After 5 min incubation, reaction progress was monitored using SpectraMax spectrophotometer (M4, Molecular Devices, Sunnyvale, USA). All reactions were performed in triplicates [199].

Table 5-11 lists ROCK inhibitory IC_{50} of eight compounds. Compounds **RK5** and **RK7** showed IC_{50}s ≤5 nM. Compound **RK7** with 2-naphthyl substitution demonstrated highest ROCK inhibition (IC_{50}=2.37 nM), which was slightly better than the original 7-azaindole substituted aminopyrimidine (IC_{50}=3 nM); whereas compound with 4-methoxyphenyl substitution **RK3** showed least inhibition (IC_{50}=1728 nM). The value for fasudil was taken from the previous study (Table 5-6). If we looked carefully, compounds with hydrophobic ring systems exhibited maximum activity (**RK5** and **RK7**; IC_{50} < 5 nM, see Table 5-11), which could be justified due to hydrophobic nature of the active site. Interestingly, one reason explaining good activity of **RK7** might be due to the presence of bulky and hydrophobic naphthyl ring substitution. Bulkiness prevented conformational changes whereas aromatic

Table 5-11. IC_{50} of synthesized compounds.

Compound	IC_{50} (nM)
RK1	111.80±3.45
RK2	11.31±0.10
RK3	1728.00±13.95
RK4	238.50±9.34
RK5	4.56±0.90
RK6	419.10 ±15.90
RK7	2.37±0.02
RK8	576.00±3.79
Fasudil	10700±0.05

Each value represents mean±SEM of three observations.

naphthyl ring got accommodated easily in the hydrophobic active site pocket. This might also explain the big difference in the activity of **RK6** and **RK7**. There was quite a lot of structural similarity between these two compounds but **RK7** had the added advantage of aromatic napthyl ring whereas **RK6** had a relatively less hydrophobic indene moiety (Figure 5-14). Also, the activity of the least active molecule **RK3** could be related due to the presence of polar oxygen atom in the tail region. Presence of polar atom in a hydrophobic cavity was non-desirable. Also, with others, less important residues like Asp369 and Ile82 in the pocket could have also affected the activity of compound **RK3**.

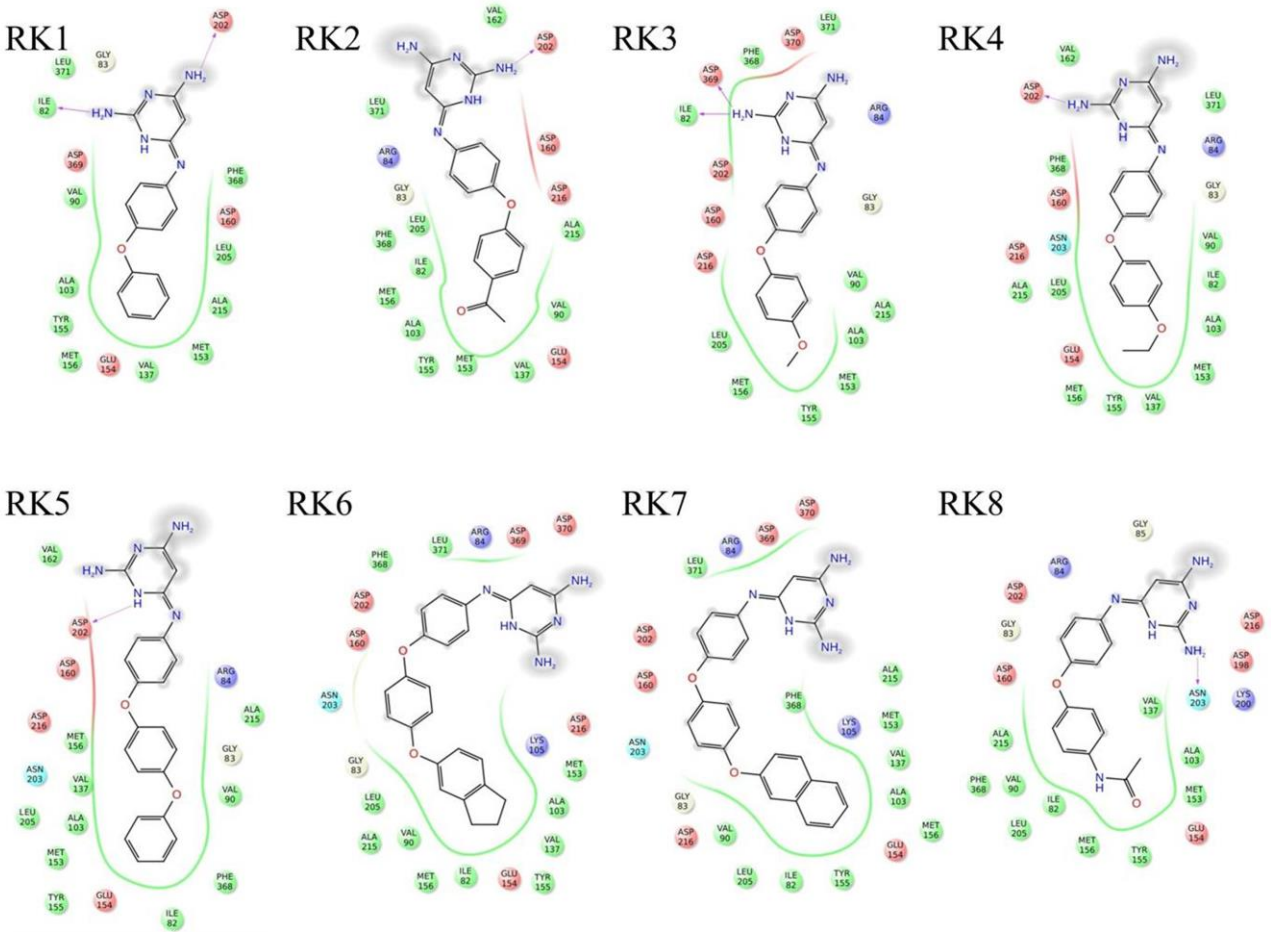

Figure 5-15. Ligand interaction diagram of synthesized ROCK inhibitors.

Binding pocket characteristics are displayed using color-coded spheres indicating surrounding amino acids, whereas protein-ligand interactions are represented as lines: hydrogen bonds as purple arrows, and π-π stacking interactions as green lines. Colour coding of amino acids spheres: light-orange, negatively charhed; purple, positively charged; cyan, polar; green, hydrophobic; yellow, glycine. Grayed out areas represent solvent exposure. These images were generated using Ligand interaction diagram module of Schrodinger.

5.3.3 Structure-activity relationship of RK1-8

Looking at the structure and activity data of **RK1-8**, it appeared that compounds with shorter substitutions like **RK1** (phenyl), **RK3** (4-methoxyphenyl), **RK4** (4-ethoxyphenyl) and **RK8** (4-acetamidophenyl) exhibited low activity (Table 5-11 and Figure 5-15). On the other hand, compounds with bulkier substitution like **RK5** and **RK7** exhibited better activity. It could be also noted that the amino group of head region was exposed to the solvent (Figure 5-15) in all

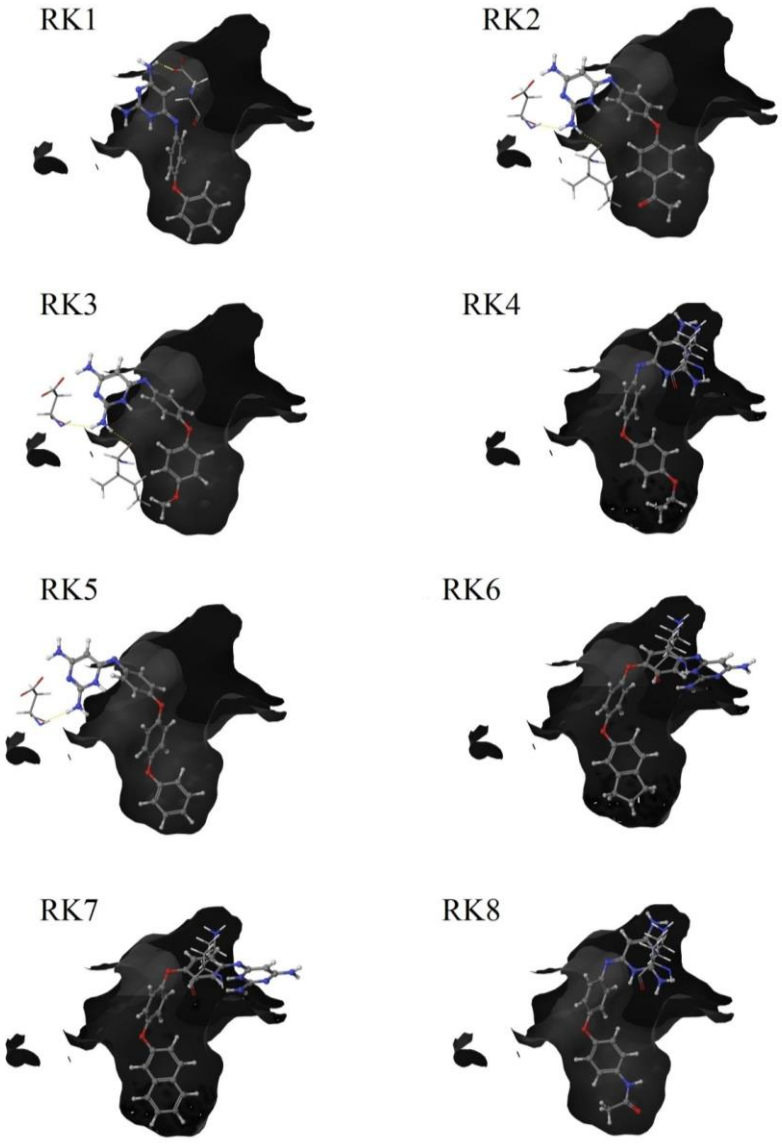

Figure 5-16. Docking pose of compounds **RK1-8**.

The receptor surface is shown as van der Waals surface and is coloured grey. Docked poses of inhibitors are shown as ball and stick model and interacting residues are shown as wireframe model. Elements are colour coded as: carbon, grey; hydrogen, white; nitrogen, blue; oxygen, red; sulphur, yellow and halogens (chlorine and fluorine) as green.

the compounds except **RK3**. This also might be a reason behind lower activity of **RK3**. Considering the 3D docked pose of the molecules in the cavity (Figure 5-16), it could be easily depicted that **RK7** was almost filled up in the pocket volume due to its hydrophobic napthyl ring substitution. In addition, bulky naphthyl ring prevented conformational change in **RK7**, eventually contributing towards activity.

Another reason for the high activity of **RK5** and **RK7** could be attributed to their rigid structure, as these compounds exhibited relatively less conformational change than the others due to the presence of planar naphthalene ring or 4-phenoxyphenyl substituent. Furthermore, delocalized π electrons over the substituted head region might also contributed towards activity (**RK2**, **RK5** and **RK7;** IC_{50} < 12 nM).

5.3.4 Biophysical characterization

DSF analysis of ligand binding was based on a concept that proteins get stabilized upon binding with their ligands and the difference between denaturation/melting temperatures of the ligand-bound and ligand free forms could be measured as ΔT_m. A positive ΔT_m value indicated protein-ligand interaction leading to greater thermal stabilization of the bound form *versus* unbound form of the protein. DSF studies were carried out to investigate the effect of inhibitor binding on ROCK protein stability. The reaction mixture (30 µL) consisted of 10x sypro orange dye, 12 µL ROCK enzyme, 100 mM HEPES buffer and inhibitors in different concentrations (50-100 µM). ROCK melting point (T_m) in the absence of any inhibitor was also calculated in each case. Interestingly, all compounds except **RK4** and **RK8** stabilized the ROCK-inhibitor complex as indicated by their positive T_m shifts (Table 5-12). It was observed that ROCK protein exhibited a T_m value of 40.20 ºC, whereas ROCK-**RK7** complex exhibited an increased T_m value (44.90 ºC), with $\Delta T_{m=}$4.7 ºC. A positive ΔT_m value indicated that ROCK- **RK7** complex was more thermally stable than ROCK alone when compared to fasudil (Figure 5-17). Also, it was worth noticing that compound **RK1**, **RK2** and **RK3** showed much higher ΔT_m than **RK7** out of which **RK1** and **RK3** were not as active as **RK7** in the enzyme inhibition assay. The ligand interaction diagram (Figure 5-15) clearly revealed that compounds **RK1**, **RK2** and **RK3** form hydrogen bonds with nearby residues (Asp202 and Ile82), whereas **RK7** did not formed any such interactions. Thus, these interactions might need more thermal energy to break during protein denaturation.

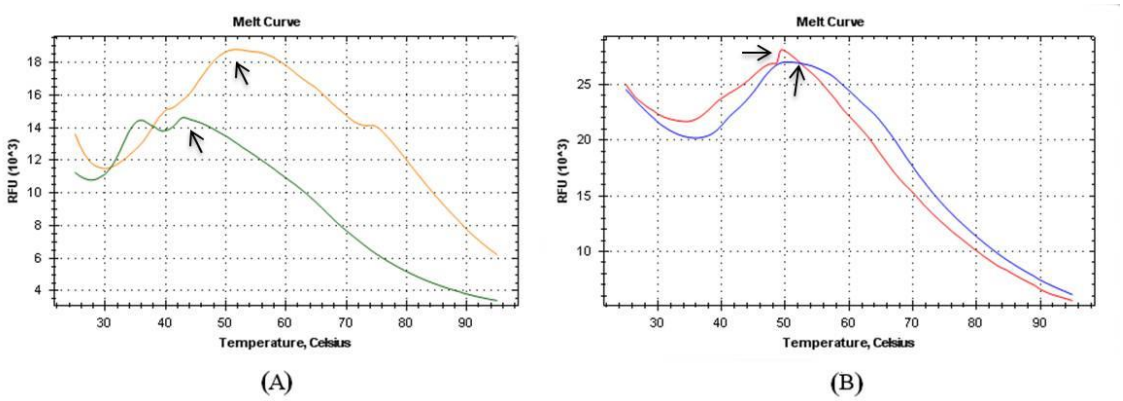

Figure 5-17. DSF analysis of compound **RK7** in comparison with fasudil.

(A) DSF graph of ROCK (green line) and ROCK with inhibitor fasudil (orange line). (B) DSF graph of ROCK (blue line) and ROCK with inhibitor **RK7** (red line). $T_{m(ROCK)}$=40.20˚C; $T_{m\ (ROCK\ +\ \mathbf{RK7})}$=44.90 ˚C. Arrows indicate the infliction temperatures.

Interestingly, these compounds showed better ROCK binding than standard ROCK inhibitor fasudil. Also, compounds showing a negative ΔT_m values exhibited a very minimal deviation (~ 1 ºC). Overall, the higher T_m of the six compounds relative to ROCK alone signified ROCK stabilization upon binding, thus accounting for effective ROCK inhibition.

Table 5-12. ΔT_m shifts of synthesized compounds.

Compound	ΔT_m (ºC)
RK1	9.40
RK2	5.10
RK3	8.60
RK4	-0.70
RK5	1.20
RK6	3.20
RK7	4.70
RK8	-1.10
Fasudil	0.50

DSF studies were carried out to investigate the effect of inhibitor binding on ROCK stability. A positive change in the melting points (ΔT_m) indicated protein-ligand interaction leading to stabilization.

5.3.5 Cell based assays

5.3.5.1 Cell cytotoxicity studies

MTT assay, which measured cell proliferation rate that could be applied to determine apoptosis or necrosis was employed to access **RK1-8** for toxicity. After subjecting HEK-293 cells to MTT assay, all synthesized compounds were found to exhibit no or negligible toxicity at 100 µM (Table 5-13). Compounds containing 4-phenoxyphenyl and 2-naphthyl substituents (**RK7** and **RK5**) showed more or less activity as that of fasudil. Interestingly

Table 5-13. Cell based studies of synthesized compounds.

Compound	% Cytotoxicity (100 µM) [c]	GI_{50} (µM)[a]	ROS Inhibition[a,b]
RK1	1.56±0.23	27.67±0.30	12.03±0.09
RK2	5.95±0.15	12.88±0.76	10.75±0.87
RK3	0.02±0.01	13.48±0.91	8.79±0.37
RK4	17.33±2.55	0.78±0.07	3.30±0.06
RK5	26.69±4.85	6.79±0.56	0.08±0.01
RK6	0.13±0.01	13.49±0.98	2.85±0.03
RK7	38.65±7.05	11.36±0.45	14.45±0.95
RK8	6.75±1.02	22.23±1.03	13.93±0.98
Fasudil	30.00±5.10	0.02±0.01	4.96±0.05

[a] Studies were conducted using IMR-32 cell lines pretreated with MeHg. [b] IC_{50} for ROS inhibition. [c]Studies were conducted using HEK-293 cell lines.

compounds **RK1, RK2, RK3, RK6** and **RK8** showed slightly lower percent cytotoxicity than standard drug fasudil. These results clearly indicated that the compounds exhibited low cytotoxicity.

5.3.5.2 Growth inhibition assay

It has been reported that ROCK overexpression by MeHg leads to axonal degeneration caused by incoordination in neuronal extension/retraction [191]. Growth inhibition assay was performed to test the protective effects of test compounds against degenerative effects of MeHg. Here, test drug concentration inhibiting cell-growth by 50% was termed as GI_{50}, which indicated that all test compounds were able to inhibit IMR-32 cell growth, which was pre-treated with MeHg. Compound **RK4** with 4-ethoxyphenyl substitution showed maximum activity with GI_{50} of 0.78 µM whereas compounds **RK1** and **RK8** with phenyl and 4-acetamidophenyl substitutions showed low activity (Table 5-13). The order of activity was **RK4** (4-ethoxyphenyl) > **RK5** (4-phenoxyphenyl) > **RK7** (2-naphthyl) > **RK2** (4-acetylphenyl) > **RK3** (4-methoxyphenyl) > **RK6** (indenyl) > **RK8** (4-acetamidophenyl) > **RK1** (phenyl). ROCK involvement in neuronal growth and guidance was already reported. Thus ROCK inhibition leading to neuronal growth inhibition further supplemented our hypothesis and indicated that these compounds were actually inhibiting ROCK and leading to lower proliferation. Also, ROCK was involved in differentiation of neuroblastoma cells [200]. Hence it could be postulated that ROCK inhibition resulted in inhibition of neuroblastoma cells.

5.3.5.3 Measurement of ROS production

We conducted test with the synthesized compounds to measure ROS inhibition after MeHg exposure in IMR-32 cells. All test compounds showed effective ROS inhibition (ROS inhibition IC_{50} < 15 µM, Table 5-13). Compound with 4-phenoxyphenyl (**RK5**) substitution showed maximum ROS inhibition (ROS inhibition IC_{50}=0.08 µM). Additionally, compounds with 2,3-dihydro-1H-indenyl and 4-ethoxyphenyl (**RK6** and **RK4**) substitutions effectively inhibited ROS expression (ROS inhibition IC_{50} < 3.5 µM). Overall the order of activity was **RK5** (4-phenoxyphenyl) > **RK6** (indenyl) > **RK4** (4-ethoxyphenyl) > **RK3** (4-methoxyphenyl) > **RK2** (4-acetylphenyl) > **RK1** (phenyl) > **RK8** (4-acetamidophenyl) > **RK7** (2-naphthyl). Three compounds (**RK4**, **RK5** and **RK6**) exhibited better ROS inhibition than standard drug fasudil. It has been already reported that ROS production activated ROCK pathways [201] Thus, ROS inhibition by test compounds indicated that these eight compounds could down-regulate ROS production and promote cell survival, which in turn could help in alleviating allodynia and hyperalgesia.

Overall, compound **RK7** was the most potent ROCK inhibitor (IC_{50}=2.37 µM). In DSF studies, compounds **RK1**, **RK2**, **RK3** and **RK7** thermally stabilized ROCK-I enzyme. In cell based assays, **RK6** appeared to be the most effective molecule as it exhibited relatively low GI_{50}, significant ROS inhibition and low cytotoxicity (Table 5-13). Compounds **RK2** and **RK3** showed low GI_{50} values and low cytotoxicity. On the other hand, compounds **RK4** and **RK5** showed effective GI_{50} and ROS inhibition, but low cell reproducibility and high cytotoxicity. Overall, compound **RK8** showed least efficacy in cell-based assays.

Based on these studies, it could be concluded that we have subjected these molecules to cell-based assays. Thus, for the first time, we report the efficacy of these molecules in cell based study for these scaffolds. We have also found that some of the molecules had shown better efficacy than the standard drug. Thus, these promising molecules could possibly lead to an effective ROCK inhibitor for the treatment of diabetic neuropathy and related complications.

5.4 Neuropharmacological interventions

MeHg is an environmental pollutant known to induce serious neurological effects. Neuronal degeneration accompanied by cell loss had been recognized in both central nervous and peripheral sensory nervous systems in humans [202]. Some of the molecular targets to relieve MeHg induced neurodegeneration have been identified. These included N-methyl-D-aspartate (NMDA) receptor blockers [203], Ca^{+2} channel blockers [204], antioxidants [205], selenium compounds [206] and prostaglandin derivatives [207]. Though axonal degeneration

produced sufficient neuronal deficit, available information regarding MeHg induced neurodegeneration was limited.

Recently, it has been confirmed that Rho family proteins were associated with axonal development and apoptotic neuronal cell death [208]. It has also been reported that RhoA promoted neurite retraction and was responsible for disappearance of growth cones, followed by neuronal cell death. A recent study established that inhibition of ROCK pathway using ROCK inhibitors, fasudil and Y-27632 significantly protected against MeHg-induced neurodegeneration and in cultured cortical cells neurons [209]. The study also revealed that loss of neurons in dorsal root ganglia and axonal degeneration in dorsal spinal root nerves was partially prevented with fasudil administration. In addition, hind limb crossing sign, which was characteristic of MeHg-intoxication, was significantly suppressed in rats that received MeHg in drinking water. These results suggested that inhibition of the Rho/ROCK pathway could improve MeHg-induced neuronal cell death.

On the other hand, there were some reports that subjects with diabetes mellitus have a greater chance of AD and a decline in cognitive function [210]. As it was a difficult to simulate the model of neurodegeneration by diabetes induction, we employed the ROCK-specific neurodegeneration model of MeHg. In previous sections we had already discussed up-regulation of ROCK and PKCβ-II in diabetic conditions *via* a common pathway. So we hypothesized that inhibition of the ROCK pathway might be beneficial against diabetes-induced neuropathy and MeHg-induced neurodegeneration. Here we investigated the effect of ROCK inhibitors (**RK1-8**) against diabetic neuropathy and MeHg-induced neurodegeneration.

5.4.1 Neurotoxicity assessment

Before testing the compounds in disease-specific models, it was important to perform neurotoxicity assessment. Hence in the present study, neurotoxicity was assessed using two animal models, *viz* rotarod and actophotometer based screening.

Compounds were administered at three dose levels. Minimal motor impairment was measured by rotarod test and neurotoxicity was indicated by the inability of the animal to maintain balance on the rotating rod for at least 1 min. Compounds **RK5**, **RK6** and **RK7** showed neurotoxicity at highest dose in both rotarod and actophotometer evaluations (300 mg/kg, Table 5-14) Neurotoxic effects of compounds on locomotor activity was determined by actophotometer test. All other compounds were non-neurotoxic in all the three doses

Table 5-14. Neurotoxicity of synthesized compounds.

Treatment	Neurotoxicity			
	Rotarod		Actophotometer	
	1 h	2 h	1 h	2 h
Vehicle	-	-	-	-
RK1	-	-	-	-
RK2	-	-	-	-
RK3	-	-	-	-
RK4	-	-	-	-
RK5	300	300	300	300
RK6	300	300	300	300
RK7	300	300	300	300
RK8	-	-	-	-

Doses of 300, 100 and 30 mg/kg were administered. The figures in the table indicate the minimum dose whereby bioactivity was demonstrated in half or more of the mice. The line (-) indicates an absence of neurotoxicity at the tested doses.

tested. The results of rotarod and actophotometer tests indicated motor-deficit only at the highest dose tested (300 mg/kg, see Table 5-14). Interestingly, all neurotoxic compounds possessed a bicyclic ring system. Thus, the toxicity could be attributed with increased lipophilicity, when administered at higher dose. Based on these results for bioactivity, subneurotoxic dose <300 mg/kg was decided. Since fasudil was reported to be non-neurotoxic at 30 mg/kg dose [211], we fixed the dose of fasudil at 30 mg/kg for further experiments.

5.4.2 Diabetic painful neuropathy

In the next phase of screening, two well-known neuropathic pain models were used. These models included STZ-induced painful diabetic neuropathy and CCI model for neuropathy in rats. Diabetic neuropathy was one of the most frequent complications of diabetes mellitus. However, the exact etiology and pathogenesis of diabetic neuropathy was unclear. Diabetic neuropathy was one of the long term indications of diabetes. Interestingly, fasudil had been shown to attenuate diabetic neuropathy. Also, various reports highlighted the usefulness of ROCK inhibitors in diabetic neuropathy and other complications. Thus, we decided to investigate the effect of our compounds against diabetic neuropathy.

Several animal models of diabetes have been established to study the pathophysiology of diabetic painful neuropathy. Most commonly used model for diabetic neuropathy was the administration of STZ, a pancreatic β-cell toxin, that induced diabetes. STZ-induced diabetic rats developed hyperalgesia at approximately 2-3 weeks post induction.

Diabetes was induced in rats by a single *i.p.* injection of STZ (30 mg/kg, dissolved in Citrate buffer pH 4.5). Animals with a non-fasting glucose level above 200 mg/dL were considered diabetic and were used for experiments. Nociceptive behavioral assessment was undertaken on 21st day post-diabetes induction as reported earlier [171]. All eight ROCK inhibitors (**RK1-8**) were studied at 30 mg/kg dose level. The animals were subjected to mechanical allodynia, hot plate test and cold water tail immersion tests. Prior to the experiment, the latencies were measured and compared with STZ-induced diabetic rats and normal rats (non-diabetic).

5.4.2.1 Mechanical allodynia

The 50% paw withdrawal threshold to mechanical stimuli was measured using von-Frey fibers. A series of von-Frey fibers were applied to the hind paw surface. A brisk paw withdrawal or flinching was considered as positive response. In diabetes induced-mechanical allodynia, all compounds (**RK1-8**) demonstrated significant activity by alleviating 50% paw withdrawal threshold at 30 mg/kg dose. Among these compounds, **RK1** and **RK5** showed

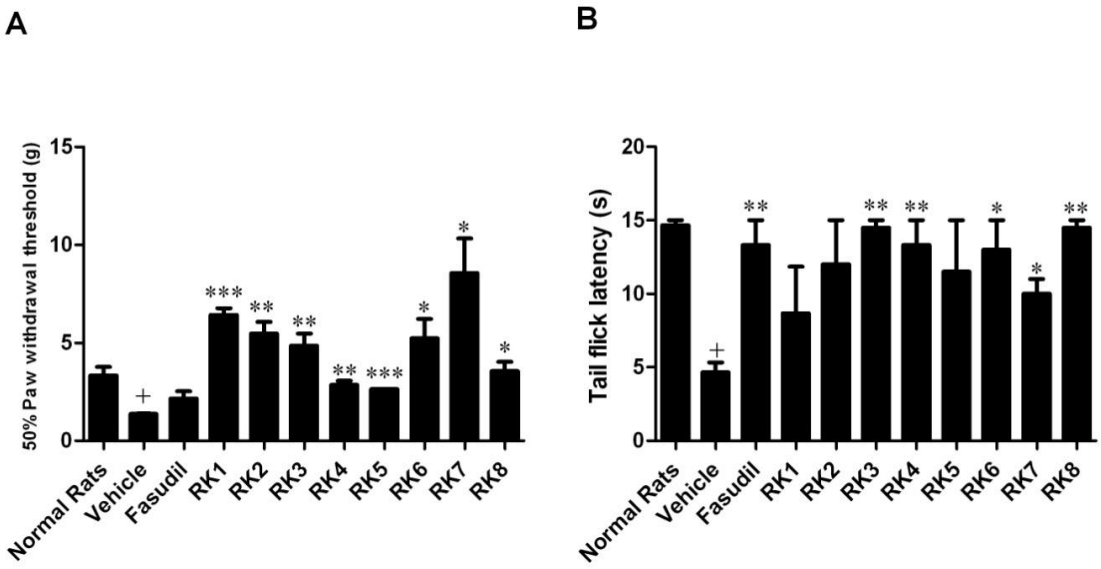

Figure 5-18. Effect of ROCK inhibitors on mechanical allodynia and cold water tail flick test.

(A) Mechanical allodynia, (B) Cold water tail flick test. Compounds were tested at 30 mg/kg dose given through intraperitonial route. Each value represents mean±SEM of six rats. Star indicates significant difference (*, p <.05; **, p <.01; ***, p <.001, two-tailed unpaired Student's t-test). Fasudil was used as a standard drug. 30% v/v PEG 400 was used as a vehicle. Compounds were administered by intraperitoneal route at a dose of 30 mg/kg. Normal rats indicated the group that were non-diabetic. + denotes significant difference of vehicle treated group activity when compared to normal group ($p < 0.05$).

best potency ($p \leq 0.001$, see Figure 5-18A). The standard drug fasudil showed no effect when compared to vehicle control. Interestingly, all compounds in this test showed better potency than fasudil. This observation could possibly mean that the compounds could be effectively used to elevate pain thresholds in clinical cases of diabetic neuropathty.

5.4.2.2 Cold water tail flick test

Cold water tail flick method was used to assess the effect of ROCK inhibitors on cold nociceptive threshold. Briefly, the animal was restrained and the lower $3/4^{th}$ of the tail was immersed in a beaker containing ice-cold water maintained at 7±2 ºC, and the latency of tail withdrawal was noted. In this test, compounds **RK3**, **RK4** and **RK6-8** were found to be active (Figure 5-18B). Compounds with 4-methoxyphenyl, 4-ethoxyphenyl and 4-acetamidophenyl substitutions (**RK3**, **RK4** and **RK8** respectively) were found to significantly increase the tail-flick latency in cold water, when administered at a dose of 30 mg/kg (Figure 5-18B). The standard drug fasudil was also effective and exhibited tail flick latency similar to the normal animals. Interestingly, most of the effective compounds (**RK3**, **RK4** and **RK8**) were as effective as fasudil as they showed comparable activity in this test by alleviating the tail withdrawal threshold to the levels of normal animals. It possibly confirmed that these compounds could exhibit elevated pain threshold against diabetic neuropathy.

5.4.2.3 Hot plate test

Hot plate test was performed to study the effect of these compounds on thermal hyperalgesia. Briefly, animals were kept on a heated plate maintained at 50±2 ºC and the latency to show pain response (licking of the paw, jumping) was noted. Compounds **RK2**, **RK5**, **RK7** and **RK8** prolonged the paw withdrawal latency to the level observed in non-diabetic rats at a dose of 30 mg/kg (Figure 5-19A). The standard drug fasudil did not show any efficacy in this test. It was evident that compounds **RK7** and **RK8** significantly elevated hot plate latency to a level, similar to normal animals. The activity profile of **RK7** and **RK8** also indicated that these compounds could be used against diabetic neuropathy as they exhibited elevated hot plate latency to a level, which was similar to those of normal animals.

5.4.2.4 Determination of nerve conduction velocity

It has been well established that diabetic patients exhibited slow nerve conduction velocity because of demyelination and loss of large myelinated fibers, and a decrease in nerve action potentials owing to loss of axons [9]. Since ROCK inhibitors could regulate neuronal extension and cell growth, we evaluated the effect of these compounds on the nerve

conduction velocity. Tail nerve conduction velocity was measured by placing stimulating and recording electrodes 10 cm apart. The time taken by a stimulus to travel 10 cm was measured. Apparently, the nerve conduction velocity was significantly decreased by three weeks in diabetic rats, when compared to normal control rats (Figure 5-19B). All compounds except **RK1** and **RK5** showed significant improvement in nerve conduction velocity and brought it to the level of non-diabetic rats at 30 mg/kg dose. Compound **RK4** with 4-ethoxyphenyl substitution was the most active compound. Fasudil did not show any significant improvements in the nerve conduction velocity.

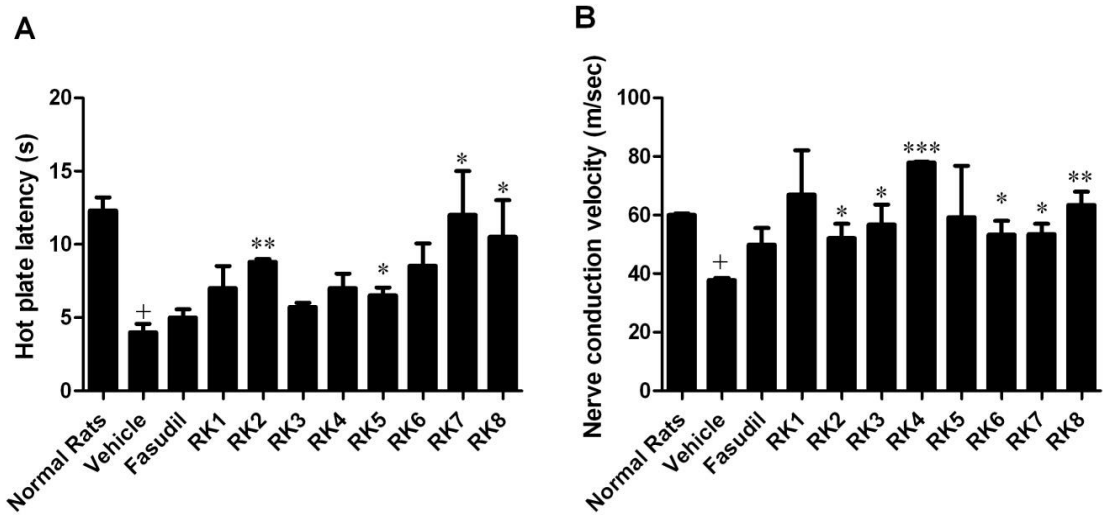

Figure 5-19. Effect of ROCK inhibitors on hot plate latency and nerve conduction velocity (NCV).

(A) Hot plate, (B) nerve conduction velocity. Compounds were tested at 30 mg/kg dose given through intraperitonial route. Each value represents mean±SEM of six rats. Star indicates significant difference (*, p <.05; **, p <.01; ***, p <.001, two-tailed unpaired Student's t-test). Fasudil was used as a standard drug. 30% v/v PEG 400 was used as a vehicle. Compounds were administered by intraperitoneal route at a dose of 30 mg/kg. Normal rats indicated the group that were non-diabetic. + denotes significant difference of vehicle treated group activity when compared to normal group ($p < 0.05$).

5.4.3 Chronic constriction injury model

Based on the promising results of these compounds in diabetic neuropathy, we were interested to evaluate their efficacy in standard neuropathy model. Hence, chronic constriction injury (CCI) model, which was a surgically induced chronic pain model, was employed to evaluate anti-neuralgic efficacy of the synthesized compounds. Gabapentin was used as standard drug for comparison. Briefly, a small incision (2-3 cm) was made at mid-thigh level of rat hind limb and common left sciatic nerve was exposed. Four loose ligatures were tied around sciatic nerve using 4-0 braided silk suture with about 1 mm spacing and the

wound was closed using a continuous suture pattern. Animals were tested 9th day post-surgery.

5.4.3.1 Mechanical allodynia

The 50% paw withdrawal threshold to mechanical stimuli was measured using von-Frey fibers. A series of von-Frey fibers were applied to the paw surface of the affected paw. A brisk paw withdrawal or flinching was considered as positive response. In mechanical allodynia, compounds **RK5** and **RK7** showed significant increase in the 50% PWT at 1 h after 30 mg/kg administration (Table 5-15). Compound **RK7** was the most active molecule, which was comparable to gabapentin that was administered at a dose of 30 mg/kg dose. The encouraging activity profile of the two compounds could also be supported by the fact that **RK5** (PWT=5.45±2.35 g) was equipotent to gabapentin (PWT=5.48±1.27 g), whereas **RK7** (PWT=6.03±0.45 g) which was promising in attenuating mechanical hyperalgesia in DPN, showed much better efficacy than gabapentin.

Table 5-15. Mechanical allodynia in CCI animals.

Compound	Mechanical Allodynia 50% PWT (g) 1 h
Vehicle	2.23±0.27
RK1	3.29±0.48
RK2	2.81±0.23
RK3	2.96±0.43
RK4	3.54±0.52
RK5	5.45±2.35*
RK6	5.12±0.45
RK7	6.03±0.45*
RK8	3.68±0.57
Gabapentin	5.48±1.27*

Each value represents 50% paw withdrawal threshold (g) (mean±SEM) of six rats. * represent the values, significantly different from control at $p < 0.05$ (One-way ANOVA, followed by post-hoc Dunnet test). Gabapentin was used as a standard drug. 30% v/v PEG 400 was used as a vehicle. Compounds were administered by intraperitoneal route at a dose of 30 mg/kg.

5.4.3.2 Cold allodynia

Since some compounds showed promising activity in mechanical allodynia at 30 mg/kg dose, we decided to further evaluate the efficacy of all the compounds against cold allodynia. In cold allodynia test, a small quantity of volatile acetone was sprayed on the effected paw of the animal and the duration of pain response was observed. The test was conducted at three time points post-administration. It was evident from Table 5-16 that except compounds **RK6**

Table 5-16. Cold allodynia in CCI animals.

Compound	Cold Allodynia % Reversal		
	0.5 h	1 h	2 h
Vehicle	4.90±0.54	2.89±3.74	5.09±1.75
RK1	48.01±5.03	63.48±5.35	81.89±8.88
RK2	49.81±16.22	80.59±10.57	73.86±8.22
RK3	46.05±13.55	51.18±10.30	59.97±18.56
RK4	68.30±1.18	63.36±7.15	74.44±7.09
RK5	44.43±14.72	25.87±1.40	55.22±8.98
RK6	31.13±6.21	15.96±23.37	37.12±6.74
RK7	44.98±9.31	42.04±12.51	50.11±8.65
RK8	24.17±6.88	37.64±8.19	38.19±13.27
Gabapentin	33.81±4.15	52.32±4.55	66.90±2.07

Each value represents % reversal of cold allodynia (mean±SEM) of six rats. Gabapentin was used as a standard drug. 30% v/v PEG 400 was used as a vehicle. Compounds were administered by intraperitoneal route at a dose of 30 mg/kg.

and **RK8**, all compounds showed >50% reversal in pain response in a time point. Compound **RK4** was the most active, as it exhibited >50% reversal at all-time points. Also, it was the only compound active at 0.5 h which revealed that the compound had a quick onset of action. Compound **RK2** showed overall maximum qualitative reversal at 1 h (>80% protection). Compounds **RK1-4** were found active at 1 h and 2 h time points, whereas **RK7** showed efficacy only at 2 h. Compounds **RK1** and **RK2** showed highest activity (>80% protection) at 2 h and 1 h respectively. The standard drug gabapentin showed moderate activity after 1 h. Compounds **RK1**, **RK2** and **RK4** showed better efficacy than gabapentin at 1 h and 2 h, indicating that these three compounds might be effective against injury-induced neuropathic pain.

5.4.3.3 Mechanical hyperalgesia

Mechanical hyperalgesia was measured by applying an incremental mechanical force to rat hind paw. Pressure was noted when animal showed the first withdrawal movement. Surprisingly, none of the test compounds showed efficacy (>50% reversal) when tested for mechanical hyperalgesia (Table 5-17). The standard compound gabapentin showed efficacy at all-time points.

Table 5-17. Mechanical hyperalgesia in CCI animals.

Compound	Mechanical Hyperalgesia % Reversal		
	0.5 h	1 h	2 h
Vehicle	5.85±0.40	15.87±0.79	15.87±0.79
RK1	0.17±0.05	1.77±0.75	2.54±1.04
RK2	2.39±1.74	1.60±0.27	0.55±0.08
RK3	2.11±1.05	2.27±0.93	3.02±1.01
RK4	2.18±0.70	2.09±1.03	0.38±0.07
RK5	0.34±0.04	1.28±0.68	2.53±0.55
RK6	1.23±0.44	1.96±0.75	1.07±0.04
RK7	1.77±0.16	1.96±0.46	1.04±0.77
RK8	0.52±0.04	1.04±0.04	0.78±0.30
Gabapentin	88.59±6.56	92.28±6.35	92.28±2.68

Each value represents % reversal of mechanical hyperalgesia (mean±SEM) of six rats. Gabapentin was used as a standard drug. 30% v/v PEG 400 was used as a vehicle. Compounds were administered by intraperitoneal route at a dose of 30 mg/kg.

5.4.4 Structure-activity relationship (SAR)

In diabetes-induced mechanical allodynia, out of all active compounds, compounds with 2-naphthyl substitution (**RK1**) showed the maximum activity. In tail flick model, compounds **RK3** (4-methoxyphenyl), **RK4** (4-ethoxyphenyl) and **RK8** (4-acetamidophenyl) significantly elevated the tail withdrawal latency. All compounds except those with 2-naphthyl (**RK1**) and 4-phenoxyphenyl (**RK5**) substitution were found to be active. Only compounds with 2-naphthyl and 4-acetamidophenyl (**RK7** and **RK8**) showed potency in hot-plate test. On the other hand, only compounds with 2-naphthyl (**RK1**), 4-phenoxyphenyl (**RK5**), 2-naphthlyl and 4-acetamidophenyl (**RK7** and **RK8** respectively) active and showed significant improvements in NCV.

In CCI model, only two compounds with 4-phenoxyphenyl substitution (**RK5**) and 2-naphthyl substitution (**RK7**) showed significant activity as in the case of DPN. In mechanical allodynia, compounds **RK5** and **RK7** showed significant increase in the PWT at 1 h after administration. The compound **RK5** was equipotent to gabapentin, whereas **RK7** exhibited better efficacy than gabapentin. Compound **RK7** was the most active molecule. In cold allodynia test, compound **RK4** with 4-ethoxyphenyl substitution was active at all-time points whereas **RK2** with 4-acetylphenyl group showed maximum reversal at 1 h. Compounds **RK1**, **RK2** and **RK4** showed better efficacy than gabapentin at 1 h and 2 h.

Overall, it appeared that compounds with alkyl substitutions (**RK3**, **RK4** and **RK8**) were inactive in diabetes induced mechanical allodynia, but showed good activity in cold water tail

flick test at 30 mg/kg dose. The activity of compounds **RK1-8** in diabetes induced mechanical allodynia could be attributed to the presence of aromatic ring systems which complimented well with the hydrophobic pocket of the receptor (see Figure 5-15). The overall effectiveness of compound **RK7** could also be explained by its structure. All the synthesized molecules in this series consisted of a polar aminopyrimidine system, linker and other substituents. Docked pose of **RK7** revealed that the aminopyrimidine nitrogens were exposed to solvent (water, Figure 5-15). On the other hand, the hydrophobic naphthalene substitution covered a major part of the hydrophobic cavity. The exceptional activity of **RK7** might be attributed to the rigid structure of the napthyl ring. Also possibly due to π- π stacking interactions with Phe368 could have contributed to bioactivity.

5.4.5 MeHg-induced memory and cognition deficit evaluation

To study the neuro-protective effect of these compounds, we performed a battery of tests using MeHg-induced neurodegeneration model in mice. Compound **RK7** was selected for further screening as it was not only the most potent ROCK inhibitor (IC_{50}=2.37 nM, Table 5-5), but also it consistently showed potency in most of diabetes-induced neuropathy testing. As MeHg induces the ROCK and PKC pathway, we were interested in this model.

Neurodegeneration was induced in mice by oral administration of MeHg. Mice were divided into three groups (n=6); *viz* naïve, control and treatment. Naïve group received only drinking water, whereas control and treatment groups received MeHg dissolved in regular drinking water. Treatment group received MeHg in drinking water for first 14 days for induction of neurodegeneration, after which they received only **RK7** dissolved in drinking water. The water was replaced daily. The mice were housed in plastic cages and were given free access to food and the respective water for 28 days. Daily water consumption did not differ between groups. Daily water consumption of naive, control and treatment groups were found to be 4.65±1.73, 5.15±0.11 and 5.91±0.34 ml per animal respectively. Based on the water consumption, daily doses of MeHg and **RK7** were calculated as 3.3 and 10 mg/kg respectively. We avoided higher dose of MeHg (>5mg/kg) because of its fast-onset of neurotoxicity, leading to increased mortality [180]. The behavioral tests were conducted once a week and were assigned as weekly results (week 0-3). In general, over a period of two weeks; MeHg-exposed groups (control and treatment groups) developed a heterogeneous motor impairment with a large variability between individuals with respect to the onset and severity of motor impairment signs.

5.4.5.1 Hind limb clasping test

Over the past two decades, many attempts have been made to generate animal models of neurodegenerative diseases. In an excellent review by Brooks and Dunnett [212], the authors had not only listed various tests but also had highlighted the most appropriate test(s) for a particular experimental program or application. Apart from other activity oriented tests, it was indicated that observational techniques could be employed as stand-alone assessments of mouse behavior. Some of these tests included rating scale assessments of general motor behavior like gait abnormalities, abnormal limb displacements during walking and running as there were some specific abnormalities like hind limb clasping being reported [213]. Hind limb clasping was characterized as a dyskinetic posture where mice clasped their hind limbs tightly into their abdomen when suspended by their tail. Hind limb clasping observations at the 21st day post-treatment for each group are shown in Figure 5-20. Naive group (Figure 5-20A) exhibited no hind limb clasping whereas MeHg treated control group (Figure 5-20B) showed severe clasping. Interestingly, **RK7** treated animals (treatment group) exhibited no sign of hind limb clasping, just like the naive group (Figure 5-20C). From these observations, it was clear that there was a MeHg dependent effect on the functional parameter of mice, and **RK7** was able to reverse the neurodegenerative effect of MeHg exposure.

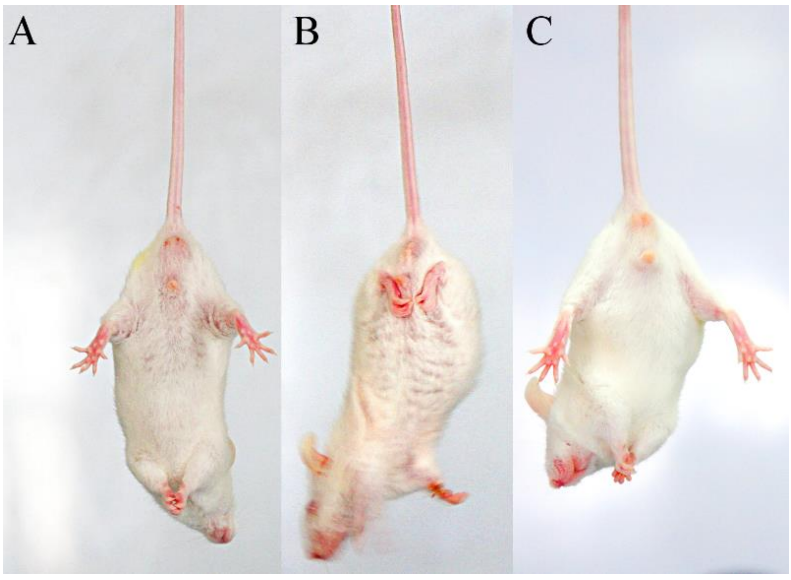

Figure 5-20. Hind limb clasping test.

Hind limb clasping behaviour after three weeks in different groups: (A) naïve group, (B) MeHg treated control group and (C) **RK7** treated treatment group. Clasping behaviour is an early manifestation of motor dysfunction. By the end of two weeks of MeHg treatment, control and treatment group animals showed extensive clasping. Interestingly, treatment with **RK7** reversed the clasping to a greater extent as seen in treatment group (panel C).

5.4.5.2 Gait test

Footprint test was conducted to understand the gradual gait impairment. It also helped us to determine the extent of motor impairment induced by oral MeHg exposure. Figure 5-21 represents the characteristic gait impairment in the three groups after three weeks. Interestingly, control group showed enhanced progressive gait impairment than either naive or treatment groups. It was evident from the figure that MeHg exposed control group mice showed a smudged footprint due to dragging of the limb while walking. Thus control mice clearly indicated gait impairment and in contrast, the footprints of naive treatment groups were sharp, indicating no alteration in gait. This also proved our hypothesis that **RK7** was able to reverse gait impairment after MeHg exposure, by inhibiting ROCK.

5.4.5.3 Locomotor test

We evaluated spontaneous locomotor activity to obtain a pattern of motor deficit. The third week results indicated a significant reduction in spontaneous motor activity ($P < 0.05$) in

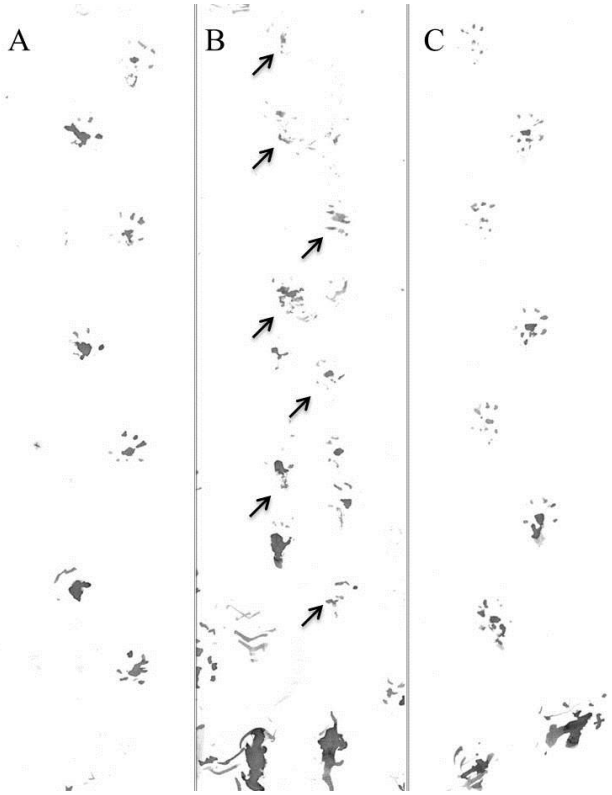

Figure 5-21. Evaluation of **RK7** in footprint test.

Representative walking footprint patterns of (A) naïve group, (B) MeHg treated control group, and (C) **RK7** treated group (treatment) mice after three weeks. The footprints were taken on white paper by applying non-toxic dye on hind limbs of mice and allowing them to walk on paper. Generated footprint patterns of control group clearly differ from naïve and treatment groups. Control group mice had irregularly spaced, smudged and unclear footprints (marked by arrows in panel B) indicating MeHg induced motor impairment. On the other hand, treatment group animals showed clear footprint indicating reduced motor dysfunction.

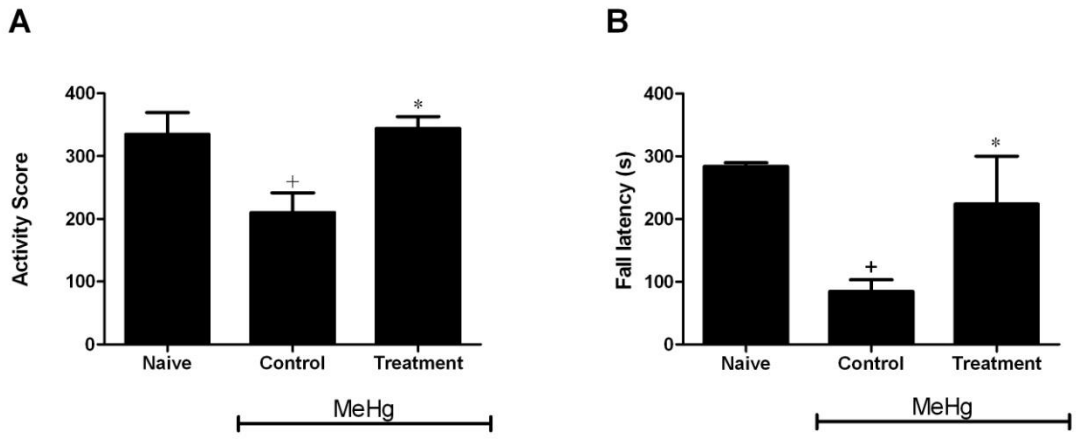

Figure 5-22. Evaluation of **RK7** in actophotometer and rotarod tests.

(A) Actophotometer test, (B) rotarod test. Data are given as the mean ± SEM of six mice. Statistically significant differences of treatment relative to MeHg group (control) are denoted by *(*, p <.05; **, p <.01; ***, p <.001, two-tailed unpaired Student's t-test). + Significant difference of control group activity when compared to naïve group ($p < 0.05$). + denotes significant difference of vehicle treated group activity when compared to normal group ($p < 0.05$).

control group, but not in treatment group, which showed similar locomotor behavior as naïve group (Figure 5-22A). This finding complemented the earlier observations of hind limb clasping phenomena and indicated that **RK7** clearly reversed the MeHg induced neurodegeneration.

5.4.5.4 Motor co-ordination test

We also subjected the three groups of animals to rotarod test to measure the ability to balance itself on a rotating rod. Mice were kept on a rotating metallic rod at 20 rpm, and the latency to fall from the rod was observed. This test was very useful as it could test minimal motor impairment and also it was an indicator of gripping strength. It was observed that MeHg treated control group animals exhibited statistically significant difference in fall latencies when compared to naïve group whereas treatment group animals showed elevated fall latencies, similar to naïve group (see Figure 5-22B). This clearly suggested that MeHg exerted a declining effect on fall latencies, but **RK7** was able to reverse this effect and significantly increased the animal stay duration on the rotating rod.

5.4.5.5 Novel object recognition test

One of the recently identified side effects of MeHg exposure was the alteration in learning and memory disturbances. In a recent publication, Onishchenko *et al.* [213] proposed that developmental exposure to MeHg altered learning and induced depression like behavior in male mice. Consistent with this, increasing neurogenesis after the formation of a memory was

sufficient to induce forgetting in adult mice. Plasticity was the ability to incorporate new information. In the hippocampus, new neurons continued to be generated in the sub-granular zone of the dentate gyrus, beyond development and provided potential substrates for new learning. Promoting the production of new neurons in adult mice facilitated the formation of new hippocampal memories [214].

Neurogenesis was the process by which new neurons were created. In adulthood, neurogenesis was confined to two brain areas: the olfactory bulb and the dentate gyrus (part of the hippocampus). New neurons born in the dentate gyrus during adulthood were thought to promote learning and memory processes, including the formation of new hippocampal memories. However, as new neurons were integrated into preexisting learning circuits, they have to compete with existing cells for inputs and outputs as well as formed, replaced and even coexisted with older synaptic connections. Thus, continuous neurogenesis would result in constant remodeling of hippocampal circuits. In recent past, many scientists have indicated that increasing neurogenesis promotes forgetting in adult mice because new cells containing no memory take place of dying memory-containing cells [215-217]. We hypothesized that since MeHg had been already identified as a neurotoxic agent, it would promote death of the neuronal cells including the dentate gyrus. This, in turn should induce neurogenesis, which would be reflected as memory loss or forgetting. Administration of potent ROCK inhibitor should be able to prevent neuronal death by reversing the deteriorating effect of MeHg, thus preventing or reversing the memory loss due to MeHg administration. Hence we decided to test the impact of **RK7** on reversing MeHg-induced memory loss.

Novel object recognition (NOR) test was used to access animal's behavior when it was exposed to a novel object along with a familiar object. This test was first studied and reported by Ennaceur and Delacour [182]. The NOR task had become a widely used model for the investigation into memory alterations [218]. We measured the difference in exploration time for novel *versus* familiar objects. A positive difference indicated more exploration of novel object, than familiar object. It also meant that the mice had retained the memory of the familiar object and thus, it could easily recognize the novel object and spent more time exploring it. On the other hand, a negative difference indicated that the animal explored familiar object more. In case of memory loss, the mice would lose the memory acquired during habituation phase and would treat the familiar object as novel object during the test phase.

Third week results of the NOR test implicated that the naive group mice were able to clearly discriminate between familiar and new objects, which was reflected by a positive difference (Figure 5-23A). On the other hand, animals from control group, explored familiar object more, over the novel. Whereas treatment group animals showed a positive trend. Since the animals of treatment group were subjected to 2 weeks of MeHg, it was obvious that these animals had undergone memory impairment process. But one week after **RK7** administration, the animals retained some memory of the familiar object.

Interestingly, MeHg treated control group mice explored familiar object more as the experiment progressed. The third week data revealed that MeHg had an impact on memory of the familiar object. Interestingly, naive animals explored novel object for more time as indicated by their positive score. On the other hand, treatment group animals initially showed a negative score for first three weeks, but the score was negative, and gradually shifted toward positive axis when compared to control group. Hence it could be concluded that over the time of treatment, **RK7** treated animals recovered from MeHg induced memory loss.

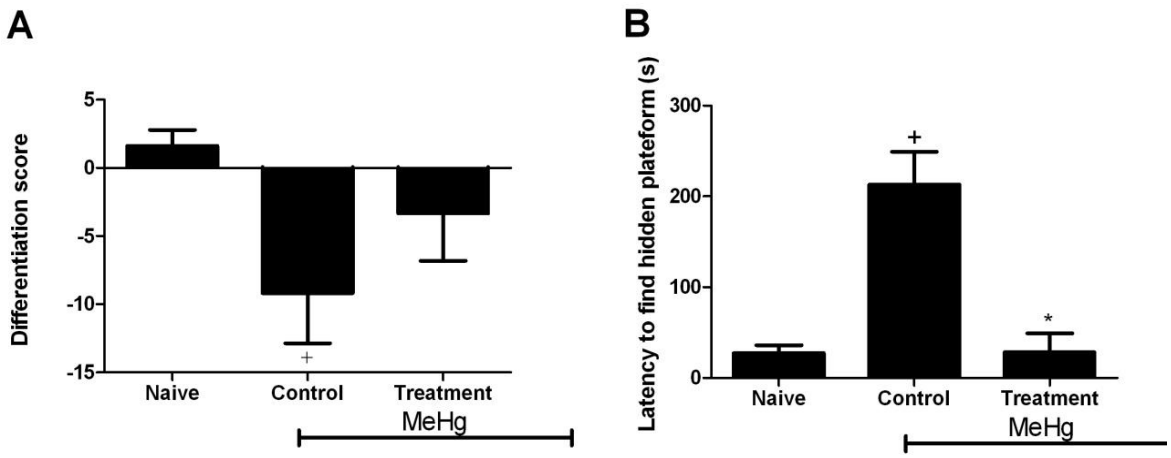

Figure 5-23. Evaluation of **RK7** in novel object recognition (NOR) and morris water maze test.

(A) Novel object recognition test, (B) Morris water maze test. Data are given as the mean ± SEM of six mice. Statistically significant differences of treatment relative to MeHg group (control) are denoted by *(*, p <.05; **, p <.01; ***, p <.001, two-tailed unpaired Student's t-test). + denotes significant difference of control group activity when compared to naïve group ($p < 0.05$).

5.4.5.6 Morris water maze test

The morris water maze was first described by Morris R. [183]. This was a test of spatial learning for rodents. This test relied on visual cue placed around the perimeter of an open swimming arena to locate a submerged escape platform. The spatial learning was assessed

across repeated trials and reference memory was determined by preference for the platform area when the platform was absent. In this test, we used an open circular pool with unobtrusive seams and uniform, smooth interior to minimize the attempts of animals to climb the walls during early trials.

The pool was approximately filled half-way with water. To the pool, two principal axis were designated, each line bisecting the maze perpendicular to one another to create an imaginary "+". The end of each line represented four cardinal points (North, South, East and West, see materials and methods section, Figure 4-3). A coin-sized (2 cm diameter) yellow colored paper was used as visual cue and was stuck to the wall midway between north-east quadrants. The visual cue was positioned 5 cm above the water level to maintain proper visibility and also to avoid wetting. The experimenter quietly noted the observations while staying 2 m away in the south-west side of the pool. Learning trials were conducted over 2-3 days, with 4 trials per day. Each trial lasted for 5 min with 1 min interval between each trial. The animal was left on platform, facing the visual cue for 30 sec and then was randomly and gently dropped in the pool, at least 15 cm away from the platform. A timer was started the moment animal was dropped in the water and was stopped when it reached the hidden platform. If the animal failed to locate the platform within 5 min, the animal was taken out, dried for 1 min and again was kept on platform facing the visual cue for 1 min followed by being dropped in the pool. In the test runs, the hidden platform was removed and the trained animal was observed for 5 min.

It was observed that control group mice took considerably longer time to return to the learned place using visual clue when compared to naïve and treatment groups (see Figure 5-23B). By the third week, treatment group animals showed similar latency as that of naive group. Longer time taken by control group animals indicated diminished learning tendency. In contrast, treatment group animals exhibited reduced latency, similar to that of naïve group. Thus it could be concluded that under the influence of MeHg, animals showed an increased trend of forgetting and the same was reduced by **RK7** administration, to a level shown by naive group.

5.4.5.7 Mechanical allodynia

The 50% PWT to mechanical stimuli was measured using von-Frey fibers. Briefly, a series of von-Frey fibers were applied to the hind paw surface. A brisk paw-withdrawal was considered as positive response. The MeHg teated control group exhibited statistically

significant difference in allodynia, when compared to naive group, as control group mice showed paw withdrawal threshold at lower pressures than naive. On the other hand, **RK7** treated animals (treatment group) exhibited partially elevated 50% PWT than MeHg ($p \leq 0.05$), but still it showed statistically significant difference when compared to control group. Thus, **RK7** was able to partially reverse the effect of MeHg induced allodynia (see Figure 5-24A). This also indicated that **RK7** was able to partially reverse the degenerative effects of MeHg exposure on neurons by ROCK inhibition. A complete reversal could be expected if **RK7** would have been administered for a longer period or at a higher dose.

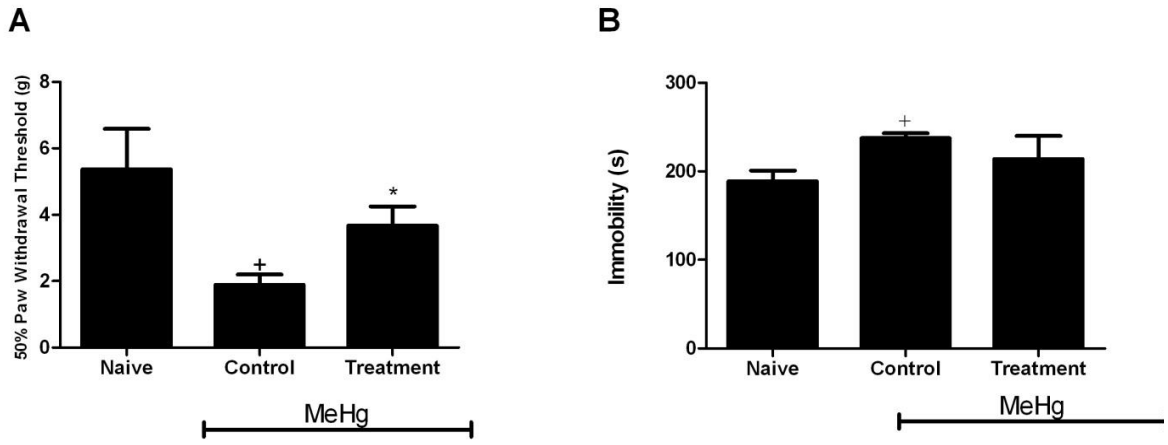

Figure 5-24. Effect of **RK7** on mechanical allodynia and tail suspension test.

(A) Mechanical allodynia, (B) Tail suspension test. Data are given as the mean ± SEM of six mice. Statistically significant differences of treatment relative to MeHg group (control) are denoted by *(*, p <.05; **, p <.01; ***, p <.001, two-tailed unpaired Student's t-test). + denotes significant difference of control group activity when compared to naïve group ($p < 0.05$).

5.4.5.8 Tail suspension test

In order to evaluate the response of MeHg effect on animals to an inescapable aversive situation, we conducted tail suspension test. In this test, the mice were suspended upside-down with their tail secured at a height of 50 cm from the ground. The animals demonstrated alternative active phase (struggling to get rid of inescapable situation) or inactive (lying idle) behaviour. The latter was interpreted as a measure of depression-like behaviour [219]. In this test, the third week results suggested that MeHg treated control group animals spent significantly more time as inactive, when compared to naïve group mice. Whereas treatment group (**RK7** treated animals) exhibited statistically equal immobility time as that of control animals (Figure 5-24B). The result indicated that MeHg treated animals showed enhanced tendency of depression, but the effect reversal was non-significant when animals were treated

with **RK7**. The depressive effect of human exposure to elemental MeHg had already been known [220]. Further in-depth studies on potential effects of MeHg on emotional behaviour would be required.

To conclude, in the present study a series of eight aminopyrimidine derivatives, were identified *in silico* by optimizing a previously reported compound. These compounds were synthesized and were subjected to extensive *in vitro* as well as *in vivo* studies including ROCK inhibition assays, cell based studies, models of neuropathic pain including DPN and neurodegeneration. Overall compound **RK7** emerged as most active ROCK inhibitor. In cell based assays, many of these compounds were found to be effective in neuronal cell growth inhibition and ROS inhibition in MeHg induced system. Some of these molecules were found to be very effective in models of neuropathic pain. Compound **RK7** also showed its efficacy in the model of neurodegeneration as it could reverse the neurodegenerative effects of MeHg. Thus, these molecules could be utilized as promising leads for further optimization and development as ROCK inhibitors.

5.5 Summary

Overall two design strategies were employed to design and identify novel ROCK inhibitors.

Design-I It utilized multiple crystal structures to design and validate pharmacophore hypotheses for *in silico* identification, followed by biophysical and *in vitro* biological characterization of lead molecules.

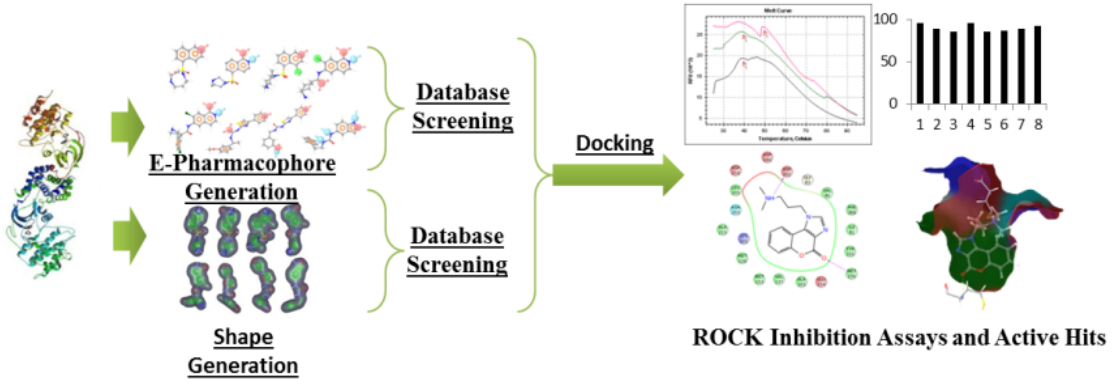

Compound **R8** emerged as most potent compound with ROCK inhibitory IC_{50}=1.5±0.04 µM, and was found to be more potent than fasudil in DSF studies. Apart from having similar ADME profile with standard drug fasudil, **R8** exhibited similar binding pose in the active site. Most of the compounds inhibited MeHg-induced ROCK overexpression in cell based assays and were non-toxic at higher concentrations.

Design-II The second strategy incorporated lead optimization of previously reported scaffold using *in silico* methods.

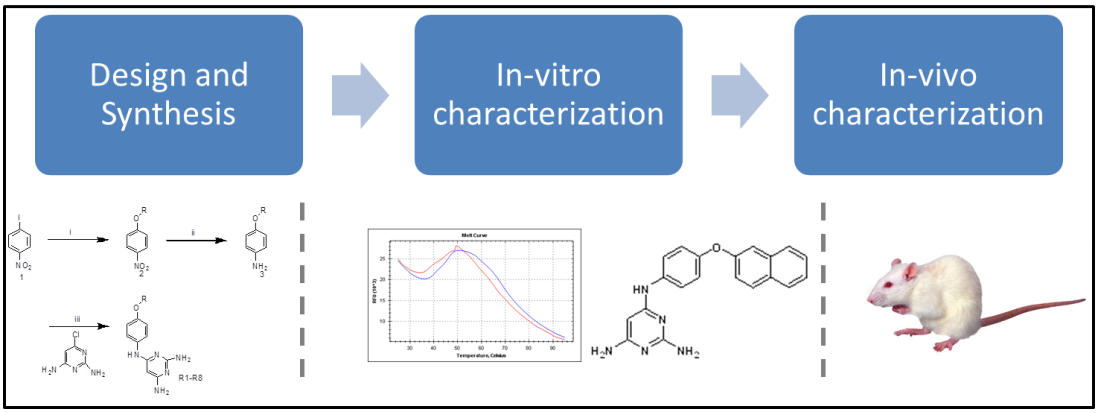

Total 8 promising were synthesized and were subjected to biophysical, *in vitro* and *in vivo* characterization. Compound **RK7** emerged as most potent compound (IC_{50}=2.37±0.02 nM), and offered better thermal stabilization of ROCK-**RK7** complex. All synthesized compounds were non-cytotoxic, and demonstrated ROCK inhibition in cell-based assays. In addition to diabetic as well as surgically induced CCI models of neuropathic pain; compound **RK7** also reversed the neurodegenerative effects of MeHg on gait impairment, allodynia, memory impairment and cognition deficit.

"Do not figure out big plans at first, but, begin slowly,
feel your ground and proceed up and up."
-Swami Vivekananda

Chapter 6.
Results and Discussion:
Design of Novel PKC β-II Inhibitors

PKC's are Ca^{2+} and phospholipid dependent protein kinases which play a variety of roles in cell proliferation, differentiation and apoptosis. They have also been implicated in phosphorylation of many neuronal proteins, thus effecting long-term potentiation and memory formation. It has also been established that PKCs were found to be involved in diabetic complications (see section 2.4.2). As PKCs were implicated to be upregulated in diabetic conditions along the RhoA/ROCK pathway, it was important to study this as an independent target for treating diabetic complications.

In this chapter, we introduce the key concepts, illustrate strategies and applied techniques and explained their results. In a nutshell, the entire process of novel PKCβ-II inhibitor design could be divided into two major phases:

(a) **Phase I**: Lead identification using crystal structure-bound to inhibitor and biological characterization of Asinex and *in house* databases.
(b) **Phase II**: Extensive pharmacological characterization of promising leads.

For the design of inhibitors, we decided to analyse the active site pocket containing bound ligand 2-methyl-1H-indol-3-yl-BIM-1 (Figure 6-1). The crystal structure revealed that there were five stranded β sheets (β1-β5) in the N-terminal lobe and also, two α helices (αB and αC) in the C-terminal lobe (residues 426-620) constituting the kinase domain of PKCβ-II. These two terminal lobes were found connected by a linker region defined by residues 422-

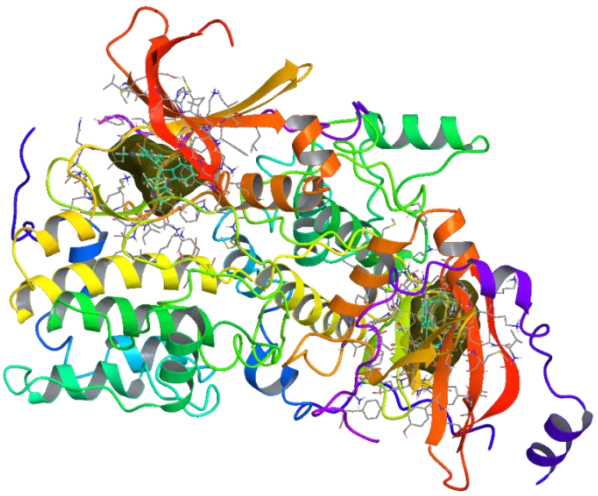

Figure 6-1. PKCβ-II pdb crystal structure.

The protein backbone is shown as rainbow coloured ribbon, the active site van der Wall radius is shown as yellow surface, bound inhibitor is shown as ball and stick model whereas residues within 6 Å of the bound inhibitors are shown as pipes. The image was generated using Schrodinger.

425 [221]. The bottom of the cavity was mostly lined by hydrophobic residues. Glu421, Thr404 and Val423 were the key active site residues. The bound conformation revealed that pyrrole-2,5-dione moiety acted as both, hydrogen bond acceptor and donor, making important interactions with the above three key amino acids of the active site (Figure 6-2).

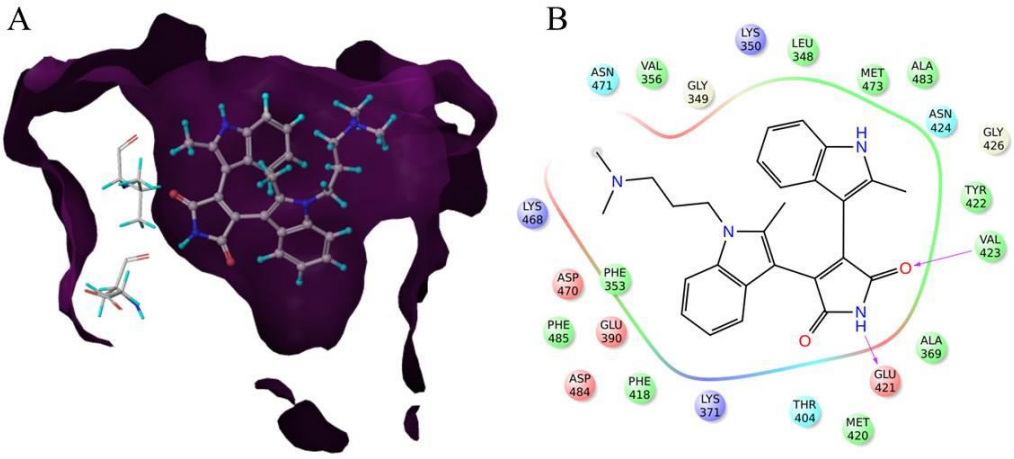

Figure 6-2. Active site of PDB 2I0E.

Panel A shows bound conformation of the inhibitor. The active site surface is shown as maroon surface, inhibitor as ball and stick model, and key amino acids (Glu421 and Val423) are shown as pipes and are colour coded as: carbon, white; hydrogen, cyan; oxygen, red and nitrogen in blue colour. **Panel B** shows 2D interaction diagram of the inhibitor. Binding pocket characteristics are displayed using color-coded spheres indicating surrounding amino acids, whereas protein-ligand interactions are represented as lines: hydrogen bonds as purple arrows, and π-π stacking interactions as green lines. Colour coding of amino acids spheres: light-orange, negatively charhed; purple, positively charged; cyan, polar; green, hydrophobic; yellow, glycine. These images were generated using Schrodinger.

6.1 Lead identification

We employed two different libraries for virtual screening which included commercially available Asinex database and *in house* compounds database. For Asinex database screening, generated e-pharmacophores were validated and only selected e-pharmacophores were used for database screening process. On the other hand, structurally optimized *in house* database molecules were directly docked to the receptor. Hits identified from docking process were further subjected to biological assays (Figure 6-3).

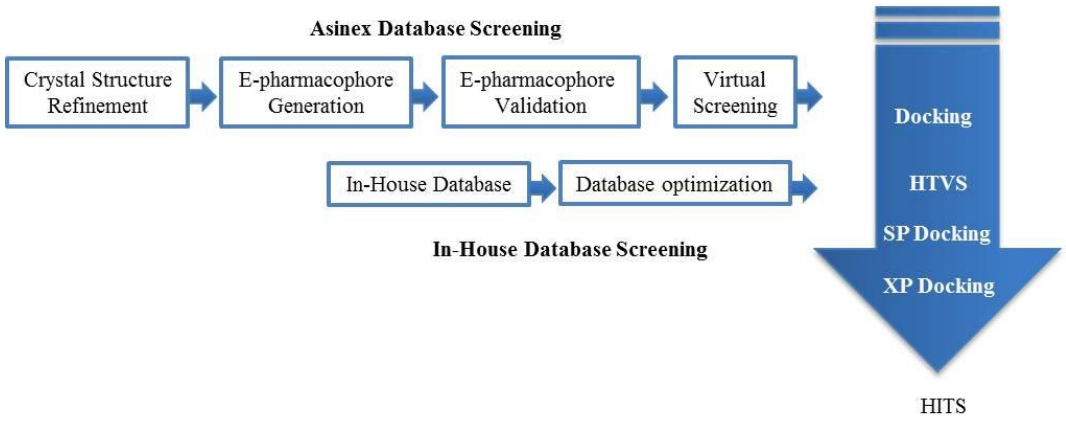

Figure 6-3. Flowchart of *in silico* screening process for PKCβ-II inhibitor design.

6.1.1 E-pharmacophore generation and validation

We intended to design novel PKCβ-II inhibitors while keeping the key interactions in focus. The x-ray crystal structure (PDB ID: 2I0E) was downloaded from the protein databank. Protein preparation was performed for the structure to correct missing hydrogen atoms and ambiguous protonation states as given in materials and methods section 4.2.

The bound ligand (Figure 6-2) was subjected to energy minimization by converging the heavy atoms to RMSD 0.30 Å using OPLS_2005 as force field, after removal of water molecules and subsequently the protein structure was refined.

Then we employed energy-based pharmacophore approach, which utilized both, ligand information as well as the protein information along with the favourable contacts with energetic information between the protein and the ligand into the pharmacophore model. The crystal ligand was re-docked onto the prepared protein to generate e-pharmacophore. The binding and docked poses were superimposed and RMSD was found to be less than 1 Å (Figure 6-4).

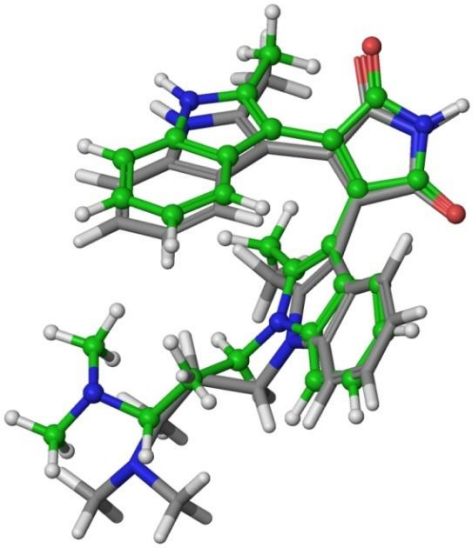

Figure 6-4. Comparison of binding pose and docked pose.

The bound conformation of crystal structure ligand is shown in stick model (C: grey, H, white, N, blue, O, red); whereas the docked conformation is shown superimposed to the bound conformation in ball and stick model (C: green, H, white, N, blue, O, red). The root mean square deviation (RMSD) between the two superimposed molecules was less than 1 Å.

The e-pharmacophore hypotheses was developed by mapping Glide XP energetic terms onto pharmacophore sites which were calculated based on the structural and energy information between the protein and the ligand. Finally, a six-featured pharmacophore was produced as output (Table 6-1 and Figure 6-5). The pharmacophoric sites were represented as six chemical features, two hydrogen bond acceptors (A), two hydrogen bond donors (D) and two aromatic rings (R).The distance geometry between these pharmacophoric features were calculated and presented in Table 6-2. It was found that the distances except A1-A2, A1-D3, A1-R11, A2-D3 and D4-R12 were beyond 5 Å.

Table 6-1. E-pharmacophore features.

S. No.	Feature	Score
1	D3	-2.04
2	A1	-0.66
3	A2	-0.54
4	D4	-0.54
5	R12	-1.04
6	R11	-0.88

The pharmacophoric sites represented as six chemical features *viz.* hydrogen bond acceptor (A), hydrogen bond donor (D) and aromatic ring (R). The feature scores are indicative of corresponding ligand-receptor interaction energy associated with that feature. Lesser (more negative) the feature energy score, more favoured the interaction.

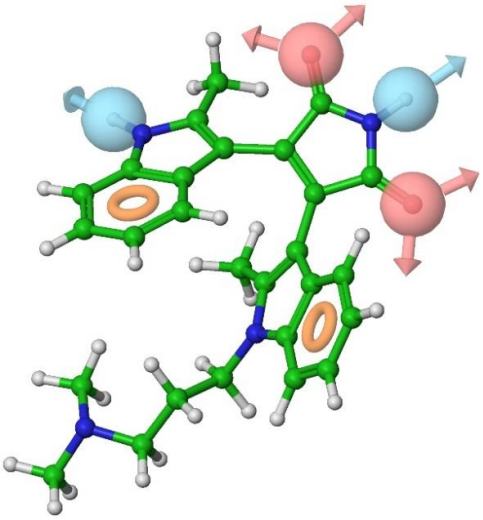

Figure 6-5. E-pharmacophore for PKCβ-II screening.

Here, the e-pharmacophore is shown as a collection of different pharmacophoric feature sets, overlapped to the docked pose of ligand. Pharmacophoric features have been depicted in different shapes and colours; pink sphere denote acceptor atom feature; cyan sphere, donor atom feature whereas orange donuts represent aromatic feature. Ligand atoms have been shown as ball and stick model with green coloured carbons, blue nitrogens, white hydrogens and red coloured oxygen atoms. The figure was generated in Maestro.

As a part of hypothesis validation, we generated all possible combinations of pharmacophoric features and further created 32 e-pharmacophore hypotheses of various feature sets (containing 6-3 feature sets). Overall $EF_{1\%}$, BEDROC, ROC, AUC and EF_{manual} were then used to measure the overall suitability of the e-pharmacophores (Table 6-3).

Table 6-2. Distance between e-pharmacophore features.

Site1	Site2	Distance
A1	A2	4.51
A1	D3	2.61
A1	D4	7.95
A1	R11	4.23
A1	R12	6.81
A2	D3	2.59
A2	D4	5.26
A2	R11	7.25
A2	R12	5.79
D3	D4	7.39
D3	R11	6.41
D3	R12	7.14
D4	R11	8.37
D4	R12	3.51
R11	R12	5.67

R: Aromatic ring, A: Acceptor, H: Hydrophobic, D: Donor.

The enrichment results for all e–pharmacophores were compared for the enrichment factor ($EF_{1\%}$), EF_{manual} and GH, based on recovery rate of actives against the ranked decoy database that consisted of 1014 compounds in which 14 were known inhibitors. Interestingly, only 10 out of 32 e-pharmacophores showed high enrichment ($EF_{1\%}$ > 40). We also considered

Table 6-3. E-pharmacophore enrichment for PKCβ-II inhibitor design.

Pharmacophores	EF1%	Ht	Ha	EF (Manual)	GH	% Yield	%A
1	14	7	2	20.41	0.25	28.57	14.29
2	7.2	17	2	8.40	0.12	11.76	14.29
3	14	12	2	11.90	0.16	16.67	14.29
4	22	11	3	19.48	0.26	27.27	21.43
5	7.2	18	1	3.97	0.06	5.56	7.14
6	14	19	3	11.28	0.17	15.79	21.43
7	51	47	7	10.64	0.23	14.89	50.00
8	7.2	55	4	5.19	0.12	7.27	28.57
9	7.2	47	3	4.56	0.10	6.38	21.43
10	7.2	54	3	3.97	0.09	5.56	21.43
11	7.2	35	3	6.12	0.11	8.57	21.43
12	7.2	41	3	5.23	0.10	7.32	21.43
13	7.2	50	3	4.29	0.09	6.00	21.43
14	7.2	48	3	4.46	0.10	6.25	21.43
15	22	55	4	5.19	0.12	7.27	28.57
16	51	73	7	6.85	0.18	9.59	50.00
17	7.2	46	2	3.11	0.07	4.35	14.29
18	65	74	9	8.69	0.24	12.16	64.29
19	51	92	7	5.43	0.17	7.61	50.00
20	51	89	9	7.22	0.22	10.11	64.29
21	7.2	63	2	2.27	0.06	3.17	14.29
22	51	103	7	4.85	0.16	6.80	50.00
23	7.2	90	2	1.59	0.05	2.22	14.29
24	7.2	75	3	2.86	0.08	4.00	21.43
25	22	78	4	3.66	0.10	5.13	28.57
26	22	100	4	2.86	0.09	4.00	28.57
27	43	147	8	3.89	0.16	5.44	57.14
28	65	138	11	5.69	0.22	7.97	78.57
29	51	194	10	3.68	0.18	5.15	71.43
30	58	161	8	3.55	0.15	4.97	57.14
31	22	100	4	2.86	0.09	4.00	28.57
32	65	115	9	5.59	0.20	7.83	64.29

$EF_{1\%}$, enrichment factor at 1% of the decoy dataset; EF(manual), manually calculated enrichment factor; GH, Goodness of hit, H_t, total number of compounds in the hit list; H_a, total number of actives in the hit list; Total number of actives in the decoy set (A=14); number of molecules in the decoy set (D=1000).

EF_{manual} and % of actives recovered (%A) for shortlisting. It was clear from Table 6-3 that e-pharmacophores 7, 16, 18-20, 27-30 and 32 exhibited high active recovery (%A) values indicating that these e-pharmacophores efficiently identified the actives amongst the decoys. Another potential e-pharmacophore no. 22 was not included because it identified less hits (relatively low Ht), also poor quality of actives (GH), and comparatively less active recovery values (%A). These selected ten e-pharmacophores (7, 16, 18-20, 27-30 and 32) were further subjected to virtual screening (Figure 6-6).

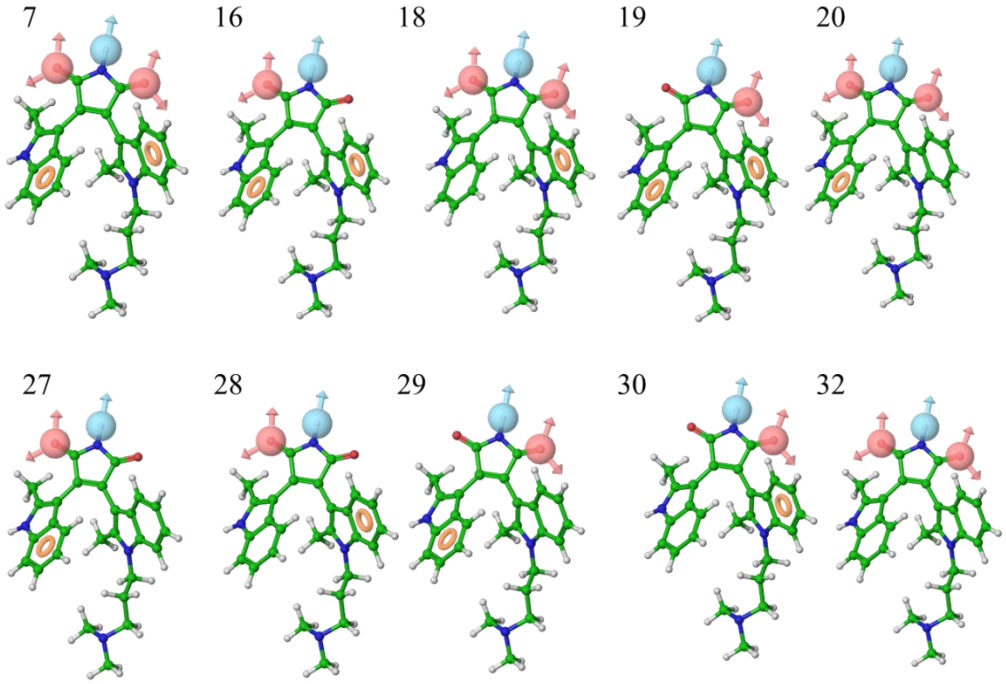

Figure 6-6. PKCβ-II E-pharmacophores selected for virtual screening.

6.1.2 E-pharmacophore based virtual screening

6.1.2.1 Virtual screening and docking of Asinex molecules

High-throughput virtual screening was performed with the commercial database (Asinex, www.asinex.com) which contained 525,807 compounds. The ten e-pharmacophores were subjected to individual database screening runs using Phase module of Schrodinger. The output of all 10 database screening runs was merged together as a single database and the compounds were sorted according to their fitness score. Compounds with fitness score <1.5 were excluded. Multiple occurrences of same molecules were identified and of these duplicates, one having maximum fitness score was retained.

Finally 105,272 molecules were subjected to docking using HTVS mode of Glide module. For consistent results, same receptor grid file was used as employed for e-pharmacophore generation. The output of HTVS docking was refined based on docking score and number of hydrogen bonds formed. Finally 20,381 molecules with docking score <-3 were selected for SP-docking. The output of SP docking was further refined (docking score <-5) and 235 molecules were selected for XP docking. Top 50 molecules with best docking score from XP output were selected for visual inspection. On visual inspection, ligand-receptor steric clashes were checked and interactions with key residues (Glu421, Thr404 and Val423) were selected. Based on docking score and visual inspection, we finally shortlisted 15 compounds and based on availability only 13 compounds were procured from Asinex for biological evaluation (see Table 6-4 and Figure 6-7). It could be observed that identified lead molecules revealed structural diversity as indicated by the presence of multiple ring systems. The bicyclic ring systems, thus presented a planar, rigid portion of the molecules which were mostly connected to another ring by a linker, thus providing flexibility to the structure.

The ADME properties of selected molecules were also calculated using QikProp module (Table 6-5). All compounds except **PA5**, **PA9**, **PA12** and **PA13** showed acceptable octanol-water partition coefficient (QPlogPo/w). All compounds showed good aqueous solubility (QPlogS). Six out of 13 compounds (**PA1**, **PA3**, **PA5**, **PA9**, **PA12** and **PA13**) were found to

Table 6-4. *In silico* parameters of Asinex hits.

Compound	Docking Score	Fitness	Interacting residues	H Bonds
PA1	-7.14	2.15	Glu390, Asp484, Val423	3
PA2	-7.42	1.84	Thr404, Val423, H20, Asp470	4
PA3	-7.6	2.4	Glu421, Thr404, h20, Asp470	4
PA4	-7.69	1.61	Val423, Asp470, Asp470	3
PA5	-9.2	1.51	Val423, H20, Thr404, Asn471, Asp470, H20	6
PA6	-7.02	1.71	Glu421, Val423	2
PA7	-6.77	1.6	Asp470, H20, Glu421, Val423	4
PA8	-7.79	1.63	H20, Val423, H20, Asp470, Asn471	5
PA9	-7.73	1.55	Glu421, H20, Val423, Asp470, Asp470	5
PA10	-7.7	1.63	Val423, H20, Asn471, Asp470	4
PA11	-7.31	1.54	Glu421, Thr404, Asp484	3
PA12	-7.01	1.53	Asp484, Glu421, Val423, H20	4
PA13	-6.73	1.81	H20, Thr404, Glu421, Val423	4
PDS	-7.44	2.70	Thr404, H2058, Val423, Glu421	4

Table depicts important *in silico* parameters of the identified hits. Fitness score ranges between 0 to 3, 0 being no match between ligand and pharmacophore whereas 3 means 100% match. PDS: bisindolylmaleimide inhibitor bound to the crystal structure (PDB ID:2I0E).

be cardiotoxic as their predicted HERG blockage IC_{50} were >-5. All compounds except **PA9** and **PA13** showed good gut permeability as indicated by their high QPPCaco values (<25), however, compounds **PA3**, **PA6** and **PA9** exhibited low predicted MDCK cell permeability which mimicked blood-brain barrier. All compounds showed good blood/brain partition coefficient (QPlogBB) and skin permeability (QPlogKp). Interestingly, all compounds showed high %oral absorption and none of them violated Lipinski's rule of five (Table 6-5). Overall, all identified compounds showed acceptable predicted ADME properties, thus rendering them a possible drug candidate.

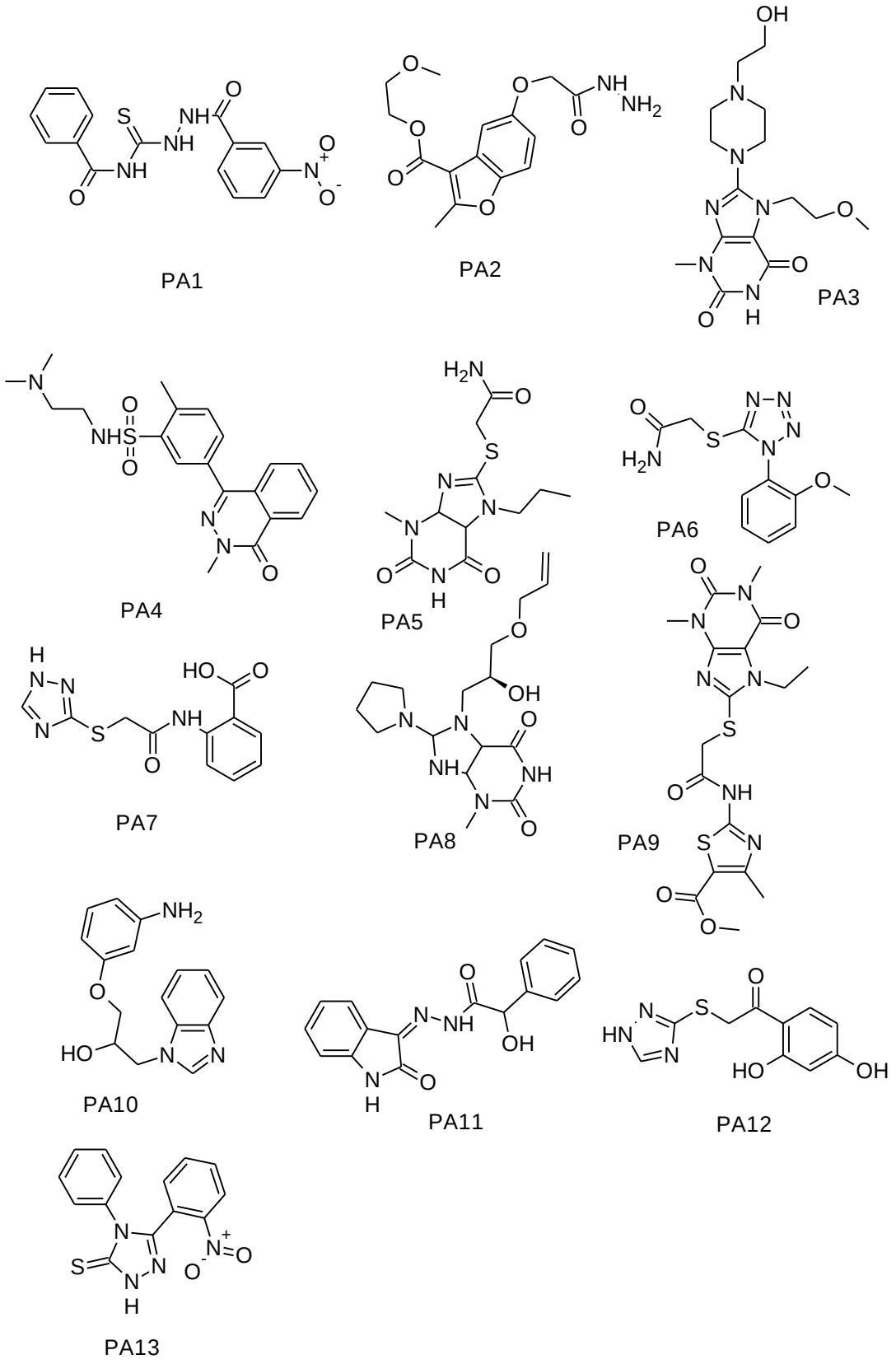

Figure 6-7. Hits identified from Asinex screening.

Table 6-5. ADME properties of selected hits identified from Asinex dataset.

Compound	QPlogPo/w	QPlogS	QPlogHERG	QPPCaco	QPlogBB	QPPMDCK	QPlogKp	% Human Oral Absorption	Rule of Five Violations
PA1	1.29	-2.79	-4.05	137.21	-1.11	152.06	-3.26	72.80	0
PA2	1.32	-3.57	-5.83	301.66	-1.62	135.45	-3.03	79.09	0
PA3	0.88	-2.94	-4.90	52.62	-1.90	20.51	-4.64	62.93	0
PA4	2.20	-3.02	-5.33	457.91	-1.12	212.66	-2.29	87.46	0
PA5	-0.38	-1.60	-2.09	57.69	-1.47	59.89	-4.94	56.19	0
PA6	3.03	-4.67	-4.68	50.12	-2.03	19.46	-4.64	75.15	0
PA7	4.05	-6.12	-6.06	494.60	-1.24	231.14	-2.56	100	0
PA8	3.33	-5.41	-6.38	131.27	-1.86	81.23	-3.33	84.38	0
PA9	0.01	-3.36	-3.76	19.40	-2.05	6.97	-6.00	50.05	0
PA10	2.31	-3.75	-6.65	100.93	-0.93	45.89	-4.88	76.38	0
PA11	2.28	-4.04	-6.04	131.61	-1.66	55.26	-3.41	78.24	0
PA12	0.60	-2.03	-4.26	111.52	-1.46	76.98	-4.14	67.10	0
PA13	-1.53	-0.46	-2.18	22.01	-1.79	26.53	-5.56	41.97	0

QPlogPo/w: Predicted octanol and water partition coefficient (acceptable range -2.0 - 6.0); Qplogs: Predicted aqueous solubility (acceptable range -6.5 - 0.5); QplogHERG: Predicted IC_{50} value for blockage of HERG k+ channels (acceptable range: below -5); QPPcaco: Predicted caco cell-2 permeability (<25 is poor and >500 high); QPlogBB: Predicted brain/blood partition coefficient (acceptable range -3.0 - 1.2); QPPMDCK: Predicted apparent MDCK cell permeability (<25 is poor and >500 is high); QPlogkP: Predicted skin permeability (acceptable range -8.0 to -1.0); % Human oral absorption (<25% is poor and >80% is high); Rule of 5: Number of violations of Lipinski's rule of 5 (mol_MW < 500, QPlogPo/w < 5, donorHB≤5, accptHB≤10) acceptable maximum 1.

6.1.2.2 Virtual screening and docking of *in house* database molecules

Additionally, we also subjected our *in house* database (BITS-DB) to the virtual screening process. The logic behind screening BITS-DB was that any identified hits were readily available in appropriate quantity for further screening. Doing so was advantageous over procured compounds, both in terms of quantity and timely availability of hits. The BITS-DB was a central repository of structurally diverse 3000 compounds, synthesized *in house* [222]. The database contained energy-optimized 3D structures ionized at pH 7. As the number of compounds were very few compared to commercial database, the BITS-DB molecules were directly docked to the PKCβ-II receptor, with a similar grid file as utilized earlier to generate e-pharmacophore. Docking process was essentially similar to that employed during e-pharmacophore based virtual screening, which incorporated three modes of docking program, HTVS, SP and XP docking, respectively. After XP docking, 15 molecules were selected based on their availability, docking score and visual inspection (Table 6-6 and Figure 6-8).

The ADME properties of selected molecules were also calculated using QikProp module. It was evident from Table 6-7 that apart from octanol/water partition coefficient, all compounds exhibited desirable aqueous solubility, Caco cell permeability and MDCK cell permeability. All compounds except **PB1**, **PB3** and **PB14** exhibited no cardiotoxicity as indicated by their predicted QPlogHERG values.

Table 6-6. *In silico* parameters of BITS-DB hits.

Compound	Docking Score	Interacting residues	H Bonds
PB1	-6.29	Thr404, Val423,H2058	3
PB2	-6.12	Val423, H2058	2
PB3	-5.99	Val423, H2058	2
PB4	-5.59	Val423, H2058, Thr404	3
PB5	-5.39	H2058, Val423	2
PB6	-5.98	Glu421, Val423, Asp470, Asp470	4
PB7	-4.95	Asp484, Asn471, Asn471, Glu421, Glu421, Val423	6
PB8	-3.59	Val423	1
PB9	-3.34	H2056, Val423	2
PB10	-2.79	Val423	1
PB11	-2.27	Asn471, H2056	2
PB12	-5.85	Asn471	1
PB13	-5.84	Asn471, H2056	2
PB14	-5.48	Asn471 H2056	2
PB15	-5.44	Asn471	1
PDS	-7.44	Thr404, H2058, Val423, Glu421	4

Table depicts important *in silico* parameters of the identified hits. PDS: bisindolylmaleimide inhibitor bound to the crystal structure (PDB ID:2I0E).

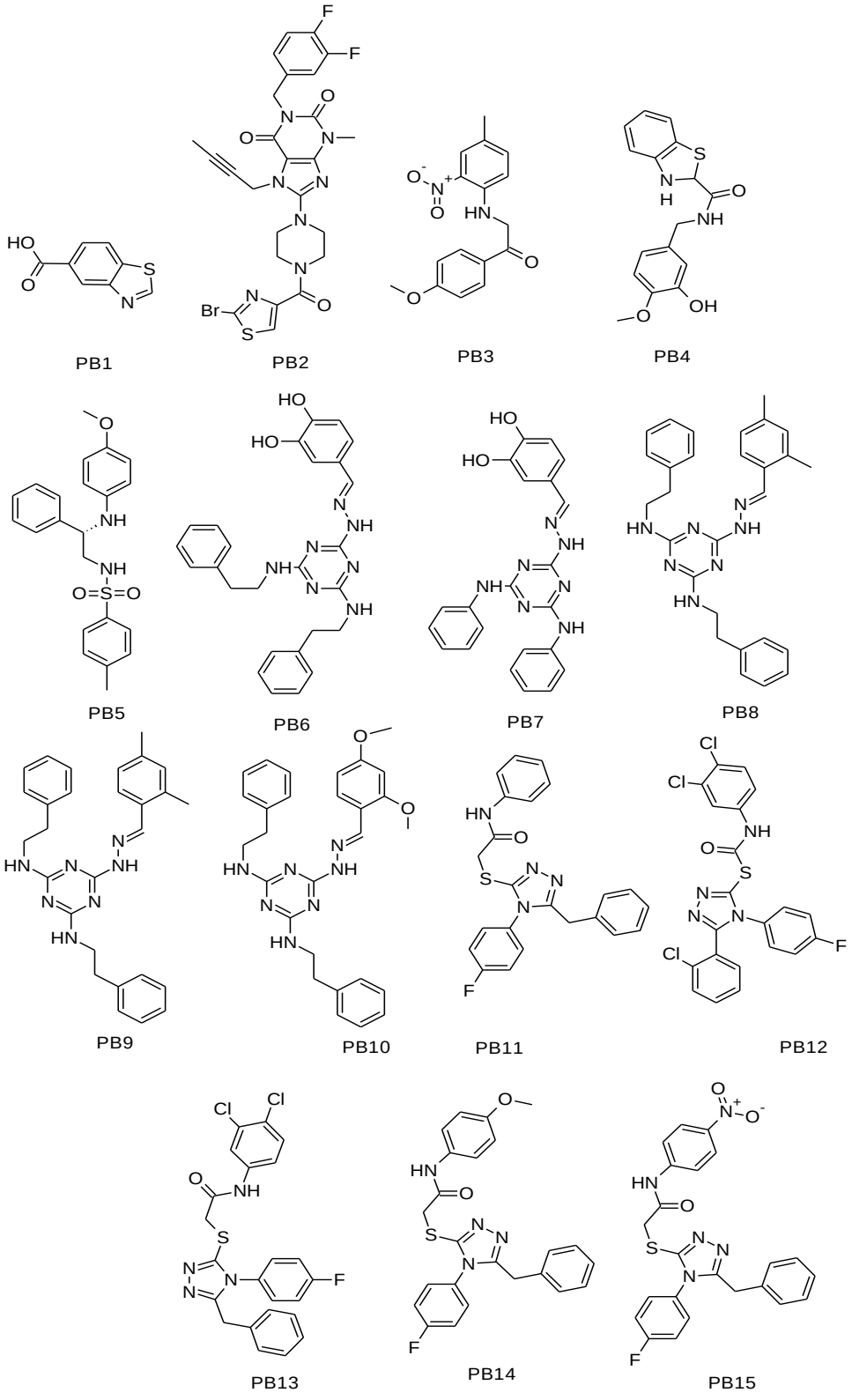

Figure 6-8. Compounds identified from BITS-DB screening.

Table 6-7. ADME properties of selected hits identified from *in house* dataset.

Compound	QPlogPo/w	QPlogS	QPlogHERG	QPPCaco	QPlogBB	QPPMDCK	QPlogKp	% Human Oral Absorption	Rule of Five Violations
PB1	1.40	-1.80	-1.90	139.73	-0.41	146.11	-3.24	73.58	0
PB2	5.19	-7.74	-6.44	1016.62	-0.41	8287.61	-2.27	85.27	2
PB3	2.76	-3.48	-4.69	840.53	-0.80	410.01	-2.28	95.44	0
PB4	2.85	-4.3	-5.92	1063.42	-0.64	905.68	-1.82	100	0
PB5	4.11	-7.05	-7.94	1053.86	-1.14	530.31	-0.93	100	0
PB6	4.33	-6.55	-8.44	170.42	-2.57	73.06	-1.67	92.28	0
PB7	2.95	-5.34	-8.28	200.79	-2.14	87.24	-1.82	85.46	0
PB8	6.43	-8.50	-8.69	1531.68	-1.26	784.32	-0.01	100	1
PB9	5.26	-7.45	-6.37	2447.45	-0.44	4130.42	-1.28	100	1
PB10	5.70	-6.61	-7.75	1667.73	-1.21	859.88	0.08	100	1
PB11	5.65	-7.00	-7.11	1238.56	-0.63	1453.79	-0.99	100	1
PB12	6.84	-9.30	-7.25	1315.19	-0.11	10000	-1.41	96.95	2
PB13	6.62	-8.49	-7.04	1269.04	-0.34	7803.32	-1.25	100	1
PB14	3.39	-4.62	-4.89	118.02	-1.41	156.48	-3.65	83.88	0
PB15	5.77	-7.34	-7.12	1268.68	-0.71	1520.60	-1.05	100	1

QPlogPo/w: Predicted octanol and water coefficient (acceptable range -2.0 - 6.0); QplogS: Predicted aqueous solubility (acceptable range -6.5 - 0.5); QplogHERG: Predicted IC_{50} value for blockage of HERG k+ channels (acceptable range: below -5); QPPcaco: Predicted caco cell-2 permeability (<25 is poor and >500 high); QPlogBB: Predicted brain/blood partition coefficient (acceptable range -3.0 - 1.2); QPPMDCK: Predicted apparent MDCK cell permeability (<25 is poor and >500 is high); QPlogKp: Predicted skin permeability (acceptable range -8.0 to -1.0); % Human oral absorption (<25% is poor and >80% is high); Rule of 5: Number of violations of Lipinski's rule of 5 (mol_MW < 500, QPlogPo/w < 5, donorHB≤5, accptHB≤10) acceptable maximum 1.

Out of 15 compounds, only six compounds (**PB5**-**PB8**, **PB10** and **PB14**) exhibited desirable blood brain partition coefficient as evident from their QPlogBB values. All compounds except **PB10** exhibited good skin permeability (QPlogKp). Compounds **PB1**, **PB3**, **PB4**, **PB7** and **PB14** showed high %human oral absorption. Two of the 15 compounds (**PB2** and **PB12**) violated two out of five Lipinski's rule. Compounds **PB6-8**, **PB10** and **PB14** showed acceptable brain/blood partition coefficient. Also, all compounds except **PB5**, **PB10** and **PB11** exhibited good skin permeability. Overall, all identified compounds showed acceptable predicted ADME properties.

6.2 PKCβ-II inhibition assay

Based on docking score, visual inspection and availability, we finally shortlisted total 28 compounds (Asinex, 13 and BITS-DB, 15 molecules) and subjected to biological screening. PKCβ-II inhibition assay was performed using ADP-Glo reagent. In this test, the kinase first acted on the substrate, which was then terminated and resulting ATP was removed. The remaining ADP was then converted to ATP, which was measured *via* luciferase reaction. The resulting light corresponded to the amount of kinase or ATPase activity. For preliminary screening, only compounds showing >50% inhibition at 25 µM concentration were considered. Among the Asinex compounds, only three out of 13 compounds showed more than 50% inhibition (compounds **PA2**, **PA8** and **PA10**). Based on their inhibition property at 25 µM, we determined the IC_{50} values of these three compounds only (Table 6-8). Compound **PA10** exhibited best potency (IC_{50}=2.814 µM). The activity of these three compounds could be correlated with their relatively better docking scores (<-7.5) than other molecules in the series (Table 6-4).

Table 6-8. IC_{50} of PKCβ-II inhibitors.

Compound	IC_{50} (µM)
PA2	12.28±0.57
PA8	9.69±0.24
PA10	2.81±0.81
PB6	5.82±0.09
PB9	12.72±0.91

Each value represents mean±SEM of three observations.

Potency of **PA10** could also be explained in terms of the number of interactions (4 hydrogen bonds and one π- π interaction with Phe353; Figure 6-9). Also, the docked pose of **PA10** almost filled the entire active site pocket (Figure 6-10) with its hydrophobic rings facing hydrophobic receptor surface, thus favouring the activity. Only two compounds from BITS-DB (**PB6** and **PB9**) showed >50% PKCβ-II inhibition at 25 µM, hence were subjected for IC_{50} determination. **PB6** exhibited better activity (IC_{50}= 12.72 µM).

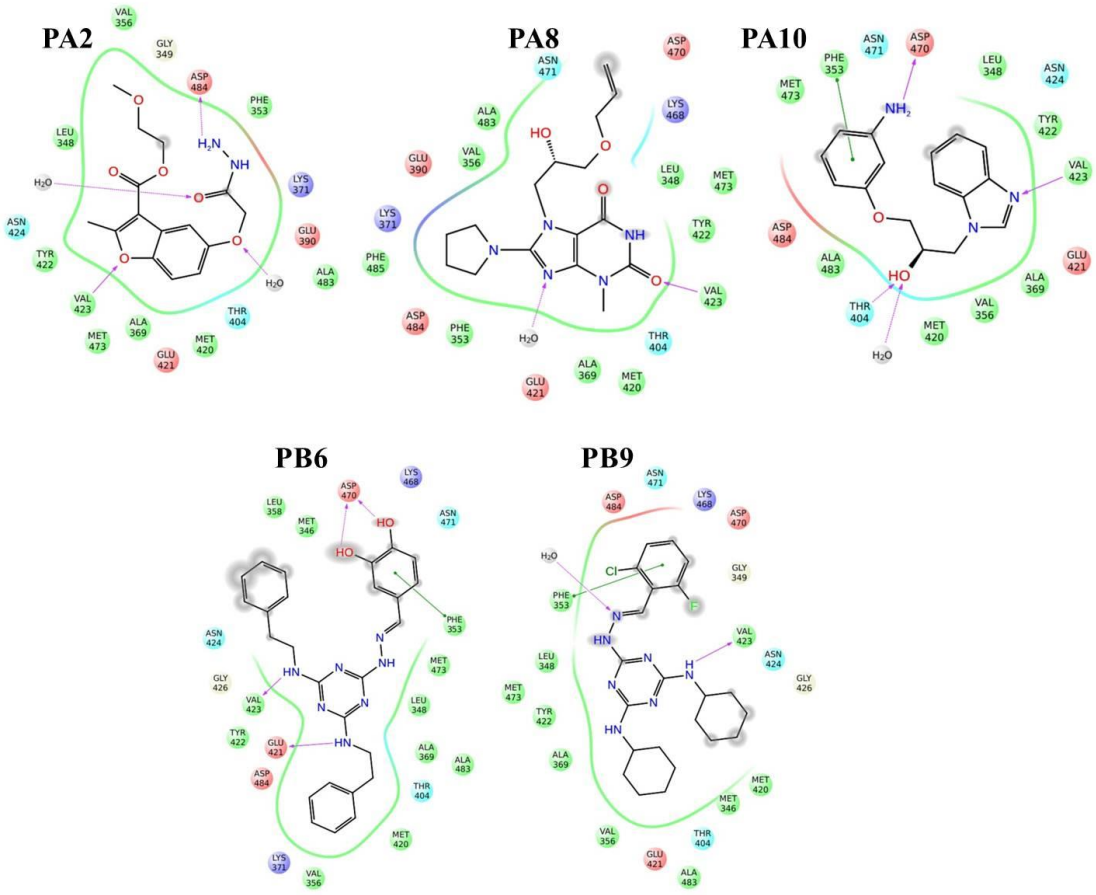

Figure 6-9. Ligand interaction diagram of identified PKCβ-II inhibitors.

Binding pocket characteristics are displayed using color-coded spheres indicating surrounding amino acids, whereas protein-ligand interactions are represented as lines: hydrogen bonds as purple arrows, and π-π stacking interactions as green lines. Colour coding of amino acids spheres: light-orange, negatively charhed; purple, positively charged; cyan, polar; green, hydrophobic; yellow, glycine. Grayed out areas represent solvent exposure. These images were generated using Ligand interaction diagram module of Schrodinger.

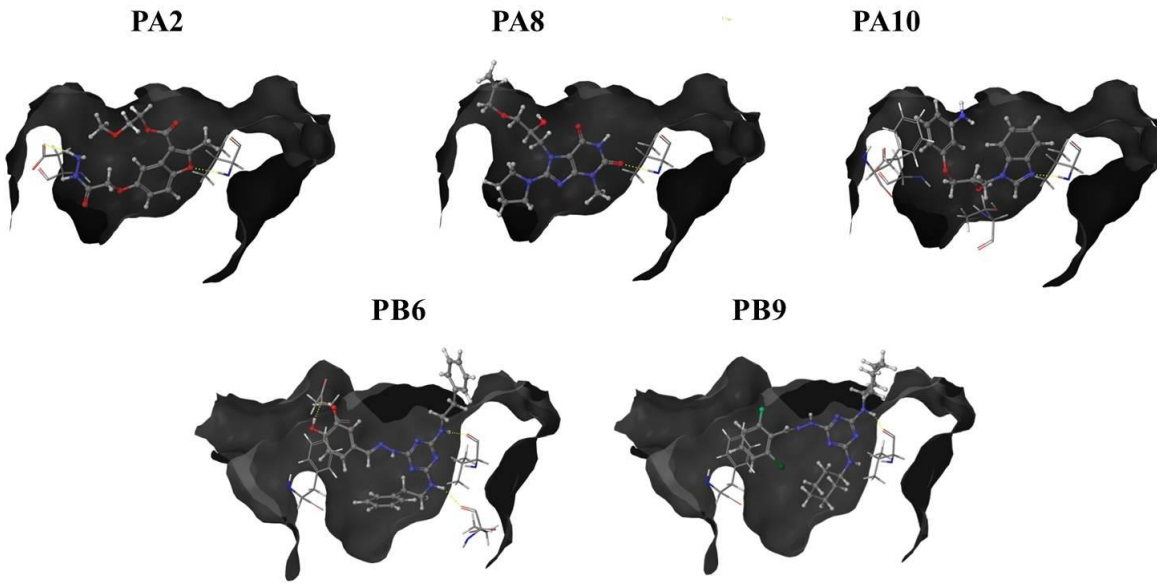

Figure 6-10. Binding pose of Asinex hits.

The receptor surface is shown as van der Walls surface and is coloured grey. Docked poses of inhibitors are shown as ball and stick model and interacting residues are shown as wireframe model. Elements are colour coded as: carbon, grey; hydrogen, white; nitrogen, blue; oxygen, red; sulphur, yellow and halogens (chlorine and fluorine) as green.

6.3 Cell based assays

MeHg is a well-known neurotoxin and was implicated in various neurological diseases. It has been already reported that MeHg in cerebral granule neurons increased the level of inositol 1,4,5-triphosphate (IP3), which was known to induce formation of DAG which, in turn stimulated PKC. Thus, it was evident that MeHg increased protein phosphorylation in neurons [223]. It has also been believed that MeHg exposure up-regulated the expression of ROCK pathway, causing axonal degeneration and apoptosis of cultured cortical neuronal cells. Since it has been known that PKC was required for activation of ROCK, it could be postulated that PKC down-regulation by PKCβ-II inhibitors in MeHg treated cultures would protect the cell against MeHg induced neurotoxicity. Thus, in this study, we utilized IMR-32 (neuroblastoma) cells treated with MeHg as a model to evaluate novel PKCβ-II inhibitors. We also tested cytotoxicity parameters of these compounds and their ability to inhibit ROS. Table 6-9 presents these results for hits identified from Asinex and *in house* BITS-DB databases respectively.

Since IMR-32 cells mimicked a large number of CNS projections under certain tissue culture conditions, the neurite growth of IMR-32 cells in specific culture could be linked to the

Table 6-9. Cell-based assay results of PKCβ-II inhibitors.

Compound	% Cytotoxicity (100 µM)[a]	GI_{50} (µM)[b]
PA2	0.01±0.00	>100
PA8	23.34±3.23	0.63±0.30
PA10	13.32±2.56	0.75±0.21
PB6	12.56±2.09	0.09±0.01
PB9	13.41±1.89	0.12±0.02

[a]Studies were conducted using HEK-293 cell lines. [b]Studies were conducted using IMR-32cell lines.

properties of culture ingredients and drugs. These cells were first treated with MeHg, followed by the drug, in order to evaluate PKCβ-II inhibitor's neuroprotective activity. In addition, the compounds were analyzed in cell based assays to determine their cytotoxicity. Test drug concentration inhibiting cell-growth by 50% was termed as GI_{50} which indicated that all test compounds were able to inhibit IMR-32 cell growth.

6.3.1 Cell cytotoxicity studies

In cell cytotoxicity assay, all the three Asinex compounds (**PA2**, **PA8** and **PA10**) exhibited low percent inhibition values which indicated no cytotoxicity at sub-micromolar concentrations. On the other hand, compounds **PB6** and **PB9** from BITS-DB also showed lesser cytotoxicity at 100 µM.

6.3.1.1 Growth inhibition assay

Among Asinex molecules, most active compound **PA10** (PKCβ-II IC_{50}=2.81 µM) exhibited lowest GI_{50} value (ROS inhibition IC_{50}=0.75±0.21 µM). Thus PKCβ-II inhibition leading to neuronal growth inhibition further supplemented our hypothesis. The two compounds from *in house* dataset (**PB6** and **PB9**) also exhibited sub-micromolar GI_{50} values. Hence it could be postulated that PKCβ-II inhibition resulted in lower GI_{50} values. Compound **PA2** exhibited high GI_{50} value (>100 µM) indicating that it could not inhibit the effect of the neurotoxin.

Overall, all compounds except **PA2** exhibited promising activity in inhibiting MeHg induced neurotoxicity of IMR-32 cells resulting from overexpression of PKCβ-II. In the cytotoxicity assay, all compounds exhibited no or negligible cytotoxicity at 100 µM. Together, this data indicated the utility of identified leads for further development as potent PKCβ-II inhibitors. Compound **PB6** and **PB9** emerged as promising leads with IC_{50}<15 µM.

6.4 Neuropharmacological interventions

Having known their efficacy in cell based assays, we further decided to study the effect of novel PKCβ-II inhibitors using *in vivo* models. Thus, we screened the molecules in models of

diabetes induced neuropathy and MeHg induced neurodegeneration. Depending on compounds availability in sufficient quantities, we selected two compounds (**PB6** and **PB9**) for *in vivo* screening.

6.4.1 Neurotoxicity assessment

Before testing the compounds on disease-specific models, it was important to perform neurotoxicity assessment. Hence, in the present study, neurotoxicity was assessed using two animal models, *viz* rotarod and actophotometer based screening. Compounds were administered at three dose levels. Minimal motor impairment was measured by rotarod test and neurotoxicity was indicated by the inability of the animal to maintain balance on the rotating rod for at least 1 min.

In the acute neurotoxicity assays (rotarod and actophotometer), none of the compounds exhibited motor deficit at the highest dose tested (300 mg/kg) up to 2 h post administration (see Table 6-10). Since the compounds did not exhibit any motor deficit in both the tests, thus lower doses (100 mg/kg and 30 mg/kg) would be non-neurotoxic. Thus, we decided to proceed with a lower dose (30 mg/kg) for further experiments.

Table 6-10. Neurotoxicity of PKCβ-II inhibitors.

Treatment	Neurotoxicity			
	Rotarod		Actophotometer	
	1 h	2 h	1 h	2 h
Vehicle	-	-	-	-
PB6	-	-	-	-
PB9	-	-	-	-

Doses of 300, 100 and 30 mg/kg were administered. The figures in the table indicate the minimum dose whereby bioactivity was demonstrated in half or more of the mice. The line (-) indicates an absence of neurotoxicity at the tested dose.

6.4.2 Diabetic painful neuropathy

In the next phase of screening, a rat model of STZ-induced painful diabetic neuropathy was employed essentially as described in materials and method section 4.19.4. These models included STZ-induced painful diabetic neuropathy and CCI model for neuropathy in rats. Thus, we decided to investigate the effect of our compounds against diabetic neuropathy.

Several animal models of diabetes have been established to study the pathophysiology of diabetic painful neuropathy. Most commonly used model for diabetic neuropathy was STZ-induced diabetes in which, rats developed hyperalgesia at approximately 2-3 weeks post diabetes-induction.

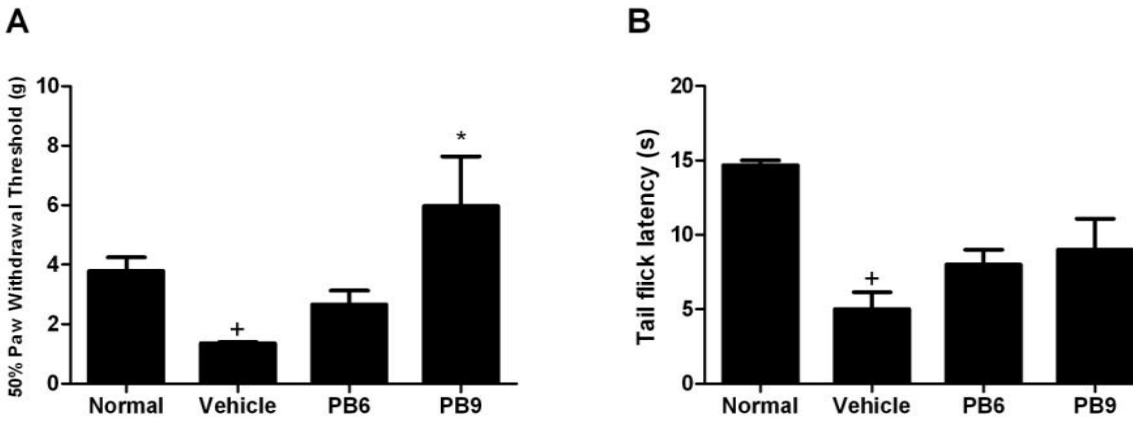

Figure 6-11. Effect of PKCβ-II inhibitors on mechanical allodynia and cold water tail flick test.

(A) Mechanical allodynia, (B) Cold water tail flick test. Compounds were tested at 30 mg/kg dose given through intraperitonial route. Normal rats=non diabetic rats. Each value represents mean±SEM of six rats. Star indicates significant difference (*, p <.05; **, p <.01; ***, p <.001, two-tailed unpaired Student's t-test). 30% v/v PEG 400 was used as a vehicle. Compounds were administered by intraperitoneal route at a dose of 30 mg/kg. + denotes significant difference of vehicle treated group activity when compared to normal group ($p < 0.05$).

Diabetes was induced in rats by a single *i.p.* injection of STZ (30 mg/kg, dissolved in Citrate buffer pH 4.5). Animals with a non-fasting glucose level above 200 mg/dL were considered diabetic and were used for experiments. Nociceptive behavioral assessment was undertaken on 21st day post-diabetes induction as reported earlier [176]. The two PKCβ-II inhibitors (**PB6** and **PB9**) were studied at 30 mg/kg dose level. The animals were subjected to mechanical allodynia, hot plate test and cold water tail immersion tests. The effect of these compounds on tail NCV was also determined by measuring NCV. Prior to the experiment, the latencies were measured and compared with STZ-induced diabetic rats and normal rats (non-diabetic).

6.4.2.1 Mechanical allodynia

The 50% paw withdrawal threshold to mechanical stimuli was measured using von-Frey fibers. A series of von-Frey fibers were applied to the hind paw surface. A brisk paw withdrawal or flinching was considered as positive response. In diabetes induced-mechanical allodynia assay, only compound **PB9** showed significant increase ($p \leq 0.01$) in 50% paw

withdrawal threshold, 1 h post-dosing at 30 mg/kg (Figure 6-11A). Compound **PB9** was not only active, but it also elevated 50% PWT beyond those of normal non-diabetic animals. Compounds **PB6** was found inactive in this test.

6.4.2.2 Cold water tail flick latency

Cold water tail flick method was used to assess the effect of PKCβ-II inhibitors on the cold nociceptive threshold. Briefly, the animal was restrained and the lower 3/4th of the tail was immersed in a beaker containing ice-cold water maintained at 7±2 ºC, and the latency of tail withdrawal was noted. None of the compounds tested were found significant in tail flick latency (Figure 6-11B).

6.4.2.3 Efficacy of compounds on nerve conduction velocity

As described in previous sections, it had been well established that diabetic patients also exhibited slow nerve conduction velocity because of demyelination and loss of large myelinated fibres, and decreased nerve action potentials owing to loss of axons. Since PKCβ-II inhibitors could regulate neuronal extension and cell growth, we studied the effect of these compounds on nerve conduction velocity. Apparently, the nerve conduction velocity was significantly decreased by three weeks in diabetic rats, when compared to normal control rats. Only compound **PB9** showed significant improvement in nerve conduction velocity 1 h post treatment ($p>0.05$) and reversed it to the level of non-diabetic rats at 30 mg/kg dose (Figure 6-12A). This proved that these compounds could be useful in attenuating the effects of diabetes.

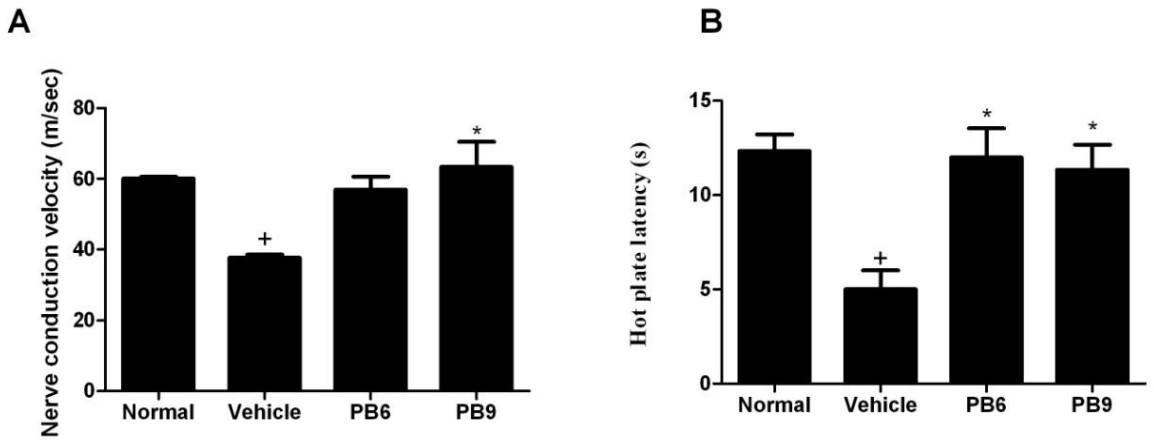

Figure 6-12. Effect of PKCβ-II inhibitors on nerve conduction velocity (NCV) and hot plate latency.

(A) Nerve conduction velocity, (B). Hot plate test Compounds were tested at 30 mg/kg dose given through intraperitonial route. Normal rats=non diabetic rats. 30% v/v PEG 400 was used as a vehicle. Compounds were administered by intraperitoneal route at a dose of 30 mg/kg. Each value represents mean±SEM of six rats. Star indicates significant difference (*, p <.05; **, p <.01; ***, p <.001, two-tailed unpaired Student's t-test). + denotes significant difference of vehicle treated group activity when compared to normal group ($p < 0.05$).

6.4.2.4 Efficacy of compounds in hot plate test

Hot plate test was performed to study the effect of these compounds on thermal hyperalgesia. Briefly, animals were kept on a heated plate maintained at 50±2 ºC and the latency to show pain response (licking of the paw, jumping) was noted. Thugh the compounds showed potency in the hot plate test, only **PB9** was found to be significantly active (Figure 6-12B).

6.4.3 Chronic constriction injury model

Based on the encouraging results on PKCβ-II inhibitors in attenuating diabetic neuropathy, we were curious to assess their potential generally on neuropathic pain, hence we also employed CCI model to evaluate anti-neuralgic efficacy of the compounds. Gabapentin was used as standard drug for comparison.

6.4.3.1 Mechanical allodynia

The 50% paw withdrawal threshold to mechanical stimuli was measured using von-Frey fibers. A series of von-Frey fibers were applied to the paw surface of the affected paw. A brisk paw withdrawal or flinching was considered as positive response. Both the compounds were found to be inactive against mechanical allodynia (Table 6-11). Gabapentin was administered at a dose of 30 mg/kg dose, which exhibited significant activity.

Table 6-11. Mechanical allodynia in CCI animals.

Compound	Mechanical allodynia 50% PWT (g) 1 h
Vehicle	2.23±0.27
PB6	2.12±0.13
PB9	2.13±0.70
Gabapentin	5.48±1.27*

Gabapentin was used as a standard drug. 30% v/v PEG 400 was used as a vehicle. Compounds were administered by intraperitoneal route at a dose of 30 mg/kg. Each value represents 50% paw withdrawal threshold (g) (mean±SEM) of six rats. * represent the values, significantly different from control at $p < 0.05$ (One-way ANOVA, followed by post-hoc Dunnet test).

6.4.3.2 Cold allodynia

We also evaluated the efficacy of these compounds against cold allodynia. A small quantity of acetone was sprayed on the effected paw of the animal and the duration of pain response was observed. None of the two compounds showed >50% reversal in pain response at any time point (Table 6-12). Gabapentin showed moderate activity at 1 h-2 h.

Table 6-12. Cold allodynia in CCI animals.

Compound	Cold Allodynia		
	% Reversal		
	0.5 h	1 h	2 h
Vehicle	5.50±0.61	3.74±2.89	5.09±1.75
PB6	23.51±8.93	43.56±2.45	31.67±6.67
PB9	45.12±7.02	43.11±1.03	32.58±13.87
Gabapentin	33.80±4.15	52.32±4.55	66.90±2.07

Gabapentin was used as a standard drug. 30% v/v PEG 400 was used as a vehicle. Compounds were administered by intraperitoneal route at a dose of 30 mg/kg. Each value represents % reversal of cold allodynia (mean±SEM) of six rats.

6.4.3.3 Mechanical hyperalgesia

Mechanical hyperalgesia was measured by applying an incremental mechanical force to rat hind paw. Pressure was noted when animal showed the first withdrawal movement. None of the test compounds showed efficacy (>50% reversal), as depicted in Table 6-13. The standard compound gabapentin showed efficacy at all-time points.

Table 6-13. Mechanical hyperalgesia in CCI animals.

Compound	Mechanical Hyperalgesia		
	% Reversal		
	0.5 h	1 h	2 h
Vehicle	5.55±1.55	15.87±0.79	15.80±0.20
PB6	1.19±0.45	2.03±0.80	2.81±0.93
PB9	1.91±0.95	1.54±0.78	2.95±1.01
Gabapentin	88.59±6.56	92.28±6.35	92.28±2.68

Gabapentin was used as a standard drug. 30% v/v PEG 400 was used as a vehicle. Compounds were administered by intraperitoneal route at a dose of 30 mg/kg. Each value represents % reversal of mechanical hyperalgesia (mean±SEM) of six rats.

6.4.3.4 Structure-activity relationship on PKCβ-II inhibitors

At a dose of 30 mg/kg, both the compounds (**PB6** and **PB9**) were effective in attenuating various diabetic implications. **PB9** (diphenethyl-1,3,5-triazine-2,4-diamine) was more effective than **PB6** (4,6-bis(phenethylamino)-1,3,5-triazin). In mechanical allodynia, only **PB9** (diphenethyl-1,3,5-triazine-2,4-diamine) effectively increased the 50% paw withdrawal threshold. Both the compounds (**PB6** and **PB9)** significantly elevated the nerve conduction velocity to normal level. On the other hand, none of the compounds exhibited significant activity in hot plate model.

Overall, it appeared that the compounds tested in *in vivo* belonged to 1,3,5-triazine-2,4,6-triamine core, with substituted cyclohexyl or phenyl groups. If we analyzed the ligand interaction diagram of the docked pose of these compounds, we could clearly understand that **PB6** and **PB10** exhibited good interactions. Interestingly, **PB6** showed hydrogen bonds with Glu421 and Val423, whereas **PB9** formed only one hydrogen bond with key residue (Val423). The conformation of **PB9** projected the two hydrophobic dicyclohexyl rings in the hydrophobic pocket, thus favouring hydrophobic interactions. Also, the π-π stacking interaction between Phe353 and the tail region also contributed towards the activity of **PB9**. Also, amongst the two active compounds, **PB9** exhibited least solvent exposure, which yielded lesser conformational changes in the ligand due to solvent molecules, leading to greater binding stability.

6.4.4 MeHg induced memory and cognition evaluation

To study the neuroprotective effect of these compounds, we performed a battery of tests using MeHg-induced neurodegeneration model in mice. Compound **PB9** was selected for further screening as it was effective in DPN model. Neurodegeneration was induced in mice by oral administration of MeHg. Mice were divided into three groups (n=6); *viz* naïve, control, and treatment groups. Naive group received only water, whereas control and treatment (**PB9** treated) groups received MeHg dissolved in regular drinking water. Treatment group received MeHg in drinking water for initial 14 days for induction of neurodegeneration, after which they received only water, along with daily doses of **PB9** (30 mg/kg in PEG- 300, 30% v/v; *i.p.*). The mice were housed in plastic cages and were given free access to food and respective water for 28 days. Daily water consumption did not differ between groups. Daily consumption of MeHg solution was found to be 5.5 ml/animal on an average. Based on water consumption, daily doses of MeHg was found to be 2.77 mg/kg respectively. We avoided higher dose of MeHg (>5 mg/kg) because of its fast-onset neurotoxicity, that could lead to mortality [180]. Different tests were conducted once a week on different days and were assigned as weekly results (week 0-3). In general, over a period of two weeks; MeHg-exposed groups developed heterogeneous motor impairment with a large variability between individuals with respect to the beginning and severity of motor impairment signs. All the observations were made at the end of 3rd week.

6.4.4.1 Hind limb clasping test

Hind limb clasping behaviour was observed on the 21st day of treatment for each group and is shown in Figure 6-13. Naive group (normal mice) exhibited no hind limb clasping whereas

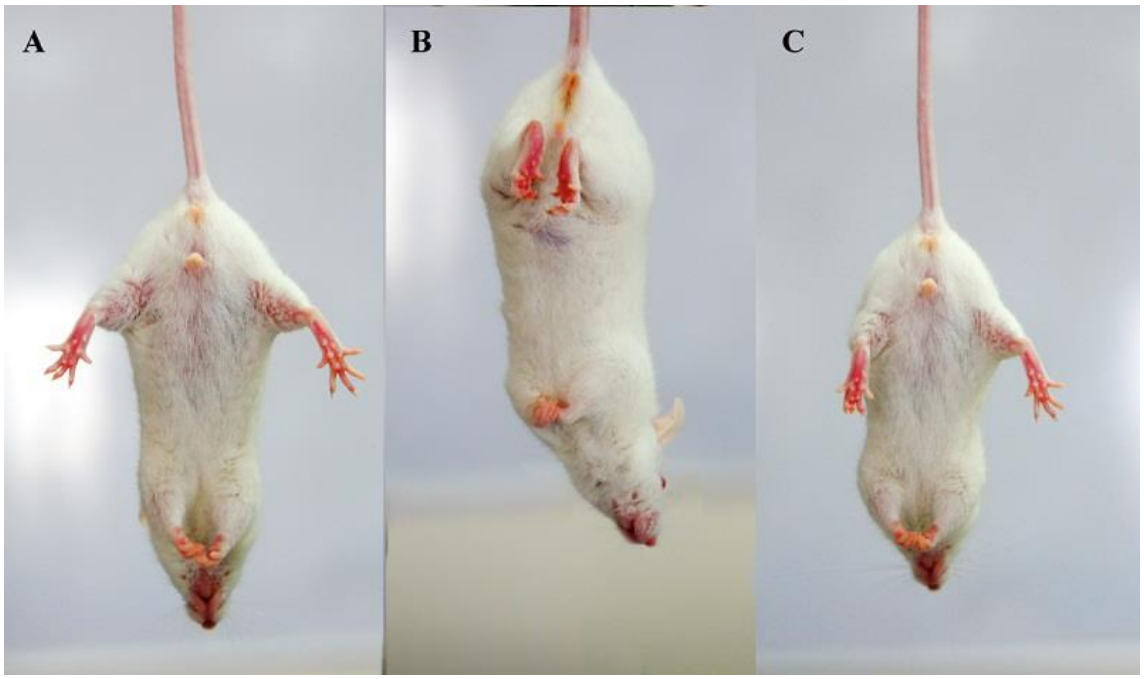

Figure 6-13. Evaluation of **PB9** in hind lclasping test.

Clasping behavior after three weeks in different groups: (A) Naive group, (B) control group and (C) treatment group. Clasping behaviour is an early manifestation of motor dysfunction. By the end of two weeks of MeHg treatment, animals showed extensive clasping. Interestingly, treatment with **PB9** reversed the clasping to a greater extent.

control group showed severe hind limb clasping. Interestingly, treatment group animals (**PB9** treated animals) did not show any sign of hind limb clasping, and appeared similar to naïve group. From the observation of clasping, it could be clearly concluded that MeHg exerted some effect on neurophysiological functions and **PB9** reversed this effect and hence useful as neuroprotectant.

6.4.4.2 Gait test

A footprint analysis was conducted to understand the gradual gait impairment which helped us to determine the extent of motor impairment induced by oral MeHg exposure. Figure 6-14 represents characteristic gait impairment in the three groups after two weeks. Interestingly, control group animals showed enhanced progressive gait impairment than either naive or **PB9** treatment group animals.

It was evident that MeHg exposed control group mice showed a smudged footprint which was a result of dragging the limb while walking, indicative of gait impairment. In contrast, the footprints of naive and treatment group animals were sharp, and hence there were no alterations in gait in these cases. This also proved our hypothesis that **PB9** was able to reverse gait impairment after MeHg exposure through its neuroprotective property.

Figure 6-14. Evaluation of **PB9** on MeHg induced neurodegeneration in footprint test.

Representative walking footprint patterns of (A) naive group, (B) control group, and (C) treatment mice after three weeks. The footprints were taken on white paper by applying non-toxic dye on hind limbs of mice and allowing them to walk on paper. Generated footprint patterns of control group clearly differ from naive and treatment groups.

6.4.4.3 Locomotor test

In addition, we also evaluated spontaneous locomotor activity to obtain a pattern of motor deficit. The third week results indicated a significant reduction in spontaneous motor activity ($P < 0.05$) in control, but not in treatment group, which showed similar locomotor behaviour as naive group mice (Figure 6-15A). This finding complemented our earlier observations of hind limb clasping phenomenon and indicated that MeHg induced neurodegeneration led to significantly reduced locomotor activity in both, control and treatment groups. **PB9** treated animals did not showed significantly different effect when compared to control group animals.

6.4.4.4 Motor co-ordination test

We also subjected the three groups of animals to rotarod test to assess the ability of animals to balance on a rotating rod. Mice were kept on a metallic rotating rod at 20 rpm, and the latency to fall from the rod was observed. This test was very useful as it could test minimal

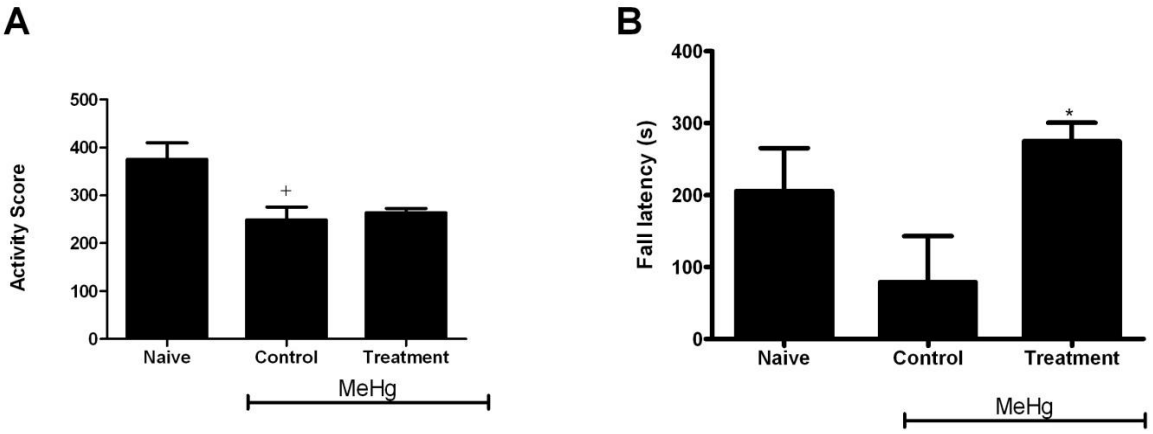

Figure 6-15. Evaluation of **PB9** in actophotometer and rotarod tests.

(A) Actophotometer test, (B) rotarod test. Data are given as the mean ± SEM of six mice. Statistically significant differences of treatment relative to MeHg group (control) are denoted by *(*, p <.05; **, p <.01; ***, p <.001, two-tailed unpaired Student's t-test). + denotes significant difference of control group activity when compared to naïve group ($p < 0.05$).

motor impairment and also it was an indicator of gripping strength. Treatment and control groups exhibited significantally different fall latencies (Figure 6-15B). qualitative analysis of the latencies revealed that control group mice stayed for relatively shorter duration of time on the rotating rod, when compared to naive or treatment groups. This clearly suggested that MeHg exerted a declining effect on fall latencies, but **PB9** was able to reverse this effect and relatively increased the stay duration of the animals on the rotating rod.

6.4.4.5 Novel object recognition test

Third week results for the NOR test implicated that naiv group mice were able to clearly discriminate between familiar and new objects, which was reflected by a positive difference (Figure 6-16A). On the other hand, animals from control group showed no difference in exploration time between the two objects, or alternatively, they explored familiar object more, than the novel object, as indicated by a negative score. Whereas **PB9** treated treatment group animals showed a positive trend. Since the animals of treatment group were subjected to 2 weeks of MeHg, it was obvious that these animals would have undergone memory impairment process. But one week after **PB9** administration, the animals were found to retain some memory of the familiar object. Interestingly, MeHg treated control mice explored familiar object more as the experiment progressed. Hence it could be concluded that over the time of treatment, **PB9** animals partially recovered from MeHg induced memory loss and cognition.

6.4.4.6 Morris water maze test

The effect of MeHg exposure on cognition was determined using Morris water maze test. In this test, animals were first trained to find a hidden platform using a fixed visual clue in a pool of water. During the test phase, the hidden platform was removed and the latency to reach the learned place was recorded. During third week, it was observed that control group mice took considerably longer time to return to the learned place using visual clue than other groups (Figure 6-16B). By third week, treatment group animals showed similar latency as that of naïve group, thus indicating that **PB9** treated group could significantly overcome the deteriorating effect of MeHg on learning. This result of **PB9** was encouraging to be utilized for cognition deficit conditions.

6.4.4.7 Mechanical allodynia

It has been already discussed that MeHg induced neurodegeneration. One of the many deteriorating effects of neurodegeneration was allodynia. Thus, we decided to evaluate the protective effect of **PB9** in MeHg exposed animals. The test was conducted using a set of calibrated von-Frey fibres and 50% PWT was determined. It was observed that control group animals exhibited lower 50% PWT with respect to the naïve group. On the other hand, treatment group exhibited significantly elevated paw withdrawal threshold than control group ($p \leq 0.05$), indicating that **PB9** was successfully able to reverse the effect of MeHg induced

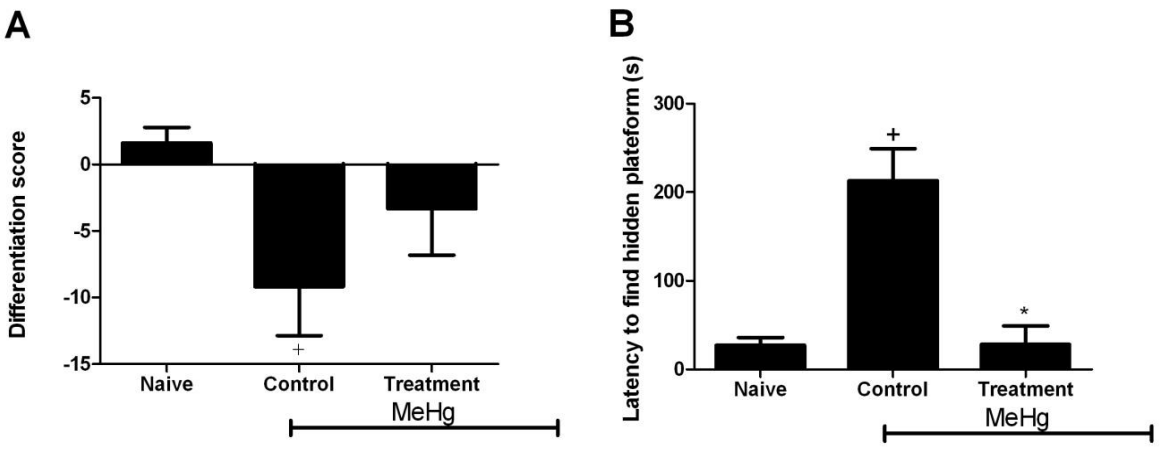

Figure 6-16. Evaluation of **PB9** in novel object recognition (NOR) and morris water maze tests.

(A) Novel object recognition test, (B) Morris water maze test. Data are given as the mean ± SEM of six mice. Statistically significant differences of treatment relative to MeHg group (control) are denoted by *(*, p <.05; **, p <.01; ***, p <.001, two-tailed unpaired Student's t-test). + denotes significant difference of control group activity when compared to naïve group ($p < 0.05$).

allodynia (Figure 6-17A). It need to be noted that in earlier similar tests in DPN and CCI, **PB9** was found ineffective in mechanical allodynia but surprisingly, it was found to be active against MeHg induced neurodegeneration model. Further molecular level understanding on the effect of these disease models and its effect on PKCβ-II expression could be fruitful.

6.4.4.8 Tail suspension test

In order to evaluate animal's response to an inescapable aversive situation, we conducted tail suspension test. In this test, the mice were suspended upside-down with their tail secured at a height of 50 cm from the ground. The animals demonstrated either active phase (struggling to get rid of inescapable situation) or inactive (lying idle) behaviour. The latter was a measure of depression-like behaviour. In this test, the third week results revealed that MeHg treated control animals spent significantly more time as inactive, when compared to naive mice, whereas **PB9** treated treatment group animals exhibited similar immobility time as that of control (Figure 6-17B). The depressive effect of human exposure to elemental MeHg had already been reported.

To conclude, the present study utilized different pharmacological models of neuropathy (DPN and CCI) and neurodegeneration (MeHg induced neurodegeneration). These compounds were previously identified *in silico* by screening Asinex and *in house* databases. Two of these molecules were found to be effective in models of neuropathic pain. Compound

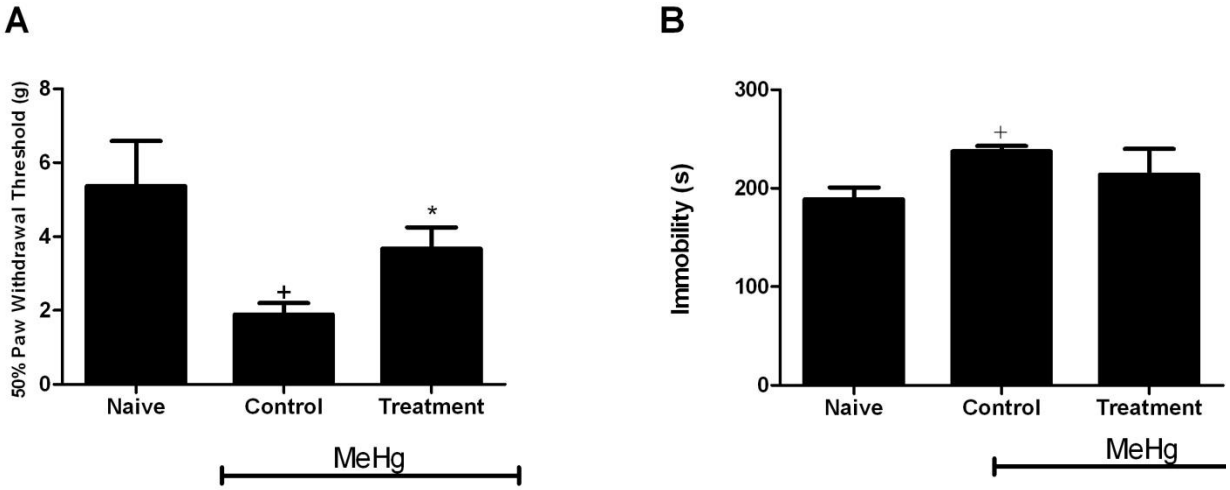

Figure 6-17. Effect of **PB9** on mechanical allodynia and tail suspension test.

(A) Mechanical allodynia, (B) Tail suspension test. Data are given as the mean ± SEM of six mice. Statistically significant differences of treatment relative to MeHg group (control) are denoted by *(*, p <.05; **, p <.01; ***, p <.001, two-tailed unpaired Student's t-test). + denotes significant difference of control group activity when compared to naïve group ($p < 0.05$).

PB9 also showed its efficacy in model of neurodegeneration as it reversed the neurodegenerative effects of MeHg. Thus, **PB9** could be utilized as promising lead for further optimization and development as PKCβ-II inhibitors. Further characterization utilizing more animals and different doses and extension of time points of observations would be fruitful.

6.5 Summary

Overall the design strategy consisted of two phases. **Phase-I** briefly consisted of hypothesis generation, validation and screening of commercial and *in house* databases. After docking studies, promising leads were identified. **Phase-II** involved pharmacological characterization of promising leads.

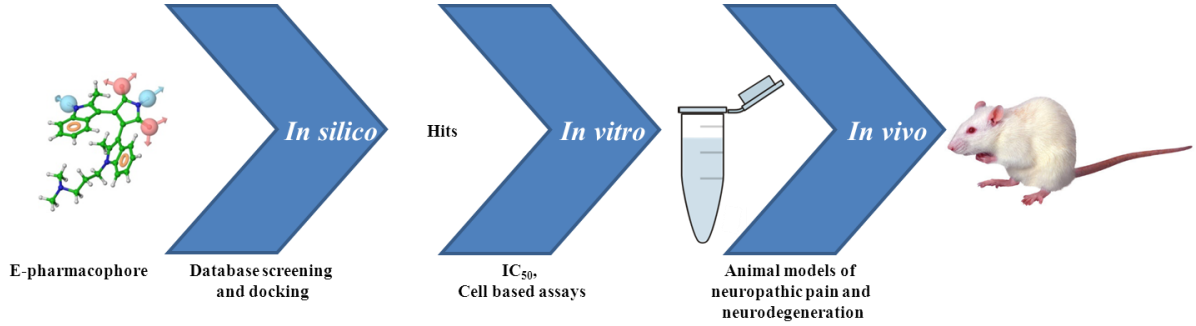

Amongst identified PKCβ-II inhibitors, compound **PA10** emerged as most potent compound with IC_{50}=12.72±0.91 µM. On The other hand, compound **PB9** was not only effective against animal model of diabetic neuropathic pain, it also indicated it's promising activity against neurodegenerative effects of MeHg on gait impairment, allodynia, memory impairment and cognition deficit.

"I think and think for months and years.
Ninety-nine times, the conclusion is false.
The hundredth time I am right."

-Albert Einstein

Chapter 7.
Summary and Conclusion

7.1 Summary

With the intention of developing novel protein kinase inhibitors effective against various diabetic complications including diabetic neuropathy and neurodegeneration, we explored the structure-based inhibitor design of two most important protein kinases implicated in these conditions: ROCK and PKCβ-II. We employed a series of computer-aided drug design based approaches and various *in vitro* and *in vivo* interventions to identify potential inhibitors of these two protein kinases.

7.1.1 Rho kinase (ROCK)

Identification of new ROCK inhibitors

1. To identify potential hits, first the reported ROCK crystal structures (eight structures) with bound inhibitors were retrieved from PDB.
    a. A combination of e-pharmacophore based and shape based design approach was applied to identify potential ROCK inhibitors.
    b. Multiple e-pharmacophores and shape-based queries were generated based on crystal structures bound to inhibitors and validated using a combined set of known inhibitors and drug-like inactive molecules.
    c. Validated e-pharmacophore hypotheses were utilized as template to screen Asinex database.

d. The docking program Glide employed HTVS, SP and XP modes to yield a list of molecules as potential hits. These molecules were visually inspected and finally, we selected and procured 8 molecules for further studies.

e. We performed a battery of tests to evaluate ROCK inhibition, protein binding, cytotoxicity and cytoprotective properties of these molecules. The most potent compound **R8** exhibited an IC_{50} value of 1.5 µM against ROCK activity and inhibited methymercury-induced IMR-32 cells with GI_{50} of 0.27 µM. Notably, DSF analysis revealed that ROCK protein complexed with compound **8** exhibited enhanced stability relative to fasudil, a validated nanomolar range ROCK inhibitor. The identified lead thus constituted as a prototypical molecule for further optimization and development as anti-ROCK inhibitor.

2. Previously known 7-azaindole hinge-binding scaffold tethered to aminopyrimidine core (ROCK-II IC_{50}~3 nM) was selected for further optimization after review of available literature.

   a. This core was retained and various substitutions were applied to the corresponding head region of the molecule. A series of molecules thus created were docked to ROCK active site using XP model of Glide script. After visual inspection, top eight molecules were selected for further studies.

   b. The most potent compound **RK7** exhibited an IC_{50} value of 2.37 nM against ROCK kinase activity and inhibited methymercury-induced neurotoxicity of IMR-32 cells at GI_{50} value of 11.36 µM. Notably, differential scanning fluorometric analysis revealed that ROCK protein complexed with compound **RK7** with enhanced stability relative to fasudil.

   c. Furthermore, we studied the effect of these compounds in two animal models: STZ induced painful diabetic neuropathy and MeHg induced neurodegeneration. The studies were carried out at sub-neurotoxic dose.

   d. Compound **RK7** was found efficacious at 30 mg/kg dose amongst the selected eight compounds in diabetic neuropathy model.

   e. Neuroprotective effects of **RK7** (10 mg/kg) were studied against MeHg induced neurodegeneration. The compound showed a promising neuroprotective efficacy in different tests of gait impairment, memory, learning and depression and reversed the detrimental effect of MeHg to a level, comparable to control animals.

7.1.2 Protein kinase C-βII (PKCβII)

Identification of new PKCβ-II inhibitor

1. To identify potential hits, first the reported PKCβ-II crystal structure with bound inhibitor was retrieved from PDB.
    a. An e-pharmacophore model was generated using the crystal structure. The six feature e-pharmacophore was shuffled to create a series of three, four, five and six feature e-pharmacophores. All the e-pharmacophores were validated using a combined set of known inhibitors and drug-like inactive molecules.
    b. Ten e-pharmacophores adhering to validation criteria were utilized as template to screen Asinex database.
    c. The output from database screening was merged together and was subjected to docking studies.
    d. The docking program Glide employed HTVS, SP and XP modes to give a list of molecules as potential hits. These molecules were visually inspected and finally, we procured 13 molecules for further studies.
    e. We performed a battery of tests to evaluate PKCβ-II inhibition, cytotoxicity and cytoprotective properties of these molecules. The most potent compound **PA10** exhibited best potency (PKCβ-II inhibition IC_{50}= 2.81±0.81 μM) and was selective towards neuronal cells.
2. Identification of PKCβ-II inhibitors using molecules effective for other indications.
    We decided to screen the *in house* BITS-database (BITS-DB) against PKCβ-II to identify novel inhibitors.
    a. BITS-DB is a structural repository of molecules synthesized at our institute.
    b. These molecules were directly docked to the PKCβ-II receptor and from the output, molecules were selected based on good docking score and availability. Total 13 molecules were selected for further study.
    c. The most potent compound **PB6** exhibited best potency (PKCβ-II inhibition IC_{50}= 5.82±0.09 μM).
    d. Furthermore, based on availability, we studied the effect of selected compounds for neurotoxicity. We also employed two animal models of neuropathic pain: STZ induced painful diabetic neuropathy and surgically induced pain model. Except neurotoxicity, all studies were carried out at 30 mg/kg dose.

e. Compound **PB9** was the most efficacious amongst the two compounds in diabetic neuropathy model.
f. Neuroprotective effects of **PB9** were studied against MeHg induced neurodegeneration. The compound showed a promising neuroprotective efficacy in different tests of gait impairment, memory, learning and depression and reversed the detrimental effect of MeHg to a level, comparable to control animals.

7.2 Achievements of this study

This study represents, in a miniscule form, the drug discovery process starting from the target (protein crystal structure), creation and validation of effective feature template using structure and shape based approach, which were used to search similar molecules from a large database of structures. The *in silico* ligand-receptor docking process identified a set of important hits, which were tested in a battery of neurobiological assays including characterization enzyme inhibition, cell-based assays, and animal models of neuropathic pain and neurodegeneration. For the first time, we have subjected out hits to extensive pre-clinical studies including neuropathic pain models and models for neurodegeneration, provided that our compounds were less neurotoxic. This study was also unique in a sense that we have identified hits from our *in house* database molecules, which were intended to be used in other CNS indications as a process of repurposing. Overall it appeared that ROCK inhibitors were promising compared to PKCβ-II inhibitors.

7.3 Value addition to existing scientific knowledge

A systemic literature review revealed highlights of available inhibitors, their structural insights, design process and characterization of activity. In addition, it also highlighted another dilemma: most of the recently identified molecules were restricted to a particular structural class. In this study, we have utilized multiple crystal-structure-based studies for adding significant value involving diverse models to yield structurally diverse ligands.

We had successfully identified ROCK inhibitors which, in many aspects, were better, or equivalent to the most widely used ROCK inhibitor. Likewise, we identified novel inhibitors for PKCβ-II. In addition, we tried a unique approach of utilizing multiple e-pharmacophore based screening. E-pharmacophore based screening in itself was a robust and widely adopted approach, but to maintain structural diversity, this approach seemed to be fruitful. Identification of PKCβ-II inhibitors using *in house* BITS-DB molecules was also a milestone as it gave additional target to molecules which were synthesized for a different target. After

identification of molecules, we did enzyme inhibition studies and DSF studies to prove that the ligand interacted with the enzyme. In the next step, we carried various cell-based assays to confirm cytotoxicity and protective effect of these molecules. Selected molecules were studied and found to be efficacious in diabetic neuropathic pain model. Another unique component of this study was the incorporation of MeHg induced neurodegeneration model. For the first time we evaluated our molecules in the model of MeHg induced neurodegeneration.

To conclude, this study utilized various aspects of drug discovery and development process and identified some potent ROCK and PKCβ-II inhibitors. These molecules could be used in future to design better molecules effective against neurological disorders.

"The future depends on what you do today."

-Mahatma Gandhi

Chapter 8.
Future Perspective

In the present work, we had attempted to design novel protein kinase inhibitors. Apart from inhibition studies and biological characterization, we could also screen the molecules in various animal models of neuropathic pain and neurodegeneration.

To fully utilize the unique potential of these identified hits against their respective targets, it was required to have the complete characterization of their modes of actions. The only way to make progress in this respect is to check the various factors in the molecular environments of these proteins, thus identifying the factors contributing towards the activity. Further extension of the pharmacological assays with more animal numbers and different dose and time point assessment would be first required for development of these lead molecules. Second, since these two proteins share a common pathway, it would be beneficial to identify the selectivity of the inhibitors either towards ROCK or PKCβ-II. Third, the e-pharmacophore queries used in this study could be further used either without any modification to screen other databases, or they could be optimized further to give better hits. Fourth, newly reported inhibitors could be utilized to generate better pharmacophoric models, or the collective structure-activity data could be utilized to develop QSAR models which would further add knowledge to the existing models. Fifth, molecular dynamics simulations could be beneficial to track the movement of key amino acids. Sixth, the MeHg model of neurodegeneration is a complex, yet definitive test as it can give a lot of information about the role of protein kinase inhibitors in locomotor and cognitive behavioural aspects including depression and allodynia. Determination of nitric oxide levels, free radicals, protein and mRNA expression levels in

various tissues of animals could help to reveal the molecular mechanisms involved in such behavioural responses. Seventh, the STZ-induced painful diabetic neuropathy model could shed some light on the effect of these protein kinase inhibitions on various short-term and long term indications of diabetes. Also, histopathological examination of nerves, brain, vascular tissues and retina in diabetic animals receiving the identified inhibitors could also shed some light on their usefulness of these inhibitors in other diabetic complications. Last, but not the least, the calculated pharmacokinetic parameters in this study could help us to decide the type of suitable dosage form, for a better ADME profile. Oral efficacies of the compounds along with pharmacokinetic studies to determine bioavailability, half-life, C_{max} etc. should be undertaken. Metabolism and elimination pattern of the compounds could also be explored.

BIBLIOGRAPHY

1. Polonsky, K. S. The past 200 years in diabetes. *N. Engl. J. Med.* **2012**, *367*(14), 1332-1340.
2. Dobson, M.; Fothergill, J. Experiments and Observations on the Urine in a Diabetes. **1776**.
3. IDF Diabetes, Atlas: The International Diabetes Federation. *Int. Diabetes Fed.* **2013**, 30-34.
4. National Diabetes Data Group. Classification and diagnosis of diabetes mellitus and other categories of glucose intolerance. *Diabetes* **1979**, *28*(12), 1039-1057.
5. Vinik, A. I.; Park, T. S.; Stansberry, K. B.; Pittenger, G. L. Diabetic neuropathies. *Diabetologia* **2000**, *43*(8), 957-973.
6. Malik, R. A.; Veves, A.; Walker, D.; Siddique, I.; Lye, R. H.; Schady, W.; Boulton, A. J. M. Sural nerve fibre pathology in diabetic patients with mild neuropathy: relationship to pain, quantitative sensory testing and peripheral nerve electrophysiology. *Acta Neuropathol.* **2001**, *101*(4), 367-374.
7. Seaquist, E. R.; Goetz, F. C.; Rich, S.; Barbosa, J. Familial clustering of diabetic kidney disease. *N. Engl. J. Med.* **1989**, *320*(18), 1161-1165.
8. Geerlings, S. E.; Hoepelman, A. I. Immune dysfunction in patients with diabetes mellitus (DM). *FEMS Immunol. Med. Microbiol.* **1999**, *26*(3-4), 259-265.
9. Behse, F.; Buchthal, F.; Carlsen, F. Nerve biopsy and conduction studies in diabetic neuropathy. *J. Neurol. Neurosurg. Psychiatry* **1977**, *40*(11), 1072-1082.
10. Feldman, E. L.; Stevens, M. J.; Greene, D. A. Pathogenesis of diabetic neuropathy. *Clin. Neurosci.* **1996**, *4*(6), 365-370.
11. Sheetz, M. J.; King, G. L. Molecular understanding of hyperglycemia's adverse effects for diabetic complications. *JAMA*, **2002**, *288*(20), 2579-2588.
12. Sima, A. A. F.; Sugimoto, K. Experimental diabetic neuropathy: an update. *Diabetologia* **1999**, *42*(7), 773-788.
13. Cameron, N. E.; Eaton, S. E. M.; Cotter, M. A.; Tesfaye, S. Vascular factors and metabolic interactions in the pathogenesis of diabetic neuropathy. *Diabetologia* **2001**, *44*(11), 1973-1988.
14. Sims-Robinson, C.; Kim, B.; Rosko, A.; Feldman, E. L. How does diabetes accelerate Alzheimer disease pathology? *Nat. Rev. Neurol.* **2010**, *6*(10), 551-559.

15. Takeda, S.; Naoyuki, S.; Kozue, U. Y.; Kyoko, S.; Takanori, K.; Daisuke, T.; Hitomi K.; Shinohara, H. R.; Ryuichi, M. Diabetes-accelerated memory dysfunction via cerebrovascular inflammation and Aβ deposition in an Alzheimer mouse model with diabetes. *Proc. Natl. Acad. Sci. U S A* **2010**, *107*(15), 7036-7041.
16. Threadgill, R.; Kathryn, B.; Anirvan, G.; Regulation of dendritic growth and remodeling by Rho, Rac, and Cdc42. *Neuron* **1997**, *19*(3), 625-634.
17. Nakayama, A. Y.; Matthew, B.; Liqun, L. Small GTPases Rac and Rho in the maintenance of dendritic spines and branches in hippocampal pyramidal neurons. *J. Neurosci.* **2000**, *20*(14), 5329-5338.
18. Billuart, P.; Winter, C. G.; Maresh, A.; Zhao, X.; Luo, L. Regulating axon branch stability: the role of p190 RhoGAP in repressing a retraction signaling pathway. *Cell* **2001**, *107*(2), 195-207.
19. Wang, H. G., Lu, F. M., Jin, I., Udo, H., Kandel, E. R., de Vente, J. Ulrich W.; Suzanne M. L.; Robert, D. H.; Irina, A. A. I. Presynaptic and postsynaptic roles of NO, cGK, and RhoA in long-lasting potentiation and aggregation of synaptic proteins. *Neuron* **2005**, *45*(3), 389-403.
20. Nakagawa, O.; Fujisawa, K.; Ishizaki, T.; Saito, Y.; Nakao, K.; Narumiya, S. ROCK-I and ROCK-II, two isoforms of Rho-associated coiled-coil forming protein serine/threonine kinase in mice. *FEBS Lett.* **1996**, *392*, 189-193.
21. Raftopoulou, M.; Hall, A. Cell migration: Rho GTPases lead the way. *Dev. Biol.* **2004**, *265*(1), 23-32.
22. Jaffe, A.B.; Hall, A. Rho GTPases: biochemistry and biology. *Ann. Rev. Cell. Devel. Biol.* **2005**, *21*, 247-269.
23. Doran, J.D.; Liu, X.; Taslimi, P.; Saadat, A.; Fox, T. New insights into the structure-function relationships of Rho-associated kinase: a thermodynamic and hydrodynamic study of the dimer- to-monomer transition and its kinetic implications. *Biochem. J.* **2004**, *384*, 255-262.
24. Kitazawa, T.; Eto, M.; Woodsome, T. P.; Brautigan, D. L. Agonists trigger G protein-mediated activation of the CPI-17 inhibitor phosphoprotein of myosin light chain phosphatase to enhance vascular smooth muscle contractility. *J. Biol. Chem.* **2000**, *275*, 9897-9900.
25. Amano, M.; Ito, M.; Kimura, K.; Fukata, Y.; Chihara, K.; Nakano, T.; Matsuura, Y.; Kaibuchi, K. Phosphorylation and activation of myosin by Rho-associated kinase (Rho-kinase). *J. Biol. Chem.* **1996**, *271*, 20246-20249.

26. Ohashi, K.; Nagata, K.; Maekawa, M.; Ishizaki, T.; Narumiya, S.; Mizuno, K. Rho-associated kinase ROCK activates LIM-kinase 1 by phosphorylation at threonine 508 within the activation loop. *J. Biol. Chem.* **2000**, *275*(5), 3577-3582.
27. Kaneko, T.; Amano, M.; Maeda, A.; Goto, H.; Takahashi, K.; Ito, M.; Kaibuchi, K. Identification of calponin as a novel substrate of Rho-kinase. *Biochem. Biophys. Res. Commun.* **2000**, *273*(1), 110-116.
28. Vahebi, S.; Kobayashi, T.; Warren, C. M.; de Tombe, P. P.; Solaro, R. J. Functional effects of rho-kinase–dependent phosphorylation of specific sites on cardiac troponin. *Circ. Res.* **2005**, *96*(7), 740-747.
29. Riento, K.; Ridley, A. J. Rocks: multifunctional kinases in cell behaviour. *Nat. Rev. Mol. Cell. Biol.* **2003**, *4*(6), 446-456.
30. Etienne-Manneville, S.; Hall, A. Rho GTPases in cell biology. *Nature* **2002**, *420*(6916), 629-635.
31. Woolf, C. J.; Salter, M. W. Neuronal plasticity: increasing the gain in pain. *Science* **2000**, *288*(5472), 1765-1768.
32. Scholz, J.; Woolf, C. J. Can we conquer pain? *Nat. Neurosci.* **2002**, *5*, 1062-1067.
33. Inoue, M.; Rashid, M. H.; Fujita, R.; Contos, J. J.; Chun, J.; Ueda, H. Initiation of neuropathic pain requires lysophosphatidic acid receptor signaling. *Nat. Med.* **2004**, *10*(7), 712-718.
34. Tatsumi, S.; Mabuchi, T.; Katano, T.; Matsumura, S.; Abe, T.; Hidaka, H.; Suzuki, M.; Sasaki, Y.; Minami, T.; Ito, S. Involvement of Rho-kinase in inflammatory and neuropathic pain through phosphorylation of myristoylated alanine-rich C-kinase substrate (MARCKS). *Neuroscience* **2005**, *131*(2), 491-498.
35. Ramer, L. M.; Borisoff, J. F.; Ramer, M. S. Rho-kinase inhibition enhances axonal plasticity and attenuates cold hyperalgesia after dorsal rhizotomy. *J. Neurosci.* **2004**, *24*(48), 10796-10805.
36. Ohsawa, M.; Mutoh, J.; Hisa, H. Mevalonate sensitizes the nociceptive transmission in the mouse spinal cord. *Pain* **2008**, *134*(3), 285-292.
37. Büyükafşar, K.; Yalçın, İ.; Kurt, A. H.; Tiftik, R. N.; Şahan-Fırat, S.; Aksu, F. Rho-kinase inhibitor, Y-27632, has an antinociceptive effect in mice. *Eur. J. Pharmacol.* **2006**, *541*(1), 49-52.
38. Brownlee, M.; Cerami, A.; Vlassara, H. Advanced glycosylation end products in tissue and the biochemical basis of diabetic complications. *N. Engl. J. Med.* **1998**, *318*(20), 1315-1321.

39. Sauzeau, V.; Le Jeune, H.; Cario-Toumaniantz, C.; Smolenski, A.; Lohmann, S. M., Bertoglio, J.; Chardin, P.; Pacaud, P.; Loirand, G. Cyclic GMP-dependent protein kinase signaling pathway inhibits RhoA-induced Ca^{2+} sensitization of contraction in vascular smooth muscle. *J. Biol. Chem.* **2000**, *275*(28), 21722-21729.
40. Xie, Z.; Su, W.; Guo, Z.; Pang, H.; Post, S. R.; Gong, M. C. Up-regulation of CPI-17 phosphorylation in diabetic vasculature and high glucose cultured vascular smooth muscle cells. *Cardiovasc. Res.* **2006**, *69*(2), 491-501.
41. Naik, J. S.; Xiang, L.; Hester, R. L. Enhanced role for RhoA-associated kinase in adrenergic-mediated vasoconstriction in gracilis arteries from obese Zucker rats. *Am. J. Physiol. Regul. Integr. Comp. Physiol.* **2006**, *290*, R154-R161.
42. Massey, A. R.; Miao, L.; Smith, B. N.; Liu, J.; Kusaka, I.; Zhang, J. H.; Tang, J. Increased RhoA translocation in renal cortex of diabetic rats. *Life Sci.* **2003**, *72*(26), 2943-2952.
43. Kanda, T.; Wakino, S.; Homma, K.; Yoshioka, K.; Tatematsu, S.; Hasegawa, K.; Takamatsu, I.; Sugano, N.; Hayashi, K.; Saruta, T. Rho-kinase as a molecular target for insulin resistance and hypertension. *FASEB J.* **2006**, *20*(1), 169-171.
44. Peng, F.; Wu, D.; Gao, B.; Ingram, A. J.; Zhang, B.; Chorneyko, K.; Krepinsky, J. C. RhoA/Rho-kinase contribute to the pathogenesis of diabetic renal disease. *Diabetes* **2008**, *57*(6), 1683-1692.
45. Nobes, C. D.; Hall, A. Rho, rac, and cdc42 GTPases regulate the assembly of multimolecular focal complexes associated with actin stress fibers, lamellipodia, and filopodia. *Cell* **1995**, *81*, 53-62.
46. Goalstone, M.; Kamath, V.; Kowluru, A. Glucose activates prenyltransferases in pancreatic islet β-cells. *Biochem. Biophys. Res. Commun.* **2010**, *391*(1), 895-898.
47. Lee, S. P.; Saltsman, K. A.; Ohashi, H.; King, G. L. Activation of protein kinase C by elevation of glucose concentration: proposal for a mechanism in the development of diabetic vascular complications. *Proc. Natl. Acad. Sci. U S A* **1989**, *86*(13), 5141-5145.
48. Mehta, D.; Rahman, A.; Malik, A. B. Protein kinase C-alpha signals rho-guanine nucleotide dissociation inhibitor phosphorylation and rho activation and regulates the endothelial cell barrier function. *J. Biol. Chem.* **2001**, *276*, 22614-22620.
49. Schreibelt, G.; Kooij, G.; Reijerkerk, A.; van Doorn, R.; Gringhuis, S. I.; van der Pol, S.; De Vries, H. E. Reactive oxygen species alter brain endothelial tight junction dynamics via RhoA, PI3 kinase, and PKB signaling. *FASEB J.* **2007**, *21*(13), 3666-3676.

50. Sawada, N.; Itoh, H.; Yamashita, J.; Doi, K.; Inoue, M.; Masatsugu, K.; Nakao, K. cGMP-dependent protein kinase phosphorylates and inactivates RhoA. *Biochem. Biophys. Res. Commun.* **2001**, *280*(3), 798-805.
51. Mustafa, S.; Vasudevan, H.; Yuen, V. G.; McNeill, J. H. Renal expression of arachidonic acid metabolizing enzymes and RhoA/Rho kinases in fructose insulin resistant hypertensive rats. *Mol. Cell. Biochem.* **2010**, *333*(1-2), 203-209.
52. Chang, J.; Xie, M.; Shah, V. R.; Schneider, M. D.; Entman, M. L.; Wei, L.; Schwartz, R. J. Activation of Rho-associated coiled-coil protein kinase 1 (ROCK-1) by caspase-3 cleavage plays an essential role in cardiac myocyte apoptosis. *Proc. Natl. Acad. Sci. U S A* **2006**, *103*(39), 14495-14500.
53. Low, P. A. Recent advances in the pathogenesis of diabetic neuropathy. Clues from human diabetic neuropathy. *Muscle. Nerve.* **1987**, *10*(2), 121-128.
54. Brownlee, M.; Cerami, A.; Vlassara, H. Advanced glycosylation end products in tissue and the biochemical basis of diabetic complications. *N. Engl. J. Med.* **1988**, *318*(20), 1315-1321.
55. Koya, D.; King, G. L. Protein kinase C activation and the development of diabetic complications. *Diabetes* **1998**, *47*(6), 859-866.
56. Dyck, P. J.; Giannini, C. Pathologic alterations in the diabetic neuropathies of humans: a review. *J. Neuropathol. Exp. Neurol.* **1996**, *55*(12), 1181-1193.
57. Nakayama, A. Y.; Harms, M. B.; Luo, L. Small GTPases Rac and Rho in the maintenance of dendritic spines and branches in hippocampal pyramidal neurons. *J. Neurosci.* **2000**, *20*(14), 5329-5338.
58. Inoue, M.; Rashid, M. H.; Fujita, R.; Contos, J. J.; Chun, J.; Ueda, H. Initiation of neuropathic pain requires lysophosphatidic acid receptor signaling. *Nat. Med.* **2004**, *10*(7), 712-718.
59. Tatsumi, S.; Mabuchi, T.; Katano, T.; Matsumura, S.; Abe, T.; Hidaka, H.; Ito, S. Involvement of Rho-kinase in inflammatory and neuropathic pain through phosphorylation of myristoylated alanine-rich C-kinase substrate (MARCKS). *Neuroscience* **2005**, *131*(2), 491-498.
60. Ramer, L. M.; Borisoff, J. F.; Ramer, M. S. Rho-kinase inhibition enhances axonal plasticity and attenuates cold hyperalgesia after dorsal rhizotomy. *J. Neurosci.* **2004**, *24*(48), 10796-10805.
61. Ohsawa, M.; Mutoh, J.; Hisa, H. Mevalonate sensitizes the nociceptive transmission in the mouse spinal cord. *Pain* **2008**, *134*(3), 285-292.

62. Büyükafşar, K.; Yalçın, İ.; Kurt; A. H.; Tiftik, R. N.; Şahan-Fırat, S.; Aksu, F. Rho-kinase inhibitor, Y-27632, has an antinociceptive effect in mice. *Eur. J. Pharmacol.* **2006**, *541*(1), 49-52.
63. James, S. E.; Dunham, M.; Carrion-Jones, M.; Murashov, A.; Lu, Q. Rho kinase inhibitor Y-27632 facilitates recovery from experimental peripheral neuropathy induced by anti-cancer drug cisplatin. *Neurotoxicology* **2010**, *31*(2), 188-194.
64. Yoshimi, E.; Yamamoto, H.; Furuichi, Y.; Shimizu, Y.; Takeshita, N. Sustained analgesic effect of the Rho kinase inhibitor AS1892802 in rat models of chronic pain. *J. Pharm. Sci.* **2010**, *114*(1), 119-122.
65. Ohsawa, M.; Aasato, M.; Hayashi, S. S.; Kamei, J. RhoA/Rho kinase pathway contributes to the pathogenesis of thermal hyperalgesia in diabetic mice. *Pain* **2011**, *152*(1), 114-122.
66. Jin, L.; Burnett, A. X. RhoA/Rho-kinase in erectile tissue: mechanisms of disease and therapeutic insights. *Clin. Sci.* **2006**, *110*, 153-165.
67. Kolavennu, V.; Zeng, L.; Peng, H.; Wang, Y.; Danesh, F. R. Targeting of RhoA/ROCK signaling ameliorates progression of diabetic nephropathy independent of glucose control. *Diabetes* **2008**, *57*(3), 714-723.
68. Kikuchi, Y.; Yamada, M.; Imakiire, T.; Kushiyama, T.; Higashi, K.; Hyodo, N.; Yamamoto, K.; Oda, T.; Suzuki, S.; Miura, S. A Rho-kinase inhibitor, fasudil, prevents development of diabetes and nephropathy in insulin-resistant diabetic rats. *J. Endocrinol.* **2007**, *192*(3), 595-603.
69. Gojo, A.; Utsunomiya, K.; Taniguchi, K.; Yokota, T.; Ishizawa, S.; Kanazawa, Y.; Kurata, H.; Tajima N. The Rho-kinase inhibitor, fasudil, attenuates diabetic nephropathy in streptozotocin-induced diabetic rats. *Eur. J. Pharmacol.* **2007**, *568*(1-3), 242-247.
70. Meyer-Schwesinger, C.; Dehde. S.; von Ruffer. C.; Gatzemeier. S.; Klug. P.; Wenzel. U. O.; Stahl, R.A.; Thaiss. F.; Meyer. T. N. Rho kinase inhibition attenuates LPS-induced renal failure in mice in part by attenuation of NF-kappaB p65 signaling. *Am. J. Physiol.* **2009**, *296*(5), F1088-F1099.
71. Löhn, M.; Plettenburg, O.; Ivashchenko, Y.; Kannt, A.; Hofmeister, A.; Kadereit, D.; Schaefer, M.; Linz, W.; Kohlmann, M.; Herbert, J. M.; Janiak, P.; O'Connor, S. E.; Ruetten, H. Pharmacological characterization of SAR407899, a novel rho-kinase inhibitor. *Hypertension* **2009**, *54*(3), 676-683.

72. Honjo, M.; Tanihara, H.; Inatani, M.; Kido, N.; Sawamura, T.; Yue, B. Y.; Narumiya, S.; Honda, Y. Effects of rho-associated protein kinase inhibitor Y-27632 on intraocular pressure and outflow facility. *Invest. Ophthalmol. Vis. Sci.* **2001**, *42*(1), 137-144.
73. Nagaoka, T.; Hein, T. W.; Yoshida, A.; Kuo, L. Simvastatin elicits dilation of isolated porcine retinal arterioles: role of nitric oxide and mevalonate-rho kinase pathways. *Invest. Ophthalmol. Vis. Sci.* **2007**, *48*(2), 825-832.
74. Kawahara, S.; Hata, Y.; Kita, T.; Arita, R.; Miura, M.; Nakao, S.; Mochizuki, Y.; Enaida, H.; Kagimoto, T.; Goto, Y.; Hafezi-Moghadam, A.; Ishibashi, T. Potent inhibition of cicatricial contraction in proliferative vitreoretinal diseases by statins. *Diabetes* **2008**, *57*(10), 2784-2793.
75. Yamaguchi, H.; Kasa, M.; Amano, M.; Kaibuchi, K.; Hakoshima, T. Molecular mechanism for the regulation of rho-kinase by dimerization and its inhibition by fasudil. *Structure* **2006**, *14*(3), 589-600.
76. Yamaguchi, H.; Miwa, Y.; Kasa, M.; Kitano, K.; Amano, M.; Kaibuchi, K.; Hakoshima, T. Structural basis for induced-fit binding of Rho-kinase to the inhibitor Y-27632. *J. Biochem.* **2006**, *140*(3), 305-311.
77. Dvorsky, R.; Blumenstein, L.; Vetter, I. R.; Ahmadian, M. R. Structural insights into the interaction of ROCK-I with the switch regions of RhoA. *J. Biochem.* **2004**, *279*, 7098-7104.
78. Wang, D. H.; Qu, W. L.; Shi, L. Q.; Wei, J. Molecular docking and pharmacophore model studies of Rho kinase inhibitors. *Mol. Sim.* **2011**, *37*(06), 488-494.
79. Accelrys, Inc.10188 Telesis Court, Suite 100San Diego, CA, USA.
80. Gong, L. L.; Fang, L. H.; Peng, J. H.; Liu, A. L.; Du, G. H. Integration of virtual screening with high-throughput screening for the identification of novel Rho-kinase I inhibitors. *J. Biotechnol.* **2010**, *145*(3), 295-303.
81. Montes, M.; Miteva, M. A.; Villoutreix, B. O. Structure-based virtual ligand screening with LigandFit: Pose prediction and enrichment of compound collections. *Proteins* **2007**, *68*(3), 712-725.
82. Qin, J., Lei, B., Xi, L., Liu, H., & Yao, X. Molecular modeling studies of Rho kinase inhibitors using molecular docking and 3D-QSAR analysis. *Eur. J. Med. Chem.* **2010**, *45*(7), 2768-2776.
83. Takami, A.; Iwakubo, M.; Okada, Y.; Kawata, T.; Odai, H.; Takahashi, N.; Shindo, K.; Kimura, K.; Tagami, Y.; Miyake, M.; Fukushima, K.; Inagaki, M.; Amano, M.;

Kaibuchi, K.; Iijima, H. Design and synthesis of Rho kinase inhibitors (I). *Bioorg. Med. Chem.* **2004**, *12*(9), 2115-2137.

84. SYBYL software package, Tripos Inc., 1699 South Hanley Rd., St. Louis, MO, USA.
85. Iwakubo, M.; Takami, A.; Okada, Y.; Kawata, T.; Tagami, Y.; Ohashi, H.; Sato, M.; Sugiyama, T.; Fukushima, K.; Iijima, H. Design and synthesis of Rho kinase inhibitors (II). *Bioorg. Med. Chem.* **2007**, *15*(1), 350-364.
86. Iwakubo, M.; Takami, A.; Okada, Y.; Kawata, T.; Tagami, Y.; Sato, M.; Sugiyama, T.; Fukushima, K.; Taya, S.; Amano, M.; Kaibuchi, K.; Iijima, H. Design and synthesis of rho kinase inhibitors (III). *Bioorg. Med. Chem.* **2007**, *15*(2), 1022-1033.
87. Goodman, K. B.; Cui, H.; Dowdell, S. E.; Gaitanopoulos, D.; Ivy, R. L.; Sehon, C. A.; Stavenger, R. A.; Wang G. Z.; Viet, A. Q.; Xu, W.; Ye, G.; Semus, S. F.; Evans, C. Development of dihydropyridone indazole amides as selective Rho-kinase inhibitors. *J. Med. Chem.* **2007**, *50*(1), 6-9.
88. Stavenger, R. A.; Cui, H.; Dowdell, S. E.; Franz, R. G.; Gaitanopoulos, D. E.; Goodman, K. B.; Lee, D. Discovery of aminofurazan-azabenzimidazoles as inhibitors of Rho-kinase with high kinase selectivity and antihypertensive activity. *J. Med. Chem.* **2007**, *50*(1), 2-5.
89. Fang, X.; Yin, Y.; Chen, Y. T.; Yao, L.; Wang, B.; Cameron, M. D.; Feng, Y. Tetrahydroisoquinoline derivatives as highly selective and potent Rho kinase inhibitors. *J. Med. Chem.* **2010**, *53*(15), 5727-5737.
90. Newton, A. C. Protein kinase C: structure, function, and regulation. *J. Biol. Chem.* **1995**, *270*(48), 28495-28498.
91. Tatsuo, S. Protein kinases involved in the expression of long-term potentiation. *Int. J. Biochem.* **1994**, *26*(6), 735-744.
92. Pasinelli, P.; Ramakers, G. M. J.; Urban, I. J. A.; Hens, J. J. H.; Oestreicher, A. B.; De Graan, P. N. E.; Gispen, W. H. Long-term potentiation and synaptic protein phosphorylation. *Behav. Brain Res.* **1995**, *66*(1), 53-59.
93. Mellor, H.; Parker, P. The extended protein kinase C superfamily. *Biochem. J.* **1998**, 332, 281-292.
94. Ohkusu, K.; Isobe, K. I.; Hidaka, H.; Nakashima, I. Elucidation of the protein kinase C-dependent apoptosis pathway in distinct subsets of T lymphocytes in MRL-lpr/lpr mice. *Eur. J. Immunol.* **1995**, *25*(11), 3180-3186.
95. Asaoka, Y.; Nakamura, S. I.; Yoshida, K.; Nishizuka, Y. Protein kinase C, calcium and phospholipid degradation. *Trends Biochem. Sci.* **1992**, *17*(10), 414-417.

96. Nishizuka, Y. Intracellular signaling by hydrolysis of phospholipids and activation of protein kinase C. *Science* **1992**, *258*(5082), 607-614.
97. Nishizuka, Y. Protein kinase C and lipid signaling for sustained cellular responses. *FASEB J.* **1995**, *9*(7), 484-496.
98. Nishizuka, Y. Studies and perspectives of protein kinase C. *Science* **1986**, *233*(4761), 305-312.
99. Sando, J. J.; Maurer, M. C.; Bolen, E. J.; M Grishman, C. Role of cofactors in protein kinase C activation. *Cell Signal.* **1992**, *4*(6), 595-609.
100. Mochly-Rosen, D. Localization of protein kinases by anchoring proteins: a theme in signal transduction. *Science* **1995**, *268*(5208), 247-251.
101. Coderre, T. J.; Melzack, R. The contribution of excitatory amino acids to central sensitization and persistent nociception after formalin-induced tissue injury. *J. Neurosci.* **1992**, *12*(9), 3665-3670.
102. Mao, J.; Mayer, D. J.; Hayes, R. L.; Price, D. D. Spatial Patterns of Increased Spinal Cord Membrane-Bound Protein Kinase C and Their Relation to Increases in 14C-2-Deoxyglucose Metabolic Activity in Rats With Painful Peripheral Mononeuropathy. *J. Neurophysiol.* **1993**, *70*, 470-481.
103. Yashpal, K.; Pitcher, G. M.; Parent, A.; Quirion, R.; Coderre, T. J. Noxious thermal and chemical stimulation induce increases in 3H-phorbol 12, 13-dibutyrate binding in spinal cord dorsal horn as well as persistent pain and hyperalgesia, which is reduced by inhibition of protein kinase C. *J. Neurosci.* **1995**, *15*(5), 3263-3272.
104. Battaini, F.; Protein kinase C isoforms as therapeutic targets in nervous system disease states. *Pharmacol. Res.* **2001**, *44*(5), 353-361.
105. Castagna, M.; Takai, Y.; Kaibuchi, K.; Sano, K.; Kikkawa, U.; Nishizuka, Y. Direct activation of calcium-activated, phospholipid-dependent protein kinase by tumor-promoting phorbol esters. *J. Biol. Chem.* **1982**, *257*(13), 7847-7851.
106. Naruse, K.; King, G. L. Protein kinase C and myocardial biology and function. *Circ. Res.* **2000**, *86*(11), 1104-1106.
107. Dempsey, E. C.; Newton, A. C.; Mochly-Rosen, D.; Fields, A. P.; Reyland, M. E.; Insel, P. A.; Messing, R. O. Protein kinase C isozymes and the regulation of diverse cell responses. *Am. J. Physiol. Lung Cell Mol. Physiol.* **2000**, *279*(3), L429-L438.
108. Wilkinson, S. E.; Nixon, J. S. T-cell signal transduction and the role of protein kinase C. *Cell Mol. Life Sci.* **1998**, *54*(10), 1122-1144.

109. Ishii, H.; Jirousek, M. R.; Koya, D.; Takagi, C.; Xia, P.; Clermont, A.; King, G. L. Amelioration of vascular dysfunctions in diabetic rats by an oral PKC β inhibitor. *Science* **1996**, *272*(5262), 728-731.
110. Aiello, L. P.; Clermont, A.; Arora, V.; Davis, M. D.; Sheetz, M. J.; Bursell, S. E. Inhibition of PKC β by oral administration of ruboxistaurin is well tolerated and ameliorates diabetes-induced retinal hemodynamic abnormalities in patients. *Invest. Ophthalm. Vis. Sci.* **2006**, *47*(1), 86-92.
111. Goekjian, P. G.; Jirousek, M. R. Protein kinase C in the treatment of disease: signal transduction pathways, inhibitors, and agents in development. *Curr. Med. Chem.* **1999**, *6*(9), 877-903.
112. Kim, H.; Sasaki, T.; Maeda, K.; Koya, D.; Kashiwagi, A.; Yasuda, H. Protein kinase Cβ selective inhibitor LY333531 attenuates diabetic hyperalgesia through ameliorating cGMP level of dorsal root ganglion neurons. *Diabetes* **2003**, *52*(8), 2102-2109.
113. Sima, A. A. F.; Sugimoto, K. Experimental diabetic neuropathy: an update. *Diabetologia* **1999**, *42*(7), 773-788.
114. Yagihashi, S. Pathology and pathogenetic mechanisms of diabetic neuropathy. *Diabetes Metab. Rev.* **2007**, *11*(3), 193-225.
115. Shiba, T.; Inoguchi, T.; Sportman, J. R.; Heath, W.; Bursell, S.; King, G. L. Correlation of diacylglycerol and protein kinase C activity in rat retina to retinal circulation. *Am. J. Physiol.* **1993**, *265*, E783–E793.
116. Craven, P. A.; DeRubertis, F. R. Protein kinase C is activated in glomeruli from streptozotocin diabetic rats. Possible mediation by glucose. *J. Clin. Invest.* **1989**, *83*(5), 1667-1675.
117. Inoguchi, T.; Battan, R.; Handler, E.; Sportsman, H. W.; King, G. L. Preferential elevation of protein kinase C isoform βII and diacylglycerol levels in the aorta and heart of diabetic rats: differential reversibility to glycemic control by islet cell transplantation. *Proc. Natl. Acad. Sci. U S A* **1992**, *89*, 11059-11063.
118. Nakamura, J.; Kato, K.; Hamada, Y.; Nakayama, M.; Chaya, S.; Nakashima, E.; Naruse, K.; Kasuya, Y.; Mizubayashi, R.; Miwa, K.; Yasuda, Y.; Kamiya, H.; Ienaga, K.; Sakakibara, F.; Koh, N.; Hotta, N. A protein kinase C-β-selective inhibitor ameliorates neural dysfunction in streptozotocin-induced diabetic rats. *Diabetes* **1999**, *48*(10), 2090-2095.

119. Ruan, X.; Arendshorst, W. J. Role of protein kinase C in angiotensin II-induced renal vasoconstriction in genetically hypertensive rats. *Am. J. Physiol.* **1996**, *39*(6), F945-F952.
120. Koya, D.; Haneda, M.; Nakagawa, H.; Isshiki, K.; Sato, H.; Maeda, S.; Kikkawa, R. Amelioration of accelerated diabetic mesangial expansion by treatment with a PKC β inhibitor in diabetic db/db mice, a rodent model for type 2 diabetes. *FASEB J.* **2000**, *14*(3), 439-447.
121. Gerber, G.; Kangrga, I.; Ryu, P. D.; Larew, J. S.; Randic, M.; Multiple effects of phorbol esters in the rat spinal dorsal horn. *J. Neurosci.* **1989**, *9*(10), 3606-3617.
122. Malmberg, A. B.; Chen, C.; Tonegawa, S.; Basbaum, A. I. Preserved acute pain and reduced neuropathic pain in mice lacking PKCγ. *Science* **1997**, *278*(5336), 279-283.
123. Khaser, S. G.; Lin, Y-H.; Martin, A.; Dadgar, J.; McMahon, T.; Wang, D.; Hundle, B.; Aley, K. O.; Isenberg, W.; McCarter, G.; Green, P. G.; Hodge, C. W.; Levine, J. D.; Messing, R. O. A novel nociceptor signaling pathway revealed in protein kinase Cε mutant mice. *Neuron* **1999**, *24*, 253–260.
124. Igwe, O. J.; Chronwall, B. M. Hyperalgesia induced by peripheral inflammation is mediated by protein kinase C βII isozyme in the rat spinal cord. *Neuroscience* **2001**, *104*(3), 875-890.
125. Ahlgren, S. C.; Levine, J. D. Protein kinase C inhibitors decrease hyperalgesia and C-fiber hyperexcitability in the streptozotocin-diabetic rat. *J. Neurophysiol.* **1994**, *72*(2), 684-692.
126. Barber, L. A.; Vasko, M. R. Activation of protein kinase C augments peptide release from rat sensory neurons. *J. Neurochem.* **1996**, *67*(1), 72-80.
127. Koya, D.; King, G. L. Protein kinase C activation and the development of diabetic complications. *Diabetes* **1998**, *47*(6), 859-866.
128. Inoguchi, T.; Battan, R.; Handler, E.; Sportsman, J. R.; Heath, W.; King, G. L. Preferential elevation of protein kinase C isoform beta II and diacylglycerol levels in the aorta and heart of diabetic rats: differential reversibility to glycemic control by islet cell transplantation. *Proc. Natl. Acad. Sci. U S A* **1992**, *89*(22), 11059-11063.
129. Inoguchi, T.; Xia, P.; Kunisaki, M.; Higashi, S.; Feener, E.P.; King, G.L. Insulin's effect on protein kinase C and diacylglycerol induced by diabetes and glucose in vascular tissues. *Am. J. Physiol*. **1994**, *267*(3), E369-E379.
130. Koya, D.; Jirousek, M. R.; Lin, Y. W.; Ishii, H.; Kuboki, K.; King, G. L. Characterization of protein kinase C beta isoform activation on the gene expression of

transforming growth factor-beta, extracellular matrix components, and prostanoids in the glomeruli of diabetic rats. *J. Clin. Invest.* **1997**, *100* (1), 115-126.

131. Ring, B. J.; Gillespie, J. S.; Binkley, S. N.; Campanale, K. M.; Wrighton, S. A. The interactions of a selective protein kinase C beta inhibitor with the human cytochromes P450. *Drug Metab. Dispos.* **2002**, *30*(9), 957-961.
132. Frank, R. N. Potential new medical therapies for diabetic retinopathy: protein kinase C inhibitors. *Am. J. Ophthalmol.* **2002**, *133*(5), 693-698.
133. Löwenberg, M. Proximal signaling molecules as potential targets for anti-inflammatory therapy. *Curr. Opin. Drug Discov. Devel.* **2007**, *10*(5), 560-564.
134. Meyer, T.; Regenass, U.; Fabbro, D.; Alteri, E.; Röusel, J.; Möller, M.; Matter, A. A derivative of staurosporine (CGP 41 251) shows selectivity for protein kinase C inhibition and *in vitro* anti-proliferative as well as *in vivo* anti-tumor activity. *Int. J. Cancer* **1989**, *43*(5), 851-856.
135. Ciulla, T. A.; Amador, A. G.; Zinman, B. Diabetic retinopathy and diabetic macular edema pathophysiology, screening, and novel therapies. *Diabetes Care* **2003**, *26*(9), 2653-2664.
136. Comer, G. M.; Ciulla, T. A. Pharmacotherapy for diabetic retinopathy. *Curr. Opin. Ophthalmol.* **2004**, *15*(6), 508-518.
137. Propper, D. J.; McDonald, A. C.; Man, A.; Thavasu, P.; Balkwill, F.; Braybrooke, J. P.; Twelves, C. Phase I and pharmacokinetic study of PKC412, an inhibitor of protein kinase C. *J. Clin. Oncol.* **2001**, *19*(5), 1485-1492.
138. Campochiaro, P. A. Reduction of diabetic macular edema by oral administration of the kinase inhibitor PKC412. *Invest. Ophthalmol. Vis. Sci.* **2004**, *45*(3), 922-931.
139. PKC-dRS Study Group. The effect of ruboxistaurin on visual loss in patients with moderately severe to very severe nonproliferative diabetic retinopathy: initial results of the Protein Kinase C beta Inhibitor Diabetic Retinopathy Study (PKC-DRS) multicenter randomized clinical trial. *Diabetes* **2005**, *54*(7), 2188-2197.
140. Aiello, L. P.; Davis, M. D.; Girach, A.; Kles, K. A.; Milton, R. C.; Sheetz, M. J.; Zhi, X. E. Effect of ruboxistaurin on visual loss in patients with diabetic retinopathy. *Ophthalmol.* **2006**, *113*(12), 2221-2230.
141. Aiello, L. P.; Bursell, S. E.; Clermont, A.; Duh, E.; Ishii, H.; Takagi, C.; King, G. L. Vascular endothelial growth factor–induced retinal permeability is mediated by protein kinase C *in vivo* and suppressed by an orally effective β-isoform–selective inhibitor. *Diabetes* **1997**, *46*(9), 1473-1480.

142. Koya, D.; King, G. L. Protein kinase C activation and the development of diabetic complications. *Diabetes* **1998**, *47*(6), 859-866.
143. Donnelly R. Protein Kinase C. A novel therapeutic target in microvascular complications. *Mod. Diabetes Manage.* **2000**, *1*, 13-16
144. Gardner, T. W.; Antonetti, D. A. Ruboxistaurin for diabetic retinopathy. *Ophthalmol.* **2006**, *113*(12), 2135-2136.
145. PKC-DMES study group. Effect of ruboxistaurin in patients with diabetic macular edema: thirty-month results of the randomized PKC-DMES clinical trial. *Arch. Ophthalmol.* **2007**, *125*(3), 318-324.
146. Xu, Y.; Wang, S.; Feng, L.; Zhu, Q.; Xiang, P.; He, B. Blockade of PKC-beta protects HUVEC from advanced glycation end products induced inflammation. *Int. Immunopharmacol.* **2010**, *10*(12), 1552-1559.
147. Tuttle, K. R.; Anderberg, R. J.; Cooney, S. K.; Meek, R. L. Oxidative stress mediates protein kinase C activation and advanced glycation end product formation in a mesangial cell model of diabetes and high protein diet. *Am. J. Nephrol.* **2008**, *29*(3), 171-180.
148. Mueller, B. K.; Mack, H.; Teusch, N. Rho kinase, a promising drug target for neurological disorders. *Nat. Rev. Drug Discov.* **2005**, *4*(5), 387-398.
149. Lingor, P.; Teusch, N.; Schwarz, K.; Mueller, R.; Mack, H.; Bähr, M.; Mueller, B. K. Inhibition of Rho kinase (ROCK) increases neurite outgrowth on chondroitin sulphate proteoglycan *in vitro* and axonal regeneration in the adult optic nerve *in vivo*. *J. Neurochem.* **2007**, *103*(1), 181-189.
150. Cornell, W. D.; Cieplak, P.; Bayly, C. I.; Gould, I. R.; Merz, K. M.; Ferguson, D. M.; Kollman, P. A. A second generation force field for the simulation of proteins, nucleic acids, and organic molecules. *J. Am. Chem. Soc.* **1995**, *117*(19), 5179-5197.
151. Lippow, S. M.; Tidor, B. Progress in computational protein design. *Curr. Opin. Biotechnol.* **2007**, *18*(4), 305-311.
152. Olsson, M. H.; Søndergaard, C. R.; Rostkowski, M.; Jensen, J. H. PROPKA3: consistent treatment of internal and surface residues in empirical pKa predictions. *J. Chem. Theor. Comput.* **2011**, *7*(2), 525-537.
153. Sastry, G. M.; Adzhigirey, M.; Day, T.; Annabhimoju, R.; Sherman, W. Protein and ligand preparation: parameters, protocols, and influence on virtual screening enrichments. *J. Comput. Aided. Mol. Des.* **2013**, *27*(3), 221-234.

154. Li, H.; Robertson, A. D.; Jensen, J. H. Very fast empirical prediction and interpretation of protein pKa values. *Proteins* **2005**, *61*, 704–721.
155. Therese, P. J.; Manvar, D.; Kondepudi, S.; Battu, M. B.; Sriram, D.; Basu, A.; Yogeeswari, P.; Kaushik-Basu, N. Multiple e-pharmacophore modeling, 3D-QSAR, and high-throughput virtual screening of hepatitis C virus NS5B polymerase inhibitors. *J. Chem. Inf. Model.* **2014**, *54*(2), 539-552.
156. Zhao, W.; Hevener, K. E.; White, S. W.; Lee, R. E.; Boyett, J. M. A statistical framework to evaluate virtual screening. *BMC Bioinfo.* **2009**, *10*(1), 225.
157. Sheridan, R. P.; Singh, S. B.; Fluder, E. M.; Kearsley, S. K. Protocols for bridging the peptide to nonpeptide gap in topological similarity searches. *J. Chem. Inf. Comput. Sci.* **2001**, *41*(5), 1395-1406.
158. Fechner, N.; Jahn, A.; Hinselmann, G.; Zell, A. Estimation of the applicability domain of kernel-based machine learning models for virtual screening. *J. Cheminform*. **2010**, *2*(1), 2.
159. ROCS 3.2.0.4: OpenEye Scientific Software, Santa Fe, NM. http://www.eyesopen. com.
160. Qikprop, version 3.4, Schrodinger, LLC, New York, NY, 2011.
161. Doran, J.D.; Jacobs, M.D. ROCK enzymatic assay. *Method. Mol.Biol.* **2008**, *468*, 197-205.
162. Zegzouti, H.; Zdanovskaia, M.; Hsiao, K.; Goueli, S. A. ADP-Glo: A Bioluminescent and homogeneous ADP monitoring assay for kinases. *Assay Drug Dev. Technol.* **2009**, *7*(6), 560-572.
163. Plumb, J. A.. Cell sensitivity assays: the MTT assay. In Cancer Cell Culture. **2004**, Humana Press. 165-169.
164. Das, S.; Rao, N.; Rao, S. Mangiferin attenuates methylmercury induced cytotoxicity against IMR-32, human neuroblastoma cells by the inhibition of oxidative stress and free radical scavenging potential. *Chem. Biol. Interact.* **2011**, *193*(2), 129-140.
165. Agawane, S. M.; Nagarkar, J. M. Nano ceria catalyzed Ullmann type coupling reactions. *Tetrahedron Lett.* **2011**, *52*(41), 5220-5223.
166. Gowda, D. C.; Mahesh, B.; Gowda, S. Zinc-catalyzed ammonium formate reductions: Rapid and selective reduction of aliphatic and aromatic nitro compounds. *Ind. J. Chem.* **2001**, *40*(1), 75-77.
167. Raju, B.; Ragul, R.; Sivasankar, B. N. A new reagent for selective reduction of nitro group. *Ind. J. Chem.* **2009**, *48*(9), 1315-1319.

168. Niesen, F. H.; Berglund, H.; Vedadi, M. The use of differential scanning fluorimetry to detect ligand interactions that promote protein stability. *Nat. Protoc.* **2007**, *2*(9), 2212-2221.
169. Rao, V. S.; Rao, A.; Karanth, K. S. Anticonvulsant and neurotoxicity profile of Nardostachys jatamansi in rats. *J. Ethnopharmacol.* **2005**, *102*(3), 351-356.
170. Yogeeswari, P.; Sriram, D.; Saraswat, V.; Ragavendran, J. V.; Kumar, M.; Murugesan, S.; Thirumurugan, R.; Stables, J. P. Synthesis and anticonvulsant and neurotoxicity evaluation of *N*4-phthalimido phenyl (thio) semicarbazides. *Eur. J. Pharm. Sci.* **2003**, *20*(3), 341-346.
171. Murakami, T.; Iwanaga, T.; Ogawa, Y.; Fujita, Y.; Sato, E.; Yoshitomi, H.; Sunada, Y.; Nakamura, A. Development of sensory neuropathy in streptozotocin-induced diabetic mice. *Brain Behav.* **2013**, *3*(1), 35-41.
172. Chaplan, S. R.; Bach, F. W.; Pogrel, J. W.; Chung, J. M.; Yaksh. T. L. Quantitative assessment of tactile allodynia in the rat paw. *J. Neurosci. Methods.* **1994**, *53*(1), 55-63.
173. Espejo, E. F.; Mir, D. Structure of the rat's behaviour in the hot plate test. *Behav. Brain. Res.* **1993**, *56*(2), 171-176.
174. Courteix, C.; Eschalier, A.; Lavarenne, J. Streptozocin-induced diabetic rats: behavioural evidence for a model of chronic pain. *Pain* **1993**, *53*(1), 81-88.
175. Miyoshi, T.; Goto, I. Serial *in vivo* determinations of nerve conduction velocity in rat tails. Physiological and pathological changes. *Electroencephalogr. Clin. Neurophysiol.* **1973**, *35*(2), 125-131.
176. Bennett, G. J., Xie, Y. K. A peripheral mononeuropathy in rat that produces disorders of pain sensation like those seen in man. *Pain* **1988**, *33*(1), 87-107.
177. Colburn, R. W.; Lubin, M. L.; Stone, D. J.; Wang, Y.; Lawrence, D.; D'Andrea, M. R.; Brandt, M. R.; Liu, Y.; Flores, C. M.; Qin, N. Attenuated cold sensitivity in TRPM8 null mice. *Neuron* **2007**, *54*(3), 379-386.
178. Ahlgren, S. C.; Levine, J. D. Mechanical hyperalgesia in streptozotocin-diabetic rats. *Neuroscience* **1993**, *52*(4), 1049-1055.
179. Carter, R. J.; Lione, L. A.; Humby, T.; Mangiarini, L.; Mahal, A.; Bates, G. P.; Dunnett, S. B.; Morton, A. J. Characterization of progressive motor deficits in mice transgenic for the human Huntington's disease mutation. *J. Neurosci.* **1999**, *19*(8), 3248-3257.
180. Dietrich, M. O.; Mantese, C. E.; Anjos, G. D.; Souza, D. O.; Farina, M. Motor impairment induced by oral exposure to methylmercury in adult mice. *Environ. Toxicol. Pharmacol.* **2005**, *19*(1), 169-175.

181. Xu, Y.; Ku, B. S.; Yao, H. Y.; Lin, Y. H.; Ma, X.; Zhang, Y. H.; Li, X. J. The effects of curcumin on depressive-like behaviours in mice. *Eur. J. Pharmacol.* **2005**, *518*(1), 40-46.
182. Ennaceur, A.; Delacour, J. A new one-trial test for neurobiological studies of memory in rats: Behavioral data. *Behav. Brain Res.* **1988**, 31(1), 47-59.
183. Morris, R. Developments of a water-maze procedure for studying spatial learning in the rat. *J. Neurosci. Methods*. **1984**, *11*(1), 47-60.
184. Grant, J. A.; Gallardo, M. A.; Pickup, B. T. A fast method of molecular shape comparison: A simple application of a Gaussian description of molecular shape. *J. Comp.Chem.* **1966**, *17*(14), 1653-1666.
185. Lipinski, C. A.; Lombardo, F.; Dominy, B. W.; Feeney, P. J. Experimental and computational approaches to estimate solubility and permeability in drug discovery and development settings. *Adv. Drug Deliv. Rev.* **2012**, *64*, 4-17.
186. Fujimura, M.; Usuki, F.; Kawamura, M.; Izumo, S.; Inhibition of the Rho/ROCK pathway prevents neuronal degeneration *in vitro* and *in vivo* following methylmercury exposure. *Toxicol. Applied Pharmacol.* **2011**, *250*(1), 1-9.
187. Huyck, L.; Ampe, C.; VanTroys, M. The XTT cell proliferation assay applied to cell layers embedded in three-dimensional matrix. *Assay Drug Dev. Technol.* **2012**, *10*(4), 382-392.
188. Fournier, A. E.; Takizawa, B. T.; Strittmatter, S. M. Rho kinase inhibition enhances axonal regeneration in the injured CNS. *J. Neurosci.* **2003**, *23*(4), 1416-1423.
189. Versteeg, R.; Koster, J. J. B.; Molenaar, J. J.; Westerhout, E. Rho kinase inhiitors for use in the treatment of neuroblastoma, Europian patent publication number EP2628482 A1, August 21, **2013**.
190. Jin, L.; Ying, Z.; Webb, R. C. Activation of Rho/Rho kinase signaling pathway by reactive oxygen species in rat aorta. *Am. J. Physiol. Heart Circ. Physiol.* **2004**, *287*(4), H1495-H1500.
191. Lu, Y.; Li, H.; Jian, W.; Zhuang, J.; Wang, K.; Peng, W.; Xu, Y. The Rho/Rho-associated protein kinase inhibitor fasudil in the protection of endothelial cells against advanced glycation end products through the nuclear factor κB pathway. *Exp. Ther. Med.* **2013**, *6*(2), 310-316.
192. Schirok, H.; Kast, R.; Figueroa-Pérez, S.; Bennabi, S.; Gnoth, M. J.; Feurer, A. Design and synthesis of potent and selective azaindole-based Rho kinase (ROCK) inhibitors. *Chem. Med. Chem*. **2008**, *3*(12), 1893-904.

193. ACD/ChemSketch, version 12.01, Advanced Chemistry Development, Inc., Toronto, On, Canada, www.acdlabs.com, **2014**.
194. LigPrep, version 2.5, Schrödinger, LLC, New York, NY, USA, **2012**.
195. Maestro, version 9.2, Schrödinger, LLC, New York, NY, USA, **2011**.
196. Berman, H. M.; Westbrook, J.; Feng, Z.; Gilliland, G.; Bhat, T. N.; Weissig, H.; Shindyalov, I. N.; Bourne, P.E. The protein data bank. *Nucleic. Acid Res.* **2000**, *28*(1), 235-242.
197. Schrödinger Suite **2011** Protein Preparation Wizard; Epik version 2.2, Schrödinger, LLC, New York, NY, USA, **2011**; Impact version 5.7, Schrödinger, LLC, New York, NY, USA, **2011**; Prime version 3.0, Schrödinger, LLC, New York, NY, USA, **2011**.
198. Glide, version 5.7, Schrödinger, LLC, New York, NY, USA, **2011**.
199. Doran, J. D.; Jacobs, M. D. Methods in Molecular Biology, in: Walker, J. M., Vincan, E. Wnt Signaling: Pathway Methods and Mammalian Models. *Methods Mol. Biol*. **2008**, *468*, 197-205.
200. Chang, T. C.; Chen, Y. C.; Yang, M. H.; Chen, C. H.; Hsing, E. W.; Ko, B. S.; Liou, J. Y.; Wu, K. K. Rho kinases regulate the renewal and neural differentiation of embryonic stem cells in a cell plating density-dependent manner. *PLoS One* **2010**, *5*(2):e9187.
201. Jin, L.; Ying, Z.; Webb, R. C. Activation of Rho/Rho kinase signaling pathway by reactive oxygen species in rat aorta. *Am. J. Physiol. Heart. Circ. Physiol.* **2004**, *287*(4), H1495-H1500.
202. Eto, K.; Tokunaga, H.; Nagashima, K.; Takeuchi, T. An autopsy case of Minamata disease (methylmercury poisoning) pathological viewpoints of peripheral nerves. *Toxicol. Pathol.* **2002**, *30*(6), 714-722.
203. Park, S. T.; Lim, K. T.; Chung, Y. T.; Kim, S. U.; Methylmercury-induced neurotoxicity in cerebral neuron culture is blocked by antioxidants and NMDA receptor antagonist. *Neurotoxicology* **1996**, *17*, 37–45.
204. Sakamoto, M.; Ikegami, N.; Nakano, A. Protective effects of Ca2+ channel blockers against methyl mercury toxicity. *Pharmacol. Toxicol.* **1996,** *78*(3), 193-199.
205. Daré, E.; Götz, M. E.; Zhivotovsky, B.; Manzo, L.; Ceccatelli, S. Antioxidants J811 and 17beta-estradiol protect cerebellar granule cells from methylmercury-induced apoptotic cell death. *J. Neurosci. Res.* **2000**, *62*, 557–565.
206. Moretto, M. B.; Funchal, C.; Zeni, G.; Pessoa-Pureur, R.; Rocha, J. B. Selenium compounds prevent the effects of methylmercury on the *in vitro* phosphorylation of skeletal proteins in cerebral cortex of young rats. *Toxicol. Sci.*, **2005**, *85*, 639–646.

207. Chang, J. Y.; Tsai, P. F. Prevention of methylmercury-induced mitochondrial depolarization, glutathione depletion and cell death by 15-deoxy-delta-12, 14-prostaglandin J(2). *Neurotoxicology* **2008**, *29*, 10574–11061.
208. Tomasevic, N.; Jia, Z.; Russell, A.; Fujii, T.; Hartman, J. J.; Clancy, S.; Wang, M.; Beraud, C.; Wood, K. W.; Sakowicz, R. Differential regulation of WASP and N-WASP by Cdc42, Rac1, NCK, and PI(4, 5)P2. *Biochemistry* **2007**, *46*, 3494–3502.
209. Fujimura, M.; Fusako, U.; Miwako, K.; Izumo, S. Inhibition of the Rho/ROCK pathway prevents neuronal degeneration *in vitro* and *in vivo* following methylmercury exposure. *Toxicol. Appl. Pharmacol.* **2011,** *250*(1), 1-9.
210. Arvanitakis, Z.; Wilson, R. S.; Bienias, J. L.; Evans, D. A.; Bennett, D. A. Diabetes mellitus and risk of Alzheimer disease and decline in cognitive function. *Arch. Neurol.* **2004**, *61*(5), 661-666.
211. Boyce-Rustay, J. M.; Simler, G. H.; McGaraughty, S.; Chu, K. L.; Wensink, E. J.; Vasudevan, A.; Honore, P. Characterization of Fasudil in preclinical models of pain. *J. Pain* **2010,** *11*(10), 941-949.
212. Brooks, S. P.; Dunnett, S. B. Tests to assess motor phenotype in mice: a user's guide. *Nat. Rev. Neurosci.* **2009**, *10*(7), 519-529.
213. Onishchenko, N.; Tamm, C.; Vahter, M.; Hökfelt, T.; Johnson, J. A.; Johnson, D. A.; Ceccatelli, S. Developmental exposure to methylmercury alters learning and induces depression-like behavior in male mice. *Toxicol. Sci.* **2007**, *97*(2), 428-437.
214. Akers, K. G.; Martinez-Canabal, A.; Restivo, L.; Yiu, A. P.; De Cristofaro, A.; Hsiang, H. L. L.; Frankland, P. W. Hippocampal Neurogenesis Regulates Forgetting During Adulthood and Infancy. *Science* **2014**, *344*(6184), 598-602.
215. Lledo, P. M.; Alonso, M.; Grubb, M. S. Adult neurogenesis and functional plasticity in neuronal circuits. *Nat. Rev. Neurosci.* **2006**, *7*(3), 179-193.
216. Hardt, O.; Nader, K.; Nadel, L. Decay happens: the role of active forgetting in memory. *Trends. Cogn. Sci.* **2013,** *17*(3), 111-120.
217. Frankland, P. W.; Köhler, S.; Josselyn, S. A. Hippocampal neurogenesis and forgetting. *Trends. Neurosci.* **2013**, *36*(9), 497-503.
218. Antunes, M.; Biala, G. The novel object recognition memory: neurobiology, test procedure, and its modifications. *Cogn. Process.* **2012**, *13*(2), 93-110.
219. Steru, L.; Chermat, R.; Thierry, B.; Simon, P. The tail suspension test: a new method for screening antidepressants in mice. *Psychopharmacology* **1985**, *85*(3), 367-370.

220. Grum, D. K.; Kobal, A. B.; Arnerič, N.; Horvat, M.; Ženko, B.; Džeroski, S.; Osredkar, J. Personality traits in miners with past occupational elemental mercury exposure. *Environ. Health Perspect.* **2006**, *114*(2), 290-296.

221. Grodsky, N.; Li, Y.; Bouzida, D.; Love, R.; Jensen, J.; Nodes, B.; Grant, S. Structure of the catalytic domain of human protein kinase C β II complexed with a bisindolylmaleimide inhibitor. *Biochemistry* **2006**, *45*(47), 13970-13981.

222. Yogeeswari, P.; Sriram, D.; Reddy, S. K.; Ragavendran, J. V.; Semwal, A.; Mishra, R. K. Novel N-Spiro substituted compounds for the treatment of epilepsy and neuropathic pain. Indian Patent No. 263536 (Patent Issue date: 07/11/2014).

223. Verity, M. A.; Sarafian, T.; Pacifici, E. H.; Sevanian, A. Phospholipase A2 stimulation by methyl mercury in neuron culture. *J. Neurochem.* **1994**, *62*(2), 705-714.

APPENDIX

Patent and Publications

Patent

1. Yogeeswari, P.; Sriram, D.; Reddy, S. K.; Ragavendran, J.V.; Semwal, A.; Mishra, R. K. Indian Patent No. 263536 (Patent Issue date: 07/11/2014): Novel N-Spiro substituted compounds for the treatment of epilepsy and neuropathic pain.

Publications

1. Mishra, R. K.; Alokam, R.; Singhal, S. M.; Srivathsav, G.; Sriram, D.; Basu, N. K.; Manvar, D.; Yogeeswari, P. Design of novel Rho kinase inhibitors using energy based pharmacophore modelling, shape based screening, *in silico* virtual screening and *in vitro* assays. *J. Chem. Inf. Model*. 2014, *54(10)*, 2876-86. [Impact factor **4.06**]
2. Mishra, R. K.; Gangadhar, M.; Sriram, D.; Yogeeswari, P. Future directions in the treatment of neuropathic pain: a review on various therapeutic targets. *CNS Neurol. Disord. Drug. Targets.* 2014**,** *13(1)*, 63-81. [Impact factor **3.72**]
3. Mishra, R. K.; Alokam, R.; Sriram, D.; Yogeeswari, P. Potential role of Rho kinase inhibitors in combating diabetes-related complications including diabetic neuropathy-a review. *Curr. Diabetes. Rev*. 2013, *9(3)*, 249-66. [Impact factor **3.00**] (Most accessed article during March-2014)
4. Jha, D.; Mishra, R. K.; Pandey, R. Biosimilars: current regulatory perspective and challenges. *J. Pharm. Bioall. Sci.*, 2013, *5*, 80-81. [Impact factor **0.17**]
5. Meza-Avina, M. E.; Wei, L.; Liu, Y.; Poduch, E.; Bello, A. M.; Mishra, R. K.**;** Pai, E. F.; Kotra, L. P. Structural determinants for the inhibitory ligands of orotidine-5'-monophosphate decarboxylase. *Bioorg. Med. Chem.* 2010, *18*, 4032-4041. [Impact factor **2.90**]
6. Semwal, A.; Mishra, R. K.; Sriram, D.; Yogeeswari, P. Current approaches with the glutamatergic system as targets in the treatment of neuropathic pain. *Expert Opin. Ther. Targets.* 2009, *13*, 925-943. [Impact factor **4.13**]
7. Semwal, A.; Reddy, S. K.; Mishra, R. K.; Ragavendran, J. V.; Sriram, D.; Yogeeswari, P. Discovery of novel N-spiro substituted GABA derivatives for the treatment of epilepsy and neuropathic pain: synthesis and neuropharmacology.[Communicated to *J. Med. Chem.* (ACS), Impact factor **5.48**]

8. Mishra, R. K.; Alokam, R.; Gangadhar, M.; Sriram, D.; Yogeeswari, P. Design of novel protein Kinase Cβ-II inhibitors for the treatment of neurological complications of diabetes. [Communicated to *CNS Neurol. Disord. Drug. Targets.* (Bentham), Impact factor **3.72**]
9. Mishra, R. K.; Chowdary, R.; Racharla, S.; Singhal, S. M.; Gaus, A. Srivathsav, G.; Matharsala, G.; Sriram, D.; Yogeeswari, P. Development of novel 2,4-diaminopyrimidine derivatives as Rho-kinase inhibitors. [Communicated to *Eur. J. Med. Chem.* (Elsevier) , Impact factor **3.43**]
10. Bomba, T., Benoit, T. N.; Matharasala, G.; Mishra, R. K.; Battu, M. B.; Sriram, D.; Kamanyi, A.; Yogeeswari, P. Antihypernociceptive effects of *Petersianthus macrocarpus* stem bark on neuropathic pain induced by chronic constriction injury.[Communicated to *J. Ethnopharmacol.* (Elsevier), Impact factor **2.93**]

CONFERENCE PRESENTATION HIGHLIGHTS

1. Evaluation of anti-nociceptive properties of novel Rho kinase inhibitors using animal models of neuropathic pain, on 16th -18th December, 2013 at 46th Annual Conference of the Indian Pharmacological Society, IPSCON 2013; Bangalore, India. Mishra, R. K.; Matharsala, G.; Srivatsav, G.; Singhal, S. M.; D. Sriram and P. Yogeeswari.
2. Evaluation of anti-nociceptive properties of novel curcumin derivatives using animal models of neuropathic pain, on 2nd-5th May, 2013 at 5th ASEAPS, 2013, Singapore. Semwal, A.; Mishra, R. K.; Sriram, D.; Yogeeswari, P.
3. Design of novel Rho kinase inhibitors for the treatment of diabetic complications using energy based pharmacophore modeling, *in silico* screening and docking studies, on 27th September, 2012 at 3rd World Congress on Diabetes and Metabolism, Hyderabad, India. Mishra, R. K.; Alokam, R.; Sriram, D.; Yogeeswari, P.
4. Retro-pharmacophore mapping of the active site of orotidine-5'-o-monophosphate decarboxylase, on 31st March, 2009 at Syngenta Inc., Greensboro, USA; Mishra, R. K.; Pai, E. F.; Kotra, L. P. (2nd prize in poster presentation session).
5. Synthesis of C6-substituted-L-uridine derivatives as potential inhibitors of orotidine-5'-o-monophosphate decarboxylase, on 31st March, 2009 at Syngenta Inc., Greensboro, USA; Vanampally, C.; Meza-Avina, E. M.; Konforte, D.; Crandall, I.; Poduch, E.; Mishra, R. K.; Paige, C. J.; Kain, K. C.; Kotra, L. P.
6. Development of database for micro-computerised identification and standardization of herbal crude drugs and development of standards, on 23rd March, 2007 at APOGEE: BITS Pilani, Pilani, India. Mishra, R. K.

Biography: Ram Kumar Mishra

Mr. Ram Kumar Mishra finished his B. Pharm. from Birla Institute of Technology, Mesra, Ranchi (2006), and M. Pharm. from Birla Institute of Technology & Sciences-Pilani, Pilani, Rajasthan (2008). He worked as Research Associate at the University of North Carolina, Greensboro, NC, USA, and University Health Networks, Toronto, ON, CANADA (2008-2010). He has been working under the supervision of Prof. P. Yogeeswari since January 2011. To his name, he has one patent and six peer-reviewed publications in national and international journals. He had also presented his work at various international and national conferences. During his Ph.D., He was awarded CSIR-Senior Research Fellowship in 2012, and was the Editor of Probe magazine from 2012-2014.

Biography: Prof. P Yogeeswari

Dr. P. Yogeeswari is presently working in the capacity of Professor and Associate Dean (Sponsored Research and Consultancy Division), Department of Pharmacy, Birla Institute of Technology and Science-Pilani, Hyderabad Campus, INDIA. She received her Ph.D. degree in the year 2001 from Banaras Hindu University; Varanasi. She has been involved in research for the last 14 years and in teaching for 13 years. Association of Pharmacy Teachers of India (APTI) honoured her with "*Young Pharmacy Teacher Award"* for the year 2007. In 2010, ICMR honoured her by awarding "*Shakuntala Amir Chand Award*" for her excellent biomedical research. She has been awarded for IASP 2014 "*Excellence in Pain Research and Management in Developing Countries*" under the basic science research category at Argentina in October 2014. She has collaborations with various national and international organizations that include National Institute of Health, Bethesda, USA, National Institute of Mental Health and Neurosciences, Bangalore, Karolinska Institute, Stockholm, Sweden, National Institute of Immunology, New Delhi, India, Pasteur Institute, University of Lille, France, Bogomoletz Institute of Physiology National Academy of Science, Ukraine, and Faculty of Medicine of Porto, Porto, Portugal,. She has to her credit one Patent and more than 190 research publications. She is an expert reviewer of many international journals like Journal of Medicinal Chemistry (ACS), Journal of Chemical Information & Modelling (ACS, USA), Bioorganic Medicinal Chemistry (Elsevier), Recent Patents on CNS Drug Discovery (Bentham), etc. She has also co-authored a textbook on organic medicinal chemistry with Dr. D Sriram titled "Medicinal Chemistry" published by Pearson Education and one book chapter in in Jan 2013 by IGI Global. She is a lifetime member of Association of Pharmacy Teachers of India and Indian Pharmacological Society. She has successively completed many sponsored projects and currently on projects sponsored by DST, DBT INDO-BRAZIL, ICMR-INSERM, and CSIR. She has guided six Ph.D. students and currently thirteen students are pursuing their Ph.D. work.